University of Bath

UNIVERSITY OF
BATH

PHD

Mathematical modelling of mixed gas breathing equipment and associated systems

Lo, Julian Kwan Wa

Award date:
1995

Awarding institution:
University of Bath

Link to publication

MATHEMATICAL MODELLING OF

MIXED GAS BREATHING EQUIPMENT

AND ASSOCIATED SYSTEMS

Submitted by

Julian Kwan Wa Lo
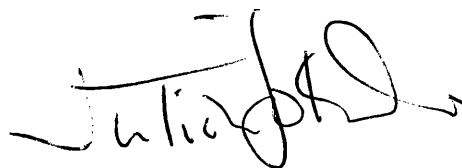
for the degree of Ph.D.

1995

COPYRIGHT

UMI Number: U076486

UMI

Dissertation Publishing

ProQuest

SUMMARY

This thesis describes the development of mathematical models for the simulation of underwater breathing apparatus and the human respiratory system. The objective is to provide the designer with a tool for the analysis and design of underwater breathing apparatus. Such a tool is likely to offer considerable insight into the assessment of the limits of a broad range of equipment without risk to human life.

Mathematical models have been developed for the individuals components of the underwater breathing apparatus to predict overall system performance. A technique to simulate the variation of gas composition in the breathing apparatus is presented which allows breathing gas poisoning to be indicated. An approach to simulate the carbon dioxide absorption in an axial flow scrubber has been developed. The models have been used to simulate the performance of a semi-closed-circuit breathing system and a surface demand diving system during unmanned test conditions. Good agreement is obtained between the predicted and measured data. Simulation has been used to assess system modifications to improve system performance.

A realistic human respiratory system model has been developed. The mass balance equations and a chemical buffering system have been used as a basis for the development of this model. The model incorporates mechanical and chemical control of breathing which provides an automatic control of respiration at different environmental conditions. The parameters required for the human respiratory system model have been obtained from published clinical measurement where possible the unknown parameters have been identified by comparing the simulation results with available experimental data. The human respiratory model has been used for assessing human interaction with different kinds of underwater breathing apparatus. The simulations of manned diving operation using the semi-closed-circuit breathing system and the surface demand diving system indicate that the models enables more detailed system performance during actual diving condition to be explored and allow decompression process to be studied.

Finally, the simulations of a submarine escape system and an industrial pneumatic system have demonstrated that the developed techniques can be applied to other gas based system, providing substantial benefit for system designers.

ACKNOWLEDGEMENTS

I would like to thank Dr. Derek Tilley and Dr. Steve Tomlinson for their excellent and valuable supervision and guidance throughout this project. Also, I would like to thank all my colleagues in the Fluid Power Centre.

Further thanks are due to Professor Cliff Burrows for his invaluable support and encouragement during my stay in the University.

I am grateful to the Defence Research Agency, Alverstoke, for supplying experimental data and financial support in the initial two years of this project.

Last but not least I would like to thank my adorable wife for her support and understanding.

CONTENTS

vi

NOTATION

Symbol	Parameters	Units
A	Contact area	m²
A_a	Interfacial area of absorbent per unit volume of bed	m²/m³
A_f	Flow area	m²
ATA	Atmospheric pressure	N/m²
B	Bulb modulas	N/m²
C	Gas concentration in blood	L/L blood
C_c	Ratio between the vena contracta area and flow area	-
C_d	Discharge coefficient	-
C_{le}	Actuator leakage coefficient	(kg/s)/(N/m²)
C_m	Mass flow parameter	(kg/s)√T/N
C_P	Specific heat at constant pressure	J/kg K
C_V	Specific heat at constant volume	J/kg K
D	Diffusion coefficient	m²/s
E	Energy	J
F	Force	N
F_C	Coulomb friction force	N
F_m	Flow momentum force	N
F_P	Net pressure force	N
F_s	Net spring force	N
G	Gain	-
H	Heat transfer	J
I	Inertia	kg m²
J	Flux	m³/s
K	K factor depends on the change of flow direction	-
L	Length	m
M	Gas molecular weight	kg/mole
Ma	Mach number	-
Me	Mass of effective moving parts	kg
MVV	Maximal Voluntary Ventilation	-
N	Number of gas types in the gas mixture, Number of elements	-
N_a	Number of airways	-
N_b	Number of breaths per minute	breath/min
N_{con}	Number of convolutions in the breathing tube	-
P	Pressure	N/m²
P_r	Counterlung resistance pressure	N/m²
$\mathcal{P}$	Hydrostatic pressure	N/m²
Q	Volumetric flow rate	m³/s
Q_r	Respiratory demand volumetric flow	m³/s

Symbol	Parameters	Units
R	Specific gas constant	J/kg K
Re	Reynolds number	-
R_f	Flow resistance	$(N/m^2)/(m^3/s)$
RMV	Respiratory minute volume	L/min
R_o	Universal gas constant	J/mole K
RQ	Respiratory quotient	-
R_v	Ventilation ratio	-
S	Sutherland constant	-
So	Gas solubility coefficient	$L/(L\ N/m^2)$
T	Temperature	K
Tor	Torque	Nm
U	Internal energy	J
V	Volume	m^3
V_v	Available flow volume	m^3
$\dot{V}_{CO2}$	Carbon dioxide production rate	L/min
$\dot{V}_{O2}$	Oxygen consumption rate	L/min
$\dot{V}_r$	Lung ventilation rate	L/min
W	Work done	J
X	Mole fraction	-
Y	Signal in Laplace transform	-
b	Constant used in demand regular model	-
c	Concentration of carbon dioxide	$mole/m^3$
d	Diameter	m
f	Friction factor	-
f_A	Apparent frequency factor	-
f_{dv}	Fraction of alveolar dead space	-
f_m	Flow force factor	-
f_{sh}	Veno-arterial shunts	-
f_v	Viscous friction (speed dependent friction)	N/(m/s)
f_ω	Speed dependent frictional torque coefficient	Nm/(rad/s)
g	Acceleration due to gravity	m/s^2
h	Specific enthalpy	J/kg
k	Stiffness	N/m
k_h	Overall heat transfer coefficient	$J/(s\ m^2\ K)$
k_m	Mass transfer coefficient	m/s
l	Length	m
δl	Length of small element	m
m	Mass of gas	kg
n	Polytropic index	-

Symbol	Parameters	Units
p	Gas pressure	N/m^2
pH	pH level	-
δp	Pressure loss	N/m^2
q	Mass flow rate	kg/s
r	Relative roughness	-
s	Specific entropy or complex variable for Laplace transformation	J/kg K, -
t	Time	second
u	Specific internal energy	J/kg
v	Fluid flow velocity	m/s
w	Concentration of carbon dioxide in the absorbent	mole/kg
x	Displacement	m
y	Signal	-
z	Distance	m
α	Valve poppet angle	degree
β	Coefficient of cubic expansion	K^{-1}
$\boldsymbol{\delta}$	Index for diffusion coefficient	-
γ	Ratio of specific heat	-
ε	Voidage	-
ζ	Equilibrium factor	-
θ	Lever rotating angle	radian
θ_{fix}	Lever fixed bending angle	radian
κ	Isothermal compressibility	m^2/N
λ	Breathing tube bending angle	degree
μ	Dynamic viscosity	Pa s
ρ	Density	kg/m^3
ρ_B	Bulb density, mass of absorbent per volume of bed	kg/m^3
τ	Time constant	-
Φ	Shape factor	-
ϕ	Angle between direction of motion and horizontal	degree
Υ	Breathing tube convolution pitch	m
$\mathcal{H}$	Pressure flow gradient	$(m^3/s)/(N/m^2)$
φ	Flow angle leaving the valve head	degree
υ	Specific volume	m^3/kg
ω	Rotary speed	rev/min

Suffices meaning

1	First
2	Second
B	Brain
D	Physiological dead space
$Dalv$	Alveolar dead space
$Danat$	Anatomical dead space
G	Guidance
H	Heart
H^+	H^+ ion
I	Integral
L	Lever
P	Proportional
T	Tidal volume
a	Artery
act	Actuator
ai	Airway
al	Alveolar
am	Ambient
as	Absorbent surface
at	Atmospheric
aw	Air/water contact
b	Blood
bc	Buoyancy control valve
bn	Small bending chamber in the demand regulator
bo	Gas bottle
bt	Breathing tube
bv	Balance piston valve in the demand regulator
c	Counterlung
ch	When choked flow happen
$chem$	Chemical
cl	Closing lung volume
com	Compressor
cr	Cracking
cv	Submarine escape system control valve head
cy	One cycle
d	Downstream
dem	Demand
di	Diaphragm
dis	For display purpose

Suffices meaning

e	Absorbent particle
eff	Effective
ep	Extrapulmonary
et	Extrathoracic
exc	Gas exchange through the alveolar membrane
exp	Expiratory
ext	External
f	At the opening of the restrictive element
fb	Feedback
fe	Feed
frc	Lung functional residual capacity
g	Gas
h	Hood
hl	Lower part of the hood
i	Gas type (O_2, CO_2, N_2 or He) or element
in	Inlet, incoming
ine	Inert gas (N_2 or He)
inp	Inspiratory
ip	Intrapulmonary
it	Intrathoracic
j	Gas type (O_2, CO_2, N_2 or He)
k	Spring initial compression
l	Lung
la	Large
last	Last
lb	Balance side of the breathing simulator
lc	Large chamber in the demand regulator
ld	Delivery side of the breathing simulator
le	Actuator leakage
lpt	Lung plotted volume
lrv	Lung residual volume
m	Mouth
mp	Mouthpiece
mv	Mushroom valve
n	Nose
nom	Nominal
out	Outlet, leaving
p	Pipe
pa	Pulmonary artery

Suffices meaning

pi	Piston head
pl	Pleural compartment
pr	Production
pv	Pulmonary vein
re	Resistive work
rest	Rest
rg	Regulating valve
rod	Rod head
rv	Reducing valve
s	Scrubber
sm	Small
sur	Component surface contact
sv	Small vent
th	Thoracic
ti	Tissue
tlc	Total lung capacity
to	Total
tow	Tower of the submarine escape system
u	Upstream
up	Uptaken
v	Valve
vs	Valve seat
w	Water
wl	Airway wall

Accents

$\dot{Z}$	Time rate of change of parameter Z
$\bar{Z}$	Mean value of parameter Z
$\tilde{Z}$	Reference value of parameter Z
$\hat{Z}$	Maximum value of parameter Z
$\check{Z}$	Minimum value of parameter Z
Z'	Known value of parameter Z

CHAPTER 1

INTRODUCTION

1.1 INTRODUCTION

A fundamental requirement of any underwater breathing system is that it must be capable of meeting a diver's respiratory demand under all operating conditions. These can vary considerably, depending on the depth of dive, the activity being undertaken, and the physical and psychological state of the diver. The success and circuit performance of such systems depends on how effectively the design can meet the above criteria. Failure to meet any of these requirements can adversely affect the diver's performance and in certain circumstances place the diver's safety at risk.

While manned and unmanned tests are clearly required for system certification, the design process needs conceptual information before hardware is built. This is an ideal application for the use of computer simulation. Such a technique is likely to offer considerable insight into the behaviour of the system under a diverse range of operating conditions and may save considerable fabrication and test expenditures as well as system development time.

The aim of this thesis is to develop a range of modelling techniques which can provide a tool in the analysis and design of underwater breathing apparatus.

1.2 OVERVIEW OF UNDERWATER BREATHING SYSTEMS AND THEIR DESIGN

Breathing apparatus used by divers falls into two main groups: self-contained equipment, in which the diver carries a supply of breathing gas in cylinders, and surface-supplied equipment, where the breathing gas is supplied to the diver through a long hose from the surface.

1.2.1 Self-contained apparatus

Self-contained diving apparatus has the advantage of making the diver far more mobile and

allowing a much greater range of action. This kind of breathing apparatus can be further divided into closed-circuit and open-circuit equipment.

(i) Closed/Semi-closed-circuit breathing apparatus

In this type of apparatus, an example of which is shown in figure 1.1, the gas breathed by the diver is rebreathed from a flexible bag called counterlung via a canister of chemical absorbent which removes carbon dioxide from the exhaled gas. Various valves are incorporated to allow rapid make-up and exhaust of gas from the counterlung in response to changes in ambient pressure. The closed/semi-closed-circuit breathing apparatus may be used for breathing pure oxygen or an oxy-nitrogen mixture. This kind of apparatus has the advantages of greater endurance and not leaving a trial of tell-tale bubbles on the surface. Hence, this kind of apparatus has been used widely for military purposes.

(ii) Open-circuit breathing apparatus

By far the most commonly used open-circuit breathing apparatus is the open circuit SCUBA (Self-Contained Underwater Breathing Apparatus) diving set. The principle of this breathing system is outlined in figure 1.2. This apparatus consists of one or more cylinders of compressed gas (usually air) connected by a manifold to a first-stage regulator which supplies a sensitive second-stage regulator or 'demand valve' actuated by the breathing of the diver. The first- and second-stage regulators may be in one housing, or they may be in separate housing connected by an interstage hose. In the latter configuration the first-stage regulator is mounted on the cylinder manifold and the second-stage demand valve is mounted in a housing attached to the mouthpiece. There are many demand valve designs in addition to that shown in figure 1.3. Some are designed such that the supply flow, once initiated, provides a venturi or vortex effect. This creates a pressure drop in the diaphragm chamber which causes the valve to be held open (ie. inhalation is 'assisted') until flow is no longer accepted by the user. Some use a pilot-operated valve assemblies design so that a very small drop in diaphragm chamber pressure will produce a relatively large increase in supply flow. The purpose of the various designs is to provide the necessary supply flow with minimum suction effort.

1.2.2 Surface supplied equipment

Surface supplied equipment is frequently used in commercial diving, because of its unlimited gas

2

supply and the suitability in communicating with other divers. The ventilated helmet and surface demand diving system are the two dominant types of surface supplied equipment in modern commercial diving.

(i) Ventilated helmet

The ventilated helmet is the only form of modern breathing apparatus which can be traced directly to the ancient diving assemblies. It is effectively an inverted bucket to which has been added a watertight suit or a neck seal to prevent water from entering, an air supply, and valves for regulating the gas flow into and out of the helmet (figure 1.4). The diver breathes the air in his helmet. The air supply to the helmet must, therefore, be sufficient to ensure adequate ventilation of the helmet and prevent a build-up of carbon dioxide.

(ii) Surface-demand diving system

The principle of this breathing system is outlined in figure 1.5. According to the figure, the second-stage demand valve is supplied via an 'umbilical' hose from a large capacity source located remotely from the diver such as the surface. The pressure of the air supply to the diver is regulated at the surface-control panel (first stage valve) according to the diver's depth. From a performance viewpoint the system can be very well modelled by envisioning the hose and regulators arrangement as in the SCUBA diving set.

1.3 PHYSIOLOGICAL DESIGN PRINCIPLES OF UNDERWATER BREATHING APPARATUS

It will be obvious from the description of the breathing apparatus that, in order to design an equipment to satisfy the diver's requirements, knowledge of respiratory physiology is essential. In particular, it is necessary first to understand the effects of both increased pressure and underwater breathing apparatus on the physiological state of the diver, and, second, to specify in a quantitative manner suitable physiological design parameters.

The physiological requirements which must be realized may be summarized as follows. First, the equipment must supply the diver with adequate ventilation at all levels of physical exertion. Second, the partial pressures of oxygen, carbon dioxide and inert gas present in the breathing gas mixture must be

3

maintained within tolerable limits. Finally, any increase in the work of breathing due to either gas density or equipment design must not become excessive. The following sections have more detailed description of these requirements.

1.3.1 Ventilation rate

As work rate increases, the lung ventilation is expected to increase so that more oxygen can be delivered. The Respiratory Minute Volume (*RMV*) is the term used to define the ventilation rate, which is the volume of gas inhaled and exhaled per minute. Table 1.1 shows the relationship between the *RMV* and the work rate. From this table it can be seen that the breathing apparatus must be capable of meeting such a specification at a severe work rate of 75 L/min *RMV*. Sometimes a *RMV* of 90 L/min is required.

1.3.2 Oxygen partial pressure

There is a great deal of information on oxygen toxicity (Bennett and Elliott, 1982) derived mainly from studies carried out under chamber conditions. The oxygen toxicity is brought on by breathing oxygen at too high a partial pressure. It is thought to be due to the intoxication of the breathing centres in the brain. The symptoms are unreliable and the onset varies both from individual to individual and from day to day. It generally occurs at any depth where oxygen has a partial pressure greater than two bar, and so diving is limited (depending upon the breathing gas) to a safe depth. Hypoxia is the other form of gas poisoning. This occurs if the partial pressure of oxygen being breathed falls below 0.2 bar and is always caused by an excess of inert gas. The first parts of the diver affected by hypoxia are the frontal lobes of the brain. A loss of awareness, judgement and responsibility results and so the symptoms are not apparent to the diver.

1.3.3 Carbon dioxide partial pressure

The presence of carbon dioxide in the inspired breathing gas will normally result in an increase of ventilation and alveolar carbon dioxide partial pressure, both of which are detrimental to the diver's efficiency, particularly during exercise. At 0.1 bar of inspired carbon dioxide partial pressure the pulse rate slows down and the blood pressure drops resulting in unconsciousness and, in extreme cases, death. Thus the onset of carbon dioxide poisoning can be recognised by the increased breathing rate followed by breathlessness and exhaustion. At rest, an inspired carbon dioxide partial pressure of 13 mbar will produce

4

an increase of 33% in alveolar ventilation (Lanphier, 1969). Although tolerable at rest, this would represent an unacceptable respiratory burden during heavy exercise. A more acceptable limit would be no more than 5 mbar.

1.3.4 Problems of inert gas

The two dominant types of inert gas used in the underwater diving equipment are nitrogen and helium. The presence of these inert gases in the breathing gas gives rise to the problems of decompression and narcosis, when the inert gas is nitrogen.

(i) Narcosis

At depths much exceeding 30 m, nitrogen becomes narcotic. It has an increasing effect as the depth increases. The diver becomes light-headed, irresponsible and lacking in powers of concentration. This leads to a limitation of depth to 24 m for inexperienced divers or those who dive infrequently. By constant regular diving to depths of up to 54 m, a diver may adapt to the narcotic effect of nitrogen and may perform better. Helium is not narcotic, and for this reason it is used for deep diving.

(ii) Decompression

The term decompression applies to a reduction in pressure either from atmospheric pressure to sub-atmospheric, as when climbing to altitude in an aircraft, or from raised pressure back towards sea level, as when leaving bottom and starting the ascent after a dive. The important of decompression lies in the effect it has on the dissolved gas in the body. When a person is exposed to a raised pressure, the volume of inert gas dissolved in the body will be increased; at first quickly and then more slowly, until no more gas will dissolve, this condition of equilibrium is called saturation. During a dive, nitrogen from the air or mixture (or helium from oxy-helium mixture) goes into the solution in the body (ie. blood, tissue and fat) at a steadily decreasing rate while oxygen bonds with the haemoglobin. On reducing pressure, when ascending fast, the inert gases come out of solution and bubbles may me formed, producing the symptoms of decompression sickness which can have the following effects:

a) Damage to tissue and nerve endings,

b) Blockage of small blood vessels, interfering with the blood supply to other parts of the body.

c) Inflammation in affected areas and possible haemorrhage.

Professor Haldane and his co-worker (Boycott, 1908), working in the early 1900s, advanced the hypothesis that bubbles would form in the body if the pressure of gas within the body was more than 2.25 times the pressure outside the body. They postulated that it would be safe to decompress rapidly at the ratio of a 2:1 after prolonged exposure on compressed air. For non-saturated air diving in which the nitrogen is not saturated in the solution of the body, higher pressure ratios may be safe. Haldane used his hypothesis to produce the first set of decompression tables. A diver ascends, stopping at intervals to allow the nitrogen in the body to be given off safely without forming bubbles. Haldane's original tables were reasonable safe and were in use for many years. The Royal Naval has modified Haldane tables in order to reduce the time spent on decompression and yet retain the greatest degree of freedom from decompression sickness. Table 1.2 shows the data most often used for air diving and is extremely safe. This table has increments in depths of 3 m. Thus stoppage data for 30 m would be used for a dive to 28 m. A steady ascent rate of 1 m in three seconds should be maintained. In this table there is a risk below the limiting line, where decompression sickness becomes more likely. When using gas mixtures instead of air (ie. $60\%O_2/40\%N_2$ or $40\%O_2/60\%N_2$), the decompression time for a given depth can be reduced, because of the reduced nitrogen tension in body tissues. For a mixture with lower level of nitrogen, the diving schedule of less deep diving depths (given in table 1.2), which have shorter decompression time, can be used. Table 1.3, known as Equivalent Air Depth table, is the diving depth conversion table for the gas mixtures of $60\%O_2/40\%N_2$ and $40\%O_2/60\%N_2$. According to table 1.3, when the breathing gas is $60\%O_2/40\%N_2$, the 18 m diving schedule shown in table 1.2 is used for a 24 m depth of dive. With a $32.5\%O_2/67.5\%N_2$ mixture the difference is insignificant and table 1.2 is to be used. It should be noted that different tables are required for oxy-helium diving.

1.3.5 Work of breathing

In establishing the respiratory effort which underwater breathing apparatus will impose upon the diver, there are a number of important independent variables. These are airway resistance, hydrostatic imbalance and compliance. Airway resistance is the pressure differential along the airways required to induce a gas flow rate. Hydrostatic pressure imbalance is the differential water pressure existing between the hydrostatic pressure at the level of the lung centroid and the breathing gas supply pressure. Compliance represents the elastic properties of the system in terms of volume change per unit of pressure applied. Each of these variables contributes to the total pressure which is generated in order to effect a change in lung

volume. On the basis of a pressure-time recording alone, it is difficult to estimate respiratory work. A more informative record is the pressure-volume diagram, as it can give some insight into the separate hydrostatic, elastic and resistive components of work. Figure 1.6 shows typical pressure-volume (P-V) loops for common types of underwater breathing apparatus. In this figure pressures are measured at the mouthpiece relative to its hydrostatic pressure. The volume is obtained by deducting a fixed reference volume from the changing lung volume. The area of the P-V loop is a measure of the respiratory work done on the apparatus by the diver (ie. external resistive work). On the basis of the literature reviewed (Bennett and Elliott, 1982), it is recommended that the external resistive work per volume of gas inhaled and exhaled should not exceed the limit of

$$\frac{W_{re}}{V_T} = 0.5 + 0.02 \; RMV \quad J/Litre \tag{1.1}$$

The coefficients (0.5 and 0.02) are chosen to maintain external work within the limits of comfort according to the available physiological data. From the test data available in the literature (Bennett and Elliott, 1982) it is clear that only a few select systems can meet this respiratory work limit within the designated ventilation range. For practical purposes a second limit of tolerance is proposed:

$$\frac{W_{re}}{V_T} = 0.5 + 0.04 \; RMV \quad J/Litre \tag{1.2}$$

Apparatus should not be accepted if the above limit is exceeded.

1.4 EXPERIMENTAL EVALUATION OF UNDERWATER BREATHING APPARATUS

Testing of underwater breathing apparatus has evolved over a number of years. It has been undertaken using both manned and unmanned tests. Unmanned tests allow underwater breathing apparatus to be evaluated to its limits of performance and, more importantly, allows potentially dangerous equipment to be identified without placing the diver at risk. Confirmation of the underwater breathing apparatus' capacity to work in real situations is established during expensive manned test. The common facilities used in the unmanned evaluation of underwater breathing apparatus comprise a hyperbaric chamber, which simulates the diving depth pressure, and a breathing simulator that reproduces human respiratory demands and gas exchange. A typical set up of the unmanned test is shown in figure 1.7. The objectives of the

7

unmanned tests can be subdivided into two basic areas: one associated with respiratory mechanics (ie. flow, resistance and work of breathing) and the second with the quality of inspired gas (ie. oxygen, carbon dioxide and inert gas partial pressure). With confidence obtained from unmanned tests, the manned trials can concentrate on more subtle human factors such as buoyancy and mobility.

1.5 A REVIEW OF THE SIMULATION OF UNDERWATER BREATHING APPARATUS

Progress has been made both in the United kingdom and the United States in the development of mathematical models for the simulation of underwater breathing apparatus (Antoon, Middleton and Nucklos, 1986 and Baz and Gilheany, 1988). However, their model performance is often either derived using data relating to steady state operation of the system components or by using 'black box' modelling techniques. Steady state models are unable to account for dynamic effects such as the inertia of moving parts or rapid pressure fluctuations and are consequently of limited use. Black box models merely replicate component performance at the actual test conditions and cannot be used with confidence at other operation conditions. Several researches have already undertaken the development of full dynamic models for diving system; notable among these are Mittleman (1989), Tilley (1991) and Tomlinson (1992). Even with the excellent work of these researches there has been a conspicuous lack of generality in the computer models that have been written to describe breathing systems, and an unfortunate disregard for certain thermodynamic variables. The present analysis represents a further step in refining and extending their models in order to obtain a general and realistic model for the design of underwater breathing apparatus.

1.6 THE USE OF COMPUTER SIMULATION PACKAGES

With conventional simulation techniques, a new simulation program has to be written each time when a component is changed or a different system encountered. This is a very time consuming and expensive procedure. Clearly, an automatic procedure is necessary to assemble already prepared component model subroutines to simulate any circuit which a designer cares to envisage. For this reason, several simulation packages have been developed. Three commonly used example are, Bath*fp* (Richard and Tilley, 1991), developed over a number of years by the Fluid Power Centre, University of Bath, DSH (Backe, 1985) developed at the Technical University of Aachen in Germany and the commercially developed

Flowmaster. Due to the availability and accessibility of Bath*fp*, it was selected as the simulation package to be used in this study. This package provides a user environment which has been targeted towards the user who is either involved in the design or assessment of systems. The following facilities are provided by the package:

i) Automatically linking the component models together to form the system simulation program,

ii) A library of models representing the behaviour of a range of components,

iii) Utilities to assist the designer in creating new models,

iv) An inbuilt facility for displaying simulation results in graphical form.

v) A facility which allows for automatic changes in dimensional and performance data or circuit configuration.

Since the analysis of dynamic systems consists of a large set of first order differential equations, an accurate numerical integration algorithm is required. Bath*fp* uses a sophisticated integration method, based on the LSODA package developed by Petzold (1983), to solve all the first order differential equations in the overall model. The algorithm has been modified by Richard (1991) to enable it to be incorporated within the Bath*fp*. The two main modification were:

a) The development of communication protocols between the component models and the integrator.

b) Special procedures allowing physical discontinuities (ie. valves opening and closing) to be handled efficiently. In addition, time and event tracking of discontinuities are controlled from within the models.

1.7 THE SCOPE OF THIS THESIS

The remainder of this thesis is divided into six chapters. Although each chapter contains its own introduction the basic topic of each is as follow;

Chapter 2 describes the modelling technique used for the simulation of the underwater breathing apparatus. In addition, the development of a breathing simulator model is described, which enables unmanned test condition to be simulated.

Chapter 3 describes the mathematical models developed for the semi-closed-circuit breathing apparatus and the surface demand diving system. Validation of the mathematical models are reported and modifications to improve system performance are discussed.

Chapter 4 described the development of an accurate human respiratory system model which enables the human interaction with the underwater breathing apparatus to be predicted.

Chapter 5 describes the work for validating and identifying the unknown parameters of the human respiratory system model. The simulation studies in which the human respiratory system model is connected to the two breathing system models developed in chapter 3 are reported.

Chapter 6 describes the further use of the developed simulation technique for other gas based systems such as the submarine escape system and industrial pneumatic systems.

Chapter 7 draws conclusions from the work described in this thesis and suggests some areas for further work.

TABLES FOR CHAPTER 1

Work effort	Breaths per minute	Tidal Volume (L)	Respiratory Minute Volume RMV (L/min)
Rest	12	0.5	6
Light work	15	1.5	22.5
Moderate work	20	2	40
Heavy work	25	2	50
Hard work	25	2.5	62.5
Extremely hard work	30	2.5	75
Maximum possible work	30	3	90

Table 1.1 Average human ventilation rate at different work rates

Depth not exceeding (m)	Duration time leaving surface to the beginning of ascent not exceeding (min)	Stoppages at different depths including the time of ascent (min) 9m	6m	3m	Total time for depression (min)
9	No limit	-	-	-	-
12	135	-	-	-	-
	165	-	-	5	5
	195	-	-	10	10
	225	-	-	15	15
	255	-	-	20	20
	330	-	-	25	25
	390	-	-	30	30
	660	-	-	35	35
	Limiting Line				
	Over 660	-	-	40	40
15	85	-	-	-	-
	105	-	-	5	5
	120	-	-	10	10
	135	-	-	15	15
	145	-	-	20	20
	160	-	-	25	25
	170	-	5	25	30
	190	-	5	30	35
	Limiting Line				
	240	-	10	40	50
	360	-	30	40	70
	450	-	35	40	75
	over 450	-	35	45	80

Table 1.2 Diving table for air

Depth not exceeding (m)	Duration time leaving surface to the beginning of ascent not exceeding (min)	Stoppages at different depths including the time of ascent (min)			Total time for depression (min)
		9m	6m	3m	
18	60	-	-	-	-
	70	-	-	5	5
	80	-	5	5	10
	90	-	5	10	15
	100	-	5	15	20
	110	-	5	20	25
	120	-	5	25	30
	130	-	5	30	35
	Limiting Line				
	140	-	10	30	40
	180	-	20	40	60
	255	10	35	45	90
	325	20	40	45	105
	over 495	35	40	50	125
21	40	-	-	-	-
	55	-	-	5	5
	60	-	5	5	10
	70	-	5	10	15
	75	-	5	15	20
	85	-	5	20	25
	90	-	5	25	30
	95	5	5	25	35
	Limiting Line				
	105	5	5	35	45
	120	5	10	40	55
	135	5	20	45	70
	150	5	30	45	80
24	30	-	-	-	-
	40	-	-	5	5
	50	-	5	5	10
	55	-	5	10	15
	60	-	5	15	20
	70	-	5	20	25
	75	-	5	25	30
	Limiting Line				
	80	5	5	30	40
	90	5	10	35	50
	105	5	20	40	65

Table 1.2 Diving table for air

Depth not exceeding (m)	Duration time leaving surface to the beginning of ascent not exceeding (min)	Stoppages at different depths including the time of ascent (min)				Total time for depression (min)
		12m	9m	6m	3m	
27	25	-	-	-	-	-
	30	-	-	-	5	5
	40	-	-	5	5	10
	45	-	-	5	10	15
	50	-	-	5	15	20
	55	-	-	5	20	25
	60	-	5	5	20	30
	65	-	5	5	25	35
	Limiting Line					
	70	-	5	10	30	45
	75	-	5	15	30	50
	80	-	5	20	35	60
	90	-	5	25	40	70
	100	-	5	30	45	80
30	20	-	-	-	-	-
	25	-	-	-	5	5
	30	-	-	5	5	10
	35	-	-	5	10	15
	40	-	-	5	15	20
	45	-	-	5	20	25
	50	-	5	5	20	30
	55	-	5	5	25	35
	Limiting Line					
	60	-	5	10	30	45
	70	-	5	20	35	60
	75	5	5	20	40	70
	80	5	5	30	40	80
33	17	-	-	-	-	-
	20	-	-	-	5	5
	25	-	-	5	5	10
	30	-	-	5	10	15
	35	-	-	5	15	20
	40	-	-	5	20	25
	45	-	5	5	20	30
	Limiting Line					
	50	-	5	10	25	40
	55	-	5	15	30	50
	60	-	5	20	35	60

Table 1.2 Diving table for air

Depth not exceeding (m)	Duration time leaving surface to the beginning of ascent not exceeding (min)	Stoppages at different depths including the time of ascent (min)				Total time for depression (min)
		12m	9m	6m	3m	
36	14	-	-	-	-	-
	20	-	-	-	5	5
	25	-	-	5	5	10
	30	-	-	5	15	20
	35	-	-	5	20	25
	40	-	5	5	25	35
	Limiting Line					
	45	-	5	10	25	40
	50	-	5	15	30	50
	55	5	5	20	35	65
	60	5	10	25	40	80
	70	5	20	30	45	100
39	11	-	-	-	-	-
	15	-	-	-	5	5
	20	-	-	5	5	10
	25	-	-	5	10	15
	30	-	-	5	20	25
	35	-	5	5	20	30
	Limiting Line					
	40	-	5	10	25	40
	45	5	5	15	30	55
	50	5	5	20	35	65
	55	5	10	25	40	80
	60	5	15	30	45	95
42	9	-	-	-	-	-
	10	-	-	-	5	5
	15	-	-	5	5	10
	20	-	-	5	10	15
	25	-	-	5	15	20
	30	-	5	5	20	30
	Limiting Line					
	35	-	5	10	25	40
	40	5	5	15	30	55
	45	5	10	15	35	65
	50	5	15	20	40	80

Table 1.2 Diving table for air

Depth not exceeding (m)	Duration time leaving surface to the beginning of ascent not exceeding (min)	Stoppages at different depths including the time of ascent (min)					Total time for depression (min)
		15m	12m	9m	6m	3m	
45	8	-	-	-	-	-	-
	10	-	-	-	-	5	5
	15	-	-	-	5	5	10
	20	-	-	-	5	15	20
	25	-	-	5	5	20	30
	Limiting Line						
	30	-	-	5	10	25	40
	35	-	5	5	10	30	50
	40	-	5	10	15	35	65
	45	-	5	15	20	40	80
	50	5	5	15	25	45	95
	55	5	10	20	30	50	115
48	10	-	-	-	5	5	10
	15	-	-	-	5	10	15
	20	-	-	5	5	15	25
	25	-	-	5	10	20	35
	Limiting Line						
	30	-	5	5	10	25	45
	35	-	5	10	15	30	60
	40	-	5	10	20	40	75
	45	5	5	15	25	45	95
	50	5	10	20	30	45	110
	55	5	15	25	40	45	130
51	10	-	-	-	5	5	10
	15	-	-	-	5	10	15
	20	-	-	5	5	15	25
	Limiting Line						
	25	-	-	5	10	25	40
	30	-	5	5	15	30	55
	35	-	5	10	20	35	70
	40	5	5	15	25	35	85
	45	5	10	20	30	40	105

Table 1.2 Diving table for air

15

Depth not exceeding (m)	Duration time leaving surface to the beginning of ascent not exceeding (min)	Stoppages at different depths including the time of ascent (min)					Total time for depression (min)
		15m	12m	9m	6m	3m	
54	10	-	-	-	5	5	10
	15	-	-	5	5	10	20
	20	-	-	5	10	15	30
	Limiting Line						
	25	-	5	5	10	25	40
	30	-	5	10	15	35	65
	35	5	5	15	20	40	85
	40	5	10	20	25	45	105
57	10	-	-	-	5	5	10
	15	-	-	5	5	15	25
	20	-	-	5	10	20	35
	Limiting Line						
	25	-	5	5	15	25	50
	30	5	5	10	20	35	75
	35	5	5	15	30	45	100
60	10	-	-	-	5	10	15
	15	-	-	5	5	15	25
	Limiting Line						
	20	-	5	5	10	20	40
	25	-	5	10	15	30	60
	30	5	5	15	20	40	85

Table 1.2 Diving table for air

Depth of dive not exceeding (m)	Equivalent air depths in metre	
	60%O_2/40%N_2 mixture	40%O_2/60%N_2 mixture
12	9	12
15	9	15
18	12	18
21	15	21
24	18	21
27		24
30		27
33		30
36		33
39		36
42		39

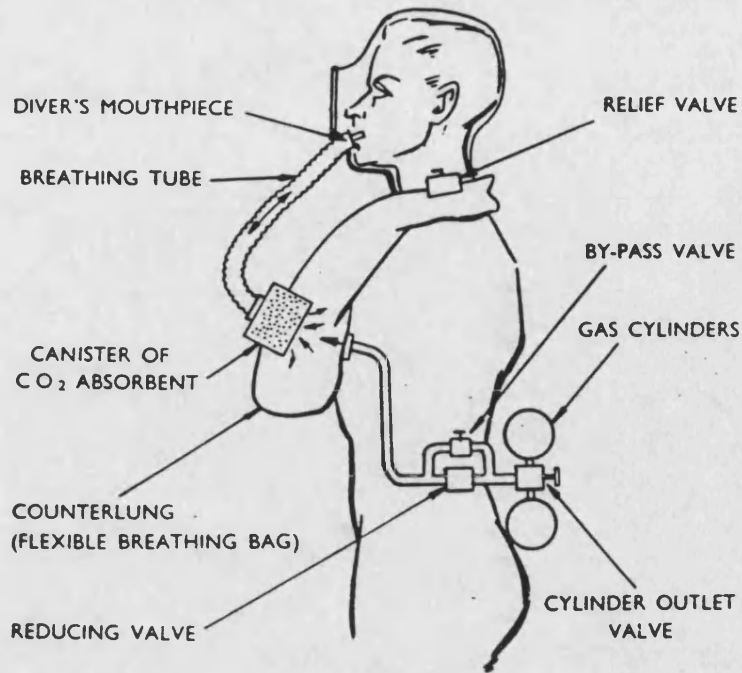**Table 1.3** Table of equivalent air depth

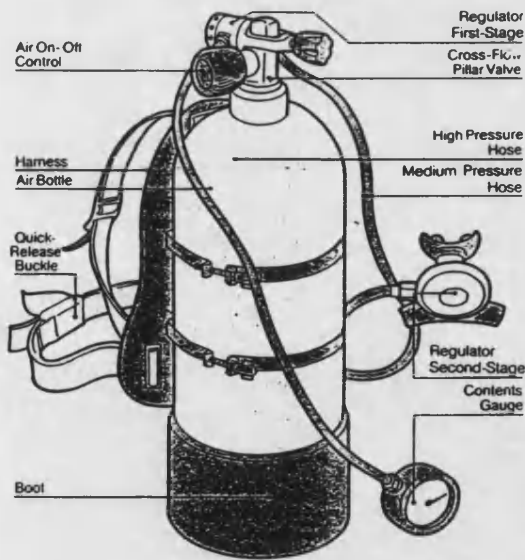Figure 1.1 Closed/semi-closed circuit breathing apparatus
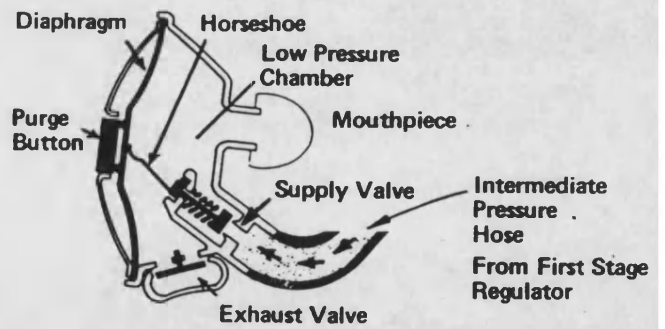

Figure 1.2 Open-circuit breathing apparatus
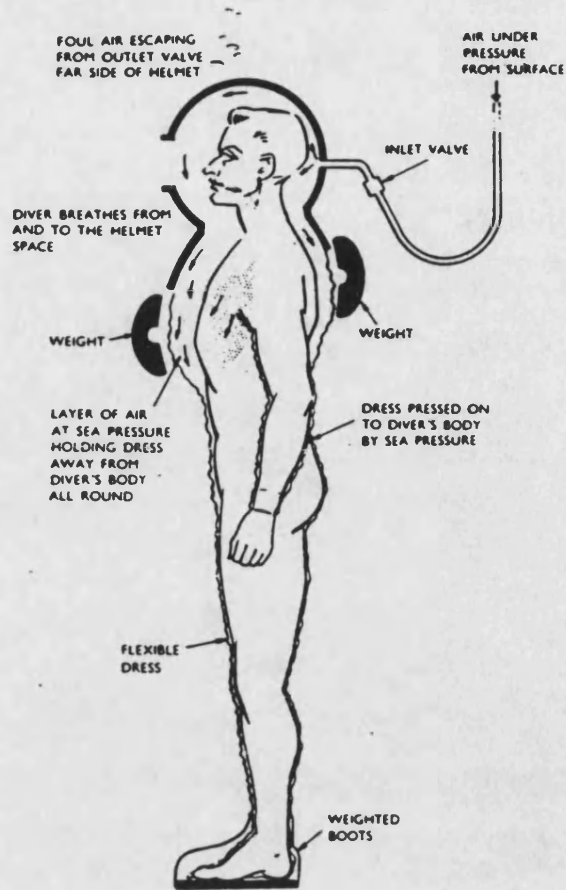

Figure 1.3 Second-stage demand valve

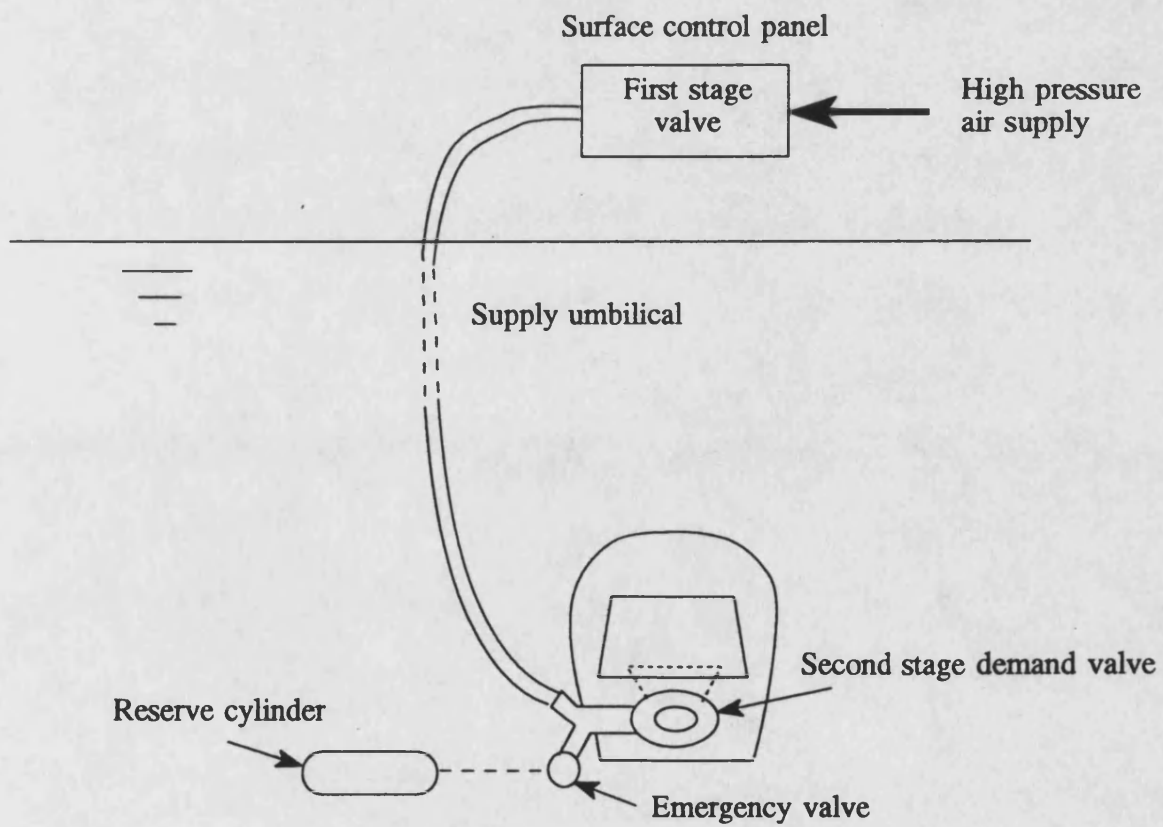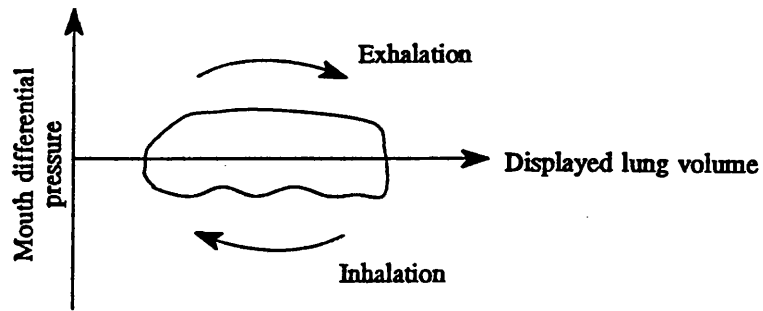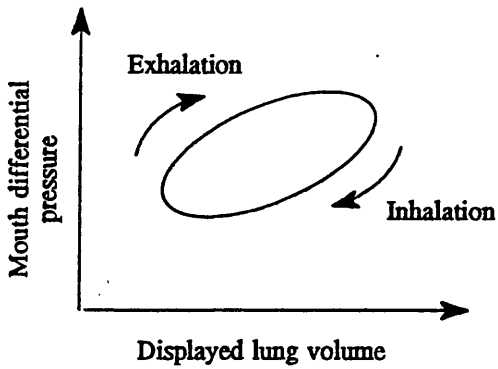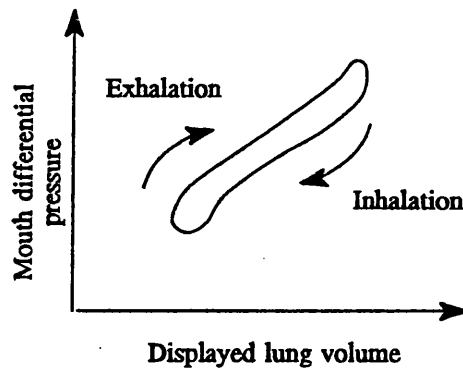**Figure 1.4** Ventilated helmet with diving dress

Figure 1.5 Surface-demand diving system

18

(a) open-circuit demand

(b) rebreathing apparatus

(c) free flow helmet

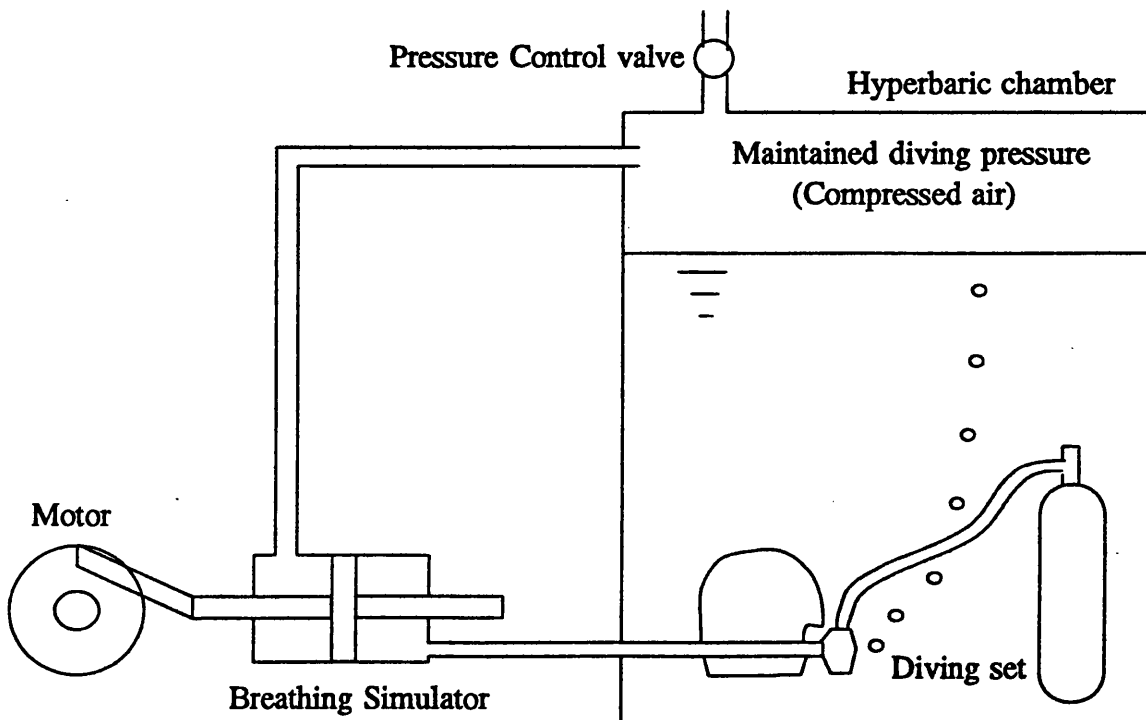**Figure 1.6** Typical pressure-volume diagrams for underwater breathing apparatus

Figure 1.7 Unmanned test set up for the assessment of underwater diving apparatus

CHAPTER 2

MATHEMATICAL MODELLING OF
UNDERWATER BREATHING APPARATUS

2.1 INTRODUCTION

A mathematical analysis of the behaviour of a gas based system, such as breathing apparatus, will generally yield a large set of algebraic and differential equations (Andersen, 1976), the latter falling into two general classes, ordinary and partial. The current research considers the solution of ordinary differential equations where the only independent variable is time. Using this approach to simulate the breathing system, it is necessary to undertake a detailed theoretical analysis of each component to formulate appropriate mathematical models. The following sections give a detailed theoretical analysis for the wide range of components used in the breathing apparatus. In addition, a model of the breathing simulator is provided so that the simulations of underwater breathing apparatus under unmanned test condition can be performed.

2.2 BASIC COMPONENT MODELS

Components commonly used in the breathing system can be divided into two basic elements. These are (a) capacitive elements (such as gas storage bottle, pipes and hoses) and (b) restrictive elements (such as orifices and valves). The theoretical analysis for these elements are developed and described in the following subsections.

2.2.1 Capacitive elements

Consider a volume of gas undergoing a change in state during a small period of time Δt as shown in figure 2.1. If the volume has fixed boundaries across which mass and energy transfer may occur, the energy change in the gas volume during the small interval Δt is given by

$$\Delta E = U_{in} - U_{out} - \Delta W_{out} + \Delta H_{in} \qquad (2.1)$$

There are other sources of energy which might be considered in some application but which are negligible for the work concerned here. These include internal heat generation due to vibrational or radioactive heating.

The energy of the gas within the volume may be considered in terms of specific internal energy u, kinetic energy and potential energy. The inflow and outflow energies include similar terms but with the addition of a 'flow-work' term $p\upsilon$. Hence,

$$\Delta E_v = \Delta \left[m \left(u + gz + v^2/2 \right) \right] \tag{2.2}$$

$$U_{in} = \Sigma \, \Delta m_{in} \left(u + gz + v^2/2 + p\upsilon \right)_{in} \tag{2.3}$$

$$U_{out} = \Sigma \, \Delta m_{out} \left(u + gz + v^2/2 + p\upsilon \right)_{out} \tag{2.4}$$

For the breathing system, it is reasonable to expect the kinetic and potential energy terms to be small, certainly negligible when compared to the specific enthalpy and specific internal energy terms. The change in kinetic or potential energy between inflow and outflow will be even less significant as the difference between the inlet and outlet flow areas is small. Using the definition of specific enthalpy, $h = u + p\upsilon$, and considering the changes in quantities to occur with respect to the time interval Δt, equation (2.1) becomes

$$\frac{\Delta[mu]}{\Delta t} = \Sigma \frac{\Delta m_{in}}{\Delta t} h_{in} - \Sigma \frac{\Delta m_{out}}{\Delta t} h_{out} - \frac{\Delta W_{out}}{\Delta t} + \frac{\Delta H_{in}}{\Delta t} \tag{2.5}$$

Then as $\Delta t \to 0$, equation (2.5) becomes

$$\dot{m}u + m\dot{u} = \Sigma \dot{m}_{in} h_{in} - \Sigma \dot{m}_{out} h_{out} - \dot{W}_{out} + \dot{H}_{in} \tag{2.6}$$

Note that $\dot{m}$ is the net mass flow rate in the gas volume (ie. $= \Sigma \dot{m}_{in} - \Sigma \dot{m}_{out}$). The thermodynamic definitions and laws are used in order to obtain the expressions of u and h in terms of gas properties. The procedure is fully described in Appendix A and leads to the expressions shown in table 2.1. Hence, equation (2.6) becomes

$$m C_V \dot{T} + \dot{m}[\bar{u} + C_V(T - \bar{T})] = \Sigma \dot{m}_{in}[\bar{h} + C_p(T - \bar{T})]_{in} - \Sigma \dot{m}_{out}[\bar{h} + C_p(T - \bar{T})]_{out} - \dot{W}_{out} + \dot{H}_{in} \tag{2.7}$$

Rearranging equation (2.7) gives

$$\dot{T} = \frac{1}{m C_V} \left[\Sigma \dot{m}_{in}(C_p T)_{in} - \Sigma \dot{m}_{out}(C_p T)_{out} - \dot{m} C_V T - \dot{W}_{out} + \dot{H}_{in} \right.$$
$$\left. + \Sigma \dot{m}_{in}(\bar{h} - C_p \bar{T})_{in} - \Sigma \dot{m}_{out}(\bar{h} - C_p \bar{T})_{out} - \dot{m}(\bar{u} - C_V \bar{T}) \right] \tag{2.8}$$

The outflow from the gas volume in equation (2.8) must have the same properties and gas temperature as those within the gas volume. Hence

$$(C_p T)_{out} = C_p T \tag{2.9}$$

$$(\tilde{h} - C_p \tilde{T})_{out} = \tilde{h} - C_p \tilde{T} \tag{2.10}$$

The inflow fluid properties in equation (2.8) will be different from the properties within the gas volume. However, the variation of C_P with temperature is small for the gas used in breathing systems. In this case the value for C_P within the gas volume can also be used for the inflow C_P, with only a small loss of accuracy. It can also be assumed that the same reference values for $\tilde{u}(\tilde{p},\tilde{T})$ and $\tilde{h}(\tilde{p},\tilde{T})$ can be used throughout the analysis. From the definition in table 2.1, (i.e. $\tilde{h} - C_p \tilde{T} = \tilde{u} - C_V \tilde{T}$), equation (2.8) reduces to

$$\dot{T} = \frac{1}{mC_V} [\Sigma \dot{m}_{in} C_p T_{in} - \Sigma \dot{m}_{out} C_p T - \dot{m} C_V T - \dot{W}_{out} + \dot{H}_{in}] \tag{2.11}$$

The rate of heat transfer $\dot{H}_{in}$ can be found from the consideration of convection, conduction and radiation and can be represented by a general expression:

$$\dot{H}_{in} = k_h A_{sur} (T_{sur} - T) \tag{2.12}$$

where k_h is the overall heat transfer coefficient.

For the breathing system the work done on or by the gas is considered to be related to the change in the gas volume. In this case,

$$\dot{W}_{out} = P \dot{V} \tag{2.13}$$

Note that negative $\dot{V}$ represents a reduction in the gas volume and the work done on the gas.

Based on the perfect gas law, the rate of change of pressure inside the gas volume is obtained by differentiating the equation of state, that is:

$$\dot{P} = \frac{RT}{V} \dot{m} - \frac{P}{V} \dot{V} + \frac{mR}{V} \dot{T} \tag{2.14}$$

22

Substituting equations (2.11), (2.12) and (2.13) in equation (2.14) gives

$$\dot{P} = \frac{1}{V} \left[\frac{C_P}{C_V} R \left(\Sigma \dot{m}_{in} T_{in} - \Sigma \dot{m}_{out} T \right) - P\dot{V} \left(1 + \frac{R}{C_V} \right) + \frac{R}{C_V} UA_{sur} (T_{sur} - T) \right]$$

(2.15)

Using the relationships of gas properties in table 2.1, equation (2.15) can be rewritten as

$$\dot{P} = \frac{\gamma}{V} \left[R \left(\Sigma \dot{m}_{in} T_{in} - \Sigma \dot{m}_{out} T \right) - P\dot{V} + \frac{(\gamma - 1)}{\gamma} UA_{sur} (T_{sur} - T) \right]$$

(2.16)

The analysis of the overall heat transfer coefficient U between the gas and the surrounding is complicated, and experimental data is desirable in order to develop reliable values. It is worth mentioning one other method of accounting for the pressure variation without taking into account the heat transfer coefficient. The determination of the pressure variation related to heat transfer may be regarded as being approximately polytropic in form (Rogers and Mayhew, 1973 and Andersen, 1976) and it can be assumed that

$$\dot{P} = \frac{n}{V} \left[R \left(\Sigma \dot{m}_{in} T_{in} - \Sigma \dot{m}_{out} T \right) - P\dot{V} \right]$$

(2.17)

It is generally assumed that for slow movements of gas, heat is transferred through the boundary maintaining an internal constant gas temperature and the polytropic index n in equation (2.17) will be 1, resulting in an isothermal process. For rapid changes in conditions, little heat can flow into or out of the gas and an adiabatic condition is assumed in which n will be equal to γ. In many instances it is sufficiently accurate to assume that the process is in between isothermal and adiabatic conditions [ie. $n=(1+\gamma)/2$].

Once the rate of change of pressure has been determined, the rate of change of gas temperature inside the gas volume can be obtained in terms of P, m and V by rearranging equation (2.14) into the following form:

$$\dot{T} = \frac{T}{PV} \left(P\dot{V} + V\dot{P} - \dot{m}RT \right)$$

(2.18)

The approach described above assumes that the pressure and temperature are uniform throughout the gas volume. This form of analysis is termed lumped parameter theory.

2.2.2 Restrictive elements

Restrictive elements are those components requiring a sizable local pressure drop to cause gas to flow. For convenience they will be classified as fixed restrictions - which have constant area and are usually called orifices - and variable restrictions - which are called valves. In the case of the breathing apparatus, gas compressibility is an important factor. Hence, the theory of compressible fluid dynamics is required for the analysis. A relevant formula which has been shown to predict the mass flow rate through an orifice fairly accurately (Andersen, 1976) is given by

$$q_f = \frac{C_d \, C_m \, A_f \, P_u}{\sqrt{T_u}} \tag{2.19}$$

The data published by Grace and Lapple (1951) has been found to be very useful in forming the relationships between the discharge coefficient C_d and the pressure drop for nozzles, square-edged orifices and sharp-edged orifices. Figure 2.2 has been re-plotted from their published. The value of the mass flow parameter C_m in equation (2.19) is obtained depending upon whether the flow is sonic or subsonic.

If $(P_d/P_u) \geq [2/(\gamma+1)]^{\gamma/(\gamma-1)}$ then the flow is subsonic and

$$C_m = \sqrt{\frac{2\gamma}{R(\gamma - 1)} \left[\left(\frac{P_d}{P_u}\right)^{2/\gamma} - \left(\frac{P_d}{P_u}\right)^{(\gamma+1)/\gamma} \right]} \tag{2.20}$$

Otherwise, the flow is sonic and is said to be choked. In this case,

$$C_m = \left(\frac{2}{\gamma + 1}\right)^{1/(\gamma-1)} \sqrt{\frac{2\gamma}{R(\gamma + 1)}} \tag{2.21}$$

The analysis of the thermodynamic behaviour of gas flow through an orifice and valve may commence with the steady state energy balance equation. For a given streamline, the energy equation is expressed as

$$C_p T + \frac{1}{2} v^2 = constant \tag{2.22}$$

This is the form of equation for steady adiabatic gas flow in which the gas neither does work on the surroundings nor has work done on. In the case of an orifice or valve used in the breathing system, the heat transfer across the boundary can be neglected as the surface area across the boundary is very small. As the

24

inlet and outlet chambers (see figures 2.3(a) and (b)) are comparatively larger than the flow area (i.e. $v_u \approx v_d << v_f$), the energy equation can be written as

$$C_p T_u = C_p T_f + \frac{1}{2} v_f^2 = C_p T_d \qquad (2.23)$$

Hence, for gas flowing through an orifice or valve, the outflow gas temperature is assumed to be equal to the inflow gas temperature as the recovery of the gas temperature occurs. If an attempt is made to determine the gas temperature T_f at the flow restriction, the isentropic relationship (Rogers and Mayhew, 1973) can be used:

$$\frac{T_f}{T_u} = \left(\frac{P_d}{P_u} \right)^{(\gamma-1)/\gamma} \qquad (2.24)$$

The above equation only applies when the flow is subsonic (i.e $(P_d/P_u) \geq [2/(\gamma+1)]^{\gamma/(\gamma-1)}$). For sonic flow conditions, equation (2.24) becomes

$$\frac{T_f}{T_u} = \frac{2}{\gamma + 1} \qquad (2.25)$$

2.3 SIMULATING THE VARIATION OF GAS COMPOSITION IN BREATHING APPARATUS

In order to determine the variation of gas composition in the system models, a capacitive element which contains N kinds of constituent gases, as shown in figure 2.4, is considered. It is assumed that the gas inside the capacitive element is well mixed. When a gas stream with mass flow rates, q_{in} and q_{out}, containing different gas mixture concentrations, flows into and out of the capacity element, the concentration of each constituent gas 'i' inside the capacity element will change with time. Each mass constituent, m_i, can be defined by continuity of mass: the mass transfer rate of constituent gas 'i' is given by

$$\frac{dm_i}{dt} = \sum q_{in} \frac{m_{in,i}}{m_{in}} - \sum q_{out} \frac{m_i}{m} \qquad (2.26)$$

Note that $m_{in,i} / m_{in}$ is the mass fraction of constituent gas 'i' in the incoming gas and m_i / m is the mass fraction of constituent gas 'i' inside the capacity element. Equation (2.26) can be solved by integration provided that the initial mass of constituent gas 'i' is known. Since the mole fraction of constituent gas 'i'

is equal to the volumetric fraction of constituent gas 'i' (ie. $y_i = V_i / V$), the initial mass of gas 'i' inside the capacitive element can be obtained from the following relationship :

$$m_i = M_i \left(\frac{m}{M}\right)\left(\frac{V_i}{V}\right)$$

(2.27)

The initial total mass of gas mixture m in equation (2.27) can be obtained by the equation of state for the gas, ie.

$$m = M\left(\frac{PV}{R_oT}\right)$$

(2.28)

According to Rogers and Mayhew (1973), the molecular weight of the gas mixture is given by

$$M = \sum_{i=1}^{N} \frac{V_i}{V} M_i$$

(2.29)

Hence, the initial mass of constituent gas 'i' can be obtained from the initial volumetric fraction of constituent gas 'i' and equation (2.26) can be used to determine the transient change inside the capacitive elements. For the restrictions, the mass fraction of the constituent gases are simply based on the incoming gas conditions.

2.4 DETERMINING THE GAS PROPERTIES OF A MIXTURE

As before, it is assumed that a mixture of gas contains N kinds of constituent gases. According to Dalton's law for the mixture of perfect gases, if a mixture of gas occupies a volume V at a temperature T, the pressure P_i of gas 'i' when it alone occupies the volume V at temperature T is given by

$$P_i = \frac{m_i}{M_i} \frac{R_oT}{V}$$

(2.30)

By substituting $V=mRT/P$, the equation of state for a gas, in the above equation, the partial pressure P_i is therefore determined from the mass fraction and total pressure using the formula

$$P_i = P\left(\frac{m_i}{m}\right)\left(\frac{R_o}{M_iR}\right)$$

(2.31)

26

An expression for the specific gas constant R in terms of the mass fractions of constituent gases is given by

$$R = \frac{R_o}{M} = R_o \sum_{i=1}^{N} \left(\frac{m_i}{m}\right)\frac{1}{M_i} \tag{2.32}$$

Further, the specific heat at constant pressure C_P of the mixture is given by

$$C_P = \sum_{i=1}^{N} \frac{m_i}{m} C_{Pi} \tag{2.33}$$

A knowledge of R and C_P enables the specific heat at constant volume C_V to be determined using the relationship

$$C_V = C_P - R \tag{2.34}$$

Hence, the ratio of specific heat can be found using

$$\gamma = C_P / C_V \tag{2.35}$$

According to Reid, Prausnitz and Sherwood (1977), the expression for determining the viscosity of a gas mixture which contains N kinds of constituent gases is given by

$$\mu = \sum_{i=1}^{N} \mu_i / \left[1 + \sum_{j=1, j\neq i}^{N} \Theta_{ij}\left(\frac{X_j}{X_i}\right)\right] \tag{2.36}$$

The ratio of the mole fractions X_i and X_j in equation (2.36) can be obtained from the mass fraction of corresponding gases using the formula

$$\frac{X_j}{X_i} = \frac{(m_j/m)M_i}{(m_i/m)M_j} \tag{2.37}$$

The term Θ_{ij} in equation (2.36) is based on the Wilke Estimation Method (Reid, Prausnitz and Sherwood, 1977) which is the best known and one of the most accurate methods for the estimation of viscosity of gas mixtures and is given by

$$\Theta_{ij} = \frac{\left[1 + (\mu_i/\mu_j)^{0.5}(M_j/M_i)^{0.25}\right]^2}{\sqrt{8}\left[1 + (M_i/M_j)\right]^{0.5}} \tag{2.38}$$

According to Sutherland's empirical formula (Engineers Year Book, 1994), the viscosity for the individual

27

constituent gas is practically independent of pressure but varies with temperature, ie.

$$\mu_i = \mu_i' \left(\frac{T'+S}{T+S}\right)\left(\frac{T}{T'}\right)^{3/2}$$ (2.39)

Hence, the viscosity of a gas mixture can be determined from the mass fractions of constituent gases and the viscosities of individual constituent gas. In addition, table 2.2, which illustrates the physical properties of individual gases, provides information to determine the gas properties of a mixture.

2.5 GAS STORAGE CYLINDER MODEL

Gas cylinders which are used as the storage supply for the breathing system can be considered as a single control volume such that equations (2.17) and (2.18) can be used to determine the rate of change of pressure and temperature inside the gas cylinders. Since the gas cylinders have a fixed volume, equations (2.17) and (2.18) can be written as

$$\dot{P}_{bo} = \frac{n}{V_{bo}}R \left(\Sigma \dot{m}_{in}T_{in} - \Sigma \dot{m}_{out}T_{bo}\right)$$ (2.40)

$$\dot{T}_{bo} = \frac{T_{bo}}{P_{bo}V_{bo}} \left(V_{bo}\dot{P}_{bo} - \dot{m}RT_{bo}\right)$$ (2.41)

It is clear that $\Sigma \dot{m}_{out} = 0$ when the gas cylinders are charging, and $\Sigma \dot{m}_{in} = 0$ when the gas cylinders are discharging. The cylinders pressure and temperature are obtained by integrating the above equations with respect to time.

2.6 PIPE & HOSE MODEL

The use of pipes and flexible hoses are common in breathing apparatus. The time required for a pressure signal to travel the length of a pipe is the length divided by the speed of sound. This time delay is neglected for relatively short pipes at present. Hence the lumped parameter approach discussed earlier can be used to determined the rate of change of pressure and temperature inside the pipe (or hose):

$$\dot{P}_p = \frac{n}{V_p}R \left(\Sigma \dot{m}_{in}T_{in} - \Sigma \dot{m}_{out}T_p\right)$$ (2.42)

$$\dot{T}_p = \frac{T_p}{P_pV_p} \left(V_p\dot{P}_p - \dot{m}RT_p\right)$$ (2.43)

The above approach considers the flow of gas in the pipe where friction is negligible. However, if the flow resistance associated with the pipes or hoses is likely to influence the overall system performance, friction must be accounted for. In this case, it is assumed that the flow in a uniform cross-section pipe is steady and the velocity is sufficiently uniform over the section for the flow to be adequately described in 'one-dimensional' terms. For steady one-dimensional flow with uniform pipe diameter d_p the momentum equation is given by

$$\frac{dP}{\rho} + v\,dv + \frac{4fdl}{d_p}\frac{v^2}{2} = 0 \tag{2.44}$$

The final term in equation (2.44) corresponds to the Darcy's formula for head loss due to friction. It is necessary to point out that the gravity term is neglected for simplicity. To integrate equation (2.44), the relation between density and pressure must be known and this depends on the degree of heat transfer. Consider first the case of zero heat transfer, which gives an adiabatic flow condition and the energy equation (2.22) can be used. The solution of equation (2.44) for adiabatic condition is most conveniently obtained in terms of the Mach number. The procedure is fully described by Massey (1987) and gives the following expression:

$$\frac{1}{2\gamma}\left(\frac{1}{Ma_d^2} - \frac{1}{Ma_u^2}\right) + \frac{\gamma+1}{4\gamma}\ln\left[\left(\frac{Ma_d}{Ma_u}\right)^2\frac{(\gamma-1)Ma_u^2 + 2}{(\gamma-1)Ma_d^2 + 2}\right] + \frac{2fL_p}{d_p} = 0 \tag{2.45}$$

where Ma_u and Ma_d are the Mach number of the flow at pipe upstream and downstream respectively.

Since $Ma^2 = v^2/(\gamma RT)$, $v = q/(\rho A_p)$, $\rho = P/(RT)$, and $C_P = R\gamma/(\gamma-1)$, equation (2.45) becomes

$$\frac{A_f^2}{2q_p^2}\left(\frac{P_d^2}{RT_d} - \frac{P_u^2}{RT_u}\right) + \frac{\gamma+1}{4\gamma}\ln\left[\left(\frac{T_d P_u}{P_d T_u}\right)^2\frac{v_u^2/2 + C_P T_u}{v_d^2/2 + C_P T_d}\right] + \frac{2fL_p}{d_p} = 0 \tag{2.46}$$

Rearranging the equation (2.46) and noting that $v_u^2/2 + C_P T_u = v_d^2/2 + C_P T_d$ for adiabatic conditions, the mass flow rate through the pipe is given by

$$q_p = A_f\sqrt{\frac{\left(\dfrac{P_u^2}{RT_u} - \dfrac{P_d^2}{RT_d}\right)}{\dfrac{4fL_p}{d_p} + \dfrac{\gamma+1}{\gamma}\ln\left(\dfrac{P_u T_d}{P_d T_u}\right)}} \tag{2.47}$$

29

In general, any quantity of heat may be transferred to or from the gas. This general case is too complicated to be considered at present, but a particular example of practical interest is that in which the heat transfer is such as to keep the temperature of the gas constant, that is, in which the flow is isothermal. The analysis for isothermal flow is very similar to that for adiabatic flow, the only difference is that the energy equation is replaced by the simple condition where T = constant or dT/T = 0. Massey (1987) has also derived an expression to determine the mass flow rate through the pipe at isothermal conditions:

$$q_p = A_f \sqrt{\frac{P_u^2 - P_d^2}{RT[\ 4fL_p/d_p + 2\ln(P_u/P_d)\ ]}}$$

(2.48)

Comparing equations (2.47) and (2.48), a single equation can be developed for both adiabatic and isothermal condition:

$$q_p = A_f \sqrt{\frac{\left(\dfrac{P_u^2}{RT_u} - \dfrac{P_d^2}{RT_d}\right)}{\dfrac{4fL_p}{d_p} + \dfrac{n+1}{n}\ln\left(\dfrac{P_u\ T_d}{P_d\ T_u}\right)}}$$

(2.49)

Similar to equation (2.17), it is sufficiently accurate to assume that the process is in between isothermal and adiabatic conditions. Hence, n equal to $(1+\gamma)/2$ is applied.

Extra losses in the pipe also occur when the flow is caused to change its direction by the external influences such as bends, end-fittings, and abrupt enlargements and contractions. These losses can be expressed in terms of an equivalent length of unobstructed straight pipe in which an equal loss will occur. According to Massey (1987), this effective pipe length is given by

$$L_{p,eff} = L_p + Kd_p/(4f)$$

(2.50)

The value of loss coefficient K depends on the change of flow angle. Table 2.3 shows a few typical values. For the analysis, the effective pipe length $L_{p,eff}$ will replace the actual pipe length L_p in equation (2.49).

The friction factor f varies according to whether laminar or turbulent conditions occur in the pipe. For laminar flow, the friction factor is given by

$$f = 16/Re$$

(2.51)

where Re = Reynolds number = $q_p\ d_p/(A_f\ \mu)$ < 2000.

30

Substituting equation (2.51) in equation (2.49), an expression for the mass flow rate in laminar pipe flow is obtained as follows:

$$(\Psi_1 + K)q_p^2 + 16\pi L_p \mu q_p - A_f^2 \Psi_2 = 0 \qquad (2.52)$$

where

$$\Psi_1 = \frac{n+1}{n} \ln\left(\frac{P_u T_d}{P_d T_u}\right) \quad , \quad \Psi_2 = \frac{P_u^2}{RT_u} - \frac{P_d^2}{RT_d}$$

Massey (1987) has suggested that when the flow is laminar (which has a very small Mach number of flow), the fluid may, with small error, be treated as incompressible and the compressible term Ψ_1 in equation (2.52) can be neglected.

In the case of turbulent flow, assumed to be when $Re>2000$, the value of friction factor f not only depends primarily on the relative roughness of the pipe surface, but also on the Reynolds number of the flow. The Colebrook equation gives an implicit relationship for the friction factor as

$$\frac{1}{\sqrt{4f}} - 1.74 + 2\log_{10}\left(2r + \frac{18.6}{Re\sqrt{4f}}\right) = 0 \qquad (2.53)$$

For a given relative roughness r and Reynolds number Re the friction factor can be obtained using iteration. However, as the determination of Reynolds number requires the mass flow rate and the mass flow rate depends on the friction factor, it is necessary to use a sophisticated iteration method to obtain a rapid and converging solution of f. For this reason Muller's method is used to solve this implicit relationship. This method converges at a rate similar to the Newton-Raphson method but does not require a derivative and, after the starting values are obtained, only requires one function evaluation per iteration. Hence, a function $F(f)$ is established in Colebrook equation in which equation (2.53) becomes

$$\frac{1}{\sqrt{4f}} - 1.74 + 2\log_{10}\left(2r + \frac{18.6}{Re\sqrt{4f}}\right) = F(f) \qquad (2.54)$$

The procedure is to substitute an estimated f value in equation (2.49) to obtain the q_p and Re values and then use equation (2.54) to obtain the function $F(f)$ value. At the beginning of the iteration, the initial estimated f value is set to be the mean of the expected highest and lowest f values. According to the Moody

31

diagram (Massey, 1987), it is reasonable to assume that the highest and lowest f values are

$$\hat{f} = \frac{70}{Re} \qquad , \qquad \hat{f} = \frac{1}{4\,[\,1.74\, -\, 2\log_{10}(2r)\,]^2}$$

During a simulation, it is convenient to use the last solution of f as the estimated value as this can lead to a faster convergence, especially when steady state conditions are approached. It is acceptable that the iteration will be terminated when function $F(f)$ is close to zero within a very small tolerance (i.e. 1×10^{-20}). After substituting the f value obtained from the iteration in equation (2.49), the q_p represents the mass flow rate in turbulent pipe flow.

It is known that the flow will be choked at the outlet of the pipe when the ratio between the downstream and upstream pressures is below a certain value, see figure 2.5. For adiabatic and isothermal flow the limiting conditions of downstream Mach number M_d, at which an initially subsonic flow becomes choked, are given by 1 and $1/\sqrt(\gamma)$ respectively. Hence, the choked mass flow rate is given by

$$q_{ch} = \rho_{ch}v_{ch}A_f = P_{ch}\sqrt{\frac{n}{RT_d}}A_f \qquad (2.55)$$

where $n = \gamma$ for adiabatic condition, $n = 1$ for isothermal condition.

Substituting equation (2.55) in equation (2.49) and replacing P_d by P_{ch}, an implicit relationship for the minimum pressure ratio (P_{ch}/P_u) at which the flow starts to choke is obtained:

$$\frac{1}{n\,(P_{ch}/P_u)^2\,T_u/T_d} - \frac{1}{n} - \frac{4f_{ch}L_p}{d_p} - k + \frac{n+1}{n}\ln\left(\frac{P_{ch}\,T_u}{P_u\,T_d}\right) = 0 \qquad (2.56)$$

In this case, the Colebrook equation is unsuitable to evaluate the friction factor f_{ch} for choked flow in equation (2.56) as the equation is implicit. For convenience an alternative explicit formula given by Haaland (1983), which varies by less than 2 percent from equation (2.53), is used:

$$\frac{1}{\sqrt{4f_{ch}}} = -1.8\,\log_{10}\left[\frac{6.9}{Re_{ch}} + \left(\frac{r}{3.7}\right)^{1.11}\right] \qquad (2.57)$$

where the Reynolds number for choked flow is given by

$$Re_{ch} = \frac{\rho_{ch}v_{ch}d_p}{\mu} = \frac{P_{ch}}{\mu}\sqrt{\frac{n}{RT_d}}\,d_p \qquad (2.58)$$

Hence, the minimum pressure ratio (P_{ch}/P_u) for choked flow can be obtained from equation (2.56) by again using Muller's method. According to figure 2.5, if the actual pressure ratio (P_d/P_u) is less than the pressure ratio (P_{ch}/P_u), the flow is said to be choked and the choked mass flow rate is determined from equation (2.49) using the value of pressure ratio (P_{ch}/P_u) for choked flow.

In this friction pipe (or hose) model, the pressure losses due to friction and fittings are simulated as a friction orifice positioned at either the middle or one end of the pipe, see figures 2.6(a) and (b), where the mass flow rate at the friction orifice is determined by equation (2.49). Referring to figure 2.6(a), the pipe model is conceptually a 'volume-restriction-volume', and for the pipe model relating to figure 2.6(b), the model is conceptually a 'volume-restriction'. In addition, equation (2.42) and (2.43) are used to determine the rate of change of pressure and temperature in these volumes. This approach can provide an extensive range of links between friction pipe models and component models.

2.7 LONG PIPE MODEL

The analysis outlined in the previous section is based upon lumped parameter theory. That is, the pressure is considered to change instantaneously at all points along the pipe/hose length. Although this is a reasonable approximation for the behaviour in relatively short pipes, the analysis breaks down with long pipe/hoses owing to wave propagation effects. As a consequence of the flow change, a pressure wave front is made to propagate through the gas at the speed of sound. This means that a time delay is introduced before the pressure at the hose inlet responds to the change in outlet conditions. A similar delay will also be introduced by the returning wave generated when the flow conditions at the inlet respond to the change in pressure. In practice, the situation is further complicated by partial reflections of the travelling waves due to a mismatch in impedances at the ends of the line. The resulting process of waves travelling in different directions along the hose is similar to those occurring in the classical analysis of water hammer in long pipelines.

In the case of surface supply diving equipment, oscillatory flow motion will occur within the supply umbilical due to the cyclic changes in the diver's respiratory demand. This repeated flow cycle can be classified as unsteady flow and the flow inertia effects need to be considered. In addition, the

gravitational head may be significant in some cases. Hence, the momentum equation for a unsteady one-dimensional flow with uniform diameter (see figure 2.7) can be written as

$$\frac{1}{\rho}\frac{dP}{dl} + \frac{4f}{d_p}\frac{v^2}{2} + g\sin\phi + v\frac{dv}{dl} + \frac{dv}{dt} = 0 \tag{2.59}$$

Since the velocity and pressure in a long line subject to pressure transients are continuous functions of position and time, the long umbilical can be modelled by representing it as a series of individual interconnected pipes as shown in figure 2.8. According to equation (2.59), the rate of change of flow at pipe element 'i' can be obtained from

$$\frac{dv_i}{dt} = \frac{1}{\bar{\rho}_i}\frac{(P_{i-1}-P_i)}{\delta l} - \frac{4f_i}{d_p}\frac{v_i\,|v_i|}{2} - g\sin\phi - \frac{v_i}{\delta l}(v_{i,out}-v_{i,in}) \tag{2.60}$$

Note that $\bar{\rho}_i$ in equation (2.60) is the mean density in element 'i' (ie. $\bar{\rho}_i=(P_{i-1}+P_i)/[R(T_{i-1}+T_i)]$) and $v_{i,out}$ and $v_{i,in}$ are the gas flow velocities entering and leaving element 'i' (ie. $v_{i,out}=q_i/(\rho_i A_f)$ and $v_{i,in}=q_i/(\rho_{i-1}A_f)$) respectively. The term $v_i\,|v_i|$ in place of v_i^2 in equation (2.60) is to ensure that the term changes sign as v_i changes sign (where $|v_i|$ means the magnitude of v regardless of its sign). After multiplying equation (2.60) by $\bar{\rho}_i A_f$, the rate of change of mass flow rate through element 'i' can be obtained from

$$\frac{dq_i}{dt} = \frac{A_f(P_{i-1}-P_i)}{\delta l} - \frac{4f_i}{d_p}\frac{q_i\,|v_i|}{2} - \bar{\rho}_i A_f g\sin\phi - \frac{q_i}{\delta l}(v_{i,out}-v_{i,in}) \tag{2.61}$$

The mass flow rate at element 'i' is determined by integrating the above equation with respect to time. Equations (2.51) and (2.53) are used to determine the friction factor f_i at element 'i' for laminar and turbulent flow. Again Muller's method is used to solve the implicit relationship in equation (2.53) for turbulent flow.

As with the short pipe model, the rate of change of pressure and temperature in element 'i' can be obtained using the same form as equations (2.42) and (2.43). In order to model the choked flow in the umbilical, the first and the end elements of the long pipe model will be modelled using the approach described in section 2.6 for steady flow in a short pipe where the pipe length is δl. Hence, this approach enables the behaviour of both unsteady and choked flow in a long line to be modelled together.

34

2.8 GAS CONTROL VALVE MODEL

Valves may be classified in various ways. Those discussed in breathing apparatus can be divided into four basic types: spool type, poppet type, diaphragm type and mushroom type. These are shown in figure 2.9. The valve can be modelled as two distinct operations. Firstly, gas flows through the valve opening. Secondly, the valve head motion is determined by the various forces acting on the valve head assembly. The mass flow rate through the opening of the valve is determined using a similar approach to that described in section 2.2.2 where the flow area A_f is related to the valve opening displacement x_v. In the case of spool type valve, the flow area is annular and is given by

$$A_f = \pi \, d_{vs} \, x_v \tag{2.62}$$

For a poppet type valve, the flow area is also annular but, in this case, is determined using the following equation:

$$A_f = \pi \, d_{vs} \, x_v \, \sin\alpha \tag{2.63}$$

The motion of the valve head is found by taking into account the forces acting on the valve head assembly. These include

(a) weight of the valve head assembly related to the direction of motion ($Me \, g \, sin\phi$);

(b) pressures acting on the valve head assembly;

(c) spring compression force ($k \, x_v$);

(d) viscous force ($f_v \, dx_v/dt$);

(e) Coulomb resistance force (F_C);

(f) flow momentum force (F_m).

The direction of the flow momentum force depends on the flow direction of the fluid which applies an equal and opposite force to the boundary walls of the valve head assembly. Hence, the valve head acceleration can be generally expressed as

$$\frac{d^2 x_v}{dt^2} = \frac{1}{Me} \left[\, Meg \sin\phi \; + F_p \; - f_v \, dx_v/dt \; \pm k(x_v + x_k) \; - F_C sign(dx_v/dt) \; - F_m \, \right] \tag{2.64}$$

The net pressure force F_p is given by the algebraic sum of the opening and closing pressure forces acting on the valve head, which vary according to the valve design. The negative sign in the term $k \, x_v$ corresponds

35

to the valve head being forced to close under the action of a spring. The Coulomb friction force F_C depends on the direction of motion. If the inflow momentum is small in relation to the outflow momentum at the opening (i.e. $v_u \ll v_f$), the flow momentum force can be determined by

$$F_m = \frac{q_f \, v_f \, \cos\varphi}{C_c} \tag{2.65}$$

where the contraction coefficient C_c is the ratio between the vena contracta area and the flow area and φ is the flow angle leaving the valve head. For convenient a flow force factor f_m is used to represent these two variables (ie. $f_m = \cos\varphi/C_c$).

2.9 AXIAL FLOW CARBON DIOXIDE SCRUBBER MODEL

An axial flow scrubber is commonly used in recirculating breathing equipment for the purpose of carbon dioxide absorption. The model developed for this device needs to take into account two performance characteristics. These are the pressure losses across the axial flow scrubber and the absorption of carbon dioxide by the absorbent.

2.9.1 Modelling the pressure losses across an axial flow scrubber

The pressure losses in the axial flow scrubber are introduced by the porous absorbent, canister and the two baffle plates as shown in figure 2.10. The frictional pressure drop through the porous absorbent can be correlated in the usual way by defining a friction factor f in the Darcy's equation (Wallis, 1969):

$$\delta p = f \, \tfrac{1}{2}\rho v_e^2 \, L_s \, (A_{e,sur}/V_V) \tag{2.66}$$

where $A_{e,sur}$ is the total surface area of the absorbent particles and V_V is the available flow volume (volume of voids). For spherical particles of diameter d_e, the hydraulic mean depth $V_V/A_{e,sur}$ is given by

$$\frac{V_V}{A_{e,sur}} = \frac{\varepsilon}{1 - \varepsilon} \frac{d_e}{6} \tag{2.67}$$

where ε is the ratio of the volume of voids to the total bed volume.

For particles which are not spherical, a shape factor Φ is often defined such that d_e is replaced by d_e/Φ. The average velocity through the interstices between the particles v_e in equation (2.66) is related to

36

the volumetric flux (ie. $v_s = v_s/\varepsilon$). Substituting equations (2.67) into equation (2.66) and redefining a friction factor $'f=3f/2$ we obtain

$$\delta p = 4\,'f\left(\frac{1-\varepsilon}{\varepsilon^3}\right)\frac{1}{2}\rho v_s^2\,\frac{L_s}{d_e} \tag{2.68}$$

The friction factor defined by equation (2.68) is usually correlated in terms of a Reynolds number (Wallis, 1969) which is defined in terms of the average fluid velocity and the hydraulic mean depth. Thus

$$Re_s = \frac{\rho\,v_s\,d_e}{(1-\varepsilon)\mu} \tag{2.69}$$

The experimentally determined friction factor $'f$ on the values of Re_s obtained by Burke and Plummer (Ergun, 1952) is shown in figure 2.11. In addition, a theoretical equation from Ergun (1952) is plotted on the graph as well, that is

$$'f = \frac{75}{Re_s} + 0.875 \tag{2.70}$$

Inclusion of the above friction factor in the Darcy equation led to the following equation for the pressure drop through the porous absorbent inside the axial flow scrubber and is applicable for both laminar and turbulent flow conditions:

$$\delta p = 2\,L_s\left[\frac{75\mu v_s(1-\varepsilon)}{d_e^2} + \frac{0.875\rho v_s^2}{d_e}\right]\left(\frac{1-\varepsilon}{\varepsilon^3}\right) \tag{2.71}$$

In addition, the pressure losses introduced by the two baffle plates at either end of the canister can be obtained using a 'k factor method' (Massey, 1987) similar to that outlined by Tilley (1990). Hence, the total pressure losses across the scrubber is given by

$$\delta p = K_s\frac{\rho v_s^2}{2} + 2\,L_s\left[\frac{75\mu v_s(1-\varepsilon)}{d_e^2} + \frac{0.875\rho v_s^2}{d_e}\right]\left(\frac{1-\varepsilon}{\varepsilon^3}\right) \tag{2.72}$$

By rearranging equation (2.72), the flow velocity v_s through the scrubber can be obtained.

2.9.2 Modelling the carbon dioxide absorption process in an axial flow scrubber

Although there has been a considerable quantity of data published on the design and efficiency of carbon dioxide absorbent scrubbers for recirculating breathing equipment (Anthony and Potts, 1979,

37

Nuckols, Purer and Denson, 1983), it is nevertheless difficult to understand how the absorption process functions. Virtually all these investigations have relied on expressing the duration and efficiency of the absorbent system as a time of breakthrough (that is the point at which the carbon dioxide concentration in the gas mixture through the absorbent system exceeds the physiological limit for human respiration). Consequently, these investigations rely heavily on experimental testing. Therefore, it is the intention of the author to develop a modelling technique which allows the performance of an carbon dioxide absorbent scrubber to be predicted. A detailed derivation of the modelling technique for the absorption process in the scrubber is beyond the scope of this thesis.

(i) Absorption chemistry

First, consider the chemical reaction involved in the absorption of carbon dioxide by the absorbent in the scrubber. In this case, sodalime (typically 3% sodium hydroxide and 97% calcium hydroxide) is used as the absorbent. The absorption process of carbon dioxide by the sodalime can be expressed by the following series of reactions:

$$CO_2 + H_2O \longrightarrow H_2CO_3 \qquad\qquad (I)$$

$$H_2CO_3 + 2NaOH \longrightarrow Na_2CO_3 + 2H_2O \qquad\qquad (II)$$

$$Na_2CO_3 + Ca(OH)_2 \longrightarrow 2NaOH + CaCO_3 \qquad\qquad (III)$$
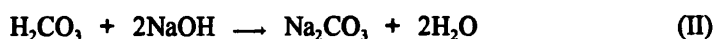
Note that, in this process, water is necessary to initiate the carbon dioxide absorption and also water is a by-product of the absorption process. If the incoming gas stream is saturated with water vapour, the water produced in the absorbent bed may not be picked up. This water will then tend to coat the outer surfaces of the absorbent particles, causing a decrease in absorption efficiency. If the incoming gas stream is too dry, the initiation of the reaction may be inhibited, thereby limiting further absorption. As a general rule, moisture levels of the incoming gas stream must be maintained above 70% RH when using sodalime (Nuckols, Purer and Denson, 1983).

(ii) Absorption in a packed-bed

Considering a flow of gas mixture through a section of porous absorbent media, an energy or mass balance across an elementary section of a column such as that shown in figure 2.12 can be written generally:

Accumulation = Input - Output - Loss by absorption

In order to obtain the fundamental equation for the absorption process, it is necessary to define certain parameters. Let $c(l,t)$ and $w(l,t)$ be the concentrations of carbon dioxide in the gas mixture and in the absorbent, respectively, at time t after the entrance of a gas mixture into the column and at distance l from the input end of the column. These c and w are expressed in moles of CO_2 in a unit volume of gas mixture and moles of absorbed CO_2 in a unit mass of absorbent respectively. Referring to figure 2.12, the mass balance on the gas and absorbent phase contained within the section dl can be expressed as

$$\frac{dc}{dt} = -v_e\frac{dc}{dl} - \frac{\rho_B}{\varepsilon}\frac{dw}{dt} \qquad (2.73)$$

Note that v_e is the average fluid velocity in the interstices between the particles (ie. $\varepsilon v_e = v_s$). In equation (2.73) it is assumed that the velocity of the fluid is constant across the bed in which the longitudual diffusion and the axial dispersion are neglected. Equation (2.73) must be coupled with another equation representing the behaviour of the absorbent. Thomas (1944) has given a most useful treatment of the absorption design problem and the rate of absorption in the absorbent can be represented by

$$\frac{dw}{dt} = \frac{k_m A_a}{\rho_B}\left[c\left(1-\frac{w}{\bar{w}}\right) - \zeta(c_{fe}-c)\frac{w}{\bar{w}}\right] \qquad (2.74)$$

The expression in the square bracket is called 'the kinetic driving force' and the mass transfer coefficient k_m describes the transition of a component from one phase to another (Sherwood, Pigford and Wilke, 1975). Note that A_a is the total interfacial area of the absorbent in a unit volume of packed bed and c_{fe} is the feed concentration of carbon dioxide to the column. The equilibrium factor ζ in equation (2.74) is used to define the chemical reaction in the absorbent which is either irreversible or reversible. The criteria for the irreversible and reversible reactions are, respectively, $\zeta = 0$ and $\zeta > 0$ (Ruthven, 1984). At present, as the reactions (II) and (III) are irreversible (Anthony and Potts, 1979, Nuckols, Purer and Denson, 1983), it is reasonable to treat the whole process to be an irreversible reaction. Therefore, equation (2.74) simply becomes

$$\frac{dw}{dt} = \frac{k_m A_a c}{\rho_B}\left(1-\frac{w}{\bar{w}}\right) \qquad (2.75)$$

Hence, the dynamic response of the absorption in the column is given by the solution $[c(l,t),w(l,t)]$ to equations (2.73) and (2.75), subject to the initial and boundary conditions imposed on the column. Bohart and Adams (1920) were able to reduce equations (2.73) and (2.75) to a linear equation by introducing a

39

transformation of the dependent variables. Their solutions for the boundary conditions on $c(l,t)$ and $w(l,t)$, such that $c(0,t)=c_{fe}=$constant and $w(l,0)=0$, are given by

$$\frac{c}{c_{fe}} = \frac{e^{\psi_1}}{e^{\psi_1} + e^{\psi_2} - 1}$$

(2.76)

$$\frac{w}{\hat{w}} = \frac{e^{\psi_2}}{e^{\psi_1} + e^{\psi_2} - 1}$$

(2.77)

where

$$\psi_1 = \frac{k_m A_a c_{fe}}{\hat{w} \rho_B}\left(t - \frac{l}{v_e}\right) \quad , \quad \psi_2 = \frac{k_m A_a l}{v_e \varepsilon}$$

These solutions will lead to the formations of the concentration profiles in the column and the output concentration curve as sketched in figures 2.13(a), (b) and (c).

However, equations (2.76) and (2.77) cannot be applied to the conditions where the input concentration of CO_2 and the flow velocity through the scrubber vary with time and also where the flow direction is changing during the breathing cycle. Therefore, it is necessary to establish an approach to model the absorption process allowing these conditions to be considered. Again consider a column divided into N numbers of small elements as shown in figure 2.14. By using equation (2.75), the rate of absorption in element 'i' can be written as

$$\frac{dw_i}{dt} = \frac{k_m A_a c_i}{\rho_B}\left(1 - \frac{w_i}{\hat{w}}\right)$$

(2.78)

Referring to figure 2.14, if the direction of flow through the column is from the left, then the rate of change of CO_2 concentration in element 'i' requires information on the CO_2 concentration from the upstream condition which is in the element 'i-1', and from equation (2.73) we can write down directly the expression for the rate equation in element 'i', that is

$$\frac{dc_i}{dt} = \frac{v_e}{\delta l}\left(c_{i-1} - c_i\right) - \frac{\rho_B}{\varepsilon}\frac{dw_i}{dt}$$

(2.79)

However, if the direction of flow through the column is from the right, then the term c_{i-1} in equation (2.79) will be changed to c_{i+1}. In this manner, all the time derivative terms dw/dt and dc/dt in each of the elements can be solved using numerical integration.

40

Referring to figure 2.14 again, the first element from the input end, which can be at either side of the column, requires the input flow concentration c_{fe} from the upstream model for the determination of the rate of change of CO_2 concentration. However, according to the analysis in section 2.3, the component models connected to the scrubber supply the mass fraction of CO_2 rather than the concentration of CO_2. Therefore, it is necessary to establish a relationship between the concentration and mass fraction of CO_2 in the scrubber model, that is

$$c_{fe} = \frac{m_{in,CO2}}{M_{CO2}} \frac{1}{V_u} = \left(\frac{m_{in,CO2}}{m_{in}}\right) \frac{P_u}{M_{CO2} \, R \, T_u} \tag{2.80}$$

At the same time, the scrubber model is required to supply the mass fraction of CO_2 to the downstream model. This output mass fraction of CO_2 can be obtained from the CO_2 concentration at the last element from the input end c_{las} imposing the downstream condition, and equation (2.80) can be rearranged into the following form for determining the output mass fraction of CO_2:

$$\frac{m_{CO2}}{m} = \frac{c_{las} \, M_{CO2} \, R \, T_d}{P_d} \tag{2.81}$$

It is reasonable to write the following equation for the determination of the total CO_2 absorption rate:

$$q_{CO2,up} = \sum_{i=1}^{N} \dot{w}_i \, \rho_B \, A_s \, \delta l \, M_{CO2} \tag{2.82}$$

Hence, the actual output mass flow rate of the scrubber can be found using the relationship

$$q_{s,ac} = q_s - q_{CO2,up} \tag{2.83}$$

where q_s is obtained from equation (2.72) and using the relation $q_s = \rho v_s A_s$.

(iii) Determination of the mass transfer coefficient

The above theoretical analysis can describe a satisfactory prediction of the absorption process provided that the mass transfer coefficient k_m is correctly chosen. Therefore, it is necessary to obtain a suitably accurate value for k_m. First, consider a CO_2 concentration profile from a gas stream to the surface of the absorbent as shown in figure 2.15(a). This figure also illustrates two phases categorized as the mass transfer of CO_2 from the gas stream to the absorbent surface (phase P) and the chemical absorption at the

41

surface (phase Q). If the transitions in these phases are described by two individual mass transfer coefficients as $k_{m,g}$ in phase P and $k_{m,chem}$ in phase Q, the overall mass transfer coefficient k_m can be defined by the following concentration flux equation (Sherwood, Pigford and Wilke, 1975):

$$k_{m,g} \ (c - c_{as}) = k_{m,chem} \ c_{as} = k_m \ c \tag{2.84}$$

Then,

$$\frac{1}{k_m} = \frac{1}{k_{m,g}} + \frac{1}{k_{m,chem}} \tag{2.85}$$

Numerous studies (Danckwerts, 1970, Szekely, Evans and Sohn, 1976) have been carried out with the object of measuring the mass transfer coefficient $k_{m,g}$ between the gas stream and particle surface. For this kind of mass transfer, Smith (1981) has summarized that the Stanton number for mass transfer $k_{m,g}/v_s$ is an empirical function of the Reynolds number $\rho v_s d_s/\mu$ and the Schmidt number $\mu/\rho D$. This is represented by the following equation, which is mostly used for the engineering estimation:

$$\frac{k_{m,g}}{v_s} \left(\frac{\mu}{\rho D}\right)^{2/3} = \frac{0.458}{\varepsilon} \left(\frac{\rho \ v_s \ d_s}{\mu}\right)^{-0.407} \tag{2.86}$$

The best determination of the diffusion coefficient D in the Schmidt number for the CO_2 mixed with the air is that due to Vargaftik (1975), which is obtained from the known diffusion coefficient value with the known condition. The equation is given by

$$D = \frac{D'P'}{P} \left(\frac{T}{T'}\right)^{\theta} \tag{2.87}$$

Experimental values of the known diffusion coefficient D' and the power index θ of CO_2 mixed with the air are available for equation (2.87) as illustrated in table 2.4. Hence, the mass transfer coefficient $k_{m,g}$ between the gas stream and the absorbent surface can be found.

The mass transfer coefficient $k_{m,chem}$ for the chemical absorption at the surface can be calculated from the Arrhenius equation (Smith, 1981), that is

$$k_{m,chem} = (f_A / A_a) \ e^{-E_{sur}/RT} \tag{2.88}$$

The value of the apparent frequency factor f_A and the activation energy of the surface reaction E_{sur} in equation (2.88) can be evaluated from molecular properties of the reacting species. Since the reaction between the sodalime and CO_2 is instantaneous (Nuckols, Purer and Denson, 1983), the value of $k_{m,chem}$ must

42

be more than the value of $k_{m,g}$ by a large amount and referring to equation (2.85), k_m will approach the value $k_{m,g}$ as shown in figure 2.15(b). Therefore, $k_{m,chem}$ can be ignored and $k_m = k_{m,g}$.

2.10 BREATHING SIMULATOR MODEL

The breathing simulator which is used for the unmanned testing can be modelled as a linear actuator with one side connected to the breathing equipment (delivery side) and the other side connected to the gas space of the hyperbaric chamber (balance side). Using equations (2.17) and (2.18), the rate of change of pressures and temperatures in the delivery and balance sides of the breathing simulator can be obtained using

$$\dot{P}_{ld} = \frac{n}{V_{ld}} [R (\Sigma \dot{m}_{in,ld}T_{in,ld} - \Sigma \dot{m}_{out,ld}T_{ld}) - P_{ld}\dot{V}_{ld}] \qquad (2.89)$$

$$\dot{T}_{ld} = \frac{T_{ld}}{P_{ld}V_{ld}} [\dot{P}_{ld}V_{ld} + P_{ld}\dot{V}_{ld} - \dot{m}_{ld}RT_{ld}] \qquad (2.90)$$

$$\dot{P}_{lb} = \frac{n}{V_{lb}} [R (\Sigma \dot{m}_{in,lb}T_{in,lb} - \Sigma \dot{m}_{out,lb}T_{lb}) - P_{lb}\dot{V}_{lb}] \qquad (2.91)$$

$$\dot{T}_{lb} = \frac{T_{lb}}{P_{lb}V_{lb}} [\dot{P}_{lb}V_{lb} + P_{lb}\dot{V}_{lb} - \dot{m}_{lb}RT_{lb}] \qquad (2.92)$$

For the delivery and balance sides of the breathing simulator the rate of change of both volumes are the same but opposite in sign. It is considered that the variation is simply equal to the respiratory demand volumetric flow rate:

$$\dot{V}_{ld} = -\dot{V}_{lb} = Q_r \qquad (2.93)$$

The complex processes associated with the human respiratory system have been simplified by assuming that the respiratory demand in the breathing simulator varies sinusoidally with time and Q_r at any time can be determined according to:

$$Q_r = \frac{\pi \ RMV}{60 \times 10^3} \sin\left(\frac{2\pi N_b t}{60}\right) \qquad (2.94)$$

In the case of the breathing simulator performing the gas exchange process, the oxygen uptaken rate $q_{O2,up}$ needs to be included in the outflow mass flow rate term $\Sigma \dot{m}_{out,ld}$ of equations (2.89) and (2.90). Similarly, the carbon dioxide production rate $q_{CO2,pr}$ needs to be included in the inflow mass flow rate term $\Sigma \dot{m}_{in,ld}$ of equations (2.89) and (2.90). These allow a more precise evaluation of the pressure and temperature inside the breathing simulator. In addition, the equations to determine the rate of change of the mass of oxygen and carbon dioxide in the breathing simulator model need to be modified.

For the oxygen,

$$\frac{dm_{O2}}{dt} = \sum q_{in} \frac{m_{in,O2}}{m_{in}} - \sum q_{out} \frac{m_{O2}}{m} - q_{O2,up} \tag{2.95}$$

For the carbon dioxide,

$$\frac{dm_{CO2}}{dt} = \sum q_{in} \frac{m_{in,CO2}}{m_{in}} - \sum q_{out} \frac{m_{CO2}}{m} + q_{CO2,pr} \tag{2.96}$$

In most of the studies (Bennett and Elliott, 1982), the oxygen consumption and CO_2 production rates are abbreviated $\dot{V}_{O2}$ and $\dot{V}_{CO2}$ respectively and also expressed in litres per minute corrected to standard conditions (STPD) where STPD stands for standard Temperature ($0°C$) and Pressure (1.013 bar) for Dry air. Using the equation of state for a gas, the oxygen consumption and CO_2 production rates in kg/s can be obtained from $\dot{V}_{O2}$ and $\dot{V}_{CO2}$ respectively by

$$q_{O2,up} = \left(\frac{P_{1.013}\, M_{O2}}{R_o\, T_{273}} \right) \dot{V}_{O2} \times \frac{1}{60 \times 10^3} \tag{2.97}$$

$$q_{CO2,pr} = \left(\frac{P_{1.013}\, M_{CO2}}{R_o\, T_{273}} \right) \dot{V}_{CO2} \times \frac{1}{60 \times 10^3} \tag{2.98}$$

Table 2.5 assembles most of the available data on the oxygen consumption and CO_2 production of human specific work efforts. The relationship between $\dot{V}_{O2}$ and $\dot{V}_{CO2}$ can be expressed by the ventilation ratio R_v:

$$R_v = \dot{V}_{CO2} / \dot{V}_{O2} \tag{2.99}$$

The value of R_v can be approximated and range from 0.7 to 1.0 (Bennett and Elliott, 1982).

2.11 RESPIRATORY WORK IN BREATHING

According to section 1.3.5, the respiratory work expended during a breathing cycle is of prime

importance to the diver's performance. During unmanned testing, the respiratory work is assessed from a breathing loop formed by plotting the mouth differential pressure against the breathing simulator displaced volume over a complete breathing cycle, similar to figure 1.6. The mouth differential pressure is the difference between the gas pressure at the mouth piece and the hydrostatic pressure acting immediately at the mouth piece. In order to compare the unmanned testing at different tidal volume conditions, the breathing simulator displayed volume is obtained by deducting a fixed reference volume from the actual breathing simulator volume:

$$V_{ld,dis} = \hat{V}_{ld} - V_{ld} \tag{2.100}$$

Referring to section 1.3.5, the area enclosed within the resulting breathing loop is the external resistive work and the work done is determined according to,:

$$W = \int P \, dV \tag{2.101}$$

Replacing dV by $(dV/dt)dt$ and noting that the rate of change of volume is equivalent to the respiratory demand volumetric flow rate Q_r, an expression can be found for the external respiratory work as follows,

$$W_{re} = -\int_0^{t_{cy}} (P_m - \mathcal{P}_m) \, Q_r \, dt \tag{2.102}$$

As the principle aim is to minimize the respiratory work of breathing, equation (2.102) can be used as the basis of a performance optimization algorithm in the simulation of breathing systems.

2.12 CLOSURE

A number of mathematical models has been developed for a wide range of underwater breathing apparatus. A technique to simulate the variations of gas composition in the breathing apparatus is described. In addition, an approach to simulate the carbon dioxide absorption process in the axial flow scrubber has been developed. It is intended that these modelling techniques will be applied for the simulation of different kinds of breathing apparatus. The simulation results of different underwater breathing apparatus are documented in the next chapter.

Definition	Specific internal energy, u	Specific enthalpy, h
$C_P - C_V = R$, $C_P / C_V = \gamma$ $\tilde{h} - C_P \tilde{T} = \tilde{u} - C_V \tilde{T}$	$\tilde{u} = C_V \tilde{T}$ $u = \tilde{u} + C_V(T - \tilde{T})$	$\tilde{h} = C_P \tilde{T}$ $h = \tilde{h} + C_P(T - \tilde{T})$

Table 2.1 The expression of u and h in terms of gas properties

Gas	Molecular Weight M (kg/mole)	Specific heat at constant Pressure C_P (J/kg K)	Specific heat at constant Volume C_V (J/kg K)	Coefficient of Viscosity at 0°C μ (10^{-6}Pa s)	Sutherland's Constant S
Air	29	1009	721	17	120
CO_2	44	858	660	13.8	240
He	4	5234	3153	18.6	100
N_2	28	1034	733	16.6	111
O_2	32	909	649	19.2	127

Table 2.2 Physical properties of gases 0°C

Conditions	Values of K
90° elbow bend	0.9
45° elbow bend	0.4
Side outlet of 'T' junction	1.8
Square-edge end fittings	0.5
Protruded pipe at end fittings	1

Table 2.3 Approximate loss coefficient K for commercial pipe fittings

Gas	D', cm^2/s	β
Air-CO_2	0.142	1.7
O_2-CO_2	0.138	1.8
N_2-CO_2	0.144	1.73
H_2O-CO_2	0.146	1.84
Air-H_2O	0.216	1.8

Table 2.4 Experimental values of diffusion coefficient D' and β at $T = 273$ K and $P = 1.013$ bar

Work effort	Breaths per minute	Tidal Volume (L)	Respiratory Minute Volume RMV (L/min)	O_2 Consumption rate (L/min)
Rest	12	0.5	6	0.25
Light work	15	1.5	22.5	0.9
Moderate work	20	2	40	1.6
Heavy work	25	2	50	2
Hard work	25	2.5	62.5	2.5
Extremely hard work	30	2.5	75	3

Table 2.5 Breathing characteristic associated with human specific work efforts
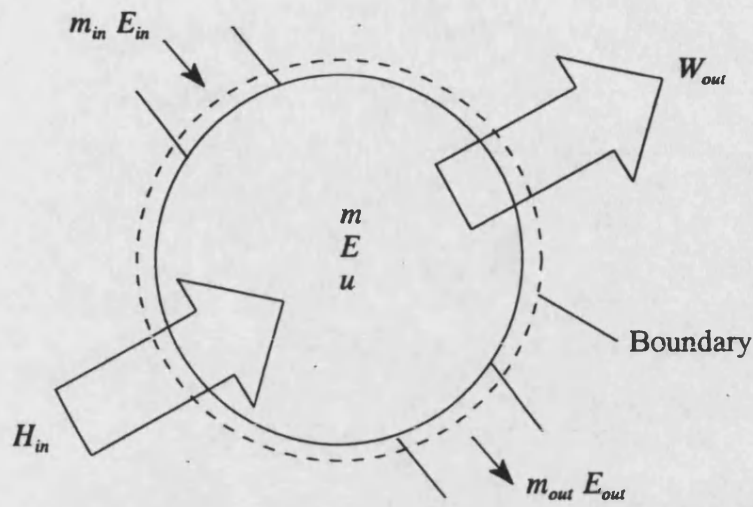
Figure 2.1 A volume of gas undergoing a flow process
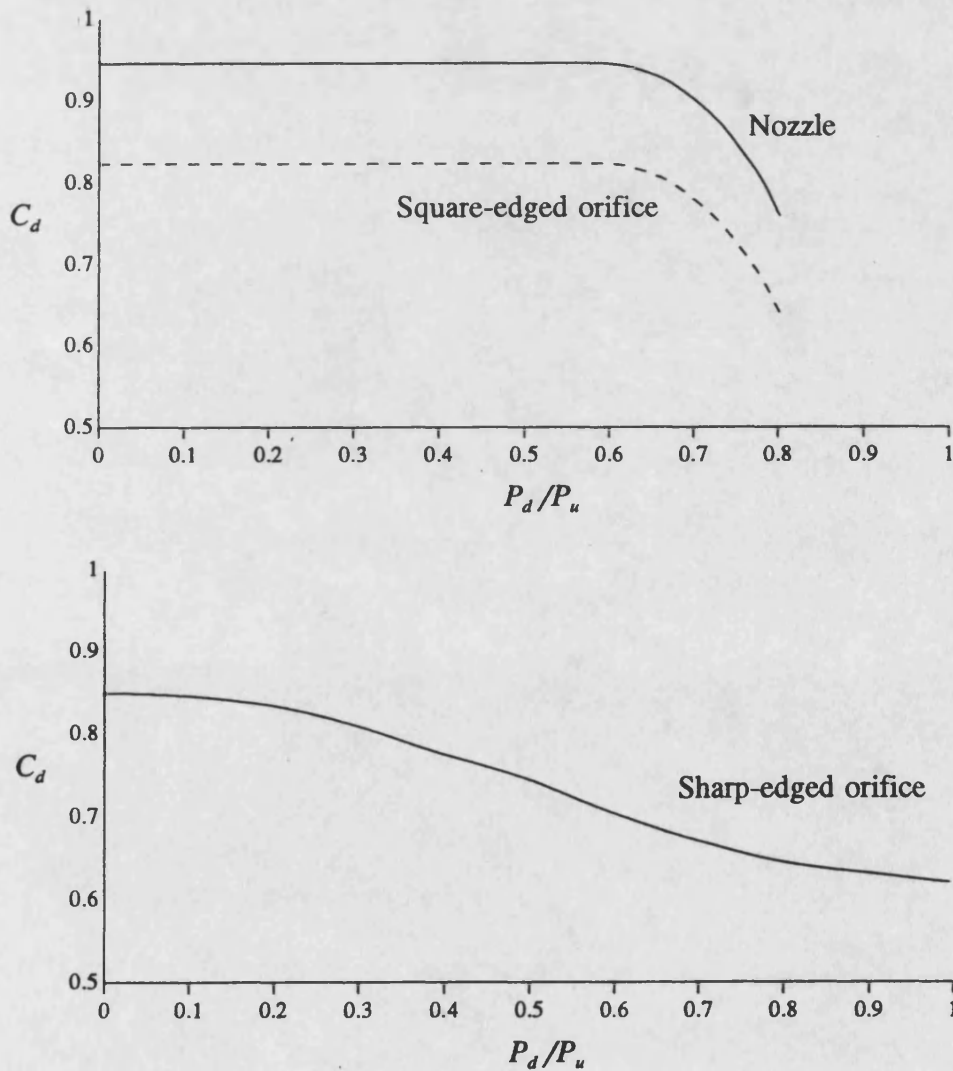
Figure 2.2 Discharge coefficient for nozzles, square-edged orifices and sharp-edged orifices

48
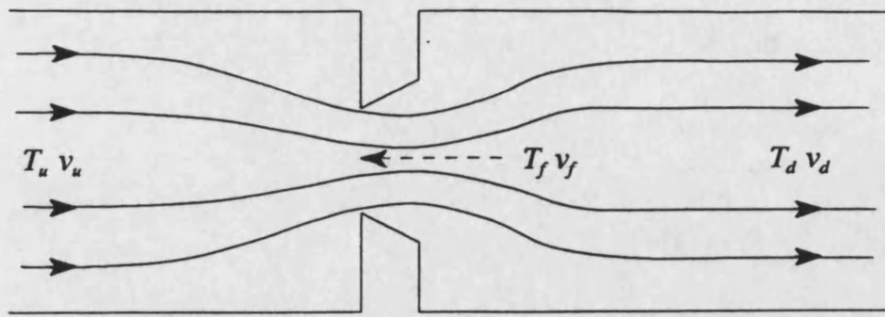
Figure 2.3(a) Flow of gas through an orifice
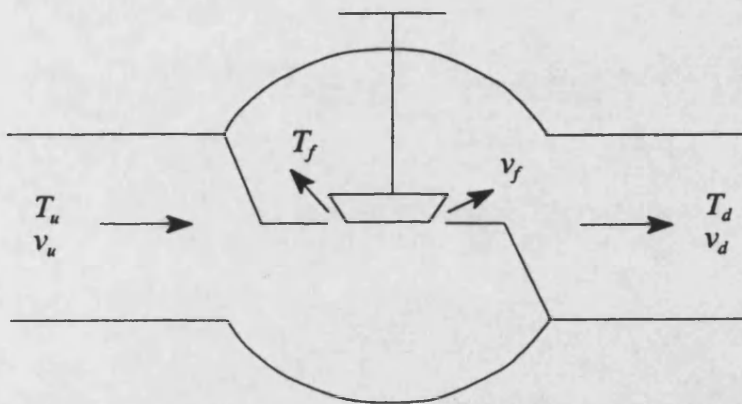
Figure 2.3(b) Flow of gas through a valve
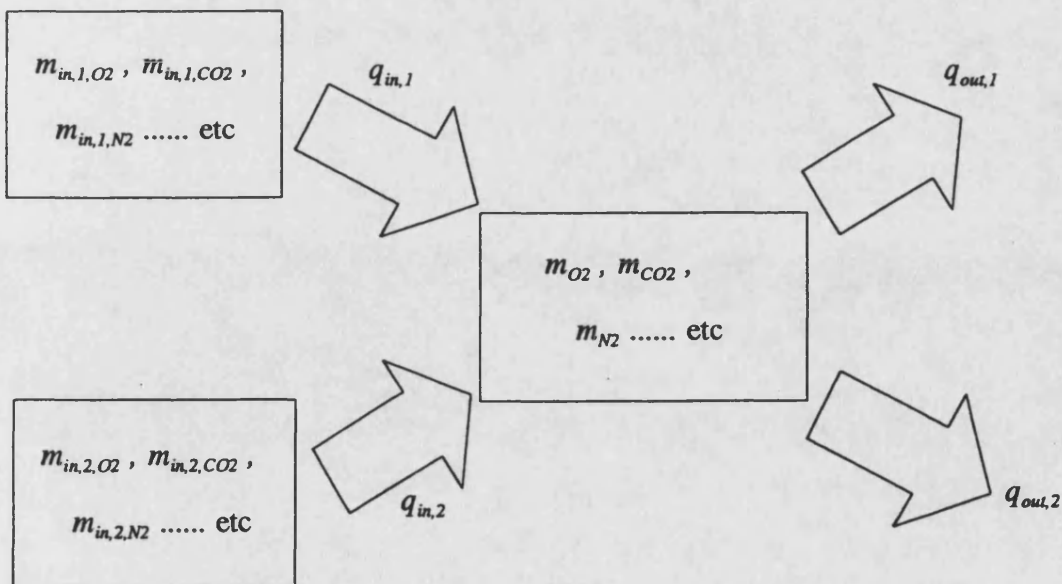
Figure 2.4 Gas streams flow into and out of a capacitive element
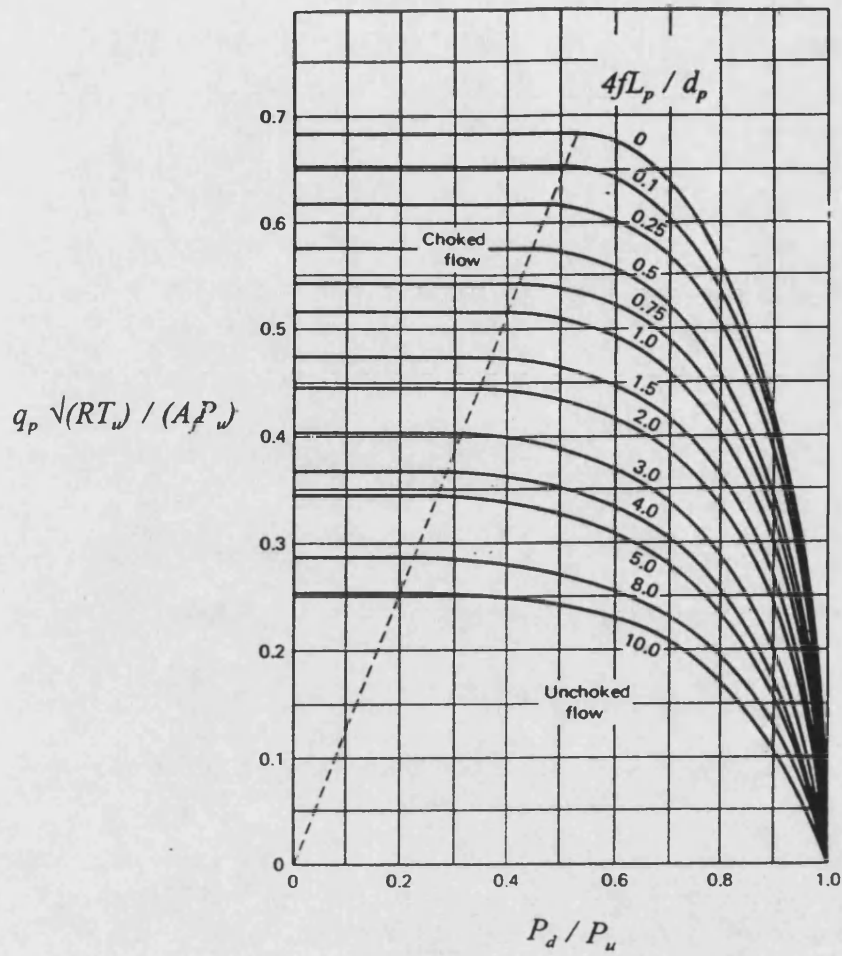
Figure 2.5 Constant $4fL_p/d_p$ lines on an $q_p\sqrt{(RT_u)}/(A_fP_u)$ versus P_d/P_u plot ($n=\gamma=1.4$)
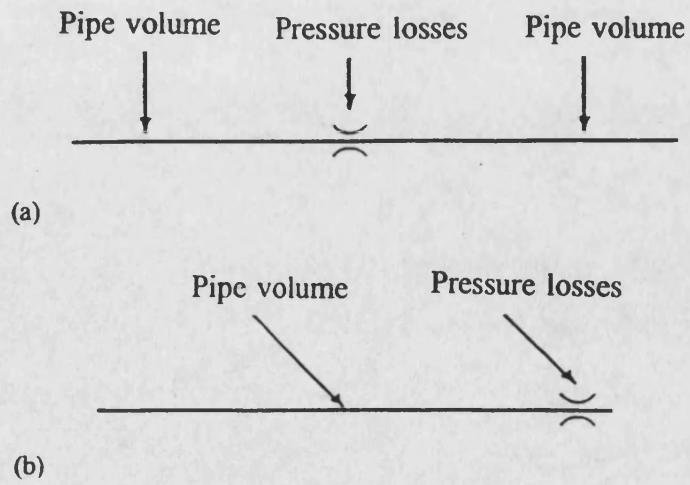
Figure 2.6 Representation of friction pipe model

50
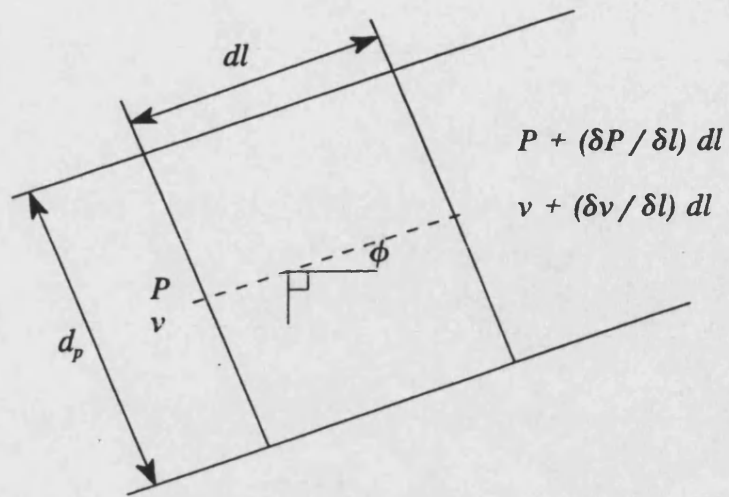
Figure 2.7 A section of flow in a long pipe
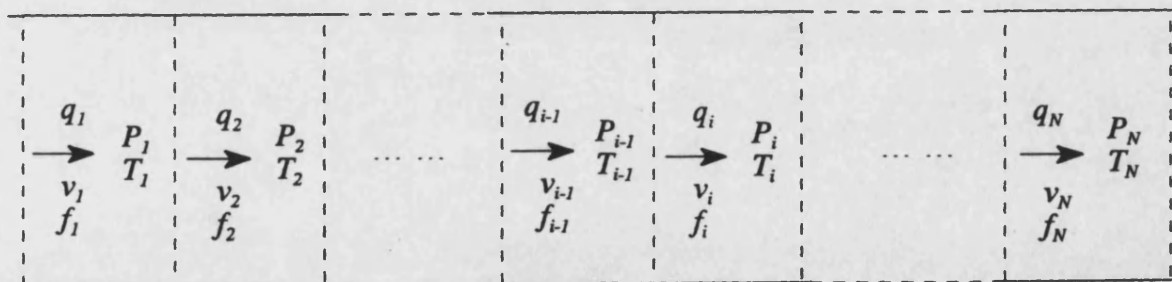
Figure 2.8 Series of individual interconnected pipes
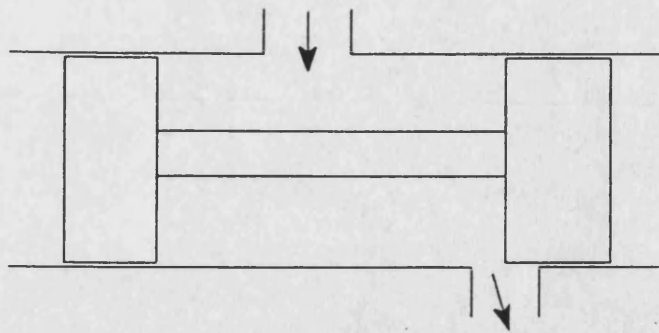
(a) Spool type
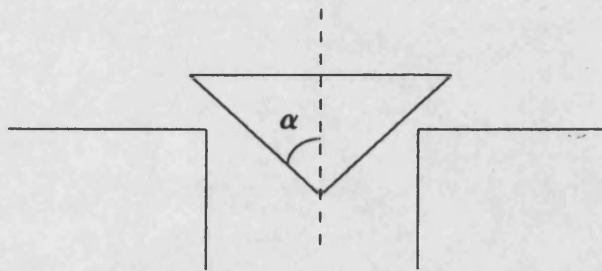
(b) Poppet type
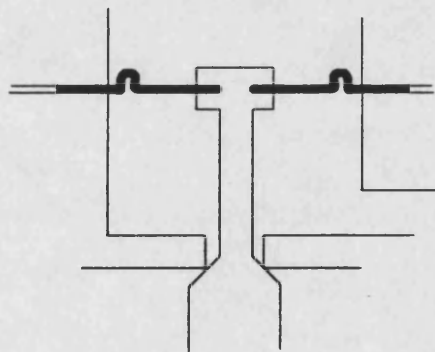
(c) Diaphragm type
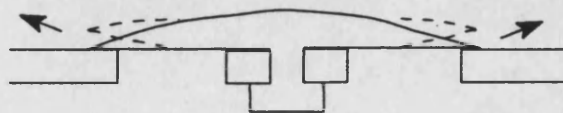
(d) Mushroom type

Figure 2.9 Basic types of valve
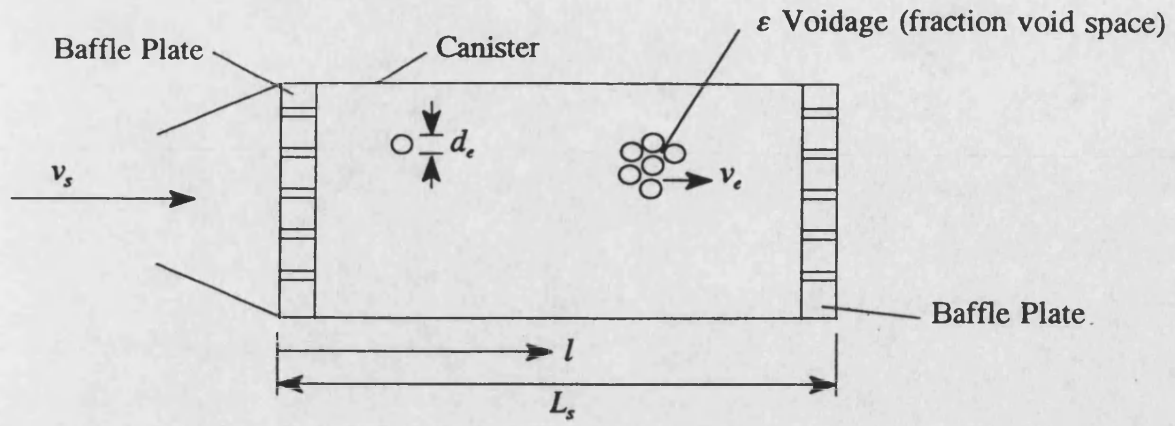
Figure 2.10 Axial flow carbon dioxide scrubber
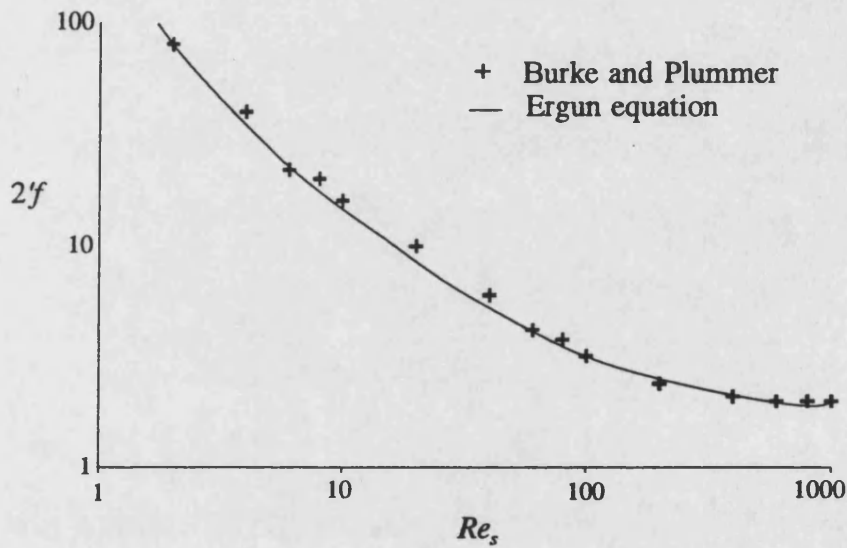
Figure 2.11 Experimental meassurement of flow through porous media compared with Ergun's equation
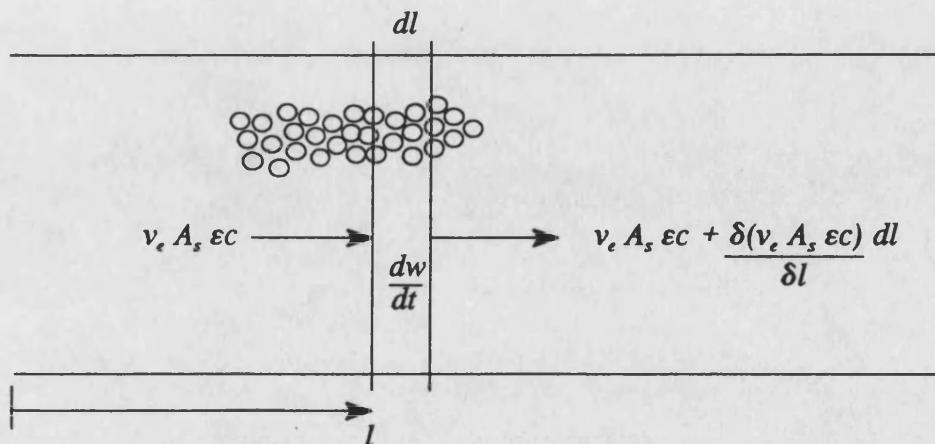
Figure 2.12 Mass conservation in a packed-bed

53
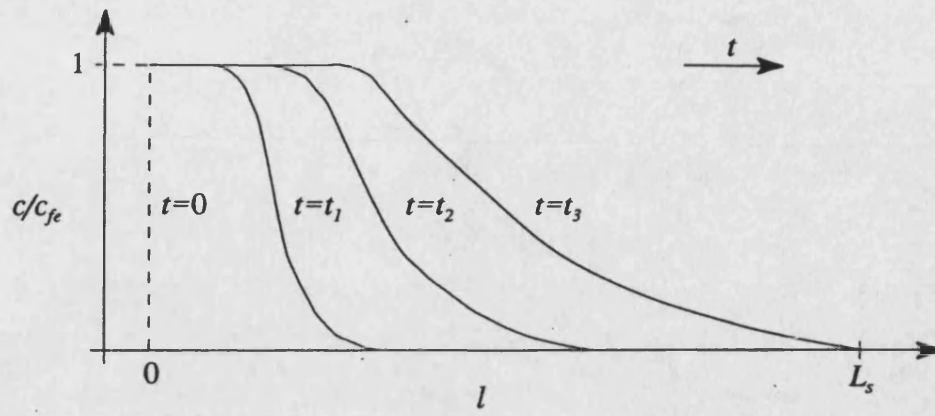
Figure 2.13(a) Gas phase CO_2 concentration profile in a packed-bed
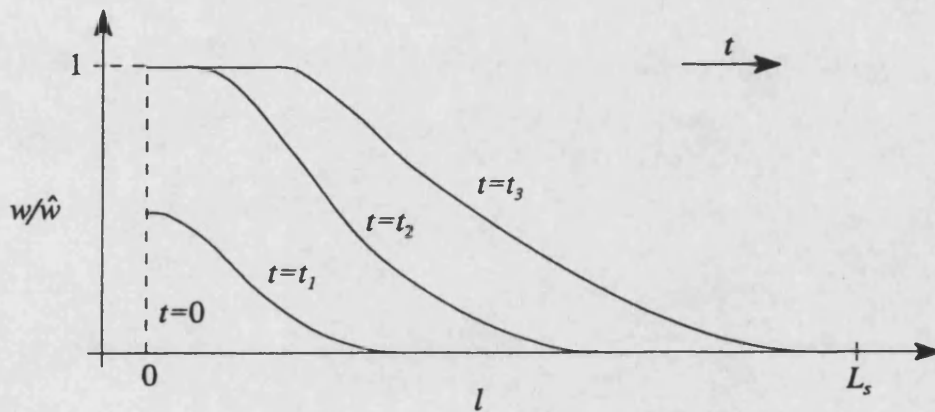
Figure 2.13(b) Absorbent phase CO_2 concentration profile in a packed-bed
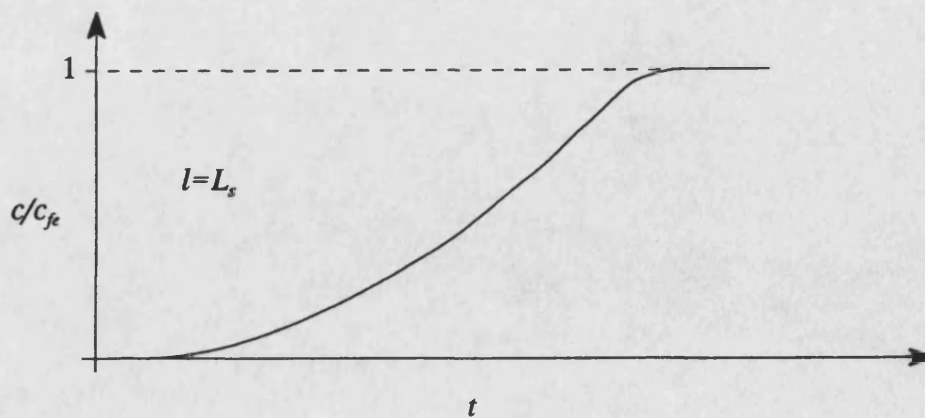
Figure 2.13(c) Output CO_2 concentration breakthrough curve from a packed-bed

54
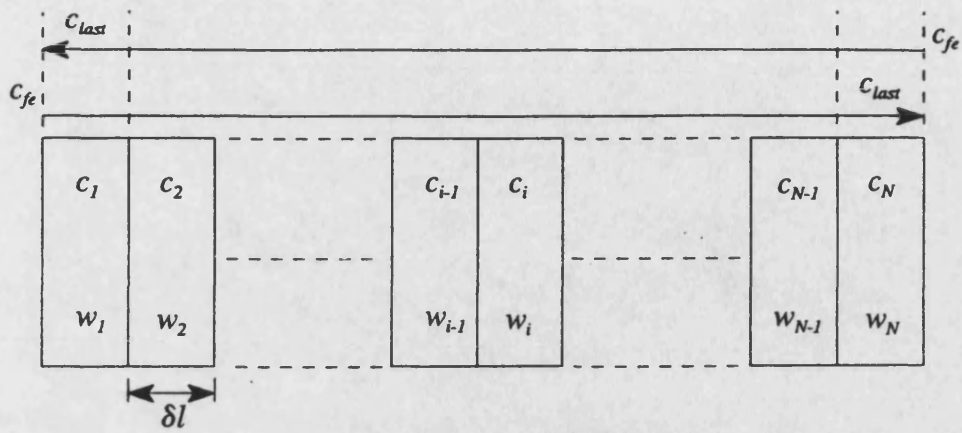
Figure 2.14 Representation of the elements in a packed-bed
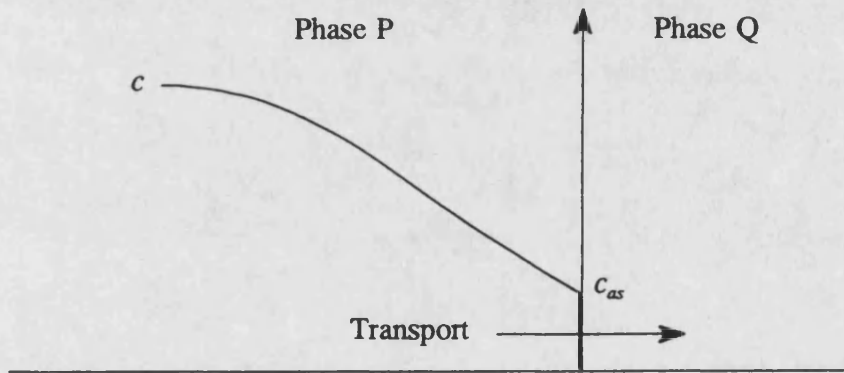
Figure 2.15(a) Concentration profile near the absorbent surface

$$k_m = \cfrac{1}{\cfrac{1}{k_{m,g}} + \cfrac{1}{k_{m,chem}}}$$
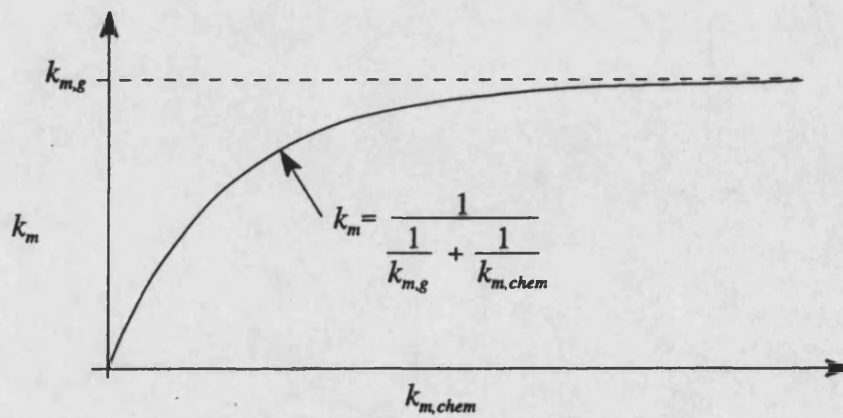
Figure 2.15(b) Solution of equation (2.85)

CHAPTER 3

COMPUTER SIMULATION OF
UNDERWATER BREATHING APPARATUS

3.1 INTRODUCTION

In order to validate the mathematical models developed in Chapter 2, two different kinds of breathing systems which have been mentioned already in section 1.2 are simulated in this chapter. The first is a semi-closed-circuit breathing system which is by far the most commonly used re-breathing apparatus for military operations. The second is a surface demand diving system which is the dominant type of apparatus used in modern commercial diving. For simplicity, these simulations are investigated under unmanned testing condition.

3.2 SIMULATION OF A SEMI-CLOSED-CIRCUIT BREATHING SYSTEM

3.2.1 Introduction

The semi-closed-circuit breathing system is a kind of recirculating breathing system. Although not exactly the same, it is similar in appearance to the equipment shown in figure 3.1. The breathing circuit is a pendulum type in which the diver breaths through the mouthpiece, convoluted breathing tube and axial flow carbon dioxide absorbent scrubber from and into an inflated bag called a counterlung. The 'constant mass flow jet' gas control unit, which is fitted in the line of gas storage bottles, pressure regulating valve, inter-connecting pipe and an acoustic jet (orifice), is preset to supply a constant oxygen fraction of mixed gas to the counterlung at any depth of water. Over-pressurization of the counterlung is prevented by the use of a pressure relief valve. The buoyancy and breathing comfort of the diver is controlled by an additional buoyancy control valve which vents gas from the counterlung to the surrounding water. A schematic of the breathing system is given in figure 3.2.

3.2.2 Previous component models development

A range of models related to the semi-closed-circuit breathing system has been developed by Tilley and Tomlinson (1990). Their models are mainly to investigate the work in breathing related to the breathing equipment. The following sections describe the theoretical analysis of their models.

(i) Models of constant mass flow jet unit

For the theoretical analysis developed by Tilley, isothermal conditions were assumed to apply such that the temperature of the gas is considered to remain constant at all points throughout the system. Hence, the rate of change of pressures inside the gas storage bottles and inter-connecting pipe can be obtained from:

$$\frac{dP_{bo,p}}{dt} = \frac{R\ T_{bo,p}}{V_{bo,p}} \left(\Sigma\ \dot{m}_{in} - \Sigma\ \dot{m}_{out} \right) \tag{3.1}$$

The mass flow rates through the acoustic jet and pressure regulating valve were obtained by equation (2.19) mentioned in section (2.2.2). The motion of the pressure regulating valve (figure 3.3) was simulated using a similar approach to that described in section (2.8) where the dynamic motion was considered. After equating the forces acting on the valve head, the net pressure force is given by;

$$F_P = P_{am}A_{di} - P_{out}(A_{di} - A_{vs}) - P_{in}A_{vs} \tag{3.2}$$

and the net spring force is given by;

$$F_s = k_{la}(x_{k,la} - x_v) - k_{sm}(x_{k,sm} + x_v) \tag{3.3}$$

(ii) Model of counterlung

In the study by Tilley, the counterlung has been modelled as a linear actuator, as shown in figure 3.4(a), subjected to the pressures acting on the frontal area. Equating the forces acting on the counterlung face gives the following expression for the counterlung face acceleration

$$\frac{d^2x_c}{dt^2} = \frac{(P_c - \mathcal{P}_c - P_r)A_c - f_v\dot{x}_c}{Me} \tag{3.4}$$

Note that $\mathcal{P}_c$ is the hydrostatic pressure acting on the centre of the counterlung face. In writing equation (3.4), the friction term has been represented by the resistance pressure model P_r. The resistance pressure was determined from practical test. A typical set of results is shown in figure 3.4(b), indicating a significant difference between the inflation and deflation curves leading to a hysteresis loop. In order to model the resistance pressure, the test data have been represented using the following polynomial:

$$P_r = \Omega_1 + \Omega_2 V_c + \Omega_3 V_c^2 + \cdots + \Omega_{n+1}V_c^n \tag{3.5}$$

where the coefficients Ω_1, Ω_2, ... , Ω_{n+1} are different for the inflation and deflation process. Satisfactory

agreement between the measured and predicted curves was obtained using polynomials of order 4 or 5. For isothermal expansion, the rate of change of counterlung pressure is obtained by;

$$\frac{dP_c}{dt} = \frac{R\ T_c}{V_c} \left(\Sigma\ \dot{m}_{in} - \Sigma\ \dot{m}_{out} - \rho \dot{V}_c \right) \tag{3.6}$$

Work has been undertaken by Tomlinson (1993) to obtain an improved model of the counterlung such that the resistance term can be predicted theoretically. The improved expression for the counterlung face acceleration is given by;

$$\frac{d^2 x_c}{dt^2} = \frac{Meg\sin\phi\ -\ \rho_w V_c g\sin\phi\ +\ (P_c - \mathcal{P}_c) A_c - f_v \dot{x}_c - k_c x_c - F_c}{Me} \tag{3.7}$$

The new counterlung model considers the material stiffness k_c and Coulomb resistance force F_C as well as the component weight $Me\ g\ sin\phi$ and buoyancy force $\rho_w\ V_c\ g\ sin\phi$ which are dependent on diver orientation. The improved counterlung model also includes the effect of changes in pressure centroid and area acted on by pressure forces.

(iii) Models of counterlung pressure relief and buoyancy control valves

The counterlung pressure relief valve, as shown in figure 3.5, operates when the difference between the counterlung pressure and the external water pressure exceeds a set level. The valve consists of a rubber diaphragm held in place by a compression spring and the valve cracking pressure is determined by the initial spring compression. Tilley neglected the flow momentum effects on the valve and assumed the valve to respond instantaneously to pressure changes. Hence, the valve opening is obtained directly by;

$$x_v = \frac{(P_c - \mathcal{P}_v)\ A_v}{k_v} - x_k \tag{3.8}$$

where $\mathcal{P}_v$ is the hydrostatic pressure acting on the outlet of the valve. Referring to figure 3.5, the flow area of the valve is annular and the discharged mass flow rate is determined using equation (2.19).

The buoyancy control valve, as shown in figure 3.6, prevents the counterlung from becoming overinflated by venting excess gases through the venting plate to the surrounding water. If the counterlung pressure falls below the external hydrostatic pressure, ingress of water is prevented by a mushroom type non-return valve. This mushroom valve which is a lightweight rubber diaphragm has been simulated using

a different approach. According to the test data reported by Imison (1985), Tilley has suggested that the pressure-flow characteristic of the mushroom valve is linear and is given by;

$$Q_{mv} = \mathcal{H}_{mv} \left(P_c - P_{bc,1} - P_{cr} \right) \tag{3.9}$$

Note that $P_{bc,1}$ is the pressure between the mushroom valve and the variable restriction.

A variable restriction is provided to allow the diver to close the valve fully if required. When the valve is opened, the flow area is annular and is given by;

$$A_f = \pi\, d_{vs}\, x_v \sin\alpha \tag{3.10}$$

The gas flow through the variable restriction was determined using equation (2.19).

The venting plate comprises a series of holes which has been represented as a single lumped flow area in Tilley's analysis. Hence, equation (2.19) was used to calculate the flow rate where the upstream pressure in equation (2.19) is the pressure between the variable restriction and the plate, $P_{bc,2}$, and the downstream pressure is the external water pressure. Tilley has assumed the changes in pressure, $P_{bc,1}$ and $P_{bc,2}$ in the small internal volume of the buoyancy control valve responded instantaneously so that the analysis of the small internal volume has been ignored. Continuity is achieved in the model by undertaken successive iterations until the mushroom valve, variable restriction and venting plate flows equate within a specified tolerance.

(iv) Pressure losses in the mouthpiece, flexible breathing tube and carbon dioxide scrubber

The flow resistance effects in the mouthpiece, flexible breathing tube and carbon dioxide scrubber are considered in Tilley's models. To take into account the reduction in flow area at the mouthpiece together with a change in flow direction, the analysis for the loss was based on 'k factor method' (Massey, 1987) obtained from measured results (figure 3.7). Thus the pressure drop and flow relationships for the mouthpiece is;

$$\delta p = 1.82\, \frac{\rho\, v_{mp}^{2}}{2} \tag{3.11}$$

The breathing tube is a kind of flexible convoluted tube. The flow resistance associated with the tube directly influences the effort expended by the diver in breathing. Inclusion of the friction introduced

by the convolutions and the bend of the tube in the analysis led to the following equation suggested by Yeaple (1966) for the pressure loss:

$$\delta p = \left[N_{con} \left[1 - \left(\frac{d_{bt}}{d_{bt} + 0.35Y} \right)^2 \right]^2 + K_{bt} \left(\frac{\lambda}{90} \right)^{0.5} \right] \frac{\rho \, v_{bt}^{\,2}}{2} \tag{3.12}$$

The pressure losses in the axial flow scrubber were simulated using the approaches similar to that outlined in section 2.9.1. However, in Tilley's model the absorption of CO_2 was not taken into account and the equation to determine the pressure loss through the porous absorbent was derived from experimental data. The pressure losses introduced by the two baffle plates at either end of the canister were obtained using the 'k factor method' as described in section 2.9.1. Thus the total pressure loss including the canister and the soda lime is

$$\delta p = K_s \frac{\rho \, v_s^2}{2} + 2L_s \left(\frac{838 \mu v_s}{d_e^{\,2}} - \frac{27.3 \mu^{0.5} \rho^{0.5} v_s^{1.5}}{d_e^{\,1.5}} + \frac{14.6 \rho v_s^2}{d_e} \right) \tag{3.13}$$

The agreement obtained between equation (3.13) and the experimental data is shown in figure 3.8.

According to the simulation studies undertaken by Tilley, equations (3.11) to (3.13) were rearranged in the form where the flow rates were determined in terms of δp. The determined flow rates were then used to calculate the rate of change of pressures inside the breathing tube and the mouthpiece using the same equation (3.1) developed for the inter-connecting pipe. In equation (3.13) the relationship between the flow rate and the pressure loss is implicitly defined and an iteration procedure is used to obtain a solution of v_s.

(v) Breathing simulator

The breathing simulator has been modelled by Tilley using a similar approach to that outlined in section 2.10, except that the gas exchange process has not been included. In addition, Tilley has simulated the pressure losses associated with the breathing simulator pipework using the k factor method which is different from the friction pipe model described in section 2.6.

(vi) Hydrostatic pressure acting on the breathing system

Slight variation in hydrostatic pressure acting on the diver and breathing apparatus have a

significant effect on performance. Tilley's models enable the difference between the pressure at the reference diving depth and the pressure acting at the diver's mouth and at the two pressure control valves to be assessed. The reference depth of dive is taken from the water surface to the centre of the counterlung face. At this condition the hydrostatic pressure acting on the centre of the counterlung face is given by;

$$\mathcal{P}_c = \rho_w g z_c + P_{at} \qquad (3.14)$$

If the distances from the centre of the counterlung face to the mouth and the counterlung valves are z_m and z_v respectively then

$$\mathcal{P}_m = \mathcal{P}_c \mp \rho_w g z_m \qquad (3.15)$$

$$\mathcal{P}_v = \mathcal{P}_c \mp \rho_w g z_v \qquad (3.16)$$

The negative signs correspond to the diver being upright and the positive signs apply when the diver is inverted. If the diver is horizontal, face up or down, the reference height is taken to be from the water surface to the back of the counterlung, that is the diver's chest. In this case $z_m = z_v = 0$.

3.2.3 System simulations and results using previous models

The block diagram shown in figure 3.9, shows how the computer models developed by Tilley are interconnected for the purposes of the simulation. Each component model is represented as a box connected by links to other boxes. The boxes have ports, which represent the order in which parameters such as flow rate and pressure are transmitted to and from the models on links. In this manner, all the capacity elements receive flow rates from their adjoining components as input and supply pressure as output. The restriction and flow resistance models receive pressure from their adjoining components as input and supply flow rate as output. Referring to the block diagram, the model of the mouthpiece combines the pressure losses due to the mouthpiece, breathing tube and the breathing simulator pipework. The model of the breathing tube combines the volume of the mouthpiece and itself. The reason for lumping the losses and volumes is to avoid small interconnecting gas volumes. If these are included, very long simulation run times will result, with no noticeable change in the simulation results. The data used in the models is presented in table 3.1.

The first simulation study made by Tilley was under the arrangement where the mass flow jet unit was tested in isolation. Under this condition, a mixture of gas was discharged from the storage gas bottles through the valve to the ambient sea water pressure. The results obtained for this simulation are shown in

figure 3.10. Comparisons were made with preliminary experimental test results obtained by the Experimental Diving Unit, Portsmouth. From the comparisons, it was shown that the predicted results were in close agreement with the experimental data.

The second simulation study made by Tilley was under the test arrangement where gas was simply transferred between the breathing simulator and the counterlung. Under this condition, there was no additional supply or loss of gas to or from the circuit. The predicted breathing loops (formed by plotting the mouth differential pressure against the breathing simulator displayed volume) obtained from the simulation using two typical respiratory demand at diving depths of 20 m and 40 m are presented in figures 3.11 and 3.12. From the figures, it can be seen that both peak-to-peak mouth differential pressure and loop area increase with breathing demand and depth. As a consequence, the diver will have to expend more energy when breathing at these conditions. This was confirmed by the predicted values of the external resistive work per volume of gas inhaled and exhaled at these conditions, see table 3.2. It was also found that these values did not exceed the recommended respiratory work limits defined in equation (1.2) (ie. 3 J/L for 62.5 RMV and 3.5 J/L for 75 RMV). It is essential to show that the simulation predicts realistic system behaviour at depth. Hence, figures 3.11 and 3.12 also include the corresponding experimental breathing loops obtained using the hyperbaric test facility at DRA, Alverstoke. Again there was good agreement between the simulation and experiment.

The third simulation study made by Tomlinson (1993) was to establish an improved counterlung model. This simulation was under the condition where gas was supplied to the counterlung using a breathing simulator in the absence of the mouthpiece and the breathing tube. The data used in the new counterlung model is presented in table 3.3. The additional supply or loss of gas to or from the circuit were not considered in this study as well. The predicted pressure-volume loop formed by plotting the counterlung differential pressure $(P_c - \mathcal{P}_c)$ against counterlung displayed volume $(\bar{V}_c - V_c)$ is compared with the experimental data as shown in figure 3.13. The simulation shows good agreement with experiment. In addition, a simulation of the semi-closed-circuit breathing system with the improved counterlung model developed by Tomlinson has been established in order to gain confidence in using this improved counterlung model with the complete system. This additional simulation was under the same condition as the simulation established by Tilley. The predicted breathing loops obtained from this simulation are presented in figure 3.14. These

figures also includes the corresponding experimental breathing loops. Again it was found that the agreement between the simulation and experiment was very good. Therefore, the improved counterlung model can be used with confidence for further work.

3.2.4 Further development of component models

Based on the success obtained during the simulation studies undertaken by Tilley and Tomlinson, further work has been made for the extension of the simulation to include the variations in the composition of breathing gas. As the pressures and the flow rates in the semi-closed-circuit breathing system can be simulated, it is convenient to apply the techniques described in section 2.3 for the further development of the system models to simulate the variation in the composition of breathing gas. Other aspects to be considered in the models include the conversion of oxygen to carbon dioxide in the breathing simulator model and the absorption of carbon dioxide in the axial flow scrubber model. Hence, the simulation techniques described in section 2.9 and 2.10 are used in the new breathing simulator and axial flow carbon dioxide scrubber models.

Comparing equation (2.71) for determining the pressure losses across the axial flow scrubber with Tilley's empirical model, ie. equation (3.13), it has found that the term with $v_s^{1.5}$ does not appear in equation (2.71). However, if the fraction void space ε of 0.35 is used in equation (2.71), two very close curves given by equations (2.71) and (3.13) are obtained, see figure 3.15. Hence, equation (2.71) can be used instead of Tilley's empirical model with the benefits of applicable for assessing different fraction void space values and avoiding the use of iteration procedure as equation (2.71) is explicitly defined.

3.2.5 System simulations and results

An important area to be investigated in the following studies is the gas composition inside the mouthpiece whose constituents determine the inspired gas conditions. Therefore, the combined mouthpiece, breathing tube and breathing simulator pipework pressure losses model mentioned in section 3.2.3 needs to be separated in order to compute the gas composition in the mouthpiece precisely. The new block diagram for the semi-closed-circuit breathing system simulation is shown in figure 3.16(a). In addition, figure 3.16(b) shows the simulation schematic of the breathing system in Bathfp. According to section 2.3, all the restriction models must allow the transfer of the mass of constituent gases between their adjoining

capacitive element models as the capacitive elements require these to determine the mass of the constituent gases. Referring to the block diagram, the mass of the constituent gases are transmitted through the links as an array of four quantities which represent the oxygen, nitrogen, helium and carbon dioxide. This array of variables is called a 'vector type variable' which can simplify the establishment of the models for the simulation. In the scrubber model ten elements are used initially. Also all the CO_2 concentrations c and w in the scrubber model are vector type variables.

(i) Constant flow through the CO_2 scrubber model

The scrubber model has been tested using a simple arrangement where a constant velocity of gas mixture flows through the scrubber in one direction only. This allows the technique for the simulation of the absorption process in the scrubber to be justified before being used in a full simulation. The test simulation was undertaken where an air mixture contained 4.76% (volume to volume ratio) of carbon dioxide was supplied constantly at a flow rate of 3.15 L/min to the scrubber. Under this condition, the pressure in the scrubber was maintained at an atmospheric pressure of 1.013 bar. This simulation was set up to follow the standard test procedure used in the Royal Navy for measuring the duration of CO_2 absorbent. During this standard test, the running time is recorded until the downstream CO_2 concentration of 0.02% (volume to volume ratio) is detected. This period of time reported as the 'ACTIVITY' is a specified parameter used in the Royal Navy to express the duration of CO_2 absorbent. The data used in the CO_2 scrubber model for this simulation is shown in table 3.4. The results obtained from this simulation are shown in figure 3.17. This figure includes the simulated partial pressure of CO_2, termed P_{CO2}, at the upstream and downstream of the scrubber. From figure 3.17(b) it can be seen that during the first 66.3 minutes of the simulated run-down test, the simulated P_{CO2} at the downstream of the scrubber is below the recommended value of 2.02×10^{-4} bar (which is 0.02% volume to volume ratio of CO_2). Comparison was made with the sodalime's 'ACTIVITY' time obtained from the standard test. Good agreement was obtained (where the experimental 'ACTIVITY' time is 67 minutes). In addition, the predicted gas and absorbent phases of CO_2 concentration at individual elements in the scrubber model are presented in figure 3.18.

(ii) Complete system simulation

It is essential to show that the scrubber model can be applied to the condition where the gas flows through the scrubber in forward and backward directions during the breathing cycle. Hence, two examples

are presented in order to assess the suitability of the scrubber model for this condition. Both examples apply to the test arrangement where the semi-closed-circuit breathing system is connected to a breathing simulator. Under this condition, the breathing simulator starts with the Respiratory Minute Volume (RMV) of 22.5 L/min and a CO_2 production of 0.9 L/min for 4 minutes. A RMV of 50 L/min and a CO_2 production of 2 L/min are then set in the breathing simulator for 6 minutes. This switching of rates is repeated continuously until the lowest inspired CO_2 level at the mouthpiece is greater than a partial pressure of 6 mbar. The above test arrangement is one of the standard test procedure used in Royal Naval for testing the closed-circuit breathing equipment. The simulated diving depth for these two examples are 25 m and 54 m. According to the Royal Navy (Diving manual, 1987), three standard mixtures have been chosen for the constant mass flow jet unit to cover the range of depths down to 54 m. The mixtures used, the required supply volumetric flow rate and the maximum depths in which they may be safely used are illustrated in table 3.5 and these will be applied in the models of the constant mass flow jet unit. Since the experimental test performed at DRA, Alverstoke, has not considered the oxygen uptaken process, the consumption of oxygen in the breathing simulator is not taken into account in the simulation at present. The data used in the models is the same as in table 3.1. Table 3.6 illustrates the additional data used in the models.

The predicted P_{CO2} at the mouthpiece obtained from the simulations at diving depths of 25m and 54 m are presented in figures 3.19 and 3.20 respectively. These figures indicate that at each breathing cycle the maximum value of P_{CO2} is the level of end tidal P_{CO2} expired by the breathing simulator and the minimum value of P_{CO2} is the level of inspired P_{CO2}. These figures also show that the level of inspired P_{CO2} at the high ventilation rate region is higher than the low ventilation rate region. This is due to the CO_2 in the gas stream passing through the scrubber without having the opportunity to move radially to contact the absorbent surface and being absorbed during the cycles of high ventilation rate. From the figures it can be seen that the time of the inspired P_{CO2} taken to reach 5 mbar in the simulation relating to 54 m depth (57 minutes) is less that the simulation relating to 25 m depth (78 minutes). As a consequent, the duration of the CO_2 scrubber will reduce with an increase in diving depth. The corresponding experimental results which were obtained by DRA, Alverstoke, were used to validate the simulation (ie. 58 minutes for 54 m depth and 77 minutes for 25 m depth). Again good agreement between the simulation and experiment was obtained.

Having validated the scrubber model, the consumption of the oxygen in the breathing simulator can now be considered in the complete system simulation. The following simulation considers the diving schedule carried out from the water surface to the depth of 54m and then returning back to the surface. The duration time from leaving the surface to the beginning of the ascent is 20 mins. Hence, the simulated diving schedule should follow the recommended schedule described in table 1.2 for 54 m dive and 20 mins descending and bottom times. Referring to table 3.5, the mass flow jet unit requires to supply a gas mixture of 32.5%O_2/67.5%N_2 at a flow rate of 13 L/min (measured at the surface) for a 54 m dive. This composition of gas mixture is also used as the initial volumetric fraction of constituent gases in all the component models of the system at the beginning of the simulation as well. Under the simulation condition, an overall oxygen consumption of 2 L/min (STPD) and a ventilation ratio of 1 are applied in the breathing simulator model. According to table 2.5, the RMV of 50 L/min and the breath per minute of 25 are used for the $\dot{V}_{O2}$ equal to 2 L/min. After these breathing characteristic have been identified, the whole system simulation can be started.

The whole system was simulated over a period of 50 mins and 10 seconds. The results obtained for this simulation are shown in figures 3.21, 3.22, 3.23 and 3.24. The simulated diving schedule as shown in figure 3.21(a) follows the recommended diving schedule. The predicted pressure and volume of the counterlung are shown in figures 3.21(b) and (c) respectively. These figures show that the pressure inside the counterlung follows the ambient hydrostatic pressure changes and the counterlung has not collapsed. Figures 3.22, 3.23 and 3.24 show the simulated partial pressures of constituents gases [oxygen (a), nitrogen (b) and carbon dioxide (c)] inside the breathing simulator, mouthpiece and counterlung respectively. These figures show that the differences of oxygen and nitrogen partial pressures between the breathing simulator, mouthpiece and counterlung are very small. For the carbon dioxide, the levels of partial pressure are, however, different between the counterlung and the breathing simulator as the scrubber absorbs the carbon dioxide in the path between the counterlung and the breathing simulator. Referring to figure 3.23, the partial pressures of all the inspired gases are within the physiological limits throughout the diving schedule. Hence, the breathing system can provide safe breathing gas for the diver under this condition.

Due to lack of the appropriate experimental data, comparison between the theoretical prediction and the current simulation is made. The following equations given by the Diving manual (1987) enable the

steady state volume percentage of oxygen inside the counterlung to be calculated:

$$O_2 \ supply \ flow = \frac{\%O_2 \ inside \ the \ storage \ bottle}{100} \times Supply \ flow$$

$$\%O_2 \ inside \ the \ counterlung = \left(\frac{O_2 \ supply \ flow - O_2 \ used}{Supply \ flow - O_2 \ used} \right) \times 100$$

Since the above parameters are known, the steady-state volume percentage of oxygen inside the counterlung can be evaluated as 20%. According to Dalton's Law, the volume fraction of a constituent gas is equal to the partial pressure fraction of this constituent gas (ie. $V_i / V = P_i / P$), therefore, the volume fraction of O_2 inside the counterlung relating to the simulation can be evaluated as well. Referring to figure 3.21(b) and 3.24(a), the steady state volumetric fractions of O_2 inside the counterlung at different diving depth are calculated as 20%, result in 1.26/6.3104 bar ratio at 54 m depth, 0.38/1.9 bar ratio at 9 m depth, 0.32/1.6 bar ratio at 6 m depth and 0.26/1.3 bar ratio at 3 m depth. Hence, it is shown that the simulation enables the oxygen composition in the breathing equipment to be predicted.

3.2.6 Improving system performance

An important aspect relating to the design of underwater breathing apparatus is to ensure that the effort expended by the diver is as low as possible. This implies that steps must be taken to minimize the flow resistances in the mouthpiece, breathing tube and CO_2 scrubber. Worthwhile improvements in performance are possible by making changes to the mouthpiece, breathing tube and scrubber dimensions. Figure 3.25 shows the effect of increasing the mouthpiece diameter by 30%. Compared with the original simulation using the respiratory demand of 30 breaths/min and 75 RMV at the diving depth of 40 m (figure 3.12(b), this modification reduced the peak-to-peak mouth differential pressure variation by 0.75 kPa and also lowered the external resistive work from 3.23 J/L to 2.68 J/L. Figure 3.25(b) shows the predicted P_{co2} at the mouthpiece obtained from the simulation at the diving depth of 25 m. This simulation was under the same condition as the simulation established relating to figure 3.19 except for the increase of mouthpiece diameter. It was found that the time of inspired P_{co2} taken to reach 5 mbar is the same as before (78 minutes). Hence, this modification has not decreased the duration of the breathing system and enables the work in breathing to be reduced. Although the simulation indicated the increase of mouthpiece diameter can improve system performance, it is impractical to increase the mouthpiece diameter larger than the diver's mouth.

Another possibility to reduce the resistive work of breathing is to increase the breathing tube diameter. Two simulation results shown in figures 3.26(a) and (b) are under the same condition as their original simulations relating to figures 3.12(b) and 3.19 respectively, except that the breathing tube diameter has been increased by 100%. From the figures it can be seen that the peak-to-peak mouth differential pressure variation is reduced by 0.5 kPa and the time of inspired P_{CO2} taken to reach 5 mbar is reduced to 4000 seconds (66.7 minutes) in which the duration of the breathing system is reduced. The reason for the reduction of system duration is due to the increased dead space which causes a larger amount of CO_2 accumulated in the breathing tube without passing through the CO_2 scrubber. Hence, this suggestion cannot be applied.

A further improvement which can reduce the breathing tube flow resistance is to use a smooth bore breathing tube instead of the convoluted tube. Again similar simulations were established but in this case, neglecting the breathing tube friction related to the convolutions. Figure 3.27 shows that the peak-to-peak differential pressure variation is reduced by 0.5 kPa and the time of inspired P_{CO2} taken to reach 5 mbar is unchanged (78 minutes). Hence, this modification is applicable for the improvement of the breathing system.

The last possibility investigated was to increase the CO_2 scrubber diameter. In order to avoid increasing the scrubber weight acting on the counterlung, the length of the absorbent bed was reduced to remain the sodalime volume constant. As before, the original simulation results were used as a reference for a comparison with the new simulation results. Figure 3.28 shows the simulation results obtained when the scrubber diameter was increased by 50%. This indicated that although the peak-to-peak mouth differential pressure variation was reduced by 1 kPa, the time of inspired P_{CO2} taken to reach 5 mbar was also reduced to 2820 seconds (47 minutes). This is due to the decreased flow velocity through the absorbent bed (caused by the increase of cross sectional area) leading to a reduced mass transfer coefficient (see equation 2.86). This modification will reduce the duration of the breathing system and clearly cannot be applied in practice.

3.3 SIMULATION OF A SURFACE DEMAND DIVING SYSTEM

3.3.1 Introduction

The surface demand diving system is a type of open circuit breathing system. The system consists of two control valves interconnected by a length of flexible hose. The principle of this breathing system is outlined in figure 3.29. The breathing gas which can be an oxy-nitrogen or oxy-helium mixture is supplied from the surface control panel through a long hose (umbilical).

3.3.2 Component models development

The simulation techniques described in chapter 2 have been used to model the gas storage cylinders, the surface supply umbilical and the breathing simulator. Since the gas composition within the surface demand diving system is constant, the technique to simulate the variation of gas composition in the breathing system is unnecessary except for the demand regulator model where the gas composition will vary due to the mixing of the diver's exhaled gas and the supply gas. The following sub-sections described the detailed theoretical analysis of the additional models required for the breathing system.

(i) Pressure reducing valve

The pressure reducing valve, as shown in figure 3.30, is connected to the storage bottle inside the control panel. Its purpose is to reduce the gas pressure from the high pressure storage bottle to an intermediate pressure of approximately 10 - 15 bar. The control action is achieved by an arrangement referred to as a piston actuated high pressure seat. The seat is pneumatically balanced, viz. the high pressure supply gas surrounding the seat does not exert a force on the seat itself. This ensures that the outlet pressure from the valve is maintained constant despite a continually decreasing supply pressure as a consequence of the cylinder discharging. The requirement of the outlet pressure is regulated according to the diver's depth.

Referring to figure 3.30, the reduced pressure acts on the piston tending to close the valve and is resisted by the ambient pressure acting on the valve. Hence, the net opening pressure force acting on the spool is given by;

$$F_{P,rv} = (P_{am} - P_{out})A_{pi} \qquad (3.17)$$

Two springs also act on the valve spool. The force generated by the larger spring acting on the piston tends to open the valve, whereas the smaller spring tends to close the valve. Hence, the net opening spring force acting on the spool is given by;

$$F_{s,v} = k_{la}(x_{k,la} - x_v) - k_{sm}(x_{k,sm} + x_v) \tag{3.18}$$

After identifying the net pressure force and net spring force acting on the valve head, the approach described in section 2.8 can be used to simulate the valve head motion and the gas flow through the valve.

(ii) Demand regulator

The basic operating principle of the demand regulator is shown diagrammatically in figure 3.31, where a lever forms a connection between a balance piston valve and a flexible diaphragm. One side of the diaphragm is exposed to external water pressure and the other to the gas pressure acting internally in a control chamber formed in the valve body. The body also incorporates a mouthpiece outlet. Gas is supplied to the balance piston valve at a pressure controlled by the reducing valve at the surface panel. When the diver inhales, the pressure in the control chamber is reduced, resulting in a pressure imbalance at the diaphragm. This causes the diaphragm to move the lever which in turn opens the balance piston valve. Hence, the supply gas flows into the balance piston chamber and then a small bending chamber, located inside the main control chamber, straight to the mouthpiece. At the completion of the inhalation phase of the breathing cycle, the pressure in the control chamber recovers, allowing the diaphragm to return to its original position thus closing the valve. As the diver exhales, the main control chamber pressure will rise until a point is reached where the gas pressure is sufficient to open the mushroom valve fitted to the valve body. This allows the exhaled gas to be vented to the surrounding water.

For the purposes of the analysis, the forces acting on the balance piston valve, diaphragm and lever are considered separately as shown in figure 3.32.

Forces acting on the balance piston valve

According to figure 3.32(a), the balance piston valve is pneumatically balanced in which the supply gas pressure does not exert a force on the valve seat itself. The pressure inside the main control chamber acts on the valve stem tending to close the valve. This force is resisted by the pressure on the other side

of the balance piston. Hence, the net opening pressure forces acting on the balance piston is given by;

$$F_{P,bv} = (P_{bv} - P_{lc})A_{pl}$$ (3.19)

The opening force is resisted by two compressed springs in the main control chamber. The initial compressed displacement of the springs are determined by the setting of an adjustor, see figure 3.31. Hence, the opening spring force acting on the balance piston is given by;

$$F_{s,bv} = -k_{la}(x_{kla} + x_{bv}) - k_{sm}(x_{ksm} + x_{bv})$$ (3.20)

As with the pressure reducing valve, the force due to fluid momentum tends to close the valve. The magnitude of the momentum force F_m is determined using equation (2.65). Also a speed dependent viscous friction force $f_v \, dx_{bv}/dt$ and stick/slip friction (Coulomb friction) F_C are assumed to be acting on the balance piston. In addition to the above forces, the piston is also subjected to an opening force due to the lever. If the force from the lever is $F_{L,bv}$, then equating the forces acting on the balance piston gives;

$$F_{L,bv} = F_m + f_v \frac{dx_{bv}}{dt} + F_C sign\left(\frac{dx_{bv}}{dt}\right) - F_{P,bv} - F_{s,bv} + Me_{bv}\frac{d^2x_{bv}}{dt^2}$$ (3.21)

Forces acting on the diaphragm

If the hydrostatic pressure acting on the diaphragm is greater than the gas pressure inside the main control chamber, the net pressure forces acting on the diaphragm will tend to deflect the lever and open the balance piston valve. The net pressure forces acting on the diaphragm is given by;

$$F_{P,di} = (\mathcal{P}_{di} - P_{lc})A_{di}$$ (3.22)

Due to the flexibility of the diaphragm, the effective area acted on by the pressure forces varies considerably throughout the operational range. When the diaphragm is fully extended, the effective area is a minimum. This effect has been accounted for in the model using a simple linear relationship with diaphragm displacement:

$$A_{di} = \hat{A}_{di} - \left(\hat{A}_{di} - \check{A}_{di}\right)x_{di}/\hat{x}_{di}$$ (3.23)

As a consequence of the movement of the diaphragm, water will be drawn into or pumped out from the end cover chamber. This will introduce a pressure loss which will either increase or reduce the

71

hydrostatic pressure acting on the diaphragm. The magnitude of the pressure loss will be dependent on the area of the slots at the end cover and can be determined as follows:

$$\delta p = \frac{\rho_w}{2}\left(\frac{Q_{di}}{A_f C_d}\right)^2$$

(3.24)

The water flow rate induced by the diaphragm can be obtained from the following expression:

$$Q_{di} = (dx_{di}/dt)\, A_{di}$$

(3.25)

When the valve is opened, water will be drawn into the end cover chamber and the actual hydrostatic pressure acting on the diaphragm will drop. Hence, the actual hydrostatic pressure acting on the diaphragm is given by;

$$\mathcal{P}_{di} = \mathcal{P}_{di,ext} - \delta p$$

(3.26)

Similarly, when the valve is closing, water will pass from the end cover chamber to the surrounding causing $\mathcal{P}_{di}$ to increase. The actual hydrostatic pressure acting on the diaphragm during valve closure is given by;

$$\mathcal{P}_{di} = \mathcal{P}_{di,ext} + \delta p$$

(3.27)

Furthermore, the net opening pressure force acting on the diaphragm is assisted by the spring located between the diaphragm and the end cover, see figure 3.32(b). Hence, the opening spring force is given by

$$F_{s,di} = k\,(x_{k,di} - x_{di})$$

(3.28)

Assuming $F_{L,di}$ is the force from the lever, equating the forces acting on the diaphragm gives;

$$F_{L,di} = F_{P,di} + F_{s,di} - f_v \frac{dx_{di}}{dt} - Me_{di}\frac{d^2 x_{di}}{dt^2}$$

(3.29)

Forces acting on the level

The lever provides the link between the diaphragm and the poppet, and is subjected to the forces shown in figure 3.32(c). Taking moments about O, then:

$$I_L \frac{d^2\theta}{dt^2} = b_1 F_{L,di} - b_2 F_{L,bv} - f_\omega\, d\theta/dt$$

(3.30)

Having established the forces acting on the lever, the next step is to determine the geometric relationships between the linear motion of the balance piston and diaphragm and the angular rotation of the lever. The following relationships apply to the lever:

$$b_1 = l_L \sin(\theta + \theta_{fix}) \quad , \quad b_3 = b_2(1 + \tan^2\theta) = b_2\sec^2\theta \quad , \quad b_4 = l_L\cos(\theta + \theta_{fix})$$
$$x_{bv} = b_2\tan\theta \quad , \quad x_{di} = l_L[\cos\theta_{fix} - \cos(\theta + \theta_{fix})]$$

and,

$$\frac{dx_{di}}{dt} = l_L \sin(\theta + \theta_{fix})\frac{d\theta}{dt} = b_1\frac{d\theta}{dt} \tag{3.31}$$

$$\frac{d^2x_{di}}{dt^2} = l_L\cos(\theta+\theta_{fix})\left(\frac{d\theta}{dt}\right)^2 + l_L\sin(\theta+\theta_{fix})\frac{d^2\theta}{dt^2} = b_4\left(\frac{d\theta}{dt}\right)^2 + b_1\frac{d^2\theta}{dt^2} \tag{3.32}$$

Similarly, the following relationships between x_{bv} and θ can be derived.

$$\frac{dx_{bv}}{dt} = b_2\sec^2\theta\frac{d\theta}{dt} = b_3\frac{d\theta}{dt} \tag{3.33}$$

$$\frac{d^2x_{bv}}{dt^2} = 2b_2\sec^2\theta\tan\theta\left(\frac{d\theta}{dt}\right)^2 + b_2\sec^2\theta\frac{d^2\theta}{dt^2} = 2b_3\tan\theta\left(\frac{d\theta}{dt}\right)^2 + b_3\frac{d^2\theta}{dt^2} \tag{3.34}$$

Substituting for $F_{L,bv}$ and $F_{L,di}$ in equation (3.30), and introducing F_{bv} and F_{di} as follow:

$$F_{bv} = F_m + f_v dx_{bv}/dt + F_C sign(dx_{bv}/dt) - F_{P,bv} - F_{s,bv}$$
$$F_{di} = F_{P,di} + F_{s,di} - f_v dx_{di}/dt$$

Then, equation (3.30) becomes:

$$I_L\frac{d^2\theta}{dt^2} = b_1\left(F_{di} - Me_{di}\frac{d^2x_{di}}{dt^2}\right) - b_2\left(F_{bv} + Me_{bv}\frac{d^2x_{bv}}{dt^2}\right) - f_a\frac{d\theta}{dt} \tag{3.35}$$

Substituting for the terms including x_{bv} and x_{di} using equations (3.32) and (3.34), the lever angular acceleration is given by;

$$\frac{d^2\theta}{dt^2} = \frac{1}{(I_L+b_1^2Me_{di}+b_2Me_{bv}b_3)}\left[b_1F_{di} - b_2F_{bv} - (b_1b_4Me_{di}+2b_3Me_{bv}b_2\tan\theta)\left(\frac{d\theta}{dt}\right)^2 - f_a\frac{d\theta}{dt}\right] \tag{3.36}$$

θ is obtained by numerically integrating equation (3.36), which allows data relating to the motion of both balance piston and diaphragm to be determined using the outlined geometrical relationships.

73

Flows through the balance piston

As the flow through the balance piston valve seat is annular, the flow area can be determined from:

$$A_f = \pi \, d_{vs} \, x_{bv} \tag{3.37}$$

The mass flow rate through the valve seat is determined using equation (2.19). After leaving the valve seat, the gas passes through a small hole from the balance piston chamber to a small bending chamber. Also there is a tiny gap in between the valve stem and the housing of the balance piston chamber, see figure 3.32(a). If the flow area of the hole or the gap is relatively large, the pressure inside the balance piston chamber, the small bending chamber and the main control chamber will be approximately the same, and $P_{lc} = P_{bm} = P_{bv}$. However, if the hole and the gap introduce a significant pressure loss, then clearly these pressures will not be equal. In this case it will be necessary to use equation (2.19) to determine the mass flow rates through the hole and the gap.

Mouthpiece flow

The flow through the mouthpiece during inhalation and exhalation is the combination of the flows from and to the main control chamber and the small bending chamber. In line with the studies undertaken by Tilley (1991), the relationship between pressure loss and gas flow for the mouthpiece can be assessed using the 'k factor method'. Hence, the mass flow rates from the main control chamber and from the small bending chamber are given by;

$$q_{mp} = A_{f,mp} \sqrt{2\rho \, \Delta p_{mp} \, / \, K_{mp}} \tag{3.38}$$

$$q_{bm} = A_{f,bm} \sqrt{2\rho \, \Delta p_{bm} \, / \, K_{bm}} \tag{3.39}$$

Mushroom valve flow

For the purpose of the analysis, the mushroom valve is assumed to react instantaneously to the change in control chamber pressure. The relationship between pressure difference and volumetric flow rate can then be found using a similar approach to that derived for the buoyancy control valve in section 3.2.2(iii). Hence, when the difference between the control chamber pressure and the mushroom valve

hydrostatic pressure is greater than the cracking pressure P_{cr}, the valve will be operated and the flow rate will be;

$$Q_{mv} = \mathcal{A}_{mv}(P_{lc} - \mathcal{P}_{mv} - P_{cr}) \qquad (3.40)$$

The mass flow rate can be obtained as follow;

$$q_{mv} = \bar{\rho} \, Q_{mv} \qquad (3.41)$$

Pressures inside the demand regulator chambers

The volumes of the balance piston chamber and the small bending chamber are fixed. Hence, the rate of change of pressures and temperatures inside these chambers can be obtained using the same form as equations (2.42) and (2.43) developed for a short pipe. However, the main control chamber volume will vary due to the movement of the diaphragm. Therefore, the expression to determine the rate of change of pressure and temperature inside the main control chamber must include an additional work done term, which is related to the change of chamber gas volume V_{lc}, where $\dot{V}_{lc} = -A_{di} \, dx_{di}/dt$, and are given by

$$\dot{P}_{lc} = n \, [\, R \, (\Sigma \, \dot{m}_{in} T_{in} - \Sigma \, \dot{m}_{out} T_{lc}) - P_{lc} \dot{V}_{lc} \,] \, / \, V_{lc} \qquad (3.42)$$

$$\dot{T}_{lc} = [\, \dot{P}_{lc} V_{lc} + P_{lc} \dot{V}_{lc} - \dot{m} R T_{lc} \,] \, T_{lc} \, / \, (\, P_{lc} V_{lc}) \qquad (3.43)$$

(iii) Hydrostatic pressure acting on the breathing system

Taking the reference depth of a dive from the water surface to the mouthpiece, the hydrostatic pressure acting on the mouthpiece is given by;

$$\mathcal{P}_{mp} = P_{at} + \rho_w g z_{mp} \qquad (3.44)$$

If the distances from the mouthpiece to the centre of the diaphragm and to the mushroom valve are z_{di} and z_{mv} respectively (both below the mouthpiece), then

$$\mathcal{P}_{di} = \mathcal{P}_{mp} \pm \rho_w g z_{di} \qquad (3.45)$$

$$\mathcal{P}_{mv} = \mathcal{P}_{mp} \pm \rho_w g z_{mv} \qquad (3.46)$$

The positive signs correspond to the diver being upright and the negative signs apply when the diver is inverted.

75

3.3.3 System simulations and results

The block diagram and the Bath*fp* simulation schematic of the surface demand diving system simulation are shown in figure 3.33(a) and (b) respectively. Currently, the conversion of oxygen to carbon dioxide is not taken into account in the breathing simulator model. The data used in the models is presented in table 3.7.

Before undertaking the simulation studies, the number of elements to be included in the long umbilical pipe model needs to be identified. Although more elements will lead to a more accurate prediction, the simulation will be obtained at the expense of longer simulation run times. Therefore, it is necessary to ascertain the minimum number of elements which can provide acceptable predictions. Figure 3.34 illustrates the simulation results of the breathing system using long pipe models consisting of 1, 5, 10 and 20 elements. Air was supplied from the panel. The simulations were obtained at respiratory demands of 25 breaths/min and 62.5 RMV for a 50 m diving depth. Referring to figure 3.34, the breathing loops formed by plotting the mouth differential pressure against the breathing simulator displayed volumes are nearly identical. However, the predicted variations in supply pressure at the demand regulator (umbilical outlet pressure), using different numbers of elements in the umbilical pipe model, are different. It is acceptable that the umbilical pipe model with 10 elements is sufficient to provide good predictions as the results obtained from 10 and 20 elements model are very close. Hence, the umbilical pipe model with 10 elements is used for further simulations. The following sections are the assessments of the breathing system under different operating conditions.

(i) Different respiratory demands

The effect of different respiratory demands on the operation of the surface supply diving system is illustrated in figure 3.35, using the breathing loops obtained at 15 breaths/min & 22.5 RMV, 25 breaths/min & 62.5 RMV and 30 breaths/min & 90 RMV. All the results were predicted at a diving depth of 50 m and at the demand regulator supply pressure 10 bar above diving depth pressure (ie. 15 bar pressure at the outlet of the surface panel). The predictions clearly indicate that the operation of the diving set is extremely sensitive to respiratory demand. In the case of higher demands, both peak-to-peak mouth differential pressure and loop area increase with breathing demand. As a consequence, the diver will have to expend more energy when breathing at the higher demands. This was confirmed by the predicted values

76

of the external resistive work per volume of gas inhaled and exhaled at these conditions, see table 3.8. It was also found that these values did not exceed the recommended respiratory work limits defined in equation (1.2) (ie. 1.4 J/L for 22.5 RMV, 3 J/L for 62.5 RMV and 4.1 J/L for 90 RMV).

(ii) Different diving depths

Three predicted responses are presented in figure 3.36, obtained at the respiratory demand of 30 breaths/min & 90 RMV for diving depths of 10, 50 and 60 m. For the 10 and 60 m depth simulations, the supply pressures at the demand regulator were set, respectively, at 10 bar and 12 bar above diving depth pressure (ie. 11 bar pressure at the outlet of the surface panel for 10 m depth and 18 bar pressure at the outlet of the surface panel for the 60 m depth simulation).

From the figures it can be seen that the breathing loops become fatter with increasing diving depth. This is due to the gas density increasing with depth, thus leading to higher mass flow resulting in more pressure losses in the flow path of the breathing system. This results in an increase in the diver's breathing effort to overcome the increased flow resistance. In addition, when the breathing system is operating at 30 breaths/min & 90 RMV at 60 m depth of dive, the predicted external resistive work which is 4.44 J/L exceeds the recommended respiratory work limit of 4.1 J/L. Hence, the diver will experience breathing difficulty at this condition.

(iii) Different gas supply mixtures

Figure 3.37 shows the difference between using air and an oxy-helium mixture (80%He/20%O_2) as the supply gas to the breathing system. The predicted breathing loops were obtained using a respiratory demand of 30 breaths/min & 90 RMV at a diving depth of 50 m. The demand regulator supply pressure is the same in both simulations. Referring to figure 3.37, both peak-to-peak mouth differential pressure and loop area are reduced when oxy-helium mixture is used as the supply gas. This is due to different gas properties (the gas constant R increases from 287 J/kg K for air to 867 J/kg K for oxy-helium mixture), leading to faster pressure responses in the components. In addition, figure 3.38 shows the predicted breathing loops, obtained at the conditions of 85 m diving depth and 30 breaths/min & 90 RMV respiratory demand using oxy-helium mixture as the supply gas. The predicted external resistive work is computed as 2.4 J/L. This indicates that the breathing system still does not exceed the recommended respiratory work

limit (4.1 J/L) even at 85 m depth. Hence, considerable benefits can be gained from using oxy-helium mixture as the supply gas.

(iv) Comparisons between predicted and measured results

It is essential to show that the simulation predicts realistic system behaviour. Hence, figures 3.35 to 3.37 also include the corresponding experimental breathing loops obtained at DRA, Alverstoke. The agreement achieved clearly demonstrates the suitability of the developed models for the simulation of the surface demand diving system.

(v) Comparing the work of breathing with the semi-closed-circuit breathing system

A further simulation has been established to compare the work of breathing for the surface demand diving system with the semi-closed-circuit breathing system. The predicted breathing loop presented in figure 3.39(a) is obtained from a simulation using the respiratory demand of 30 breaths/min and 75 L/min RMV at 40 m depth air diving. Figure 3.39(a) shows the breathing loop obtained earlier from the simulation of the semi-closed-circuit breathing system under the same breathing conditions and diving depth. These simulations show that under the same conditions the surface demand diving system has smaller peak-to-peak mouth differential pressure variation and a lower mean level of mouth differential pressure. Hence, the diver will have to expend less energy when using the surface demand diving system. It is noticeable that the semi-closed-circuit breathing system has two more components in the breathing path (ie. breathing tube and CO_2 scrubber) in which additional resistive work is required. The shapes of the two breathing loops are different. This is due to the characteristic of the counterlung which requires larger elastic work and leads to an increase in the system pressure at the end of exhalation phase.

(vi) Simulated 54m diving schedule

The performance of the surface demand diving system has been investigated under a complete diving schedule. The following simulation considers a diving schedule from the water surface to a depth of 54 m and then returning back to the surface. The same diving schedule and breathing characteristics used for the semi-closed-circuit breathing system for a 54 m dive simulation have been used. The whole system was simulated over a period of 50 mins 10 seconds. The results obtained for this simulation are shown in figures 3.40, 3.41 and 3.42. Figure 3.40(a) shows the simulated diving schedule. The simulated pressures

inside the demand regulator and the breathing simulator are shown in figures 3.40(b) and (c) respectively. These figures show that the breathing gas pressure follows ambient pressure changes. Figures 3.41 and 3.42 shows the simulated partial pressures of the constituent gases [oxygen (a), nitrogen (b) and carbon dioxide (c)] inside the breathing simulator and the demand regulator respectively. From figure 3.42 it can be seen that the partial pressures of the inspired gases are within the physiological limits throughout the diving schedule. Hence, the diver will be in no danger from gas poisoning at these conditions.

3.3.4 Improving system performance

Similar to that outlined for the semi-closed-circuit breathing system, worthwhile improvements in reducing work of breathing is possible by making changes to the mouthpiece. Figure 3.43 shows the effect of increasing the mouthpiece diameter by 30 %. This simulation was undertaken at the same condition as the earlier simulation using the respiratory demand of 30 breaths/min and 90 L/min RMV at a 60 m diving depth (figure 3.36(c)). It can be seen that although during exhalation the mouth differential pressure is reduced, there is no change during inhalation. This means that the flow resistance of the mouthpiece is insignificant when gas flows from the demand regulator to the mouth. An improvement to assist breathing during inhalation is to use a stiffer spring located between the diaphragm and the end cover. This allows the balance piston valve to open more easily during inhalation. To test this, a simulation was established with the diaphragm spring rate increased by 100 %. Figure 3.44 shows the simulation result which indicates that less work is required during inhalation. If both modification are applied, the peak-to-peak mouth differential pressure variation reduces (see figure 3.45) and, therefore, the diver will expend less energy under the same conditions.

3.4 CLOSURE

Further work has been made to extend and improve the semi-closed-circuit breathing system models developed by Tilley and Tomlinson. The variation of gas composition within the system model and the absorption of carbon dioxide in the axial flow scrubber model has now been included and the models used to predict the duration of the semi-closed-circuit breathing system. Good correlation is obtained between the predicted and measured data. The simulation studies indicate that the duration of the CO_2 absorbent scrubber reduces with increasing diving depth. The simulation studies show that increasing the

mouthpiece diameter, breathing diameter, CO_2 scrubber diameter, and using a smooth bore breathing tube enable the work for breathing to be reduced. However, the simulations have identified that increasing the breathing tube and CO_2 scrubber diameters will reduce the duration of the breathing system. Therefore, increasing the breathing tube and CO_2 scrubber diameters are not practical modifications.

Mathematical models have been developed for the surface demand diving system and have been used to predict the performance of this type of breathing system. Good correlation is obtained between predicted and measured data. The simulation studies indicate that the operation of the breathing system is sensitive to respiratory demand and diving depth. The work of breathing is found to increase with respiratory demand and diving depth. In addition, the simulation studies indicate that the diver will expend less breathing effort when using a oxy-helium mixture (20%O_2/80%He) rather than air.

Comparisons between the performances of the surface demand diving system and the semi-closed-circuit breathing system indicate that under the same operating conditions, the work of breathing of the surface demand diving system is less. Hence, the diver will expend less energy when using the surface demand diving system. In addition, a 54 m diving schedule recommended by the Royal Navy has been simulated for both breathing systems. It is shown that the developed simulation techniques enable the variation of gas composition in both breathing systems to be predicted.

Models	Variables	Values	Units
Gas bottles	Initial gas pressure	100	bar
	Total gas volume	4.4	L
Pressure regulating valve	Exposed diaphragm diameter	35.6	mm
	Valve seat diameter	1.575	mm
	Maximum valve opening	1.42	mm
	Poppet angle	45	degrees
	Effective mass of moving parts	0.01	kg
	Spring rate of inlet valve head spring	7400	N/m
	Initial compression of inlet valve head spring	2.3	mm
	Spring rate of large spring	630000	N/m
	Initial compression of large spring	4.5	mm
	Viscous friction coefficient	100	N/(m/s)
	Coulomb friction	0	N
Interconnecting pipe	Pipe internal diameter	10	mm
	Pipe length	0.07	m
Acoustic jet	Diameter of orifice	0.229	mm
Counterlung	Mean width of counterlung	0.24	m
	Distance between the top and bottom of counterlung	0.2	m
	Effective mass of moving parts	1	kg
	Viscous friction	1000	N/(m/s)
Pressure relief valve	Diameter of valve seat	20	mm
	Exposed diameter of rubber diaphragm	50	mm
	Cracking pressure due to spring pre-loaded	3	kPa
Buoyancy control valve	Pressure difference to open mushroom valve	0.1	kPa
	Mushroom valve flow/pressure gradient	500	(L/min)/kPa
	Number of turns from fully closed position	0.1	-
	Thread pitch for variable restriction	12	threads/inch
	Variable restriction poppet angle	20	degrees
	Variable restriction seat diameter	5.56	mm
	Diameter of holes in venting disc	0.432	mm
	Number of holes in venting disc	92	-
Axial flow CO_2 absorbent scrubber	Mean diameter of absorbent media granules	1.4	mm
	Depth of absorbent media	70	mm
	Diameter of canister	140	mm
	Internal diameter of breathing tube inlet connection	19	mm
	Angle of inlet connection to canister centre-line	45	degrees
	Number of holes in each baffle plate	90	-
	Baffle plate hole diameter	6.35	mm
	k factor for flow entering baffle plate holes	0.25	-
	k factor for supporting mesh	2.4	-
	Voidage	0.35	-

Table 3.1   Data used in the previous models of the semi-closed-circuit breathing system

Models	Variables	Values	Units
Breathing tube	Breathing tube internal diameter	23	mm
	Length of breathing tube	0.6	m
	Number of breathing tube convolution	28	-
	Breathing tube convolution pitch	6.2	mm
	Breathing tube bend angle	60	degrees
	Breathing tube bend radius	150	mm
	Breathing tube inlet connection diameter	19	mm
	k factor for inlet connection	0.1	-
Mouthpiece	Flow area of mouthpiece	350	mm^2
	Effective length of mouthpiece	0.068	m
	k factor for mouthpiece	1.82	-
Breathing simulator	Initial breathing simulator volume	0.5	L
	Reference volume for display	3	L
	Additional pipework volume	6	L
	Effective pipework diameter	25	mm
	k factor for pipework	9.6	-
Distances	Distance between the counterlung valve and the centre of counterlung	0.125	m
	Distance between the mouth and the centre of counterlung	0.24	m

Table 3.1   Data used in the previous models of the semi-closed-circuit breathing system

Conditions	External resistive work
62.5 L/min RMV (20 m dive)	1.62 J/L
75 L/min RMV (20 m dive)	2.17 J/L
62.5 L/min (40 m dive)	2.36 J/L
75 L/min RMV (40 m dive)	3.23 J/L

Table 3.2   Predicted external resistive work per volume gas inhaled and exhaled obtained from the simulation of the semi-closed-circuit breathing system

Variables	Values	Units
Mean width of counterlung	0.24	m
Distance between the top and bottom of counterlung	0.2	m
Effective mass of moving parts	1	kg
Viscous friction	1000	N/(m/s)
Initial counterlung material stiffness	3500	N/m
Increased counterlung stiffness	9000	N/m
Counterlung displacement when counterlung stiffness increased	0.035	m
Coulomb friction when diver in supine upright position	2	N
Increased Coulomb friction when diver in supine upright position	50	N
Coulomb friction when diver in supine upside-down position	2	N
Increased Coulomb friction when diver in supine upside-down position	50	N
Coulomb friction when diver in prone face up position	10	N
Increased Coulomb friction when diver in prone face up position	45	N
Coulomb friction when diver in prone face down position	30	N
Increased Coulomb friction when diver in prone face down position	80	N

Table 3.3   Data used in Tomlinson's improved counterlung model

Variables	Values	Units
Mean diameter of absorbent media granules	1.4	mm
Depth of absorbent media	148.54	mm
Diameter of canister	30	mm
Internal diameter of breathing tube inlet connection	30	mm
Angle of inlet connection to canister centre-line	0	degrees
Number of holes in each baffle plate	90	-
Baffle plate hole diameter	1.5	mm
k factor for flow entering baffle plate holes	0.25	-
k factor for supporting mesh	0	-
Voidage	0.35	-
Bulk density, mass of absorbent per volume of bed	900	kg/m^3
Absorbent capacity	0.01	moles/kg
Diffusion coefficient between CO_2 and air at 1 atm, 0°C	0.142	cm^2/s
Surface area per unit volume of absorbent	4.2	cm^2/cm^3
Effective factor of surface area	0.28	-

Table 3.4   Data used in the CO_2 scrubber model for the simulation of 'ACTIVITY' test

Gas mixture (Volumetric fraction)	Supply volumetric flow rate (Measured at surface)	Maximum allowable diving depth
60%O_2 / 40%N_2	6 L/min	25 m
40%O_2 / 60%N_2	12 L/min	40 m
32.5%O_2 / 67.5%N_2	13 L/min	54 m

Table 3.5   Constant mass flow jet unit required gas mixture and volumetric flow rate at their corresponding maximum depth of dive

Models	Variables	Values	Units
Axial flow CO_2 absorbent scrubber	Mean diameter of absorbent media granules	1.4	mm
	Depth of absorbent media	70	mm
	Diameter of canister	140	mm
	Internal diameter of breathing tube inlet connection	19	mm
	Angle of inlet connection to canister centre-line	45	degrees
	Number of holes in each baffle plate	90	-
	Baffle plate hole diameter	6.35	mm
	k factor for flow entering baffle plate holes	0.25	-
	k factor for supporting mesh	2.4	-
	Voidage	0.35	-
	Bulk density, mass of absorbent per volume of bed	900	kg/m^3
	Absorbent capacity	0.01	moles/kg
	Diffusion coefficient between CO_2 and air at 1 atm, 0°C	0.142	cm^2/s
	Surface area per unit volume of absorbent	4.2	cm^2/cm^3
	Effective factor of surface area	0.28	-

Table 3.6 Data used in the further developed models of the semi-closed-circuit breathing system

Models	Variables	Values	Units
Gas bottles	Initial gas pressure	150	bar
	Total gas volume	22	L
Pressure reducing valve	Exposed diaphragm diameter	36.8	mm
	Valve seat diameter	10	mm
	Maximum valve opening	3	mm
	Poppet angle	30	degrees
	Effective mass of moving parts	0.05	kg
	Spring rate of inlet valve head spring	2000	N/m
	Initial compression of inlet valve head spring	2	mm
	Spring rate of large spring	192000	N/m
	Initial compression of large spring	7.64	mm
	Viscous friction coefficient	100	N/(m/s)
	Coulomb friction	0	N
Supply umbilical	Pipe internal diameter	12.5	mm
	Pipe length	115	m
	k factor for bends and fittings	0	-
	Relative roughness	0.0001	-
Balance piston valve of the Demand regulator	Valve seat diameter	8.64	mm
	Piston end diameter	8.4	mm
	Valve head stem diameter	2.5	mm
	Valve stem and piston chamber contact tolerance	0.2	mm
	Piston chamber exit hole diameter	5	mm
	Balance piston chamber volume	2.577	mL
	Piston displacement for free flow	0.02	mm
	Valve seat flow force factor	2	-
	Speed dependent friction coefficient	20	N/(m/s)
	Balance piston Coulomb friction	0	N

Table 3.7 Data used in the models of the surface demand diving system

Models	Variables	Values	Units
Main chamber of the Demand regulator	Maximum diaphragm diameter	60	mm
	Minimum diaphragm diameter	40	mm
	Lever dimension	30	mm
	Distance from pivot point to poppet valve	2.5	mm
	Lever angle	40	degrees
	Maximum diaphragm travel distance	4	mm
	Effective mass of balance piston assembly	20	grammes
	Effective mass of diaphragm assembly	10	grammes
	Adjustor large spring stiffness	2606	N/m
	Initial compression of adjustor large spring	4.8	mm
	Adjustor small spring stiffness	635	N/m
	Initial compression of adjustor small spring	1.8	mm
	Diaphragm spring stiffness	31.3	N/m
	Initial compression of diaphragm spring	25	mm
	Speed dependent friction coefficient	20	N/(m/s)
	Main control chamber volume	38	mL
Small bending chamber of the Demand regulator	Small bending chamber volume	2	mL
	Small bending chamber flow area	64	mm^2
	k factor of small bending chamber flow path	2	-
Cover slot chamber of the Demand regulator	Cover slot flow area	270	mm^2
	Cover slot volume	40	mL
	Cover slot flow coefficient	0.9	-
Mouthpiece in Demand regulator	Mouthpiece flow area	380	mm^2
	k factor of mouthpiece flow path	2	-
Mushroom valve	Pressure difference to open the valve	0.064	kPa
	Pressure/flow gradient	570	(L/min)/kPa
Breathing simulator	Initial breathing simulator volume	4	L
	Reference volume for display	7	L
	Additional pipework volume	2.2	L
	Effective pipework diameter	31.75	mm
	k factor of the pipework	0	-
	Relative roughness for pipework	1×10^{-4}	-
Distances	Distance from mouthpiece to diaphragm's centre	20	mm
	Distance from mouthpiece to mushroom valve	40	mm

Table 3.7   Data used in the models of the surface demand diving system

Conditions	External resistive work
22.5 L/min RMV (50 m dive)	0.85 J/L
62.5 L/min (50 m dive)	2.05 J/L
90 L/min RMV (50 m dive)	3.625 J/L

Table 3.8   Predicted external resistive work per volume gas inhaled and exhaled obtained from the simulation of the surface demand diving system
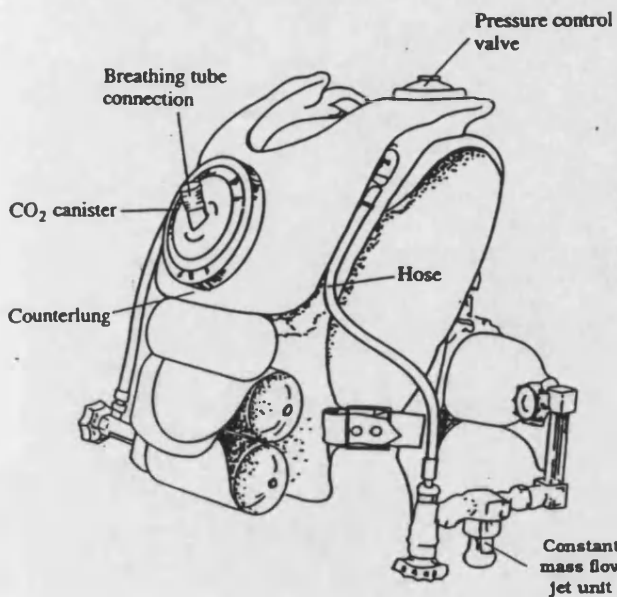
Figure 3.1 Semi-closed-circuit breathing system
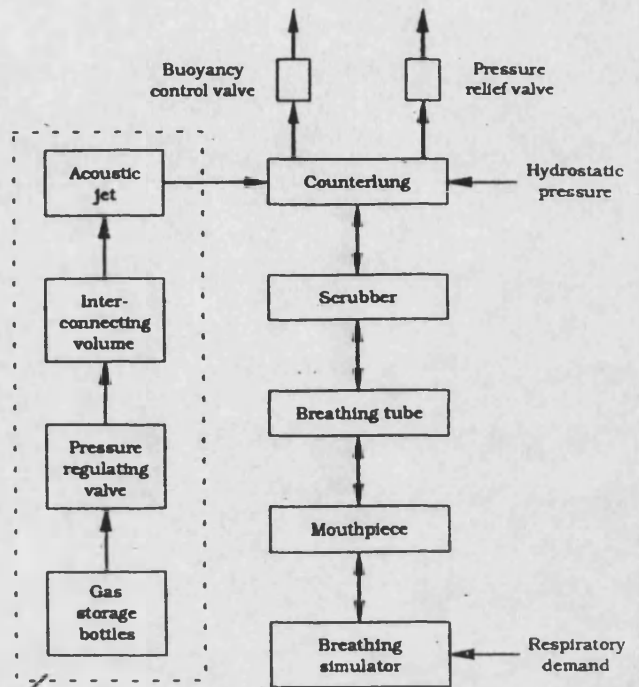
Figure 3.2 Schematic representation of the semi-closed-circuit breathing system
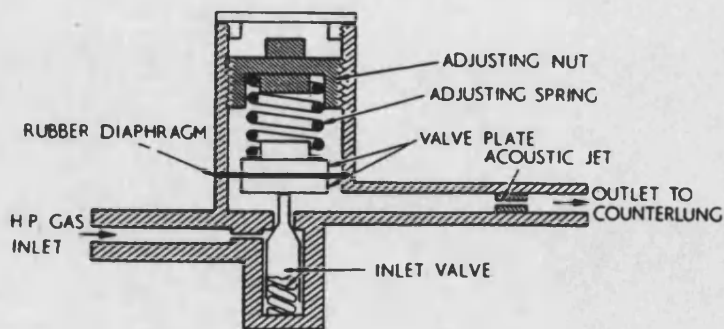
Figure 3.3 Pressure regulating valve
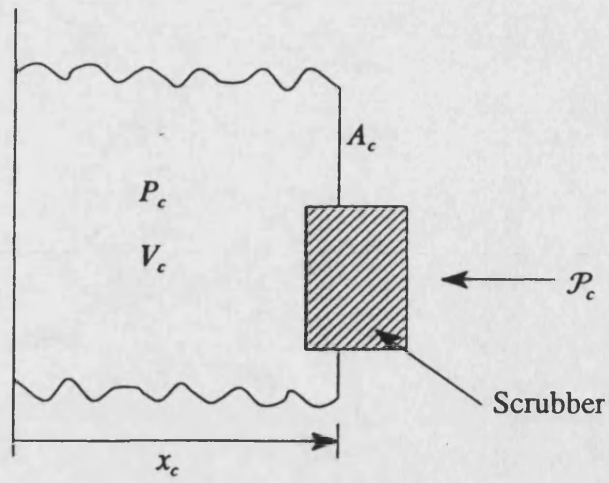
Figure 3.4(a) Representation of counterlung as a linear actuator
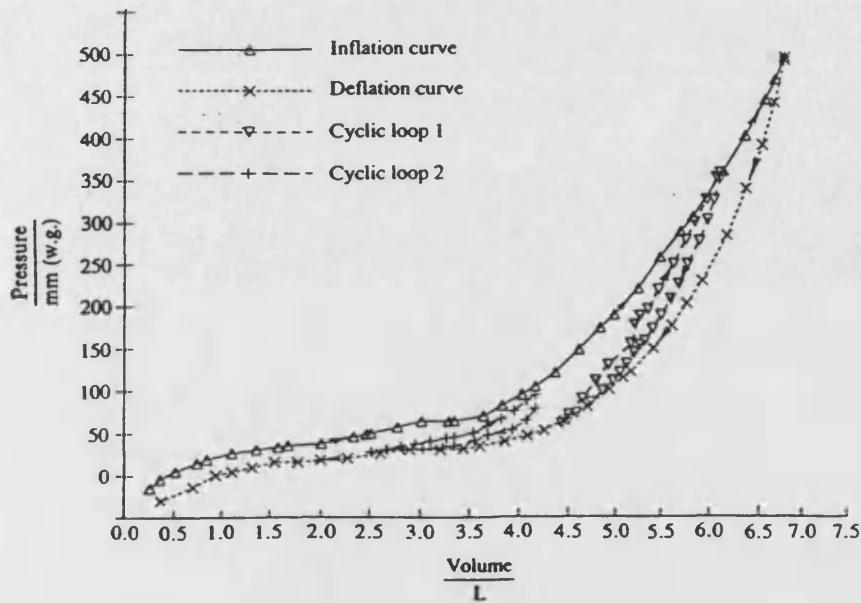
Figure 3.4(b) Counterlung hystersis loop, dry test
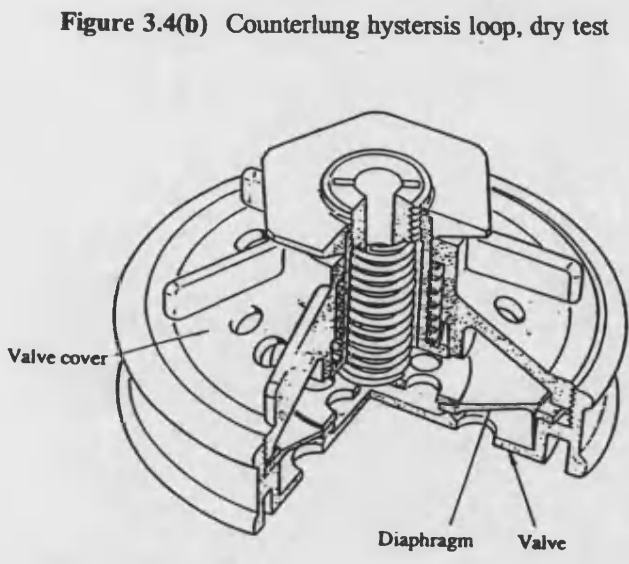
Figure 3.5 Counterlung pressure relief valve
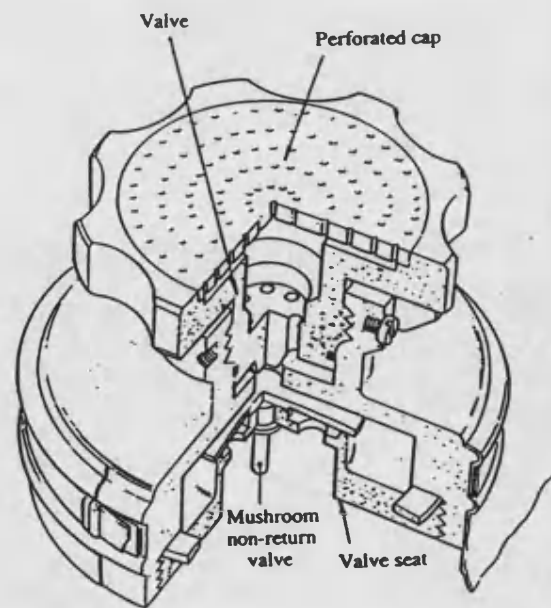
Figure 3.6 Counterlung buoyancy control valve

87
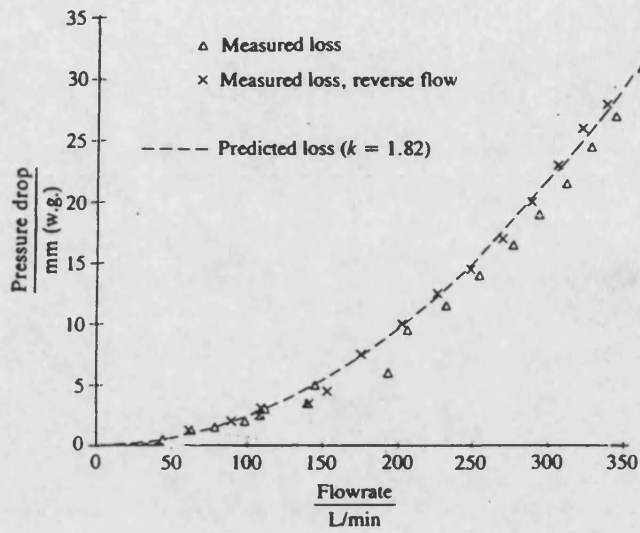
Figure 3.7 Mouthpiece pressure loss
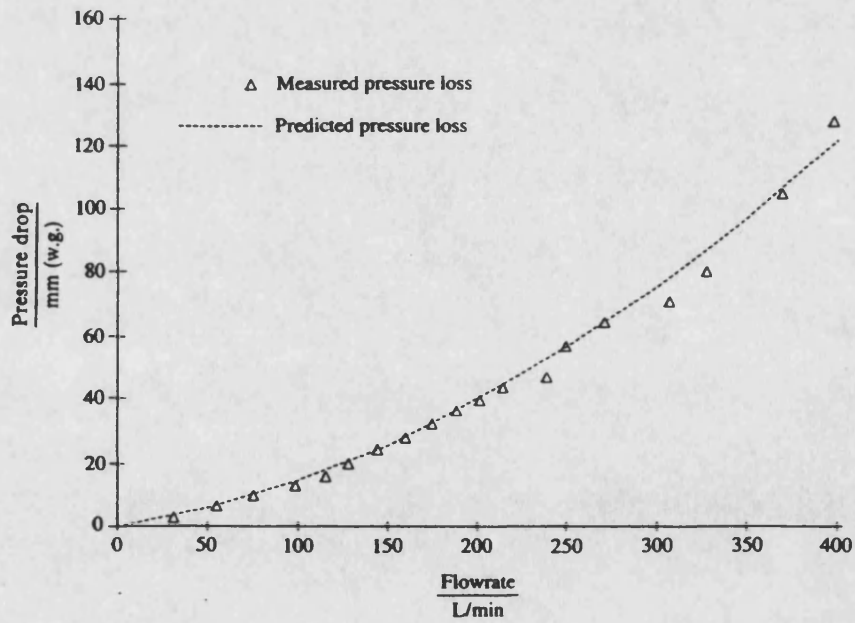
Figure 3.8 Axial flow scrubber, canister and soda lime pressure loss

88
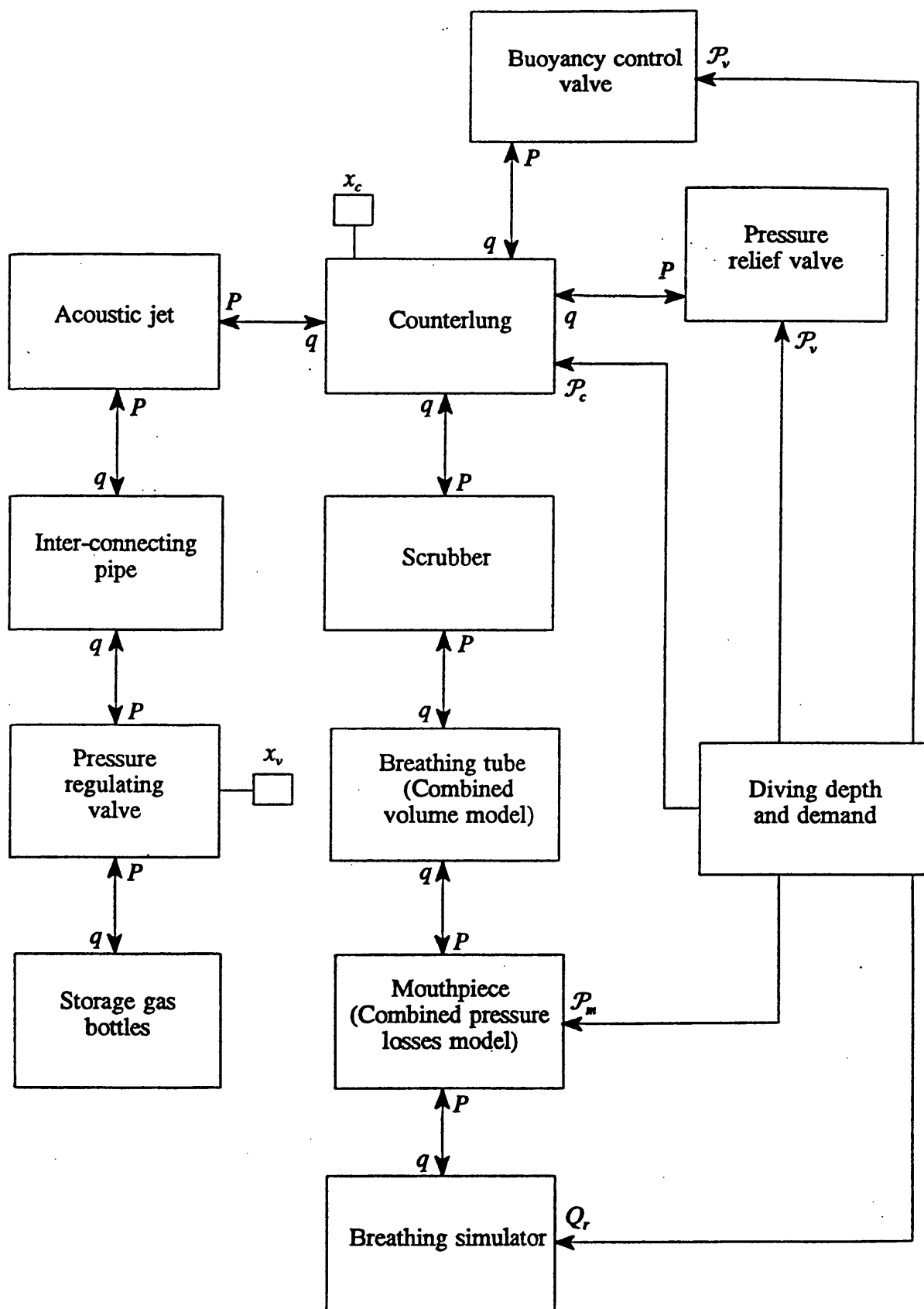
Figure 3.9 Simulation of semi-closed-circuit breathing system block diagram
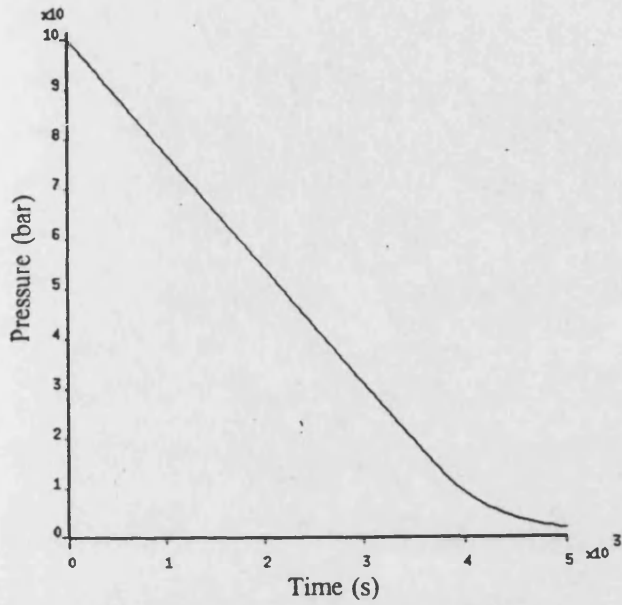
(a) Gas storage bottle pressure
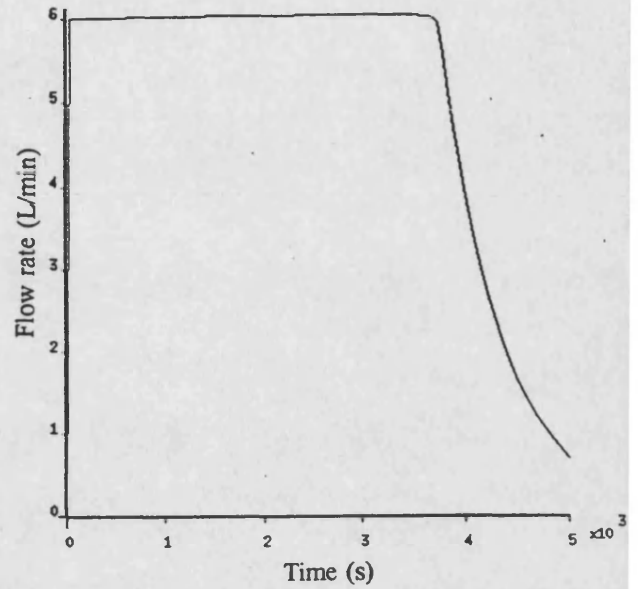
(b) Mass flow jet unit outlet volumetric flow rate
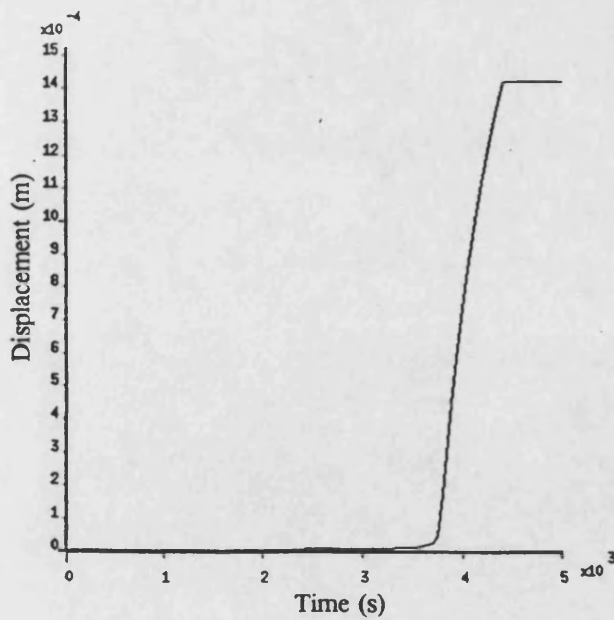
(c) Pressure regulating valve opening
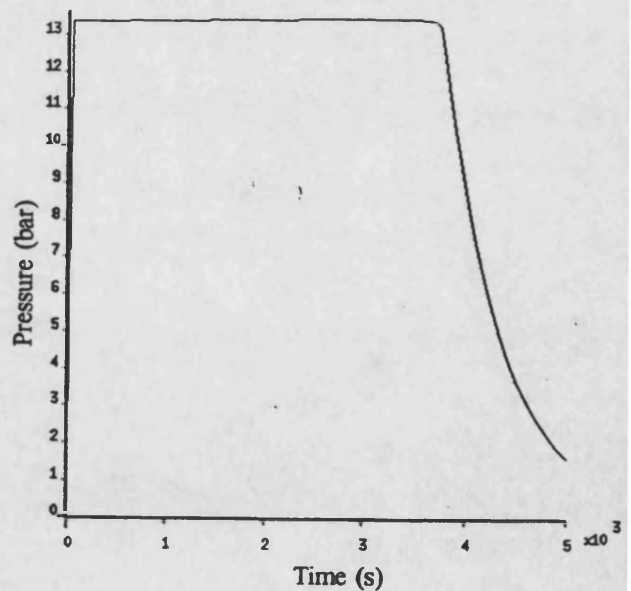
(d) Acoustic jet inlet pressure

Figure 3.10 Simulated mass flow jet unit response for 60%O_2 and 40%N_2 at a diving depth of 25 m

90
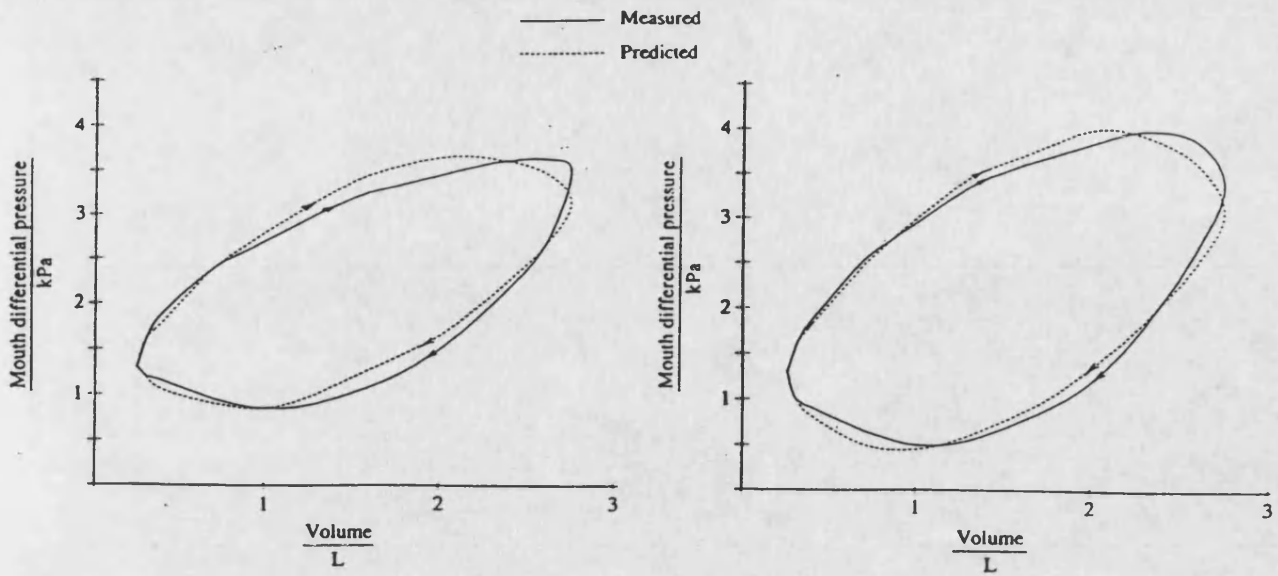
(a) 25 breaths/min, 62.5 RMV

(b) 30 breaths/min, 75 RMV

Figure 3.11 Predicted and measured breathing loops (20 m diving depth)
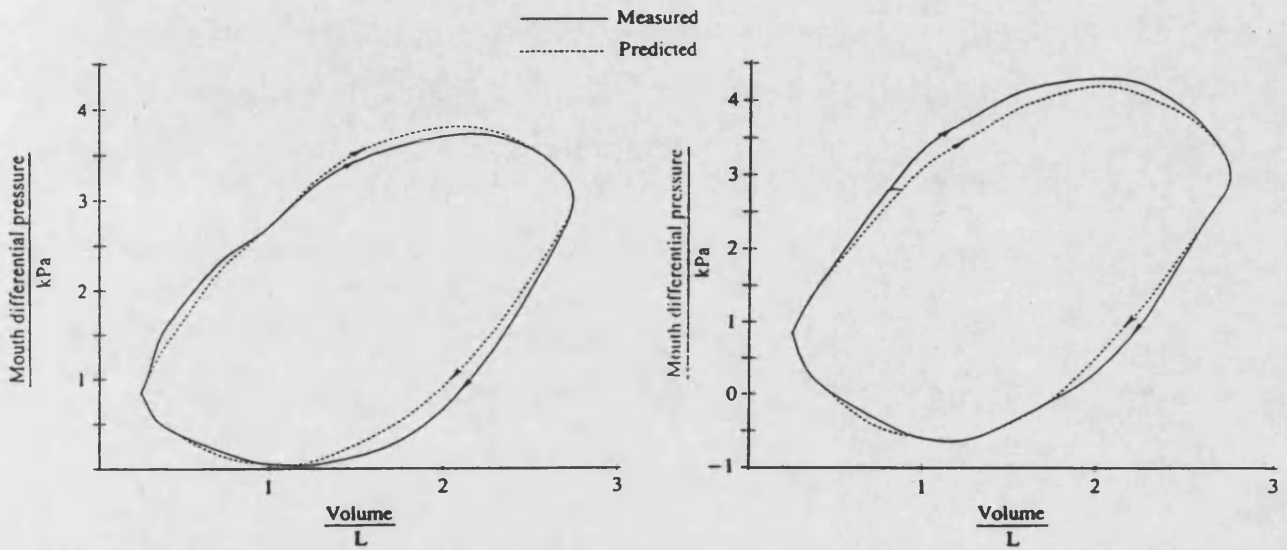
(a) 25 breaths/min, 62.5 RMV

(b) 30 breaths/min, 75 RMV

Figure 3.12 Predicted and measured breathing loops (40 m diving depth)

Measured
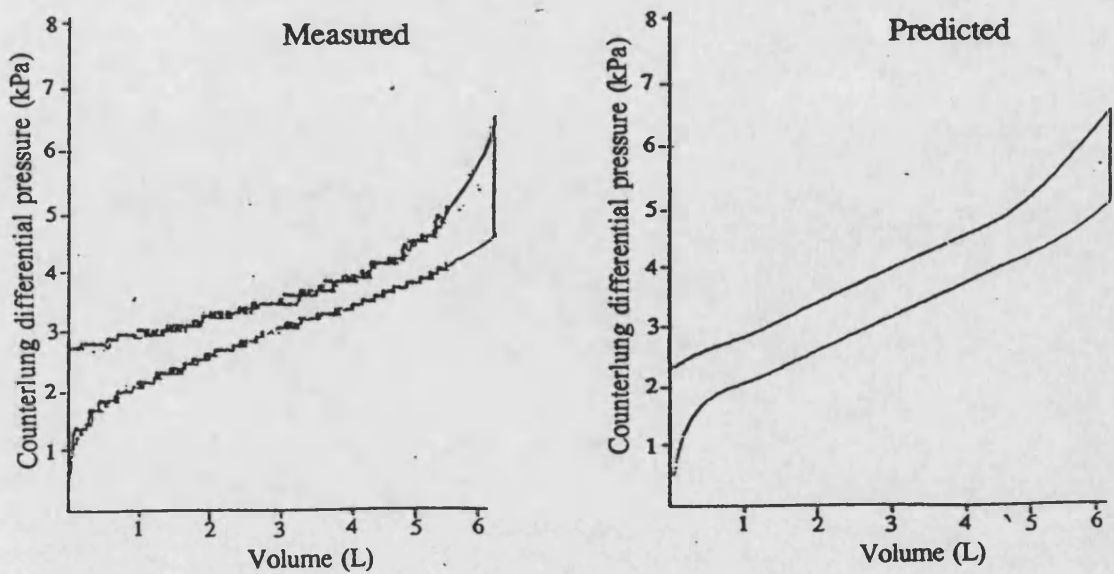
Predicted

Figure 3.13 Predicted and measured counterlung pressure-volume loops

91

(a) 25 breaths/min, 62.5 RMV (20 m diving depth)

(b) 30 breaths/min, 75 RMV (20 m diving depth)

Measured
----- Predicted

(c) 25 breaths/min, 62.5 RMV (40 m diving depth)

(d) 30 breaths/min, 75 RMV (40 m diving depth)
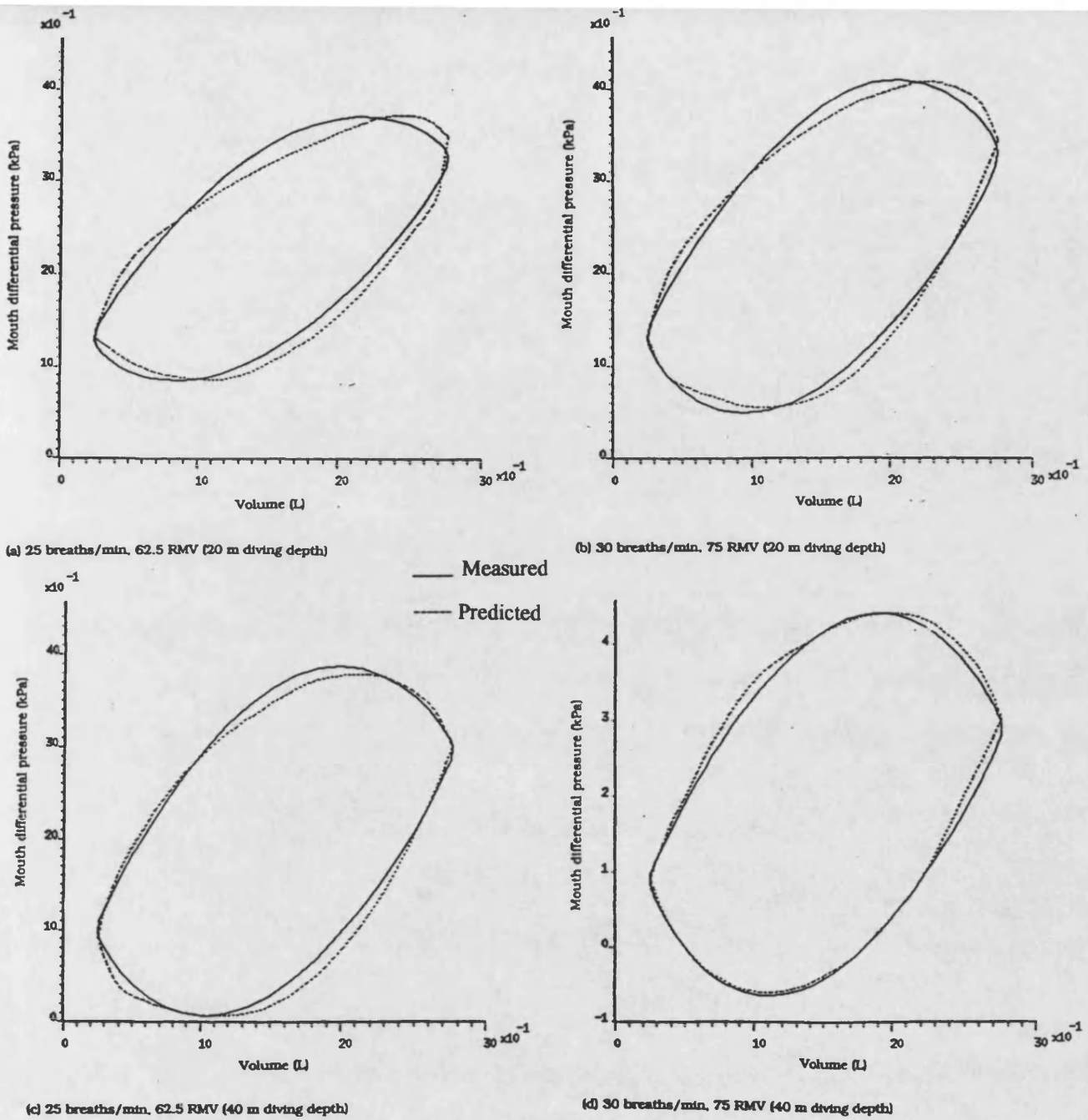
Figure 3.14 Predicted and measured breathing loops (using Tomlinson's counterlung model)
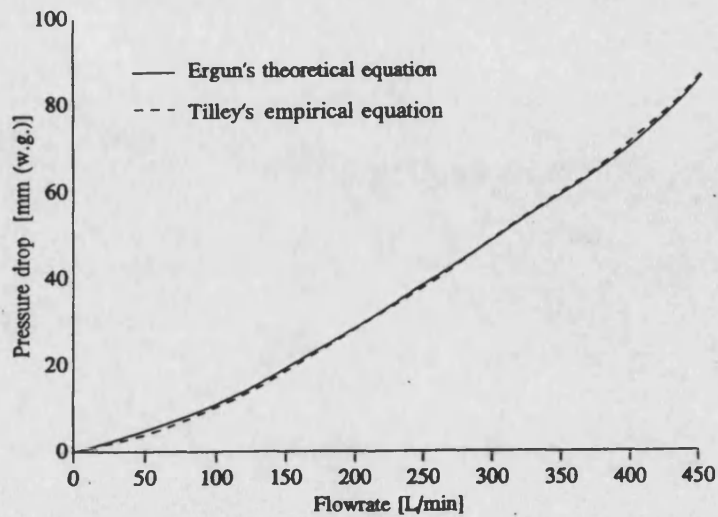
Figure 3.15 Axial flow scrubber pressure losses obtained using Ergun's theoretical equation and Tilley's imperical equation
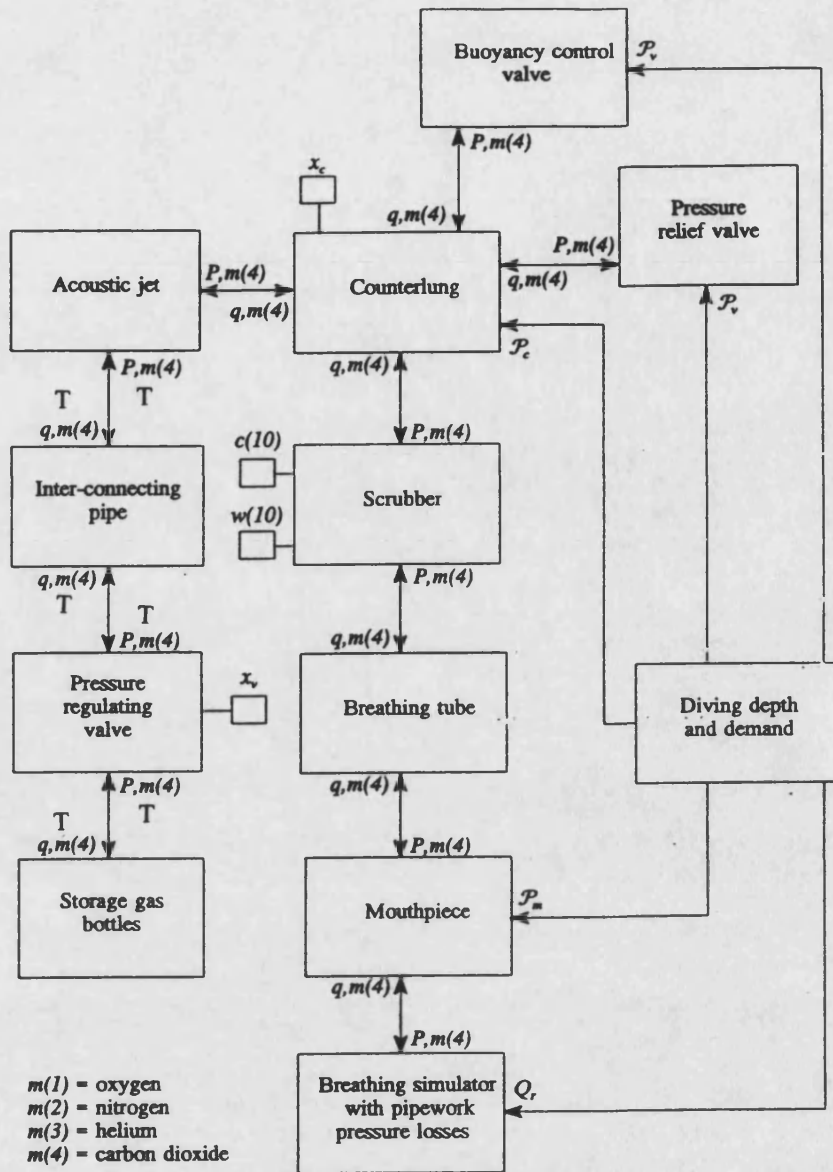
Figure 3.16(a) Simulation of semi-closed-circuit breathing system block diagram using enhanced models

$m(1)$ = oxygen
$m(2)$ = nitrogen
$m(3)$ = helium
$m(4)$ = carbon dioxide
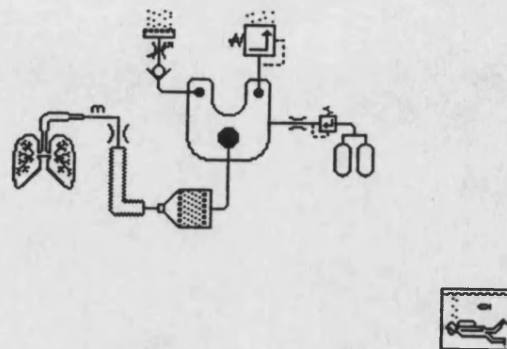
Figure 3.16(b) Simulation of semi-closed-circuit breathing system schematic diagram in Bath*fp*
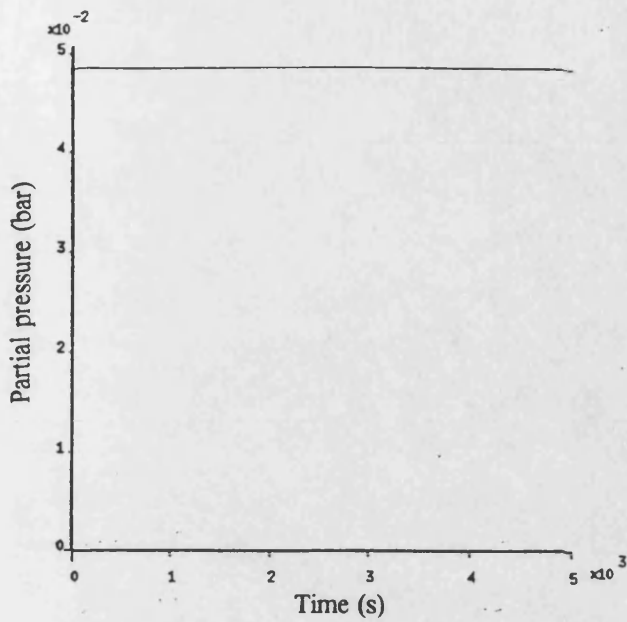
(a) P_{CO_2} at the upstream of the axial flow scrubber
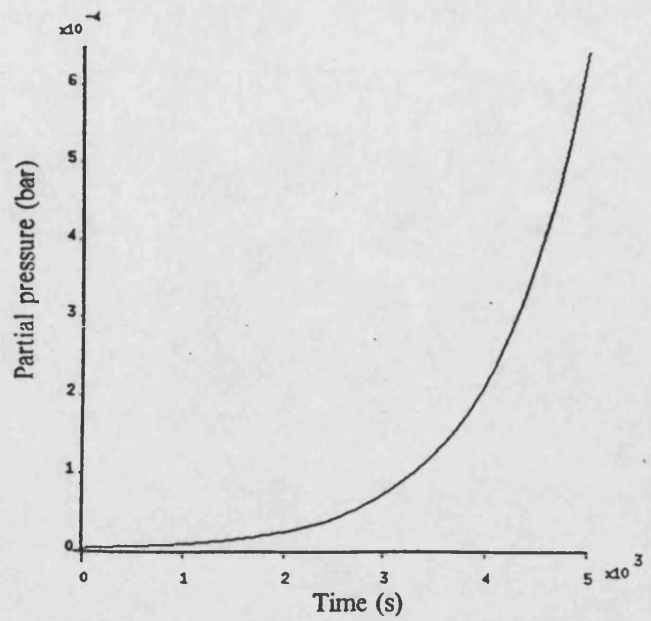
(b) P_{CO_2} at the downstream of the axial flow scrubber

Figure 3.17 Simulation results of axial flow scrubber under constant flow supply
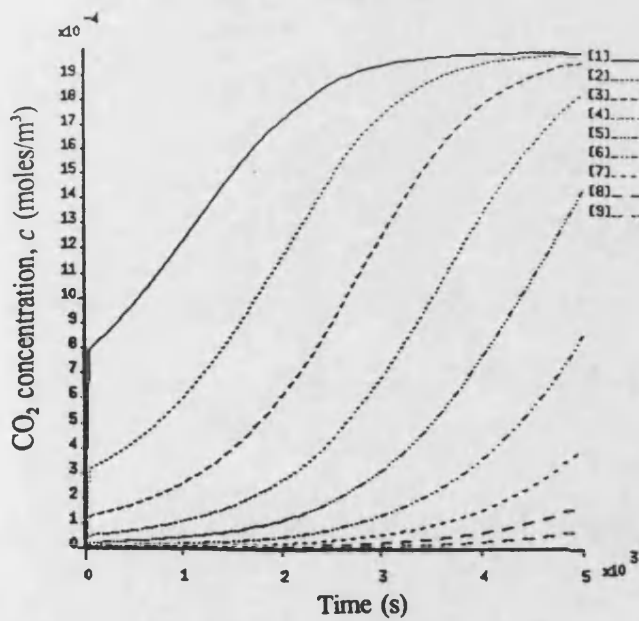
(a) Gas phase CO_2 concentration at individual elements of the scrubber model
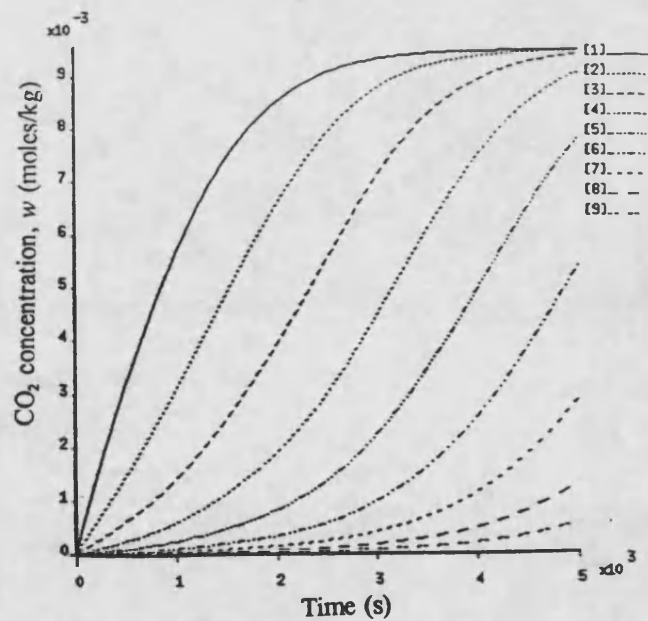
(b) Absorbent phase CO_2 concentration at individual elements of the scrubber model

Figure 3.18 Predicted gas and absorbent phases of CO_2 concentration at individual elements of the scrubber model

94
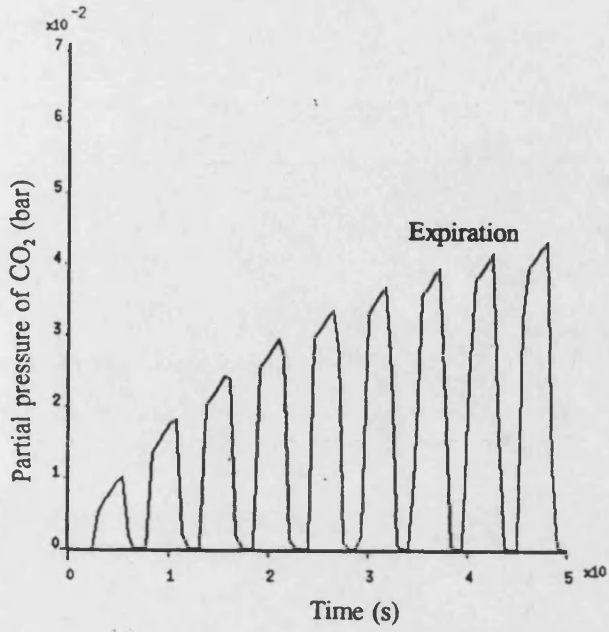
(a) During initial 50 seconds simulation
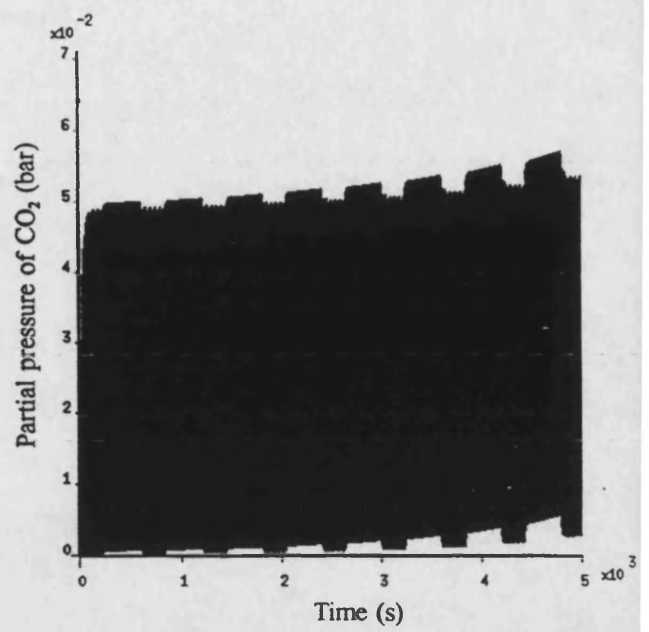
(b) Whole period of simulation

Figure 3.19 Predicted P_{CO_2} at the mouthpiece during the diving depth of 25 m
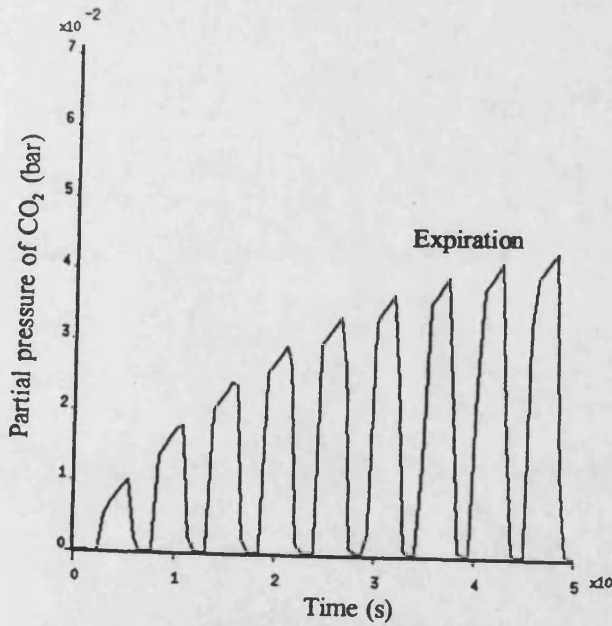
(a) During initial 50 seconds simulation
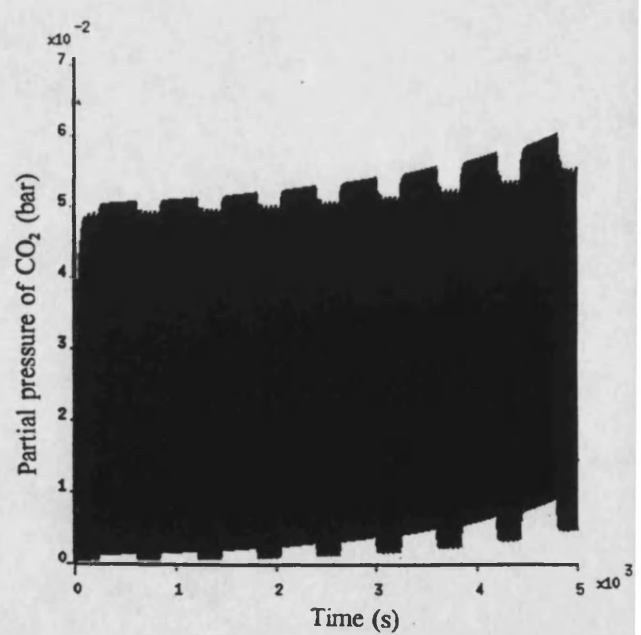
(b) Whole period of simulation

Figure 3.20 Predicted P_{CO_2} at the mouthpiece during the diving depth of 54 m

95
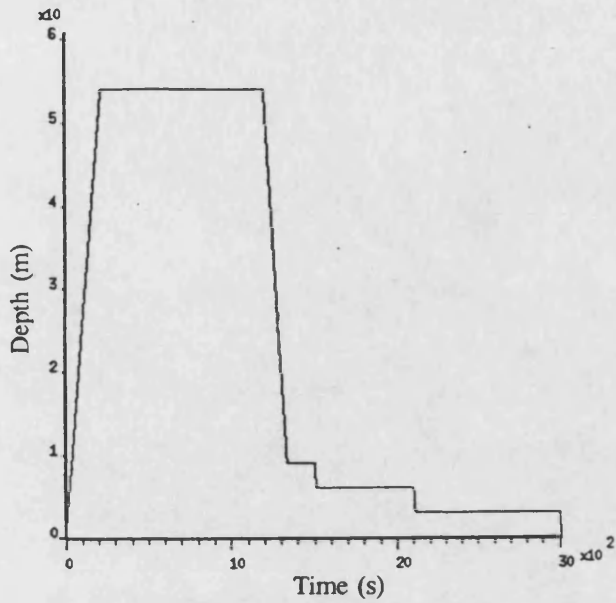
(a) Diving schedule
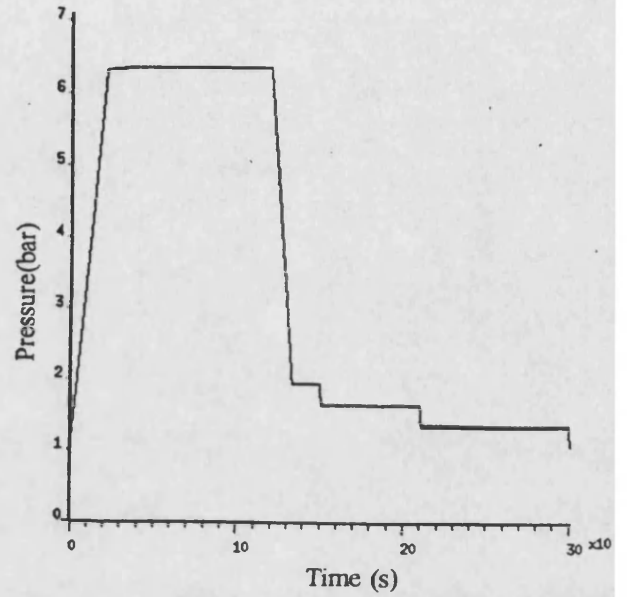
(b) Pressure inside the counterlung
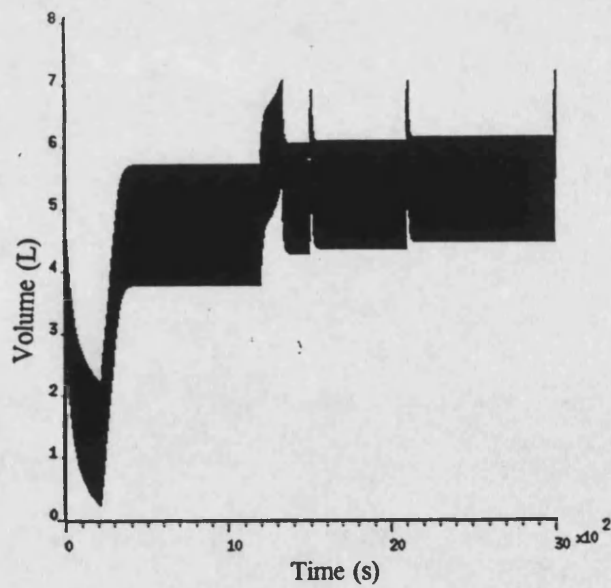
(c) Counterlung volume

Figure 3.21 Simulation results of semi-closed-circuit breathing system for 54 m dive (with O_2 uptaken process)
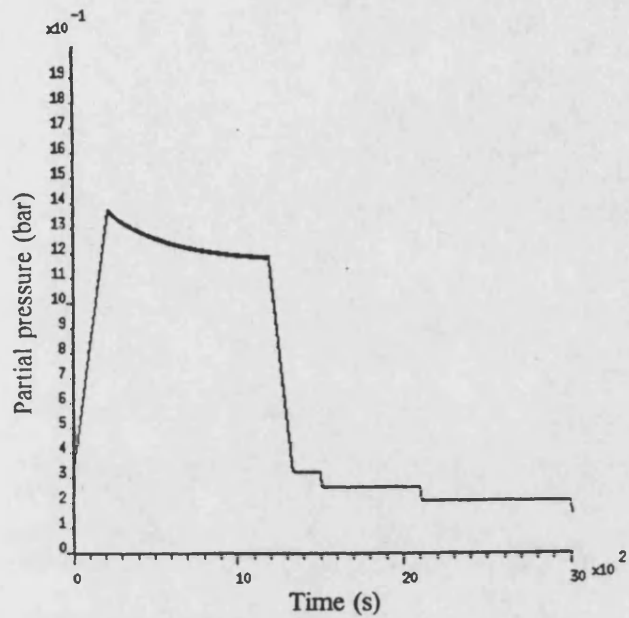
(a) P_{O2} inside the breathing simulator
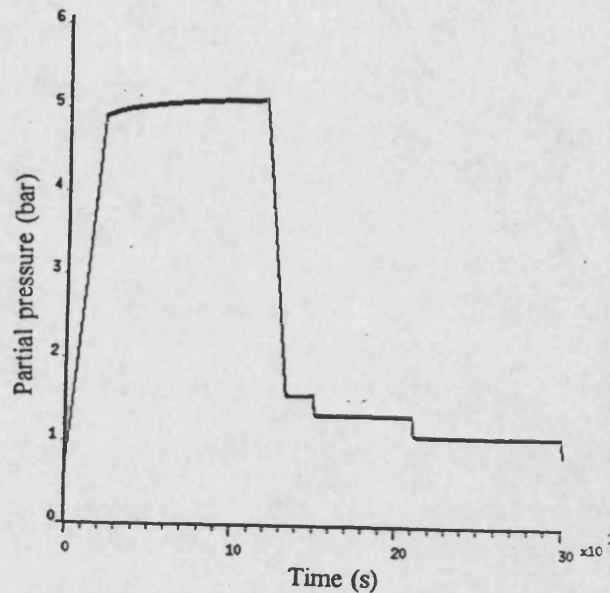
(b) P_{N2} inside the breathing simulator
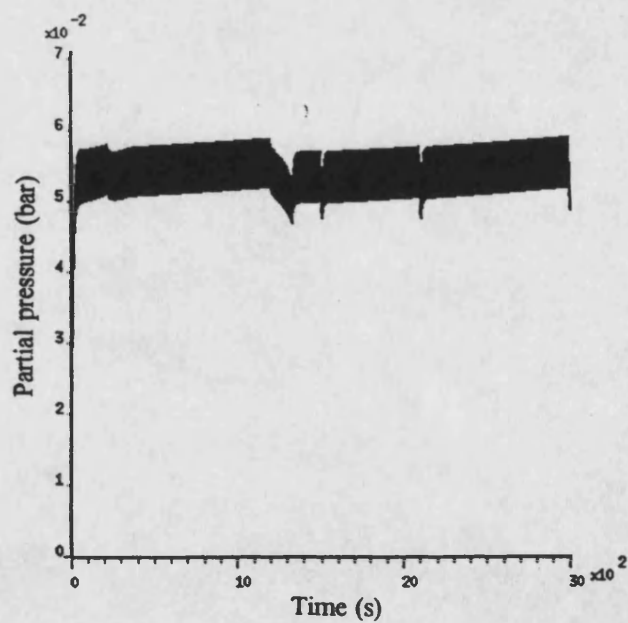
(c) P_{CO2} inside the breathing simulator

Figure 3.22 Predicted gas partial pressures inside the breathing simulator during 54 m dive
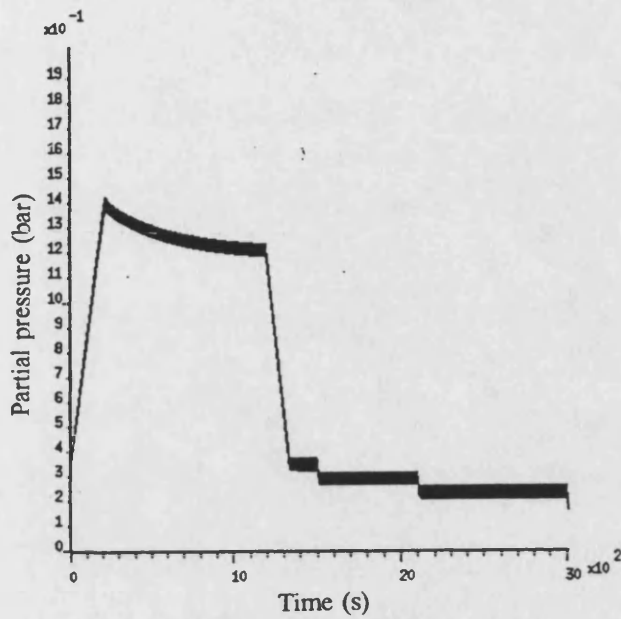
(a) P_{O2} inside the mouthpiece
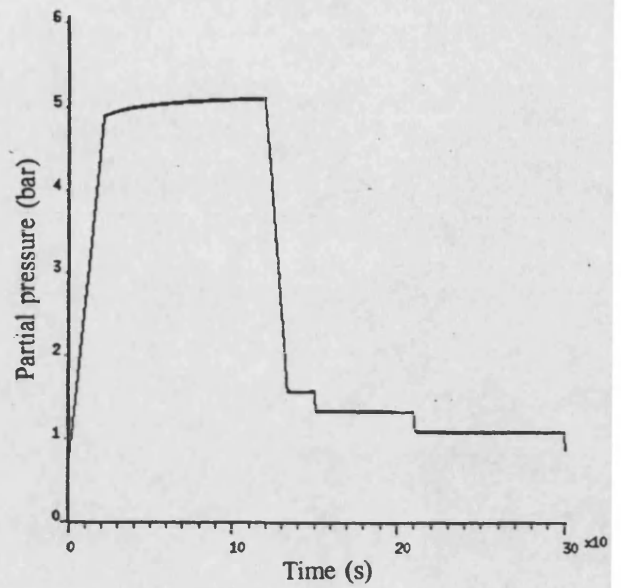
(b) P_{N2} inside the mouthpiece
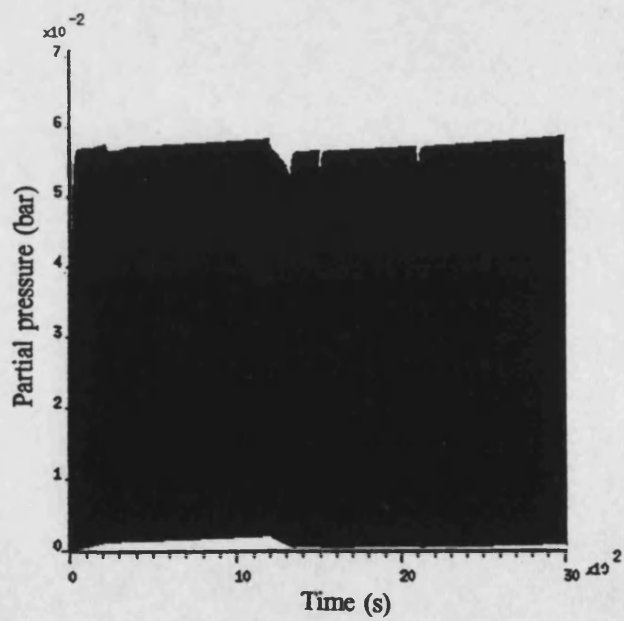
(c) P_{CO2} inside the mouthpiece

Figure 3.23 Predicted gas partial pressures inside the mouthpiece during 54 m dive
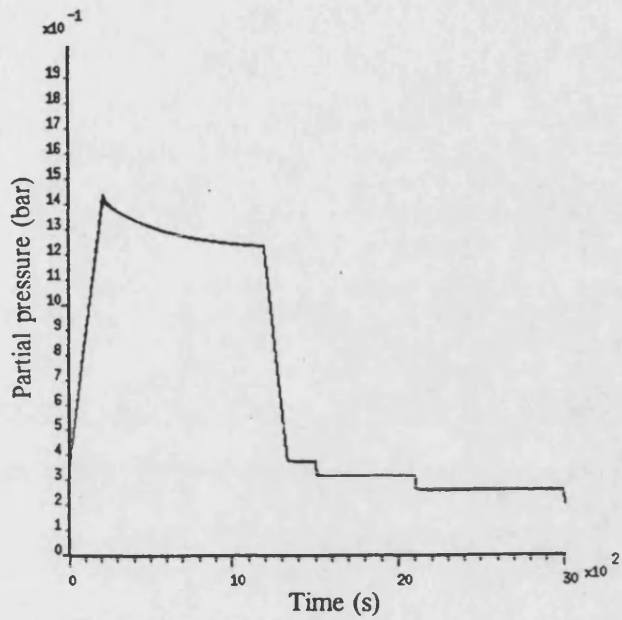
(a) P_{O2} inside the counterlung
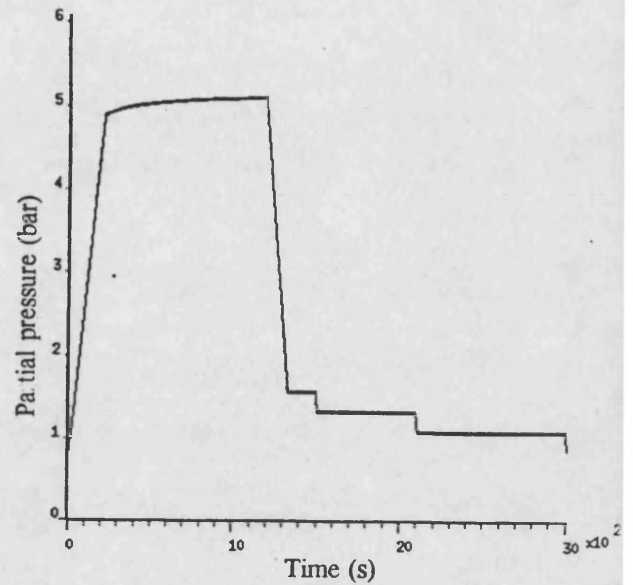
(b) P_{N2} inside the counterlung
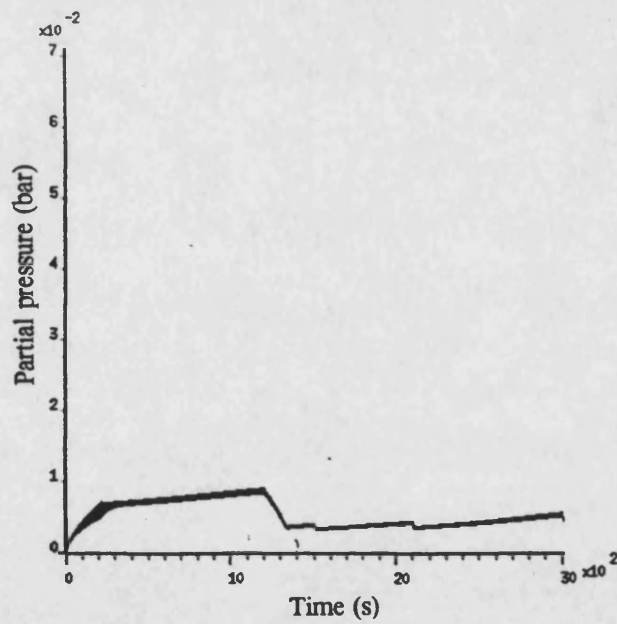
(c) P_{CO2} inside the counterlung

Figure 3.24 Predicted gas partial pressures inside the counterlung during 54 m dive
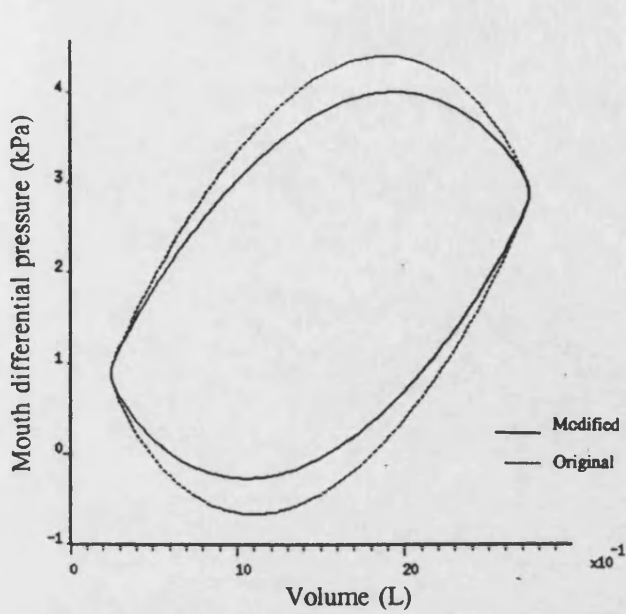
(a) Predicted breathing loops of the modified and original systems (40m depth, 30 breaths/min and 75 RMV)
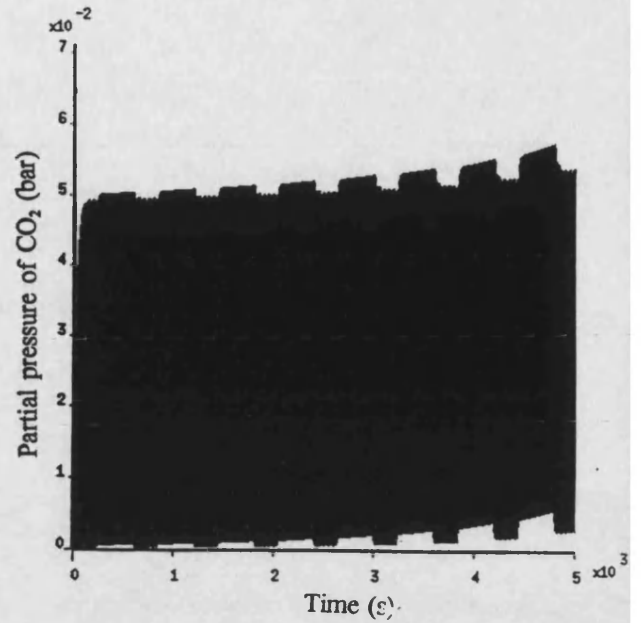
(b) Predicted P_{CO_2} at the mouthpiece of the modified system during 25 m diving depth

Figure 3.25 Simulation results of increasing the mouthpiece diameter
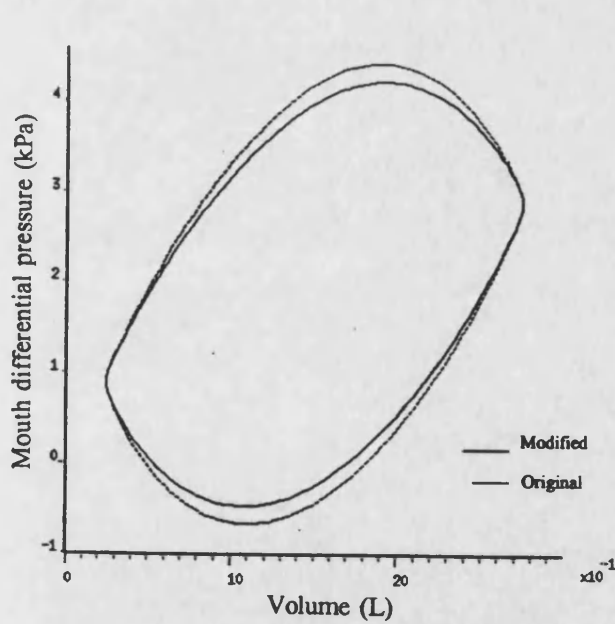
(a) Predicted breathing loops of the modified and original systems (40m depth, 30 breaths/min and 75 RMV)
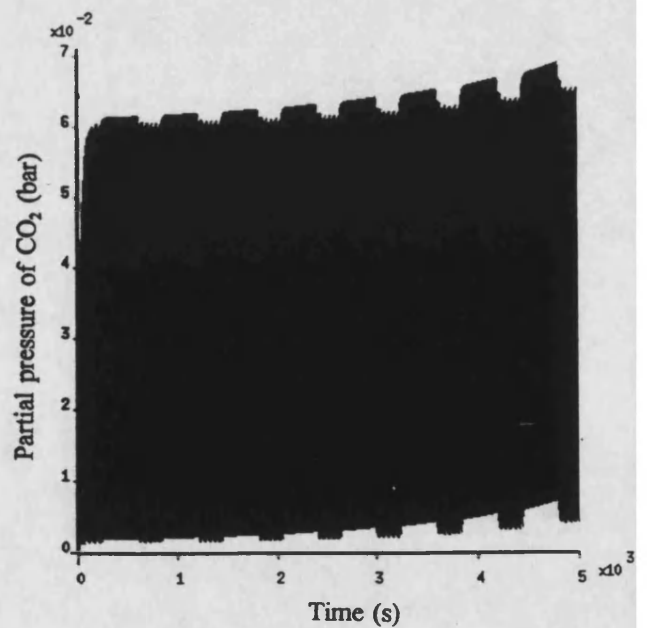
(b) Predicted P_{CO_2} at the mouthpiece of the modified system during 25 m diving depth

Figure 3.26 Simulation results of increasing the breathing tube diameter
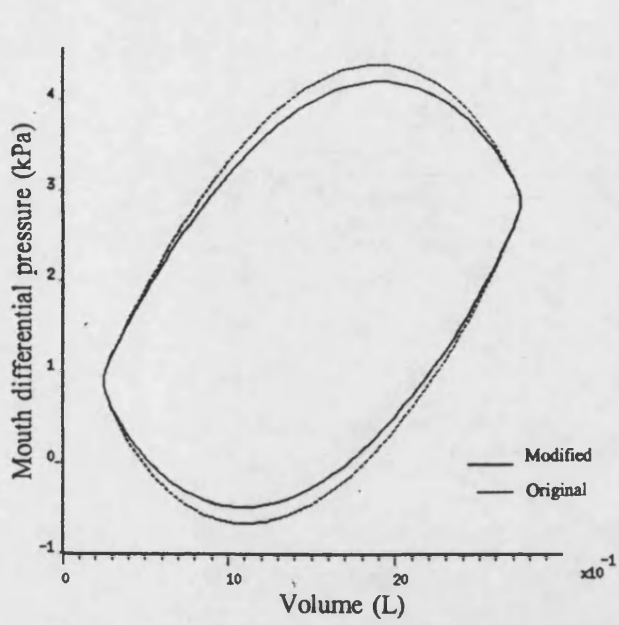
(a) Predicted breathing loops of the modified and original systems (40m depth, 30 breaths/min and 75 RMV)
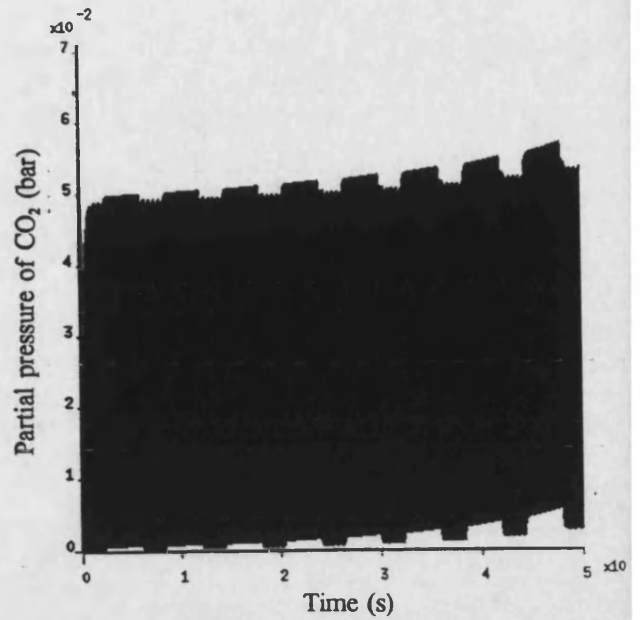
(b) Predicted P_{CO_2} at the mouthpiece of the modified system during 25 m diving depth

Figure 3.27 Simulation results of using smooth bore breathing tube
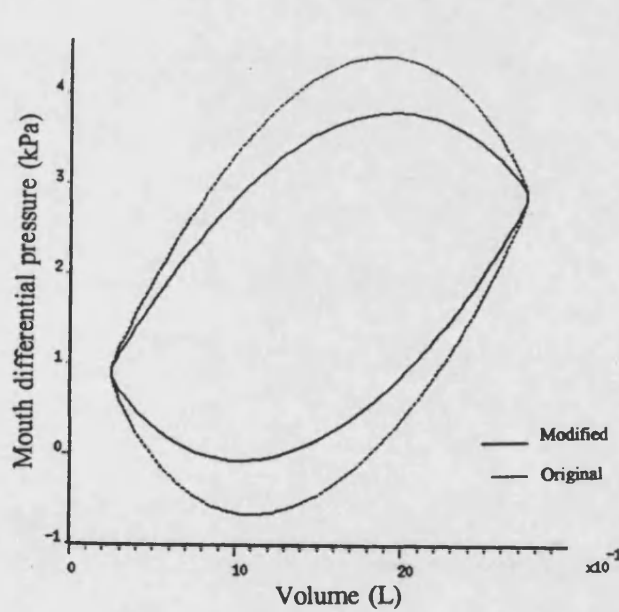
(a) Predicted breathing loops of the modified and original systems (40m depth, 30 breaths/min and 75 RMV)
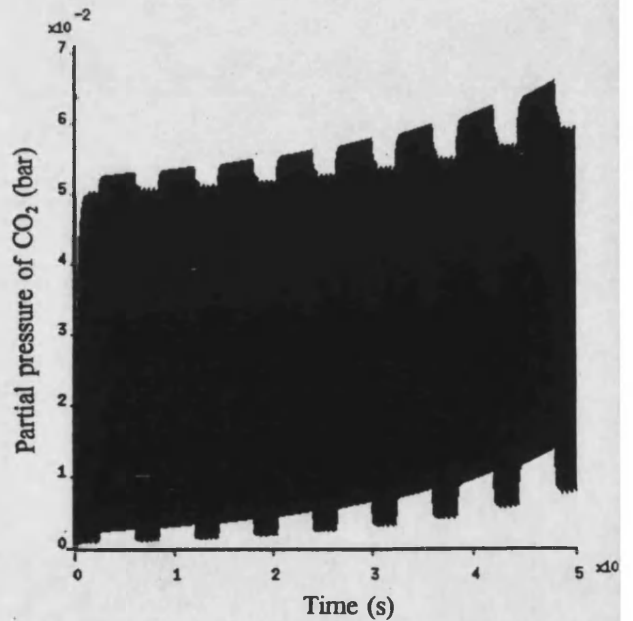
(b) Predicted P_{CO_2} at the mouthpiece of the modified system during 25 m diving depth

Figure 3.28 Simulation results of increasing the CO_2 scrubber diameter

101
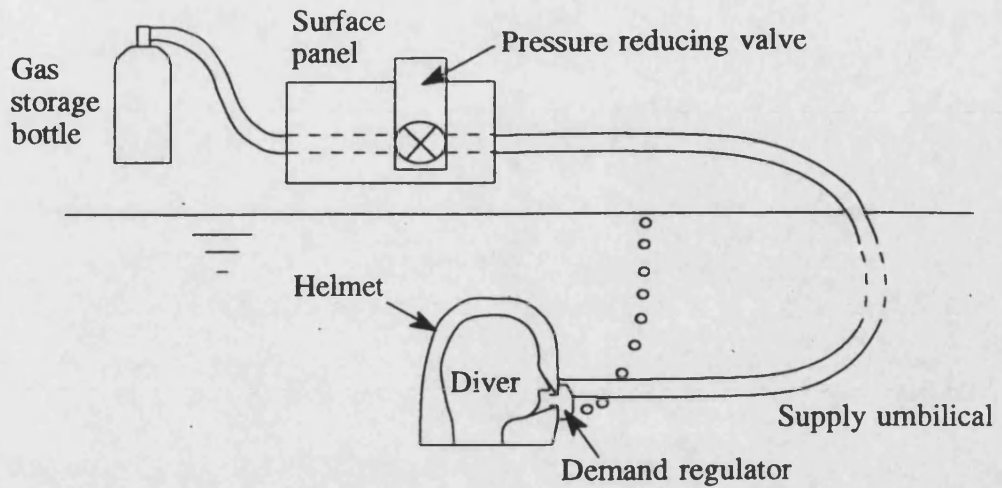
Figure 3.29 Surface demand diving system
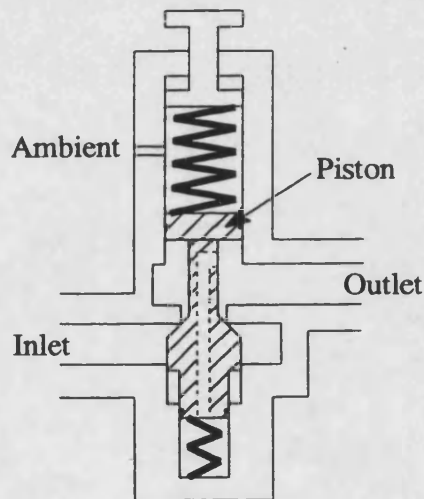
Figure 3.30 Pressure reducing valve
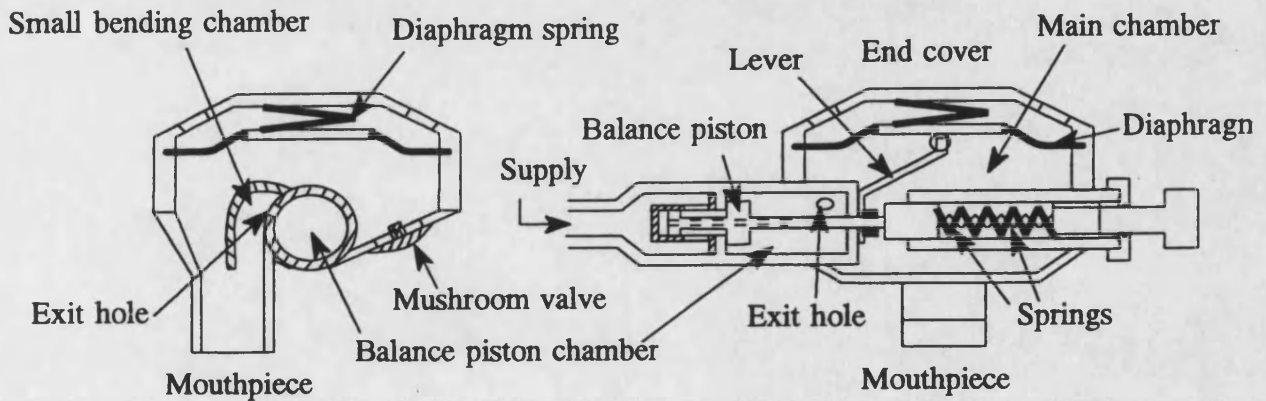
Figure 3.31 Demand regulator

102
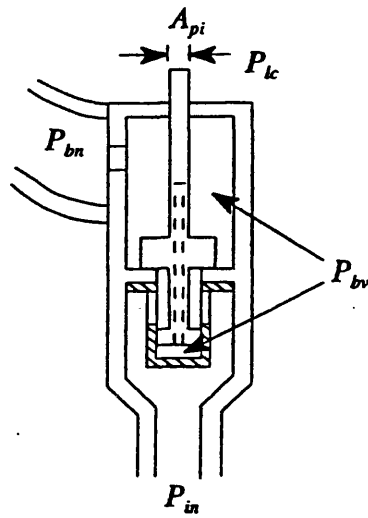
(a) Balance piston valve
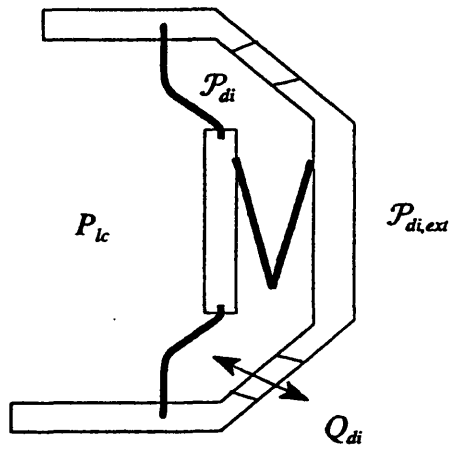
(b) Diaphragm
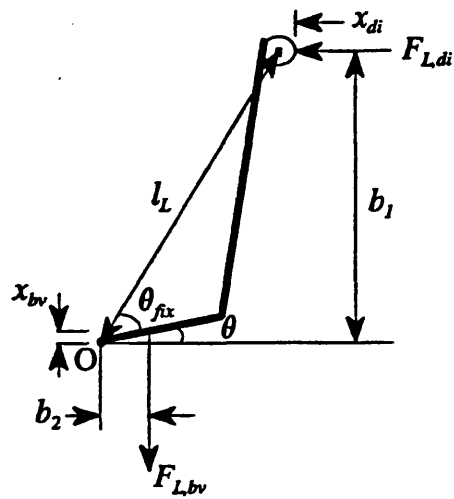
(c) Lever assembly

Figure 3.32 Forces acting on the demand regulator
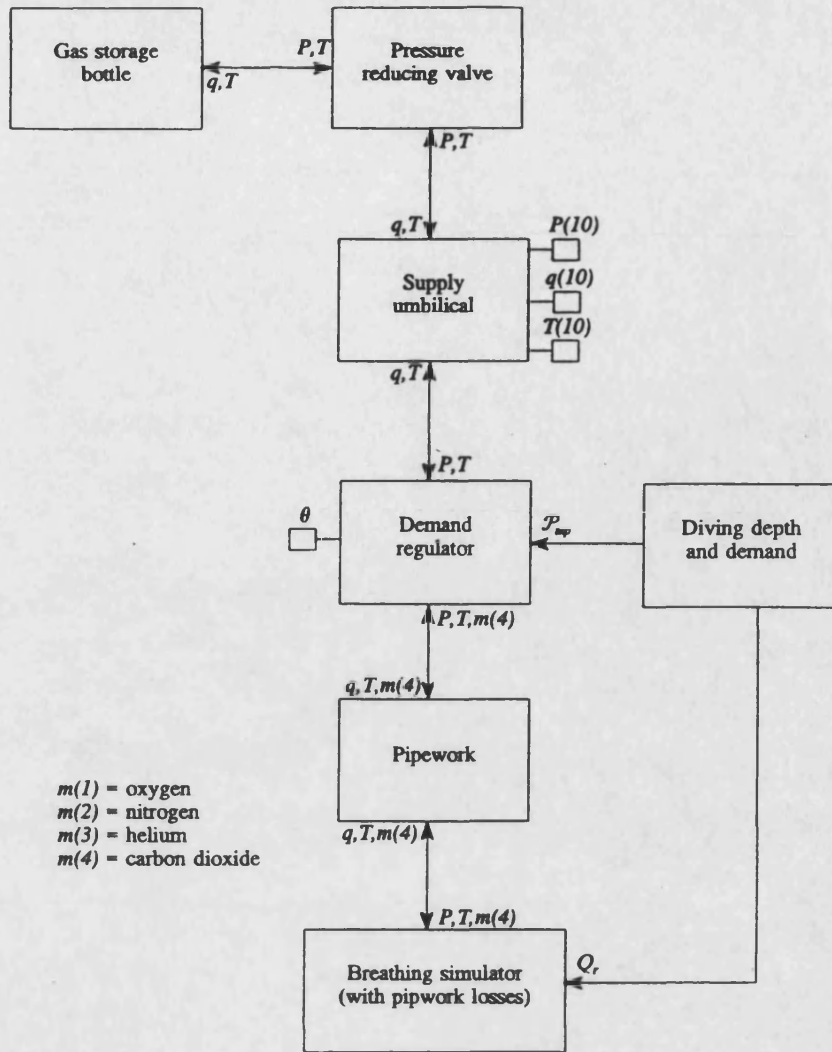
Figure 3.33(a) Simulation of surface demand diving system block diagram

$m(1)$ = oxygen
$m(2)$ = nitrogen
$m(3)$ = helium
$m(4)$ = carbon dioxide
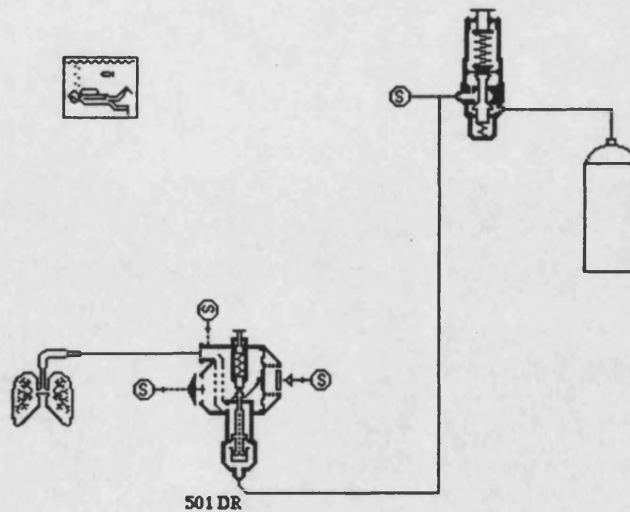
Figure 3.33(b) Simulation of surface demand diving system schematic diagram in Bath*fp*

104
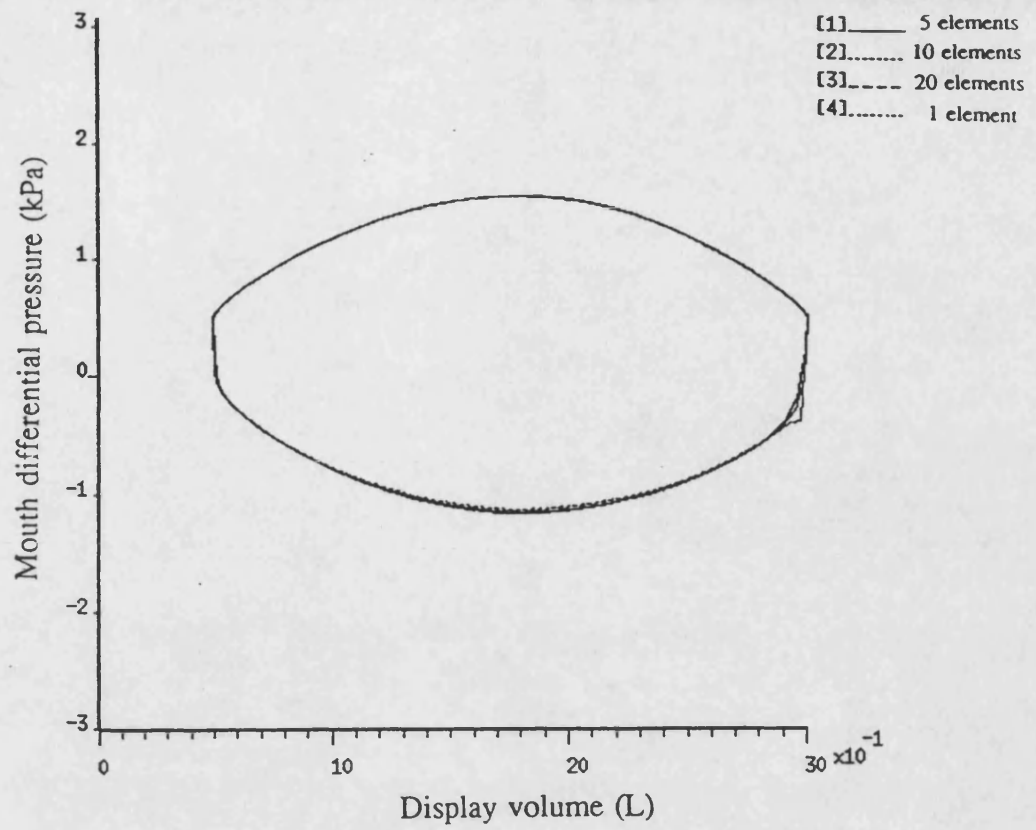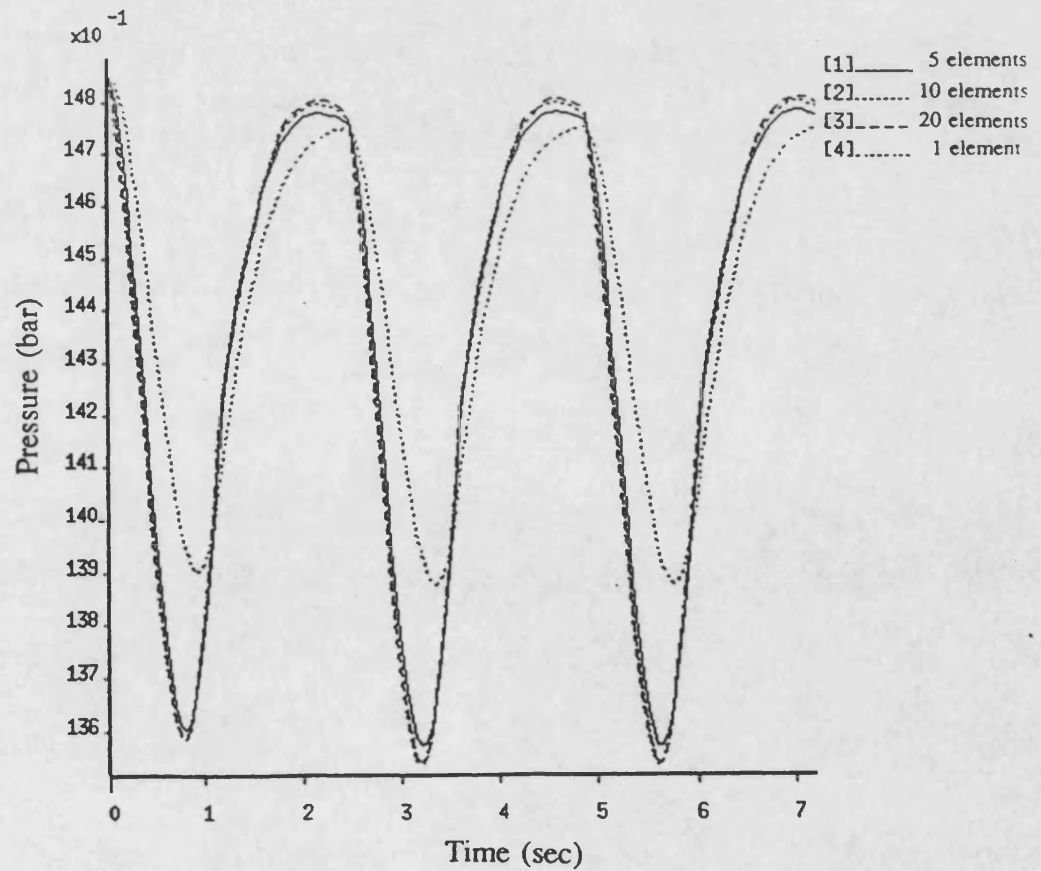
(a) Breathing loops

(b) Supply pressure to demand regulator

Figure 3.34 Simulation results using 1, 5, 10 and 20 elements of the long pipe model

105
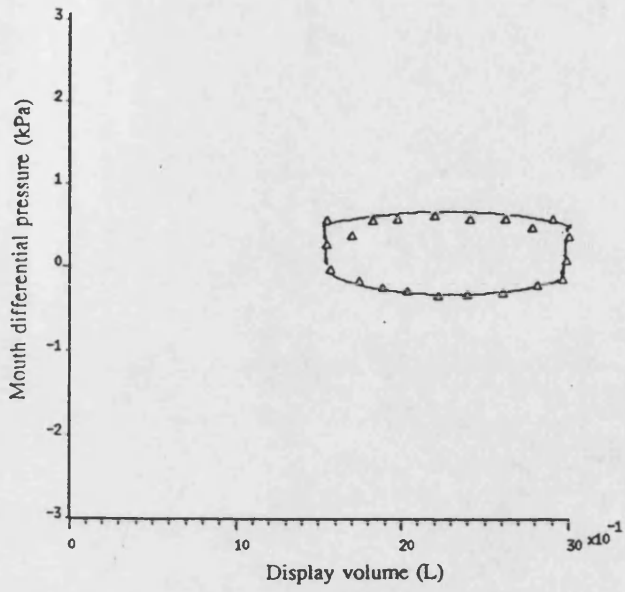
(a) 15 breaths/min & 22.5 RMV
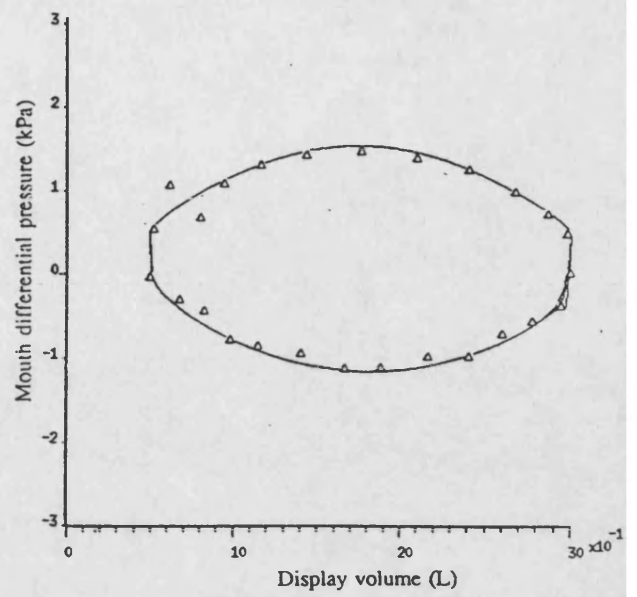
(b) 25 breaths/min & 62.5 RMV
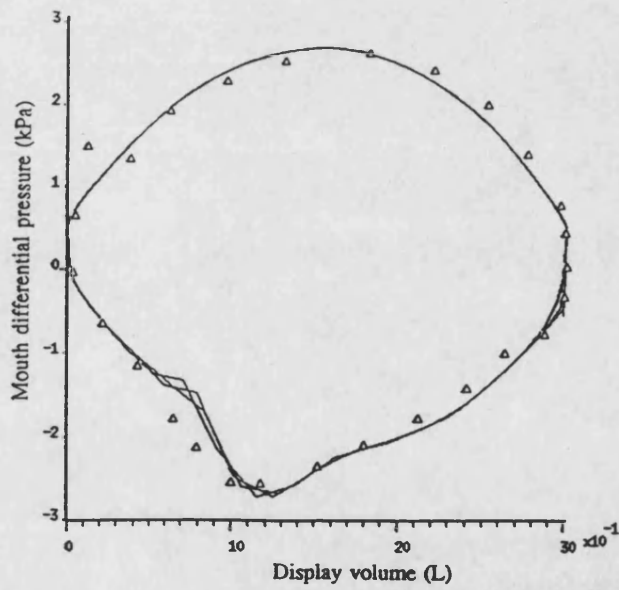
— simulated
Δ experimental data

(c) 30 breaths/min & 90 RMV

Figure 3.35 Breathing loops obtained at different respiratory demands

106
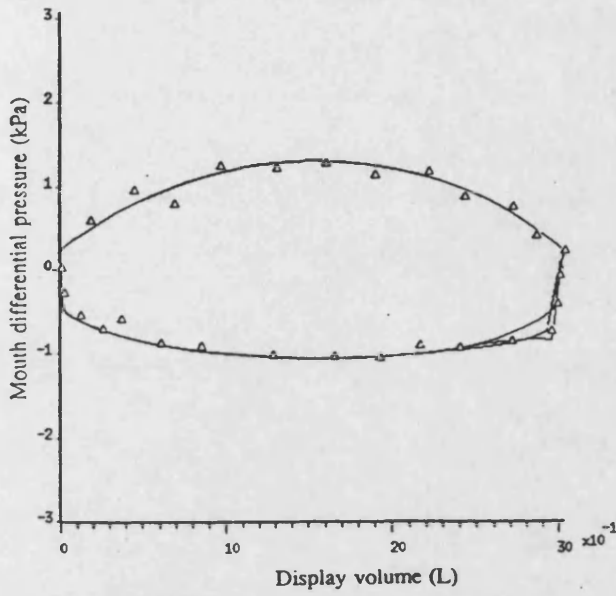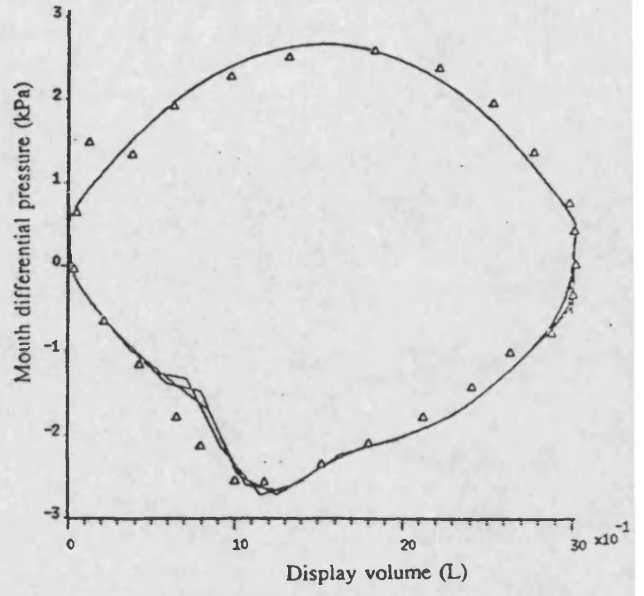
(a) 10 m diving depth

(b) 50 m diving depth

- simulated
Δ experimental data
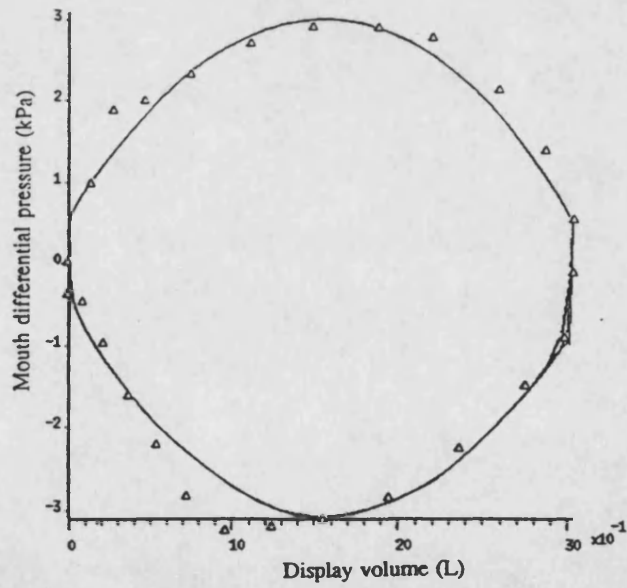
(c) 60 m diving depth

Figure 3.36 Breathing loops obtained at different diving depths

107

(a) Air

(b) Oxi-helium mixture
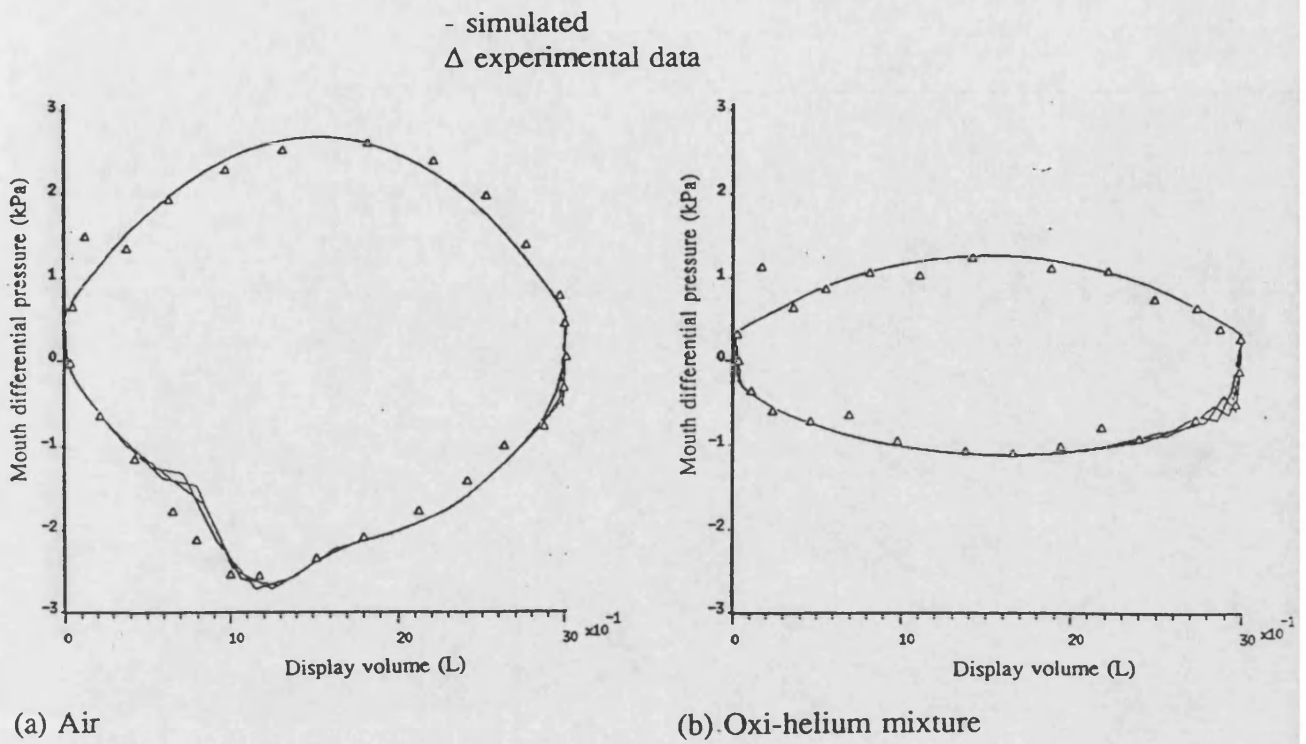
Figure 3.37 Breathing loops obtained at different gas supply mixtures

- simulated
Δ experimental data
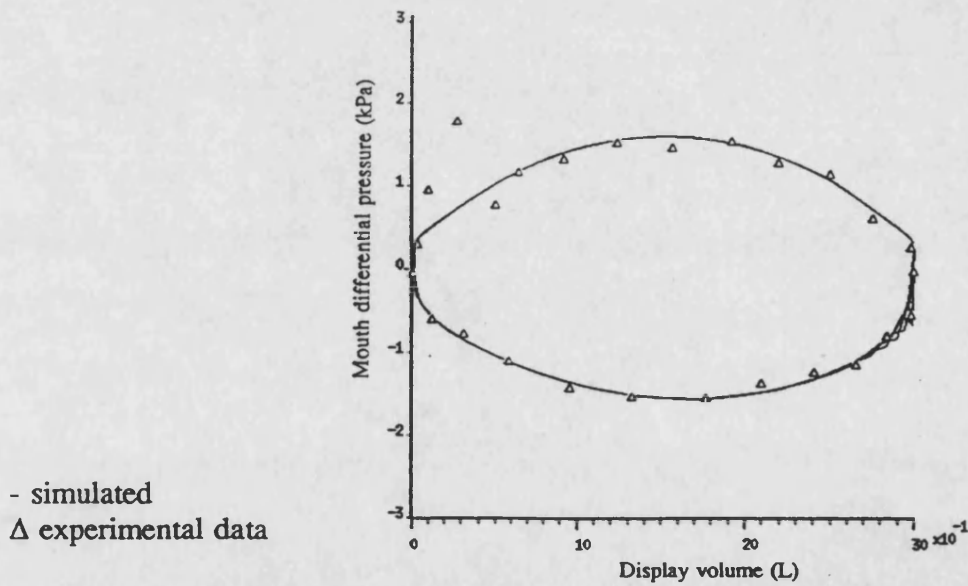
Figure 3.38 Breathing loops obtained at 30 breaths/min and 90 RMV for 85 m diving depth, using oxi-helium mixture as the supply gas
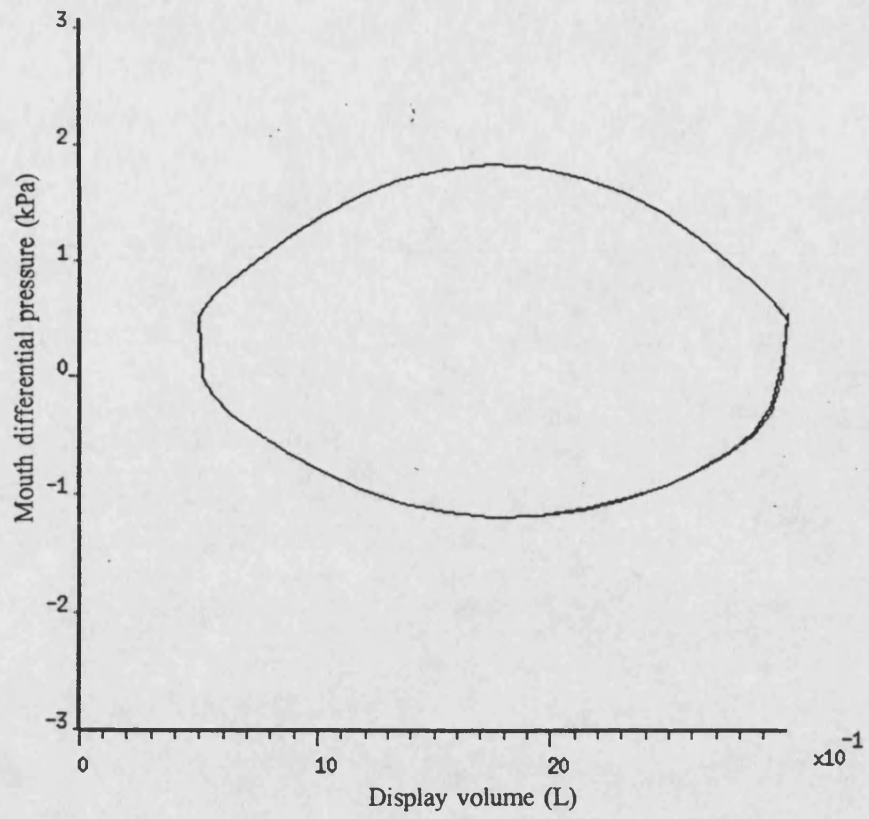
(a) Surface demand diving system
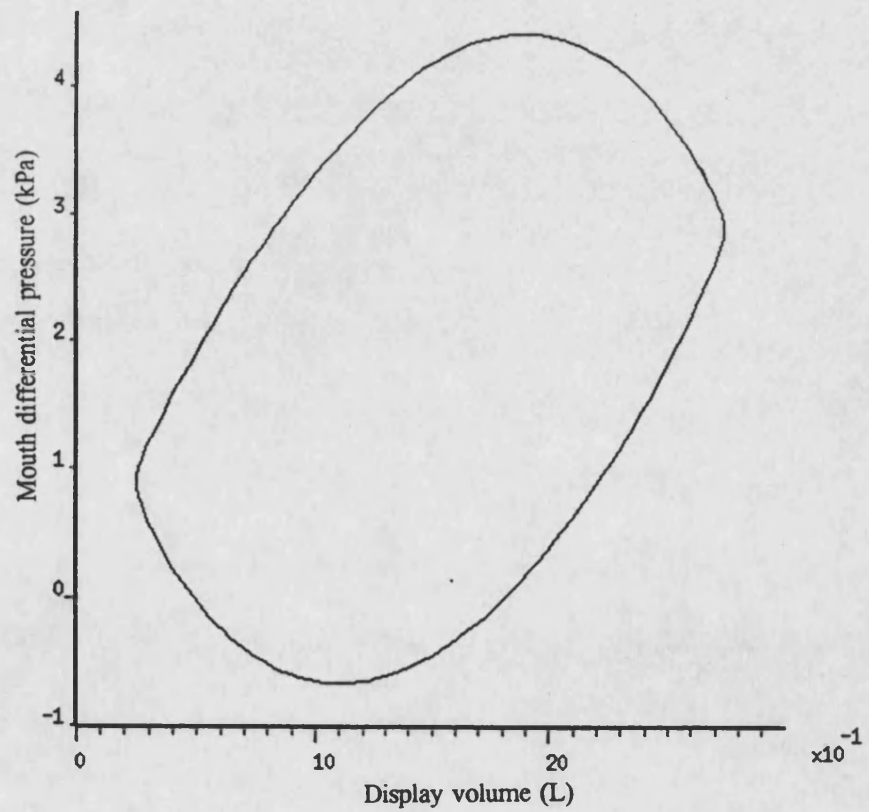
(b) Semi-closed-circuit breathing system

Figure 3.39 Breathing loops obtained at 30 breaths/min and 75 RMV for 40 m diving depth (Air supplied)
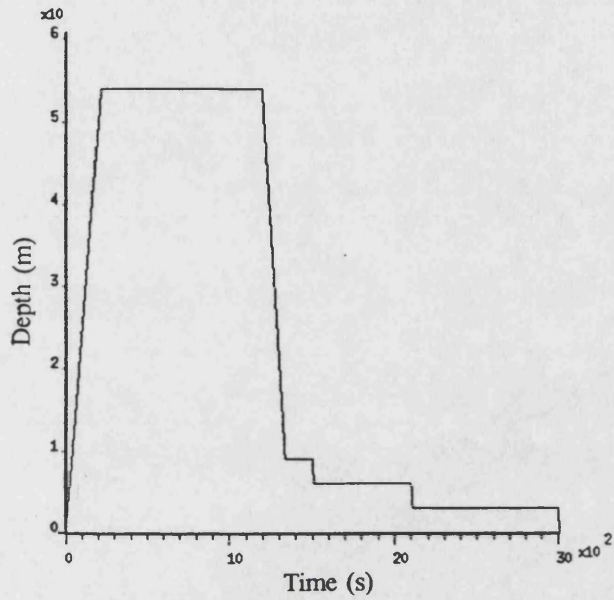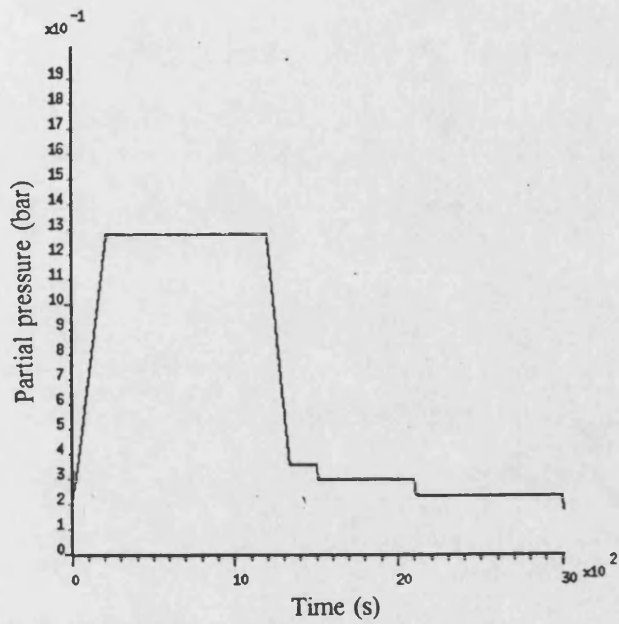
(a) Diving schedule
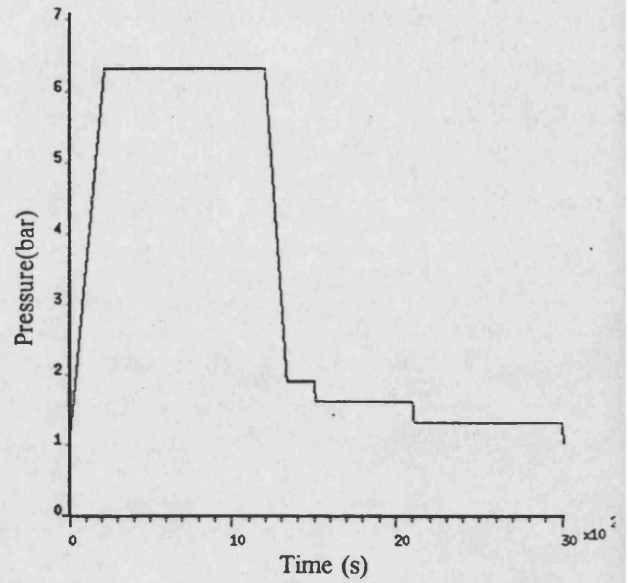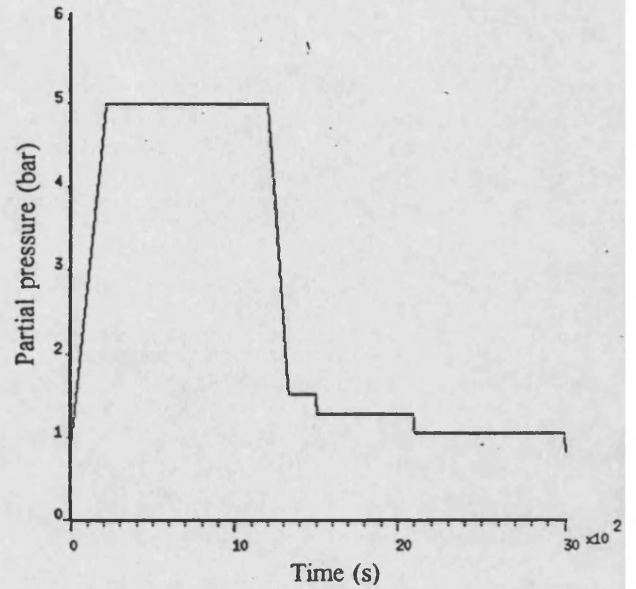

(b) Pressure inside the breathing simulator
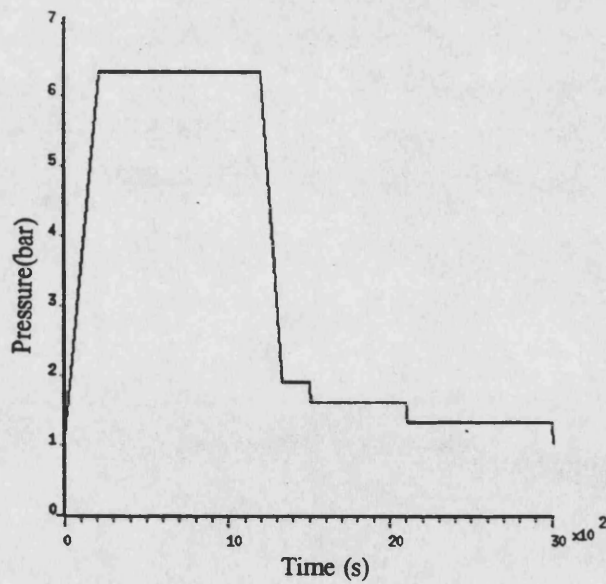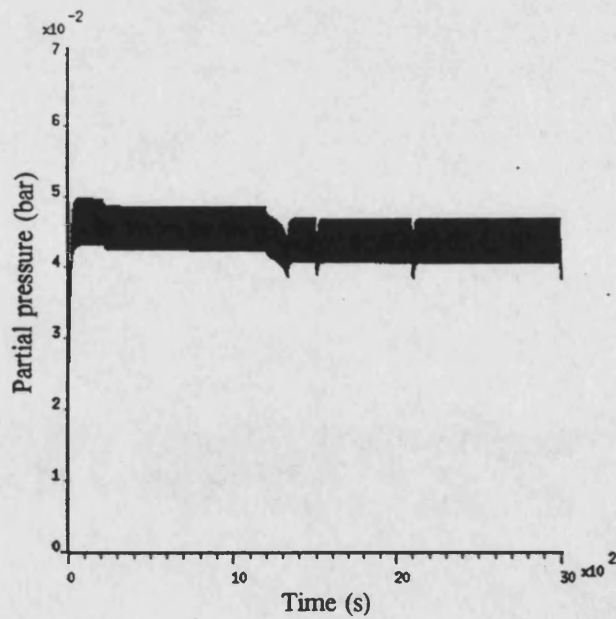

(c) Pressure inside the demand regulator

Figure 3.40 Simulation results of surface demand diving system for 54 m dive (with O_2 uptaken process)
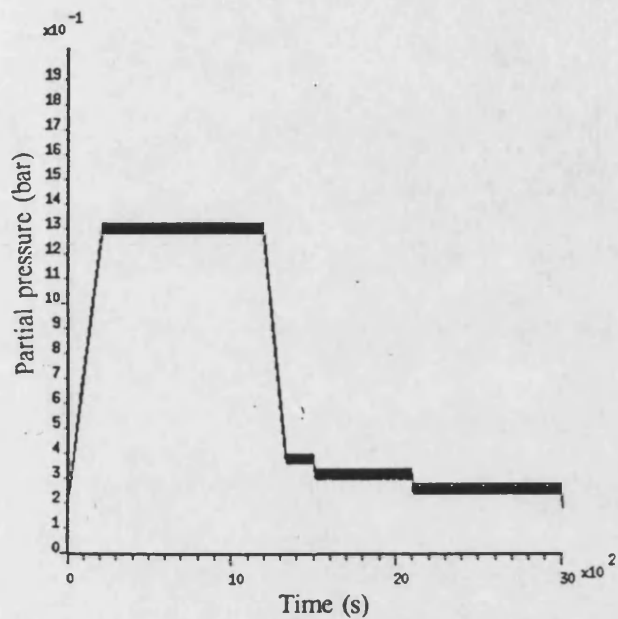
(a) P_{O_2} inside the breathing simulator

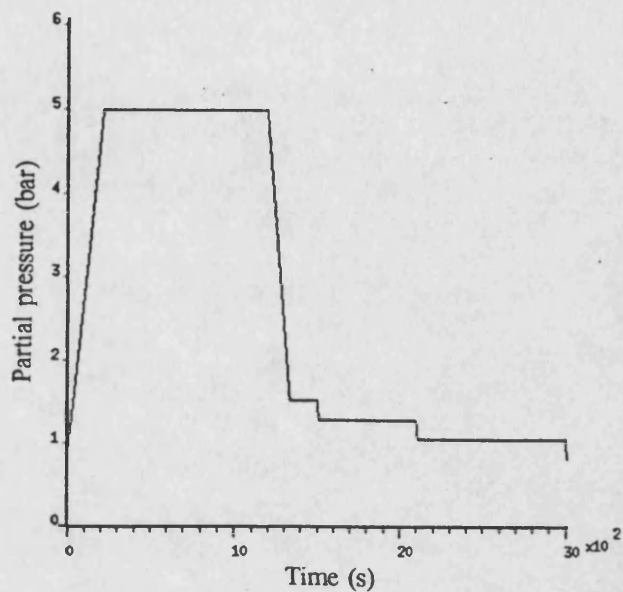(b) P_{N_2} inside the breathing simulator

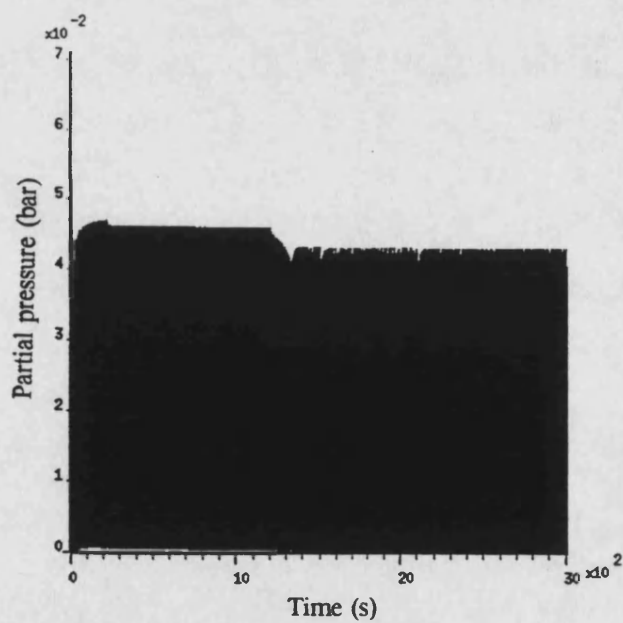(c) P_{CO_2} inside the breathing simulator

Figure 3.41 Predicted gas partial pressures inside the breathing simulator during 54 m dive

111

(a) P_{O_2} inside the demand regulator

(b) P_{N_2} inside the demand regulator

(c) P_{CO_2} inside the demand regulator

Figure 3.42 Predicted gas partial pressures inside the demand regulator during 54 m dive

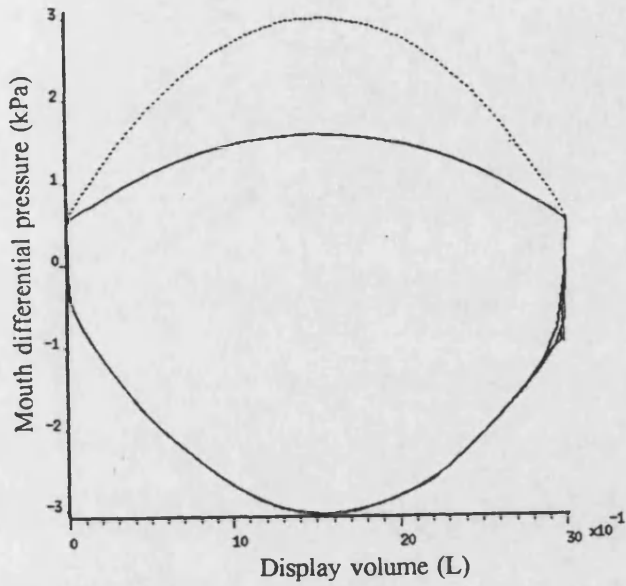**Figure 3.43** Predicted breathing loop of increasing
the mouthpiece diameter
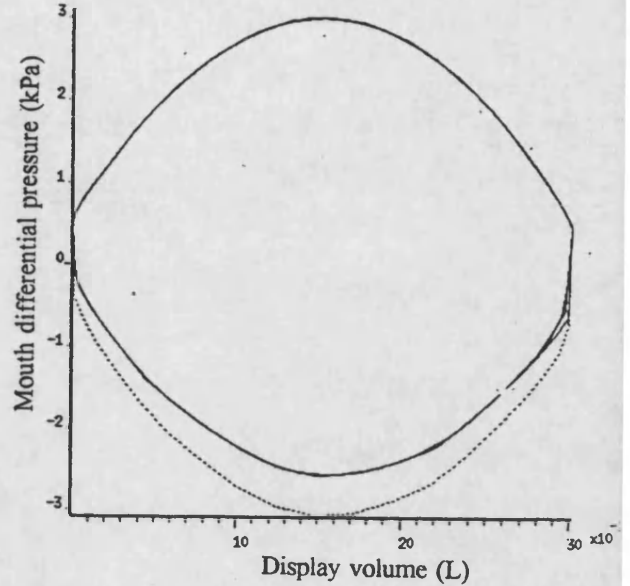(30 breaths/min and 90 RMV at 60 m depth)

Figure 3.44 Predicted breathing loop of increasing
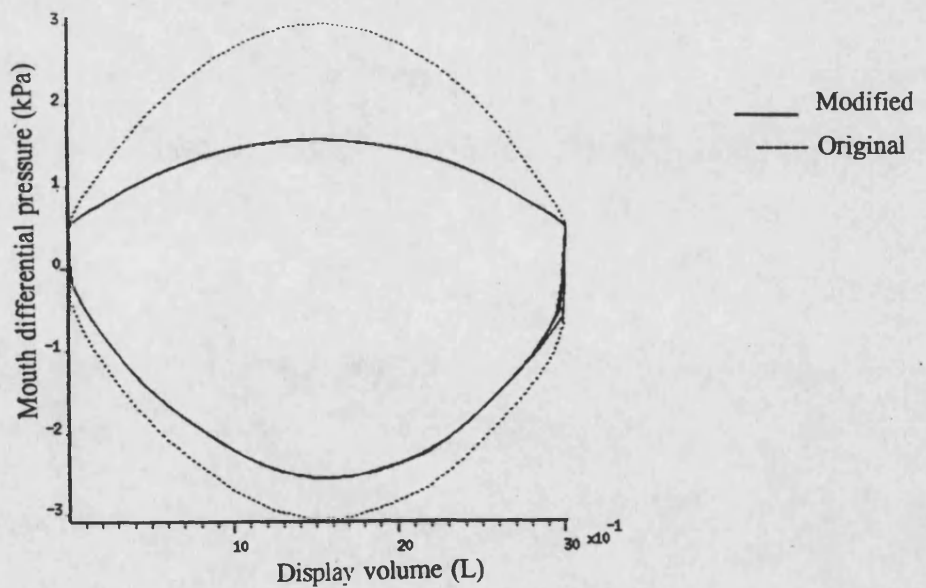the diaphragm spring rate
(30 breaths/min and 90 RMV at 60 m depth)

Figure 3.45 Predicted breathing loop of increasing the mouthpiece diameter and diaphragm spring rate
(30 breaths/min and 90 RMV at 60 m depth)

113

CHAPTER 4

MATHEMATICAL MODELLING OF
HUMAN RESPIRATORY SYSTEM

4.1 INTRODUCTION

In order to simulate the breathing apparatus under real human diving conditions, the model of the human respiratory system is required. Thus, the computer model will enable the full capabilities of the human to be assessed when using the breathing equipment, allowing the operational limits of the equipment to be assessed without risk to human life.

The first dynamic analysis of the human respiratory system appeared in 1954 (Grodins), and although it represented a step forward in considering dynamics, it was limited to a single forcing function ie. CO_2 inhalation. It also represented a much oversimplified treatment which nevertheless led to non-linear differential equations. At the time of its formulation, the state of the computer art was relatively primitive and exploration of a more general and realistic model was not practical. With the development of large-scale computing facilities, interest in the realistic dynamic analysis of complex multivariate biological control systems has increased rapidly (Grodins, 1965). Beginning with Defares in 1960, the original dynamic model of the respiratory system has been refined and extended by several workers using digital simulation (Grodins, 1967, Dickinson, 1977, Saunders, 1980, Sarhan, 1987 and Tomlinson, 1994). The present analysis represents a further step in this continuing process in order to obtain a general and realistic human respiratory model.

4.2 GENERAL DESCRIPTION OF HUMAN RESPIRATORY SYSTEM

The overall process of respiration comprises four subprocesses in series, as shown in figure 4.1. They are i) convective transport of gas to the pulmonary alveoli by ventilation, ii) diffusion from the alveoli into the blood in the pulmonary capillaries, iii) convective transport to the tissue capillaries by circulation of the blood, and iv) diffusion from the tissue capillaries into surrounding cells. Subprocesses i) and ii) together constitute pulmonary respiration (external respiration). Subprocess iii) is called blood gas transport, and subprocess iv) is known as tissue respiration (internal respiration).

114

During breathing, air passes forwards and backwards along the trachea which in turn divides into two tubes, and each of these tubes then divides into two more, and so on. In all, there are 20-23 such divisions, resulting in 1 to 8 million terminal tubes. Each of these has at its end numerous blind sacs, called alveoli, where gas exchange occurs. Oxygen continuously diffuses out of the gas in the alveoli (alveolar gas) into the bloodstream, and CO_2 continuously diffuses into the alveoli from the blood through the thin alveolocapillary membrane. On leaving the lung, the oxygenated blood passes through the pulmonary vein and then into the left heart. The blood is then ejected from the left heart into the aorta and arteries, which run in parallel to the individual organs. By repeated branching the large arteries give rise to a larger number of smaller arteries, these to still more arterioles, and these in turn to the capillaries. In the capillaries, which form dense networks, dissolved substances (such as O_2 and CO_2) are exchanged between the blood and the surrounding tissue. The capillary blood then flows into the smallest veins, the venules. These fuse, with a decrease in number and increase in lumen diameter, to form the small veins, which in turn fuse to form the large veins. The deoxygenated blood flows back to the right heart which pumps the deoxygenated blood back to the lung.

The effect of breathing are continuously monitored by chemoreceptors, which detect changes in O_2 and CO_2 partial pressures, and by mechanoreceptors, which survey changes in thoracic mechanics. The activity of these receptors allows ventilation to be adjusted automatically so that arterial blood gases are kept within acceptable limits despite changing internal and external conditions. The overall control of blood circulation is the responsibility of a population of neurons in the central nervous system, for simplicity called 'centres'. On the basis of their locations the centres involved in circulatory regulation are designated as medullary, hypothalamic and cortical. These centres are fully described by Thews and Vaupel, 1985.

In developing the mathematical model, the human respiratory system described above can be divided into three categories. These categories are mechanics of breathing, gas exchange process and control of breathing and blood circulation. Following sections describe the model development for these categories.

4.3 SIMULATING THE MECHANICS OF BREATHING

The ventilation of the alveoli required for gas exchange is brought about by a rhythmic alternation

of inspiration (breathing in) and expiration (breathing out). Each inspiration draws fresh air, rich in oxygen, through the passageways into the alveolar space, and each expiration expels oxygen-poor air charged with carbon dioxide through the same passageways into the surrounding. The air movements during inspiration and expiration result from the rhythmic alternation between expansion and diminution of the thoracic cavity. The mathematical models described below are developed to simulate such a breathing process.

4.3.1 Model of nose and mouth

The nasal passage (nose) is the natural path for air flow into and out of the lung during quiet breathing, and is largely responsible for filtering, warming and humidifying the inspired air. The resistance of the nasal passages is very high; it may comprise 50% of the total airway resistance during quiet nose breathing. The mouth accounts for about 25% of total airway resistance during quiet mouth breathing. However, these fractions may increase at increased levels of ventilation, such as those encountered during exercise.

The law relating pressure drop and flow rate for the nasal passageway and mouth is far from linear (Sullivan and Chang, 1990), being dependent on gas velocity, density and viscosity, in addition to the internal geometry, including skin friction losses and losses due to changes in flow direction. The experimental pressure loss against Reynolds number relationships for an average adult at three primary parts of the respiratory flow system are shown in figure 4.2; the nasal passage, the mouth to alveoli, and the central airways. The dimensionless relationships shown in figure 4.2 have the advantage of being valid for different breathing gases and densities. Using the data in figure 4.2 leads to the following two relationships between the pressure loss and Reynolds number associated with the nose and mouth:

i) Nose

$$\frac{\delta p}{\frac{1}{2}\rho v_n^2} = 0.05 \left[1 + \left(1000 + \frac{10^6}{Re_n} \right) \right] \tag{4.1}$$

i) Mouth

$$\frac{\delta p}{\frac{1}{2}\rho v_m^2} = 0.01 \left[1 + \left(1000 + \frac{10^6}{Re_m} \right) \right] \tag{4.2}$$

where $Re_n = \rho v_n \bar{d} / \mu$ and $Re_m = \rho v_m \bar{d} / \mu$. Note that $\bar{d}$ is the reference diameter (ie. 22.5 mm) which is defined

116

in the experiment conducted by Sullivan and Chang (1990). In this way, the results can be compared

directly in which the reference diameter is used as a characteristic dimension. Rearranging equation (4.1)

and (4.2), the mass flow rates through the nose and mouth are given by

$$q_n = \frac{A_n}{100.1} \left[\sqrt{\left(\frac{50000\mu}{d}\right)^2 + 400.4\rho\delta p} - \frac{50000\mu}{d} \right] \qquad (4.3)$$

$$q_m = \frac{A_m}{20.02} \left[\sqrt{\left(\frac{10000\mu}{d}\right)^2 + 80.08\rho\delta p} - \frac{10000\mu}{d} \right] \qquad (4.4)$$

The models of nose and mouth are acting in parallel. It is a straight forward matter to switch from normal

nasal breathing to mouth breathing, as occurs in heavy exercise or when using breathing equipment.

4.3.2 Model of tracheobronchial tree (trachea and respiratory passageways)

In order to simplify the model, the tracheobronchial tree, extending from the nasal passageway to

the alveolar compartment, has been divided into three distinct regions (figure 4.3): the extrathoracic zone,

the intrathoracic extrapulmonary zone and intrathoracic intrapulmonary zone. A uniform (but time-varying)

pressure is assumed to exist in each zone, allowing lumped parameter theory described in chapter 2 to be

used in the model. According to the models developed by Tomlinson (1994), isothermal conditions are

assumed to apply such that the temperature of the gas is considered to remain constant at all point

throughout the system.

(i) Extrathoracic zone

The extrathoracic zone includes the downstream side of the nasal passageway and extends to the

trachea. The rate of change of extrathoracic pressure P_{et} is dependent on the net flow rate from the nose,

mouth and extrapulmonary zone, and is given by

$$\frac{dP_{et}}{dt} = \frac{RT}{V_{et}} (q_n + q_m - q_{ep}) \qquad (4.5)$$

(ii) Intrathoracic extrapulmonary zone

The intrathoracic extrapulmonary airflow passageways are considered to be elastic walls, which

117

distend under the transmural (differential) pressure between the air passage and pleural compartments. The air passage pressure taken as the mean of intrathoracic and extrathoracic pressures, acts to open the airway. Pleural pressure acts on the other side of the wall, tending to close the airway. The flow rate is derived for a variable area orifice (figure 4.4) representing one passageway in the tracheobronchial tree. The smooth muscle surrounding the passageway is idealized as a mass-spring damper system acted on by the transmural force outlined above. It is assumed that the nominal displacement of a single airway, $x_{nom,ai}$, is the radius of a single airway when the transmural pressure is zero (Hyatt, 1958, Denison, 1981 and Lamdet, 1982). Hence, the full dynamic equation for the force acting on the wall of a single airway is given by

$$Me_{wl}\frac{d^2x_{ai}}{dt^2} = \left[\left(\frac{P_{et}+P_{it}}{2}\right) - P_{pl}\right]A_{wl} - f\frac{dx_{ai}}{dt} - k_{wl}(x_{ai} - x_{nom,ai}) \tag{4.6}$$

Successive integration of acceleration d^2x_{ai}/dt^2 in equation (4.6) gives the velocity dx_{ai}/dt and displacement x_{ai} of a single airway, respectively. The effective flow area of the airways is thus determined:

$$A_{ai} = N_a \pi x_{ai}^2 \tag{4.7}$$

The small airways are the site of insertion of the elastic and collagen fibres which contribute to the elastic recoil of the lung. The fibres exert traction on the walls of the airways and so help to maintain their shape; for this reason the function of the fibres has been compared to that of the guy lines of a tent. During a force expiration the volume of the lung decreases; the traction which is exerted by the guy lines then diminishes and the nominal displacement of the airway $x_{nom,ai}$ is reduced in consequence. This process leads to the static closure of the airways (Cotes, 1979). Hence, the static decrease of airway nominal displacement needs to be accounted for and is assumed to have linear relation with the lung volume:

$$x_{nom,ai} = \hat{x}_{ai} (V_l - V_{el}) / (V_{tlc} - V_{el}) \tag{4.8}$$

where $\hat{x}_{ai}$ is the maximum nominal displacement of a single airway when traction is not applied. However, during quiet breathing the airways are essentially tethered to the parenchymal lung tissue; the traction pulls outward on the airways and helps to keep them open. Hence, the expression to determine the airway nominal displacement during quiet breathing is given by

$$x_{nom,ai} = x_{add,ai} + \hat{x}_{ai} (V_l - V_{el}) / (V_{tlc} - V_{el}) \tag{4.9}$$

Using the data in figure 4.2 again, the relationship between the pressure loss and the Reynolds number (ie. $Re_a = \rho v_a \tilde{d} / \mu$) associated with the airways in the extrapulmonary zone can be obtained as

$$\frac{\delta p}{\frac{1}{2}\rho v_a^2} = 0.002 \left[1 + \left(1000 + \frac{10^6}{Re_a} \right) \right]$$

(4.10)

Rearranging equation (4.10), the mass flow rate through the intrathoracic extrapulmonary zone is given by

$$q_{ep} = \frac{A_{ai}}{4.004} \left[\sqrt{\left(\frac{2000\mu}{\tilde{d}} \right)^2 + 16.016\rho\delta p} - \frac{2000\mu}{\tilde{d}} \right]$$

(4.11)

Similar to the extrathoracic zone, the rate of change of intrathoracic extrapulmonary pressure P_{it} is dependent on the net flow rates from extrapulmonary and intrapulmonary zones and is given by

$$\frac{dP_{it}}{dt} = \frac{RT}{V_{it}} (q_{ep} - q_{ip})$$

(4.12)

(iii) Intrathoracic intrapulmonary zone

The region close to the alveolar compartment is termed the intrapulmonary zone. The order of magnitude of the velocity of flow and the Reynolds number at this part of the airways are very small as the flow area is large (Bennett and Elliott, 1982 and Fung, 1990). It is reasonable to assume that the flow in this part of airways is purely laminar (Tomlinson, 1994) and the mass flow rate is given by

$$q_{ip} = \bar{\rho} (P_{it} - P_{al}) \mathcal{H}_{ip}$$

(4.13)

where $\bar{\rho}$ is the mean density (ie. $= (P_{it} + P_{al})/(2RT)$). The flow gradient $\mathcal{H}_{ip}$ takes into account the pertinent characteristic of the airways: length, diameter, number of parallel passages, roughness of wall, etc.

4.3.3 Model of lung

Over 300 years ago, an Oxford physiologist John Mayow constructed a mechanical model of the lung using a bladder inside a pair of bellows. This was the first attempt to understand the lung as a mechanical device into which air flowed. Modern researchers have extended Mayow's original concept. The lungs have been likened to "a pair of bellows with an elastic recoil mechanism furnished by a spring" (Keele, Noil and Joels, 1982). The concept of a moving piston forms the basis of the lung model to account for the motion and gas flow processes associated with the lungs (Tomlinson, 1994). The operation of the

119

lung is idealized as a linear piston of area A_l (figure 4.5) with spring and viscous resistance effects. The motion of the piston is considered to be along the actuator axis (at approximately 90 degrees to the spinal column) and may be inclined at any angle, depending on the orientation of the human. The piston is acted on by a number of forces and is idealized as a point mass attached to the human by a spring. One side of the piston is subjected to alveolar pressure, which acts to expand the lung, and the other side is acted on by intrapleural pressure, which acts to deflate the lung. Hence, the equation of motion of the lung wall can be written as

$$Me_l \frac{d^2 x_l}{dt^2} = (P_{al} - P_{pl}) A_l - f \frac{dx_l}{dt} - k_l (x_l - x_{nom,l})$$ (4.14)

Successive integration of acceleration $d^2 x_l / dt^2$ in equation (4.14) gives the velocity dx_l / dt and displacement x_l of the lung face, respectively.

The stiffness (or elastance), k_l (inverse of compliance) of the lung varies considerably over the working range of the lung, from residual volume to total lung capacity (Bennett and Elliott, 1982). Figure 4.6 shows the variation of lung volume with the transmural (differential) pressure between the alveolar and pleural compartments (marked L), and the pleural compartment and the atmosphere (marked W) of a normal healthy human. The gradients of these graphs are proportional to compliance of the lung or chest wall and the reciprocals are the respective elastances. Hence, a relationship between the lung elastance $\Delta P_l / \Delta V_l$ and the lung volume V_l can be obtained (see figure 4.7(a)). Since stiffness is defined as the ratio of the rate of change of force with respect to displacement, $\Delta F_l / \Delta x_l$, it is related to elastance $\Delta P_l / \Delta V_l$ by

$$k_l = \frac{\Delta F_l}{\Delta x_l} = \frac{A_l \Delta P_l}{\Delta V_l / A_l} = A_l^2 \frac{\Delta P_l}{\Delta V_l}$$ (4.15)

When the spring force due to the lung (acting on the pleural compartment) is exactly balanced by the pressure force, the lung is at the rest position. Since the lung volume at the rest position is defined as the functional residual capacity (FRC) (Bennett and Elliott, 1982), the lung displacement, $x_{rest,l}$, at rest is given by

$$x_{rest,l} = \frac{V_{frc}}{A_l}$$ (4.16)

At this condition, alveolar pressure is equal to atmospheric pressure, and air flow from the lung is zero.

At FRC, the intrapleural pressure P_{pl} is sub-atmospheric (Bulfour Slonim and Hamilton, 1987), with a typical value taken as -5 cm water.

It is necessary to define the nominal displacement of the lung face, $x_{nom,l}$, at which the net force acting on the lung is zero. In steady state, equation (4.14) can be written as

$$k_l \ (x_l - x_{nom,l}) = (P_{al} - P_{pl}) \ A_l \qquad (4.17)$$

Now at FRC, $P_{al}-P_{pl} = 5$ cm water $= P_{5cm}$. Substituting in equation (4.17) for x_l and $P_{al}-P_{pl}$ we obtain

$$k_l \ (x_{rest,l} - x_{nom,l}) = P_{5cm} \ A_l \qquad (4.18)$$

Therefore:

$$x_{nom,l} = x_{rest,l} - \frac{P_{5cm} A_l}{k_l} \qquad (4.19)$$

The observations of the motion of breathing indicate that the lung effective area acted on by the forces varies considerably at some operational ranges, especially, in the small lung volume region. A linear relationship is assumed between the effective area and the lung volume:

$$A_l = \hat{A}_l - (\hat{A}_l - \check{A}_l) \frac{(V_l - V_{frc})}{(V_{lrv} - V_{frc})} \qquad (4.20)$$

but for $V_l > V_{frc}$

$$A_l = \hat{A}_l \qquad (4.21)$$

The lung is regarded as a control volume V_l varying with time during the breathing process and the variation in lung volume can be evaluated using

$$\frac{dV_l}{dt} = A_l \frac{dx_l}{dt} \qquad (4.22)$$

The analysis of alveolar pressure needs to consider all the individual gas exchanged inside the alveolar compartment (ie. O_2, CO_2 and inert gas exchange). Hence, the rate of change of alveolar pressure is given by

$$\frac{dP_{al}}{dt} = \frac{RT}{V_l} \left(q_{ip} - \rho_l \frac{dV_l}{dt} + \sum q_{ex,l} \right) \qquad (4.23)$$

121

In equation (4.23), the individual gas mass flow rate through the alveolar membrane can be obtained by

$$q_{exc,i} = \left(\frac{P_{1.013} M_i}{R_o T_{273}} \right) Q_{exc,i}$$

(4.24)

where $Q_{exc,i}$ is the individual gas volumetric flow rate through the alveolar membrane corrected to standard conditions (STPD).

3.3.4 Model of pleural compartment

The pleural compartment plays a vital role in respiration. Forces are generated in the intercostal muscles acting on the ribcage and the diaphragm due to the neurogenic messages sent by the brain. During quiet breathing, this process is involuntary but can be overridden, such as when a person fully inspires or expires. The force generated by the intercostal muscles and diaphragm creates the pleural pressure that drives lung motion.

The pleural compartment can be modelled on similar lines to that of the lung, with two notable differences. First, there is no flow of gas into and out of the pleural compartment, and second, the compartment is filled with liquid and tissue rather than gas as in the lung. The face of the pleural compartment is idealized as a plane piston of area A_{pl}, which moves under the action of the forces generated by the ribcage and diaphragm, pleural pressure, and ambient pressure. The motion of the pleural compartment face is considered to be along the same axis as the lung (90 degrees to the spinal column). The faces of the pleural compartment are subjected to pleural pressure and ambient pressure P_{am}, which together with the intercostal and diaphragm thoracic forces act to change the compartment volume. Hence, the equation of motion of the pleural wall is

$$Me_{pl} \frac{d^2 x_{pl}}{dt^2} = F_{th} + (P_{pl} - P_{am}) A_{pl} - f \frac{dx_{pl}}{dt} - k_{pl}(x_{pl} - x_{nom,pl})$$

(4.25)

The thoracic force F_{th} is the net force generated by the ribcage and diaphragm due to the neurogenic control system. This force is idealized as acting at a single point on the face of the pleural compartment. In reality, it is far more complex, being the summation of the intercostal force generated by the ribcage and the diaphragm force. Equation (4.25) can be rearranged allowing successive integration of acceleration to give the velocity and displacement of the pleural wall.

The stiffness k_{pl} of the pleural compartment varies considerably over the range of lung movement from residual volume to total lung capacity (Bennett and Elliott, 1982). The variation in lung volume with the transmural pressure is shown in figure 4.6, the curve marked W representing the variation in chest wall transmural pressure, ΔP_{pl}, (the differential between pleural and ambient pressure). From this, the variation in $\Delta P_{pl} / \Delta V_l$ with lung volume shown in figure 4.7(b) is obtained. Similar to the lung, the stiffness k_{pl} can be determined using the same form of equation (4.15):

$$k_{pl} = A_{pl}^{2} \frac{\Delta P_{pl}}{\Delta V_l} \tag{4.26}$$

The pleural displacement $x_{nom,pl}$, at which the net force on the pleural compartment is zero, can be obtained using the same approach adopted for the lung model. The pleural displacement, $x_{rest,pl}$, at rest can be calculated according to the lung functional residual capacity and the pleural volume at rest position:

$$x_{rest,pl} = \frac{(V_{frc} + V_{rest,pl})}{A_{pl}} \tag{4.27}$$

Since at FRC, the intrapleural pressure P_{pl} is sub-atmospheric (ie. $P_{pl}-P_{am}$= -5 cm water= $-P_{5cm}$) and no thoracic force is applied, the steady state equation is given by

$$k_{pl} (x_{rest,pl} - x_{nom,pl}) = -P_{5cm} A_{pl} \tag{4.28}$$

Then

$$x_{nom,pl} = x_{rest,pl} + \frac{P_{5cm} A_{pl}}{k_{pl}} \tag{4.29}$$

As the pleural compartment is attached closely to the lung face, it is reasonable to assume that the effective area of pleural compartment A_{pl} is equal to the effective area of the lung A_l.

The pleural compartment is regarded as a closed control volume of trapped pleural fluid of volume V_{pl}. The pleural volume is compressed during inhalation increasing the pleural pressure, and expands during

exhalation, decreasing the pleural pressure. According to Tomlinson (1994), the rate of change of pleural volume is determined by the velocities of the pleural and lung faces:

$$\frac{dV_{pl}}{dt} = \frac{dx_{pl}}{dt} A_{pl} - \frac{dx_l}{dt} A_l \qquad (4.30)$$

and the rate of change of pleural pressure is given by

$$\frac{dP_{pl}}{dt} = \frac{B_{pl}}{V_{pl}} \left(\frac{dx_l}{dt} A_l - \frac{dx_{pl}}{dt} A_{pl} \right) \qquad (4.31)$$

4.4 SIMULATING THE GAS EXCHANGE PROCESS

Constituent gas flow takes place through three distinct mechanisms in the respiratory system. They are i) atmosphere to alveolar compartment, ii) diffusion across the alveolar membrane and iii) carriage of gas in the blood to and from the tissue. These effects are accounted for in the models of the nasal passageways, tracheobronchial tree, alveolar membrane, pulmonary vein and artery, heart, veins, arteries and tissue.

4.4.1 Constituent gas concentrations through nasal passageway to alveolar

The mass transfer rate of constituent 'i' from the nasal passageways to alveolar can be obtained by the continuity of mass equation described in section 2.3. In the case of the alveolar compartment the control volume is divided into two zones: one which allows gas diffusion and another which does not. The latter is termed the alveolar dead zone and the rate of change of gas constituents in this zone is given by:

$$\frac{dm_{Dalv,i}}{dt} = f_{dv} \left[q_{ip,in} \frac{m_{in,i}}{m_{in}} - q_{ip,out} \frac{m_{Dalv,i}}{m_{Dalv}} \right] \qquad (4.32)$$

where f_{dv} is the fraction of alveolar dead space V_{Dalv} to the tidal volume V_T (ie. $f_{dv}=V_{Dalv}/V_T$). In addition, the rate of change of gas constituents in the alveolar compartment which allows gas diffusion is given by

$$\frac{dm_{al,i}}{dt} = (1 - f_{dv}) \left[q_{ip,in} \frac{m_{in,i}}{m_{in}} - q_{ip,out} \frac{m_{al,i}}{m_{al}} \right] + q_{exc,i} \qquad (4.33)$$

It is common to distinguish between the alveolar dead space and the anatomical dead space V_{Danat}, comprising the volume of the respiratory passages, extending from the nostrils and mouth down to (but not

including) the alveoli. A more useful conceptual explanation may instead be attributed to the physiological dead space V_D which comprises all the parts of the respiratory tract in which there is no gas exchange:

$$V_D = V_{Dalv} + V_{Danat} \tag{4.34}$$

For $V_T \geq 0.875L$, $V_D = 0.2V_T$. Hence,

$$f_{dv} = 0.2 - \frac{V_{Danat}}{V_T} \tag{4.35}$$

For $V_T < 0.875L$, $V_D = V_{Danat} = 0.175L$ and by definition

$$f_{dv} = 0 \tag{4.36}$$

4.4.2 Diffusion of gases across alveolar membrane

Gas transfer through the alveolar capillary membrane depends on the gas tension gradient, the solubility of gas in the blood, the molecular weight of the gas, and the properties of membrane. This relationship is expressed by Fick's law (Fung, 1990):

$$J = -DA\frac{\Delta C}{\Delta l} \tag{4.37}$$

The diffusion conditions in the lung are excellent as the blood in the lung capillaries is separated from the alveolar spaces by only a thin sheet of tissue. The entire diffusion path Δl extends over a distance of the order of only 1 μm (Ganong, 1987).

The O_2 and CO_2 molecules diffuse over the same path but in opposite directions. In the pulmonary capillary bed (alveolar blood), haemoglobin is oxygenated at the same time that CO_2 is eliminated, see figure 4.8. In a resting individual the red blood cells remain within the pulmonary capillary for only about 0.75 second, which imposes a limit on the time available for gas transfer. However, this contact time is still sufficient to adjust the gas partial pressures in the blood almost entirely to the alveolar compartment values (Thews and Vaupel, 1985) (see figure 4.9). Even when blood flow is increased during exercise in which the contact time is reduced to one third of normal (approximately 0.25 second), the partial pressure of O_2 in blood will still become equal to that in the alveoli before the end of the capillary is reached (Berne and Levy, 1988). The diffusion resistance presented by the alveolar membrane to CO_2 is about 23 times smaller

than that to O_2; that is, other conditions being equal, 23 times as much CO_2 as O_2 diffuses through a given layer. This means that in the lung of a healthy person the partial pressure of CO_2 in the pulmonary capillary bed becomes practically identical to those in the alveoli.

For inert gas, it is known that approximately 0.01 second is required for dissolving inert gas molecules through the alveolar membrane into the pulmonary capillary bed. Therefore, it is quite certain that the blood leaving the pulmonary bed is fully equilibrated with the inert gas pressure in the alveoli as well.

Using equation (2.31), the individual gas partial pressures inside the alveolar can be obtained. Hence, the individual gas concentrations in the alveolar blood can be calculated using Henry-Dalton law:

$$C_i = So_{b_i} P_i \tag{4.38}$$

The proportionality factor So is called the solubility coefficient, its magnitude depends on the nature of the dissolved gas and the properties of the solvent. However, the relationship between P_{O_2} and O_2 concentration in the blood is not linear as in equation (4.38), but is sigmoid in shape (see figure 4.10). The O_2 dissociation curve is shifted to the right by an increase in temperature, a rise in the CO_2 tension, or a decrease in pH (termed the Bohr shift). Therefore, at any given partial pressure of O_2, haemoglobin is less saturated with oxygen. The CO_2 dissociation curve relating the CO_2 content of the blood to P_{CO_2} is shown in figure 4.11. The relationship between CO_2 content and P_{CO_2} in the blood is not linear as well. The total quantity of CO_2 in the blood is more than twice that of O_2. The degree of oxygenated blood affects the CO_2 dissociation curve. The greater the saturation of haemoglobin with O_2, the less will be the CO_2 content for a given P_{CO_2}. This effect, called the Haldane effect, is caused by the greater ability of reduced haemoglobin to buffer H^+ ions and to form carbamino haemoglobin. According to the relations in figures 4.10 and 4.11, the CO_2 and O_2 dissociation curves can be represented in the following form adopted by Grodins (1967) with the Haldane and Bohr effects included:

$$C_{CO_2} = 0.5384(1 - e^{-0.0289 P_{co_i}}) + 0.1891 - (0.1891 - 0.125) C_{O_2} / \hat{C}_{O_2} \tag{4.39}$$

$$C_{O_2} = \hat{C}_{O_2}(1 - e^{-1.02 \eta P_{o_i}})^2 \tag{4.40}$$

The variable η in equation (4.40) is given by

$$\eta = 0.44921pH - 0.10098pH^2 + 0.0066815pH^3 - 0.454 \qquad (4.41)$$

where

$$pH = 9 - \log_{10}C_{H^+}$$

$$C_{H^+} = 795\left[\frac{0.51P_{co_2}/760}{C_{co_2} - 0.51P_{co_2}/760}\right] \qquad (4.42)$$

Note that the units of P_{o_2} and P_{co_2} are mmHg. It can be seen that equations (4.39) to (4.42) cannot be solved explicitly for the desired variables C_{o_2} and C_{co_2}. Hence, it is necessary to use an iteration procedure to obtain the solutions.

The volumes of individual gases that are exchanged in the alveolar can be calculated from the difference in the amount of gas in the blood flowing into and out of the alveolar:

$$Q_{exc,i} = Q_{b,al}(C_{pa,i} - C_{al,i}) \qquad (4.43)$$

where $C_{pa,i}$ is the concentration of individual gases from the pulmonary artery and $C_{al,i}$ is the concentration of individual gases in the alveolar blood.

4.4.3 Carriage of constituent gases through blood vessels

The transient variations in concentration of gas 'i' inside the blood vessel (ie. artery, vein and capillary) can be determined using the following mass balance equation:

$$\frac{dC_i}{dt} = \frac{Q_{b,in}C_{in,i} - Q_{b,out}C_i}{V_b} \qquad (4.44)$$

where V_b is the volume of blood inside the vessel.

A certain proportion of blood flowing from the pulmonary artery is shunted to the pulmonary vein without gas exchange taking place in the alveolar. This is termed the 'veno-arterial shunts' (Thews and Vaupel, 1985), f_{sh}. Hence, the concentration of gas flowing into the pulmonary vein is

$$C_{pv,i} = (1 - f_{sh})C_{al,i} + f_{sh}C_{pa,i} \qquad (4.45)$$

127

4.4.4 Metabolic process in tissue and brain compartment

The amount of energy obtained by metabolic processes depends on the nature of the foodstuffs that are broken down (carbohydrates, proteins, fats). For example, complete oxidation of glucose is described by the overall reaction

$$C_6H_{12}O_6 + 6O_2 \rightleftharpoons 6CO_2 + 6H_2O + \Delta E$$
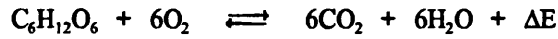
Under physiological condition, ΔE, the free energy (free enthalpy) has a value of 683kcal/mol (2.86 MJ/mol). An indication of the types of foodstuffs involved in metabolic processes is given by the respiratory quotient RQ:

$$RQ = \frac{CO_2 \ output}{O_2 \ intake} = \frac{\dot{V}_{CO2}}{\dot{V}_{O2}} \tag{4.46}$$

In oxidation of glucose and other carbohydrates the number of moles of CO_2 formed is equal to the number of moles of O_2 consumed, so that $RQ = 1.0$. The RQ for protein breakdown is 0.8, and for fat breakdown it is 0.7. In a normal individual at rest or during light work under ordinary conditions, $\dot{V}_{CO2}$ will possibly be about 0.8 of $\dot{V}_{O2}$. During very prolonged exertion, or in work done without normal recent food intake, RQ may drop towards 0.7. In many instances it is sufficiently accurate to assume that $RQ = 0.8$.

The O_2 consumption of a person under rest conditions - that is, in the absence of special physical exertion - averages 0.265 L/min. During the performance of work more oxygen is required, depending on the amount of physical effort involved. For general orientation, table 4.1 lists the O_2 consumption rate of men doing work requiring various amounts of exertion. As has been mentioned, O_2 uptake rises as work load increases. During light work O_2 uptake rises slowly in parallel with the increase in blood flow through the muscle (figure 4.12) and after 3-5 min it reaches a constant level. Referring to figure 4.12, at the beginning of the work session the O_2 uptake does not correspond to the energy requirement of the working musculature, which bridges this gap by drawing on anaerobic energy sources. The amount by which the volume of O_2 uptake fails to reach the initial O_2 requirement (shaded area in figure 4.12) is called the oxygen debt. When work is stopped, the O_2 uptake returns slowly to the initial level (repayment of the oxygen debt). According to figure 4.12, an arbitrary time constant (first order lag) can be assigned to the response of actual oxygen consumption rate in the tissue:

$$\frac{d\dot{V}_{O2,ti}}{dt} = \frac{\dot{V}_{O2,ti,dem} - \dot{V}_{O2,ti}}{\tau_m} \tag{4.47}$$

Knowing the O_2 consumption and CO_2 production rates in the tissue, the corresponding rate of change of O_2 and CO_2 concentration in the tissue, in relation to the inlet and outlet flow, can be determined from

$$\frac{dC_{ti,O2}}{dt} = \frac{Q_{b,in}C_{in,O2} - Q_{b,out}C_{ti,O2} - \dot{V}_{O2,ti}}{V_{ti}} \tag{4.48}$$

$$\frac{dC_{ti,CO2}}{dt} = \frac{Q_{b,in}C_{in,CO2} - Q_{b,out}C_{ti,CO2} + \dot{V}_{CO2,ti}}{V_{ti}} \tag{4.49}$$

In the case of brain, the rates of change of O_2 and CO_2 concentration are given by

$$\frac{dC_{B,O2}}{dt} = \frac{Q_{b,in}C_{in,O2} - Q_{b,out}C_{B,O2} - \dot{V}_{O2,B}}{V_B} \tag{4.50}$$

$$\frac{dC_{B,CO2}}{dt} = \frac{Q_{b,in}C_{in,CO2} - Q_{b,out}C_{B,CO2} + \dot{V}_{CO2,B}}{V_B} \tag{4.51}$$

Note that the sum of $\dot{V}_{O2,ti}$ and $\dot{V}_{O2,B}$ is the overall the O_2 consumption rate. The average O_2 consumption rate in the brain is 0.05 L/min (Thews and Vaupel, 1985).

4.4.5 Circulation of blood

The blood vessels together form a closed system of tubes within which the blood - driven by the heart -circulates. The output of the heart per unit time is the cardiac output $Q_{b,H}$. From the left ventricle, blood is pumped through the arteries and arterioles to the tissue and brain. This is 'major (systemic) circulation'. From the right atrium, blood flows to the right ventricle, which pumps it through the vessels of the lung - the lesser (pulmonary) circulation. The cardiac output of both systemic and pulmonary circulations are the same. It is apparent that the increase in cardiac output is observed during the performance of work and table 4.2 illustrates the change in cardiac output with exercise.

The structure of the blood vessels is such that their walls are somewhat stretchable, so that their diameter can vary depending on the momentary internal pressure. To a first approximation, however, a general idea of the way blood flows in the circulation system can be obtained by considering the rules that

govern flow in rigid tubes. The driving force for the flow of a fluid is a pressure gradient, which serves to overcome the resistance to flow. In this case the volumetric flow rate is proportional to the pressure difference between the beginning and end of the tube:

$$Q_b = \delta p \ / \ R_f \tag{4.52}$$

In this relation, analogous to Ohm's law, R_f represents the resistance to flow. The most resistance vessels in the circulation system are the arterioles. Because of their small diameters they account for almost 50% of the total resistance of the circulation. The capillaries contribute only about 25% of the total resistance of the system. Although each individual capillary presents more resistance per unit length than an individual arteriole, the contribution of the capillaries is smaller because the capillaries are shorter and there are greater numbers of them in parallel. The total resistance of the systemic circulation which is called the total peripheral resistance (TPR) is derived from all the series and parallel resistance of the various parts of the system. For the pulmonary circulation, the total resistance is about one-tenth of the TPR. The distribution of resistance mentioned above causes the pressure in the cardiovascular system to change according to the curve shown in figure 4.13.

The change in pressure in blood vessels can be obtained by solving the continuity differential equation:

$$\frac{dP_b}{dt} = \frac{B_b}{V_b} \ (\ Q_{b,in} - Q_{b,out} \ ) \tag{4.53}$$

Since the cardiac output has not considered the pulsation effect of the actual blood flow, the blood pressure P_b in the circulation system is representing the mean pressure inside the blood vessel.

4.5 SIMULATING THE CONTROLS OF RESPIRATION AND BLOOD CIRCULATION

Respiration has an automatic type of regulatory system which is housed in the brainstem. It responds to a whole variety of information about activity and environment from mechanoreceptor and chemoreceptor and reflexly adjusts breathing to best provide for a person's needs. It works completely without human conscious intervention during sleep, while under anaesthesia, or while awake but not thinking about breathing.

130

The overall control of blood circulation is the responsibility of the populations of neurons in the central nervous system, for simplicity called 'centres'. These centres (with their checks and balances) are responsible for the alteration of blood distribution necessary to meet the changing requirements of different tissues in response to a wide spectrum of physiological and pathological conditions.

In developing the mathematical model, the human respiratory system is presented in conventional control system terms with its two major components of controlled system and controller. The model adopted for the controlled systems (respiratory and blood circulation systems) have been illustrated in the previous sections. The form of the controllers for the regulation of breathing and blood circulation are described below.

4.5.1 Mechanical control of breathing

Two separate neural mechanisms regulate the mechanical movement of breathing. One is responsible for voluntary control and the other for automatic control. The voluntary activities in breathing which include speaking, clearing throats, breath holding and forced expiration and inspiration can override the automatic control of breathing. The voluntary control system is located in the cerebral cortex and sends impulses to the respiratory motor neurons via the corticospinal tracts. The automatic control system is located in the pons and medulla, and the output from this system to the respiratory motor neurons is located in the lateral and ventral portions of the spinal cord. Spontaneous respiration is produced by a rhythmic discharge of motor neurons that innervate the respiratory muscles at the pleural compartment to generate thoracic force. In addition, 'stretch receptors' in the lung parenchyma convert the stretching stimulus (which relates to the lung volume) into a burst of nerve impulses, which provide a feedback signal to the respiratory centres.

Initially, it is assumed that the combination of proportional and integral control actions can be used to define the required thoracic force to drive the lung in demand motion for both voluntary and automatic control. The equation of the controller with this combined action is given by

$$F_{th} = G_P(V_{l,dem} - V_l) + G_I \int_0^t (V_{l,dem} - V_l)\, dt \qquad (4.54)$$

Note that $V_{l,dem}$ is the demand lung volume at the end of inspiration or expiration period (ie. $V_{l,dem} = V_T + V_{frc}$ during inspiration and $V_{l,dem} = V_{frc}$ during expiration).

131

4.5.2 Chemical control of breathing

The chemical control system, which is an automatic control action, serves to maintain homeostasis and to guarantee the adjustment of respiration to the overall metabolic rate. Here the controlled variables are the CO_2 partial pressure and the O_2 partial pressure in the brain arterial blood. Elevation of the arterial P_{CO2} increases the lung ventilation $\dot{V}_r$. Figure 4.14, obtained from Bulfour Slonim and Hamilton (1987), shows the relationships of ventilation and arterial P_{CO2}. This figure also shows that at a given P_{CO2}, ventilation increases in a hyperbolic fashion as the arterial P_{O2} is reduced. It is possible to increase ventilation by increasing the tidal volume V_T or decreasing the total breath duration t_{cy} since $\dot{V}_r = V_T/t_{cy}$. Obviously, the variation of total breath duration t_{cy} is due to a variation of both of its two components, inspiratory and expiratory times, t_{inp} and t_{exp}. Variation within tidal volume and inspiratory and expiratory times are positively correlated (Cunningham and Gardner, 1977) and the findings from the average human subject is summarised in figure 4.15 which shows mean V_T plotted against mean t_{inp} to the right and against t_{exp} to the left of a common origin. It is seen how t_{inp} changes relatively little over a wide range of ventilation rates, where the decrease in t_{cy} is thus due predominantly to a shortening of t_{exp}, roughly hyperbolic in relation to V_T. At high ventilation a breakpoint is seen, above which both t_{inp} and t_{exp} decrease as V_T increases further. Cunningham (1977), Garden (1977), Murray-Smith (1988) and Sarhan (1987) have mathematically defined the chemical controllers according to the data similar to that shown in figures 4.14 and 4.15. The form of the controllers are given as follow:

Inspiratory flow controller

$$\frac{V_T}{t_{inp}} = 0.062 \left(1 + \frac{23.2}{P_{a,O2}-30}\right)(P_{a,CO2} - 35.2) \tag{4.55}$$

(for $P_{a,CO2} > 38$ mmHg)

$$\frac{V_T}{t_{inp}} = 0.062 \left(1 + \frac{23.2}{P_{a,O2}-30}\right)(2.8) \tag{4.56}$$

(for $P_{a,CO2} \leq 38$ mmHg)

Inspiratory time controller

$$t_{inp} = 1.29 - 0.07\ V_T \tag{4.57}$$

(for $V_T < 2.08$ L)

$$t_{inp} = \frac{0.65}{V_T - 0.88} + 0.59 \tag{4.58}$$

(for $V_T \geq 2.08$ L)

Expiratory time controller

$$t_{exp} = 0.67 \, t_{inp} + \frac{11.1}{(0.62/0.062)(V_T/t_{inp}) + 2.73}$$ (4.59)

Hence, the tidal volume is evaluated from

$$V_T = (V_T/t_{inp}) \, t_{inp}$$ (4.60)

where V_T/t_{inp} is taken from equation (4.55) or (4.56) and t_{inp} from equation (4.57) or (4.58), and the total time for one respiratory cycle is

$$t_{cy} = t_{inp} + t_{exp}$$ (4.61)

Therefore, the respiratory frequency and lung ventilation rate are given by

$$N_b = \frac{60}{t_{cy}} \quad breaths/min$$ (4.62)

$$\dot{V}_r = N_b \, V_T \quad L/min$$ (4.63)

Note that the partial pressures of O_2 and CO_2 from the artery, $P_{a,O2}$ and $P_{a,CO2}$ in equations (4.55) and (4.56), can be obtained by rearranging equations (4.41) and (4.42), since the concentration of O_2 and CO_2 in the artery blood can be evaluated from the mass balance equations.

4.5.3 Regulation of breathing during exercise

Simulation of the dynamics of the respiratory system in response to exercise provides a means of examining competing hypotheses concerning the interaction of the neurogenic and chemical components of the respiratory drive. As ventilation increases in exercise, changes in the breathing pattern are expected to occur, through changes in tidal volume and in t_{inp} and t_{exp}.

Sarhan (1987) has performed several simulations with the control structure exactly as described in the previous section. Some mismatch was revealed between the model response and real data indicating the need for modification of the controller. In reality, the increased ventilation during exercise cannot be ascribed exclusively to the action of the chemical drives. There is considerable evidence of a 'central co-innervation' to the respiratory centres by the motor centres, especially when the work is just beginning. As

133

work continues, additional neuronal feedback from the working musculature and moving joints influences respiration. Sarhan has considered two hypotheses for these effects:

i) Multiplicative interaction between the neurogenic and chemical components - increasing the gain of the inspiratory flow controller (ie. the parameter 0.062 in equation (4.55)) whilst keeping the threshold constant (ie. the parameter 35.2 in equation (4.55)). This corresponds to increasing the slope of the $\dot{V}_T$ versus CO_2 characteristic (see figure 4.16(a)).

ii) Additive interaction - decreasing the threshold in the inspiratory flow controller (ie. the parameter 35.2), keeping the gain constant (ie. the parameter 0.062); that is, shifting the $\dot{V}_T$ versus CO_2 characteristic to the left (see figure 4.16(b)).

In the simulations of both hypotheses, the variation in the parameter defining gain (ie. 0.062) and the threshold (ie. 35.2) was assumed proportional to the level of overall O_2 consumption $\dot{V}_{O2,to}$:

$$Gain = 0.062 \left(\frac{\dot{V}_{O2,to}}{0.265} \right) \qquad (4.64)$$

$$Threshold = 35.2 \frac{(3.5 - \dot{V}_{O2,to})}{(3.5 - 0.265)} \qquad (4.65)$$

Note that the overall O_2 consumption rate $\dot{V}_{O2,to}$ is the sum of $\dot{V}_{O2,ti}$ and $\dot{V}_{O2,B}$. According to Sarhan, the results obtained, assuming additive interaction between CO_2 chemical drive and exercise neurogenic drive, are physiologically plausible. Hence, the inspiratory flow controller including the effect of exercise becomes

$$\frac{V_T}{t_{imp}} = 0.062 \left(1 + \frac{23.2}{P_{a,O2}-30} \right) \left[P_{a,CO2} - 35.2 \frac{(3.5 - \dot{V}_{O2,to})}{(3.5 - 0.265)} \right] \qquad (4.66)$$

(for $P_{a,CO2} > 38$ mmHg)

$$\frac{V_T}{t_{imp}} = 0.062 \left(1 + \frac{23.2}{P_{a,O2}-30} \right) \left[38 - 35.2 \frac{(3.5 - \dot{V}_{O2,to})}{(3.5 - 0.265)} \right] \qquad (4.67)$$

(for $P_{a,CO2} \leq 38$ mmHg)

134

4.5.4 Control of blood circulation

While regional regulatory mechanisms are matching the blood flow through individual organs to the demands of the moment, supra-regional control processes simultaneously ensure that all cardiovascular functions are adjusted to changes in the circulatory situation. Particular aspects of this global task are the control of an adequate cardiac output, ensuring that the perfusion for each organ is sufficient. Activation of the peripheral chemoreceptors by hypoxia (decreased P_{O2}) or of the central chemosensitive structures by hypercapnia (increased P_{CO2}) can affect cardiac output to some degree. According to Asmussen (1943) and Scarborough (1951), the response of cardiac output is given by

$$\dot{Q}_{b,H} = (\ Q_{b,H,nom} + \Delta Q_{b,H,O2} + \Delta Q_{b,H,CO2} - Q_{b,H}\ )\ /\ \tau_H \tag{4.68}$$

For $P_{a,O2} < 104$ mmHg

$$\Delta Q_{b,H,O2} = 9.6651 - 0.2885\,P_{a,O2} + 2.9241 \times 10^{-3}\,(P_{a,O2})^2 - 1.0033 \times 10^{-5}\,(P_{a,O2})^3$$

and for $P_{a,O2} \geq 104$ mmHg

$$\Delta Q_{b,H,O2} = 0$$

For $P_{a,CO2} < 40$ mmHg

$$\Delta Q_{b,H,CO2} = 0$$

for 40 mmHg $\leq P_{a,CO2} \leq 60$ mmHg

$$\Delta Q_{b,H,CO2} = 0.3\ (\ P_{a,CO2} - 40\ )$$

and for $P_{a,CO2} > 60$ mmHg

$$\Delta Q_{b,H,CO2} = 0$$

Note that $Q_{b,H,nom}$ is the normal cardiac output which increases with exercise. Table 4.2 illustrates the relationship between the cardiac output and exercise.

The regulation of blood flow in the brain is of special importance in the model due to the fact that the brain contains the control mechanism for the adjustment of respiration. In addition, the brain blood flow is also under the control of metabolic factors. An increase in P_{CO2} causes the brain blood vessel to expand,

and thus increases blood flow through the brain. The decrease of P_{O2} has the same effect. Using the information from the literature (Patterson, 1965), the responses of brain blood flow rate is given by

$$\dot{Q}_{b,B} = (Q_{b,B,nom} + \Delta Q_{b,B,O2} + \Delta Q_{b,B,CO2} - Q_{b,B}) / \tau_B \qquad (4.69)$$

For $P_{a,O2} < 104$ mmHg

$$\Delta Q_{b,B,O2} = 2.785 - 0.1323 P_{a,O2} + 2.6032 \times 10^{-3} (P_{a,O2})^2 - 2.324 \times 10^{-5} (P_{a,O2})^3 + 7.6559 \times 10^{-8} (P_{a,O2})^4$$

and for $P_{a,O2} \geq 104$ mmHg

$$\Delta Q_{b,B,O2} = 0$$

For $P_{a,CO2} < 38$ mmHg

$$\Delta Q_{b,B,CO2} = 2.323 \times 10^{-2} - 3.1073 \times 10^{-2} P_{a,CO2} + 8.0163 \times 10^{-4} (P_{a,CO2})^2$$

for 38 mmHg $\leq P_{a,CO2} \leq 44$ mmHg

$$\Delta Q_{b,B,CO2} = 0$$

and for $P_{a,CO2} > 44$ mmHg

$$\Delta Q_{b,B,CO2} = -15.58 + 0.76 P_{a,CO2} - 1.295 \times 10^{-2} (P_{a,CO2})^2 + 9.39 \times 10^{-5} (P_{a,CO2})^3 - 2.1745 \times 10^{-7} (P_{a,CO2})^4$$

Note that $Q_{b,B,nom}$ is the normal blood flow rate in the brain and is 15 % of normal cardiac output $Q_{b,H,nom}$.

4.6 CLOSURE

A physio-chemical approach involving the formulation in terms of mass balance equations, chemical buffering system, etc. has been used as a basis for the development of the human respiratory model. Thus, accurate models are formed, involving the complex interaction between lung and chest wall motion, airflow through the airways, gas exchange in alveolar and tissue, blood circulation and neurogenic control of breathing.

It is intended that the model will be used for assessing human interaction with different kinds of underwater breathing apparatus.

Work Effort	Breaths per minute	Tidal volume (L)	Ventilation rate (L/min)	O_2 uptaken rate (L/min STPD)
Rest	12	0.5	6	0.265
Light work	15	1.5	22.5	0.9
Moderate work	20	2	40	1.6
Heavy work	25	2	50	2
Hard work	25	2.5	62.5	2.5
Extremely hard work	30	2.5	75	3

Table 4.1 Measured O_2 uptaken rate and breathing characteristic associated with specific work efforts

Work (kg m/min)	O_2 uptaken rate (L/min STPD)	Cardiac output (L/min)
Rest	0.265	6.4
288	0.91	13.1
540	1.43	15.2
900	2.143	17.8
1260	3.007	20.9

Table 4.2 Changes in cardiac output with exercise
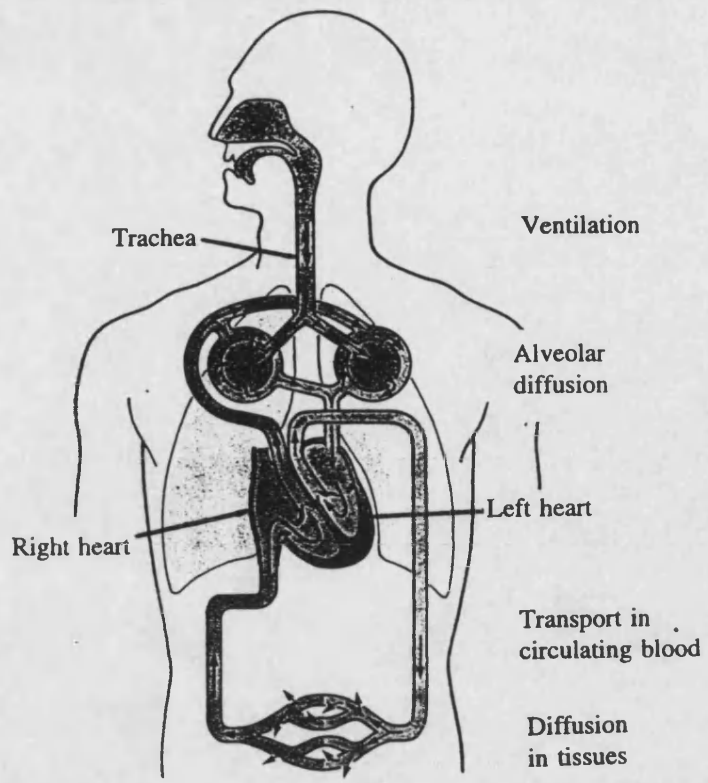
Figure 4.1 Human respiratory system
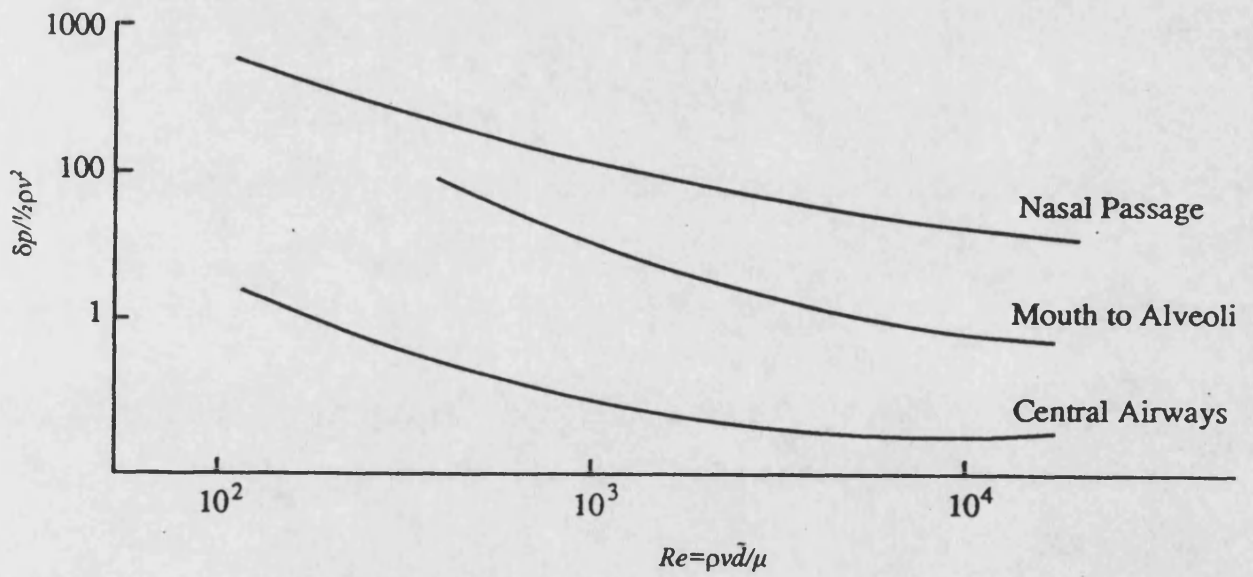
Figure 4.2 Dimensionless pressure losses within the nasal passages, mouth to alveoli and central airways

138
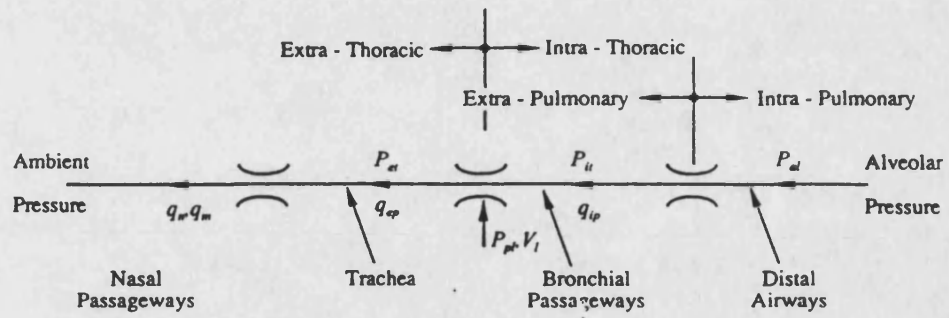
Figure 4.3 Division of tracheobronchial passageways
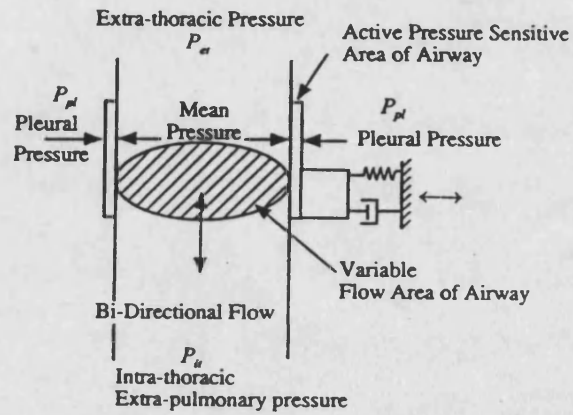
Figure 4.4 Variable flow area of a single tracheobronchial airway
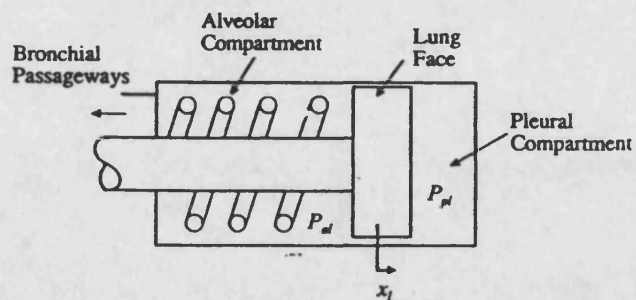
Figure 4.5 Motion of lung idealized as linear actuator

139
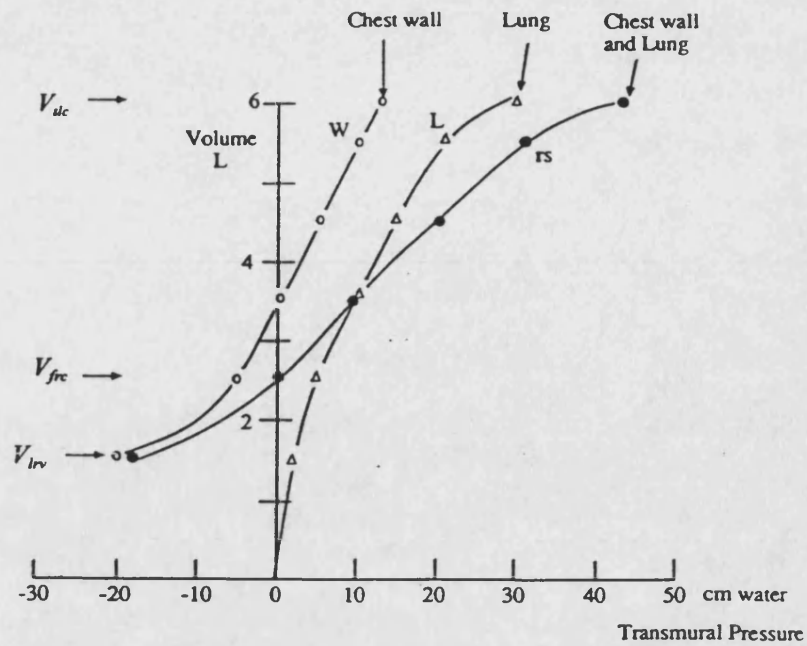
Figure 4.6 Variation in lung volume with transmural pressures
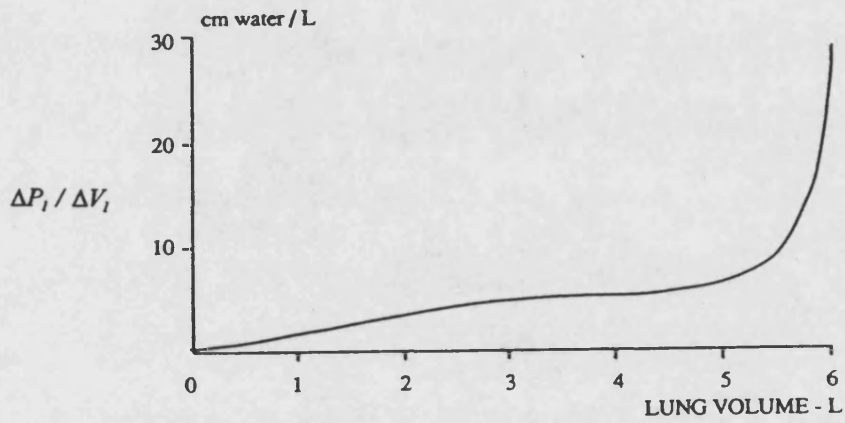
Figure 4.7(a) Lung elastance variation with lung volume
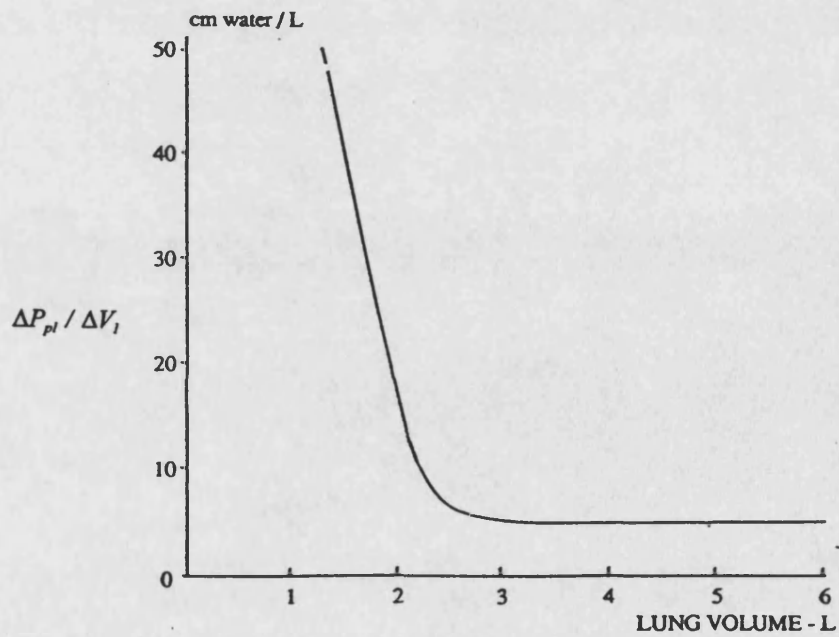
Figure 4.7(b) Chest wall elastance variation with lung volume

140
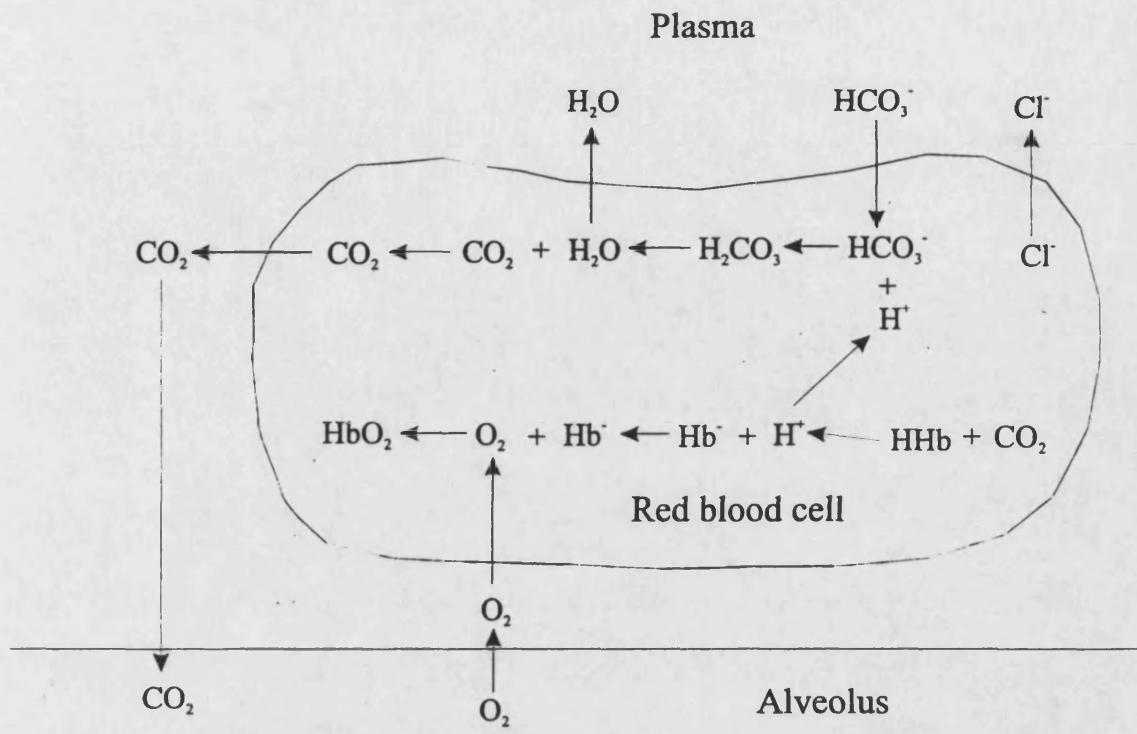
Figure 4.8 Oxygen and carbon dioxide exchange in alveolar compartment
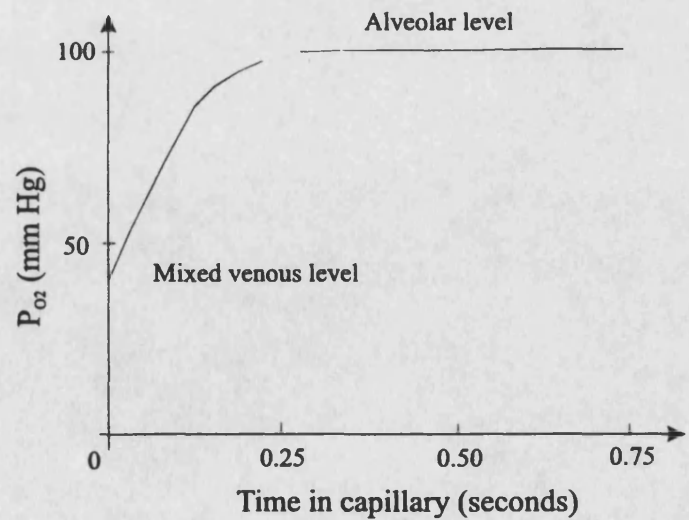
Figure 4.9 Change in partial pressure of O_2 in blood during transit through the pulmonary capillary bed

141

Percentage of satuated O_2 in blood

P_{CO_2} = 20 40 60 mmHg

$T - 37°C$

P_{O_2} (mm Hg)
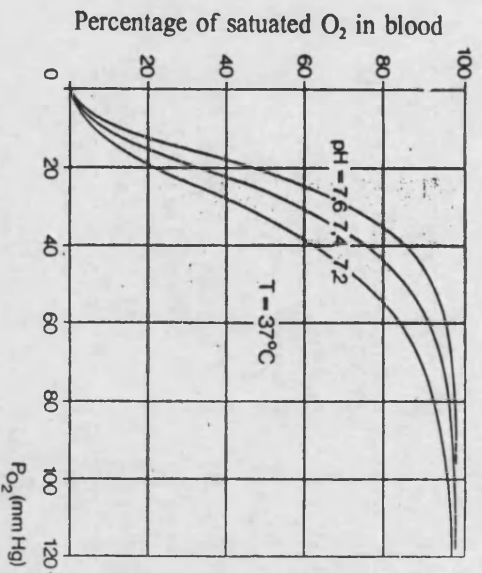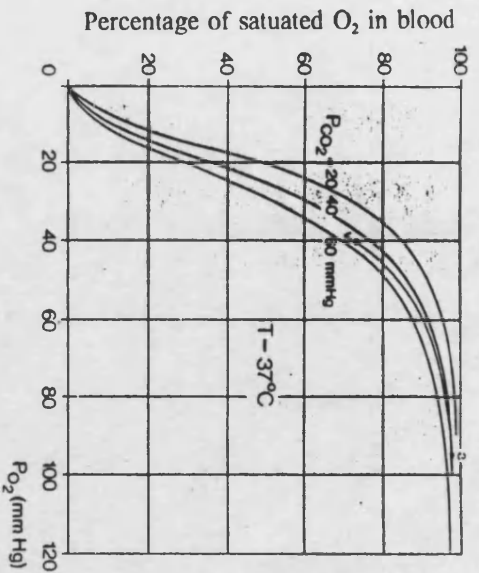
Figure 4.10 Dependence of the O_2 dissociation curve in blood

Percentage of satuated O_2 in blood

pH = 7.6 7.4 7.2

$T - 37°C$

P_{O_2} (mm Hg)

O_2 and CO_2 concentration (mL/L blood)

0% HbO_2

70% HbO_2

97.5% HbO_2

CO_2

Artery

Vein

Vein

O_2

Artery

P_{O_2} or P_{CO_2} (mm Hg)
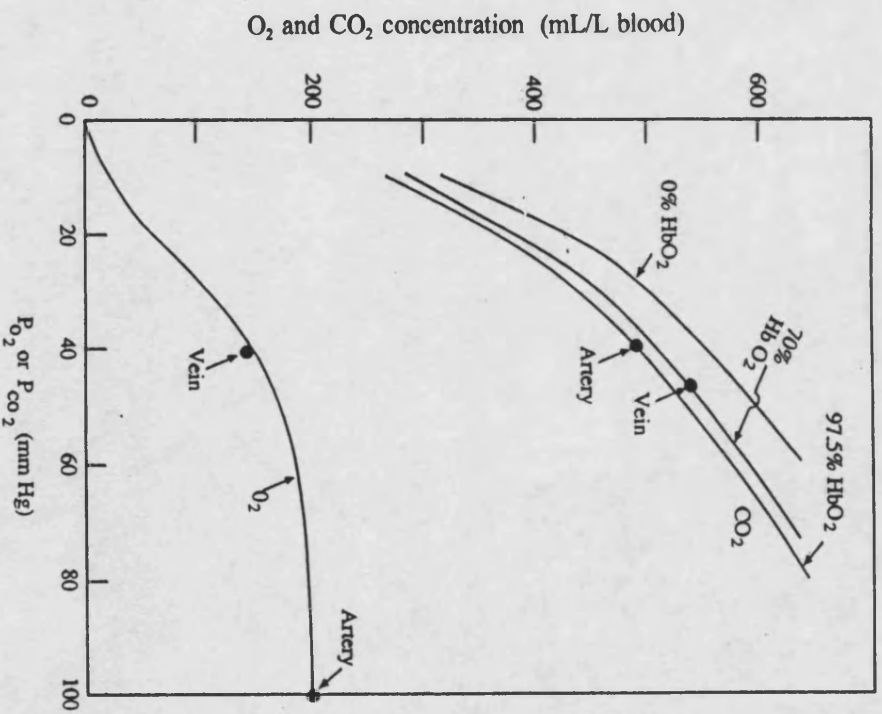
Figure 4.11 CO_2 and O_2 dissociation curves in blood

142
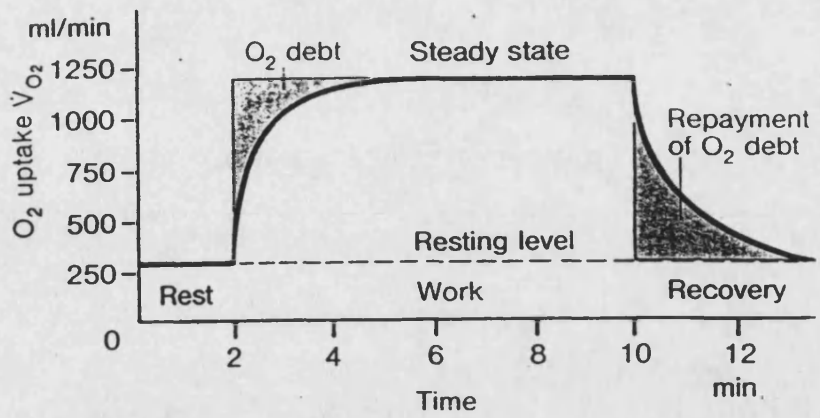
Figure 4.12 Oxygen uptake during and after light dynamic work at constant intensity
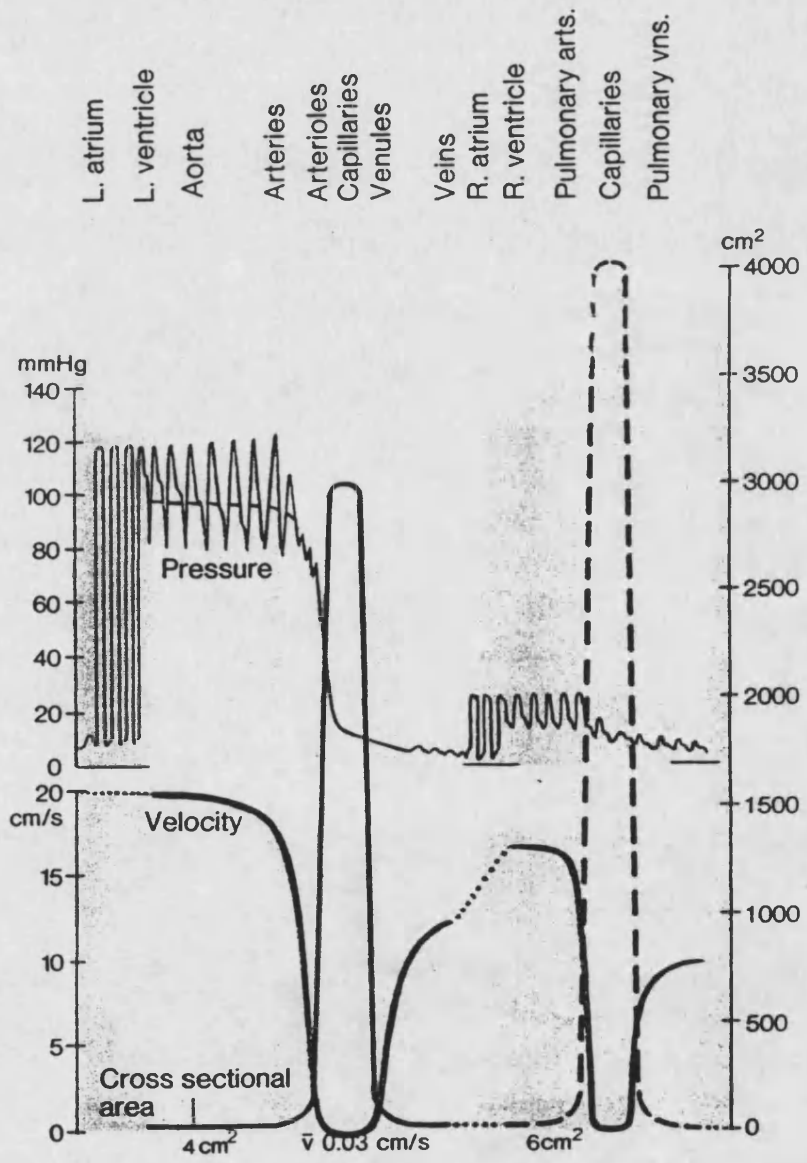
Figure 4.13 Pressure of the vascular beds in the various parts of the cardiovascular system during rest condition

143
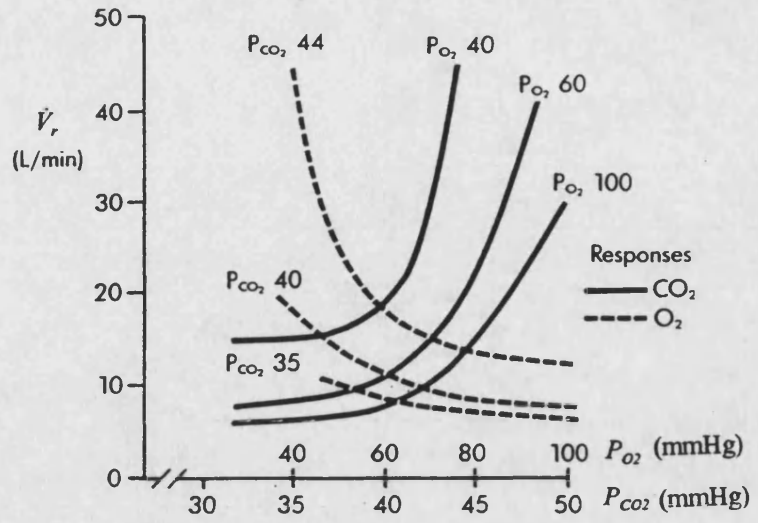
Figure 4.14 Ventilatory responses to the arterial P_{CO_2} and P_{O_2}
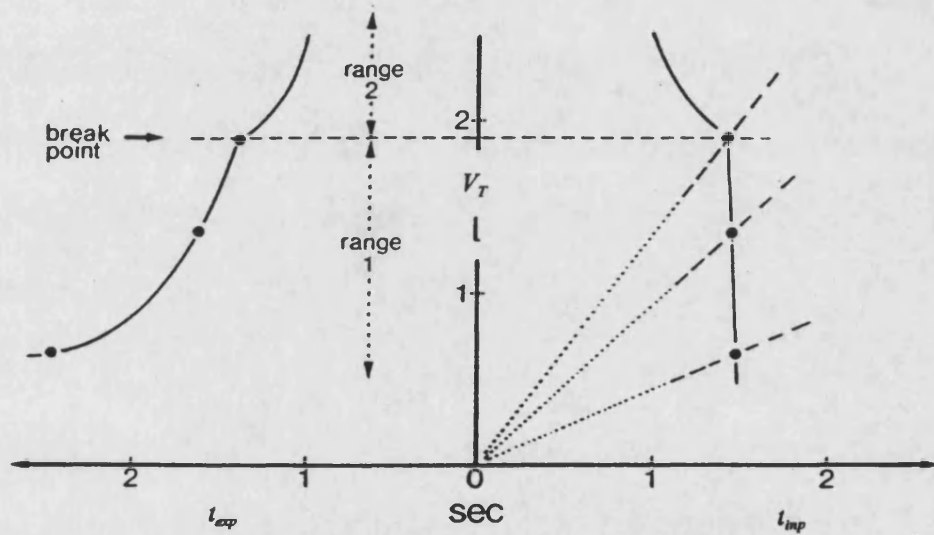
Figure 4.15 The steady state pattern of breathing in man
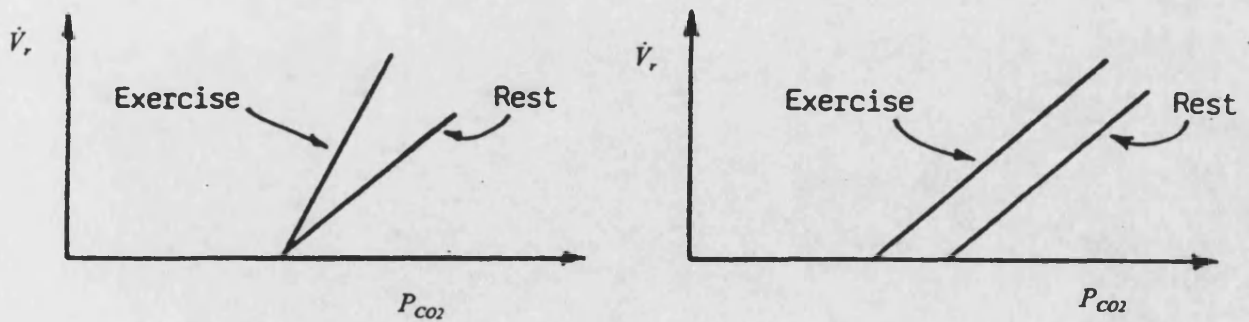
Figure 4.16 Testing of two controller hypotheses in exercise

144

CHAPTER 5

COMPUTER SIMULATION OF HUMAN RESPIRATORY
SYSTEM AND ITS INTERACTION WITH
UNDERWATER BREATHING APPARATUS

5.1 INTRODUCTION

In order to test the mathematical model developed in the last chapter, a number of simulation studies have been undertaken to provide results which can be validated using available physiological data. Once this has been established, the human respiratory system model can be used with confidence to simulate manned diving operations using various types of breathing equipment. A block diagram, shown in figure 5.1, indicates how the mathematical models developed in the last chapter interconnect for the purpose of the simulation. Figure 5.2 shows the simulation schematic of the human respiratory system in Bath/p.

5.2 DATA REQUIREMENT FOR THE HUMAN RESPIRATORY SYSTEM MODEL

The mathematical models developed in the last chapter require extensive data in order to perform an accurate simulation of the human respiratory system. Table 5.1 presents the data which has been gathered from a number of sources (Grodins, 1967, Sarhan, 1987, Sullivan, 1990, Ganony, 1987, Fung, 1990, Keele, 1982 and Bulfour, 1987). It is necessary to mention that the data is based on average healthy human subjects and is therefore applicable for assessing the breathing performance of qualified divers. Although the data is extensive, there are still several parameters which could not be found in any related literature. This is due to the difficulty in measuring these parameters (eg. neural activity of the respiratory centre in the brain) or the lack of information regarding the data required for dynamic models (eg. viscous friction). Hence, it has been necessary to simplify some of the mathematical models in order to reduce the number of unknown parameters. In the case of the tracheobronchial airways model, an instantaneous model is used to replace the dynamic model of the airway wall motion and equation (4.6) becomes

$$[\ (P_{al} + P_{lt})/2 - P_{pl} \ ] \ A_{wl} = k_{wl} \ (\ x_{al} - x_{nom,al} \ ) \qquad (5.1)$$

145

Rearranging equation (5.1), the tracheobronchial single airway radius is given by

$$x_{ai} = \left[\left(\frac{P_{et} + P_{it}}{2} \right) - P_{pl} \right] \frac{A_{wl}}{k_{wl}} + x_{nom,al} \tag{5.2}$$

For the pleural compartment model, it is assumed that the variation in pleural compartment volume is not significant and the pleural displacement can be obtained directly from the lung volume:

$$x_{pl} = (V_{pl} + V_l) / A_{pl} \tag{5.3}$$

In writing the above equation, the pleural compartment can be assumed to response instantaneously to pressure changes and the dynamic equation (4.25) can be replaced by

$$(P_{pl} - P_{am}) A_{pl} = k_{pl} (x_{pl} - x_{nom,pl}) - F_{th} \tag{5.4}$$

Therefore, the pleural pressure can be determined directly from

$$P_{pl} = \frac{k_{pl} (x_{pl} - x_{nom,pl}) - F_{th}}{A_{pl}} + P_{am} \tag{5.5}$$

Equations (5.1) to (5.5) enable the unknown parameters of Me_{wl}, Me_{pl}, B_{pl} and the viscous friction associated with the airway wall and pleural compartment motion to be neglected. This simplification leads to a faster simulation run time compared with the use of dynamic equations (4.6), (4.25), (4.30) and (4.31).

5.3 VALIDATION OF THE HUMAN RESPIRATORY SYSTEM MODEL

Experimental results are required in order to provide information which can be compared with the simulation results as part of the unknown parameter identification process. Subsequently, the validation of the complete model can then be undertaken. It is clear that model validation is an integral part of the model development process and not the final step (Murray-Smith and Carson, 1988).

In addition, careful consideration must be given to the range of experimental tests necessary to validate the model so that it can be used extensively for widely differing requirements. In order to devise meaningful correlation studies, experimental tests on average normal subjects are envisaged. The following simulations have been established to predict respiratory parameters for i) maximum inspiratory-expiratory

146

flow-volume test, ii) continuous breathing test, iii) maximal voluntary ventilation test and iv) responses at different physiological conditions test.

5.3.1 Maximum inspiratory-expiratory flow-volume test

Maximum inspiratory and expiratory flow against lung volume curves have been simulated for corresponding principal lung volumes, including residual volume V_{lrv} and total lung capacity V_{tlc}. These relationships are of major importance in assessing the condition of the lung and respiratory flow passageways and, in particular, reflect the limitations of flow. At present the chemical control of respiration is disconnected and the automatic control is overridden by voluntary control. The predicted maximum inspiratory-expiratory flow-volume curve, as shown in figure 5.3(a), was constructed by plotting the mouth volumetric flow rate against the plotted lung volume (ie. $= V_{tlc} - V_l$) when the lung inspires from residual lung volume V_{lrv} to total lung capacity V_{tlc} and then exhales as forcefully, rapidly and completely as possible to residual volume V_{lrv}. Airflow reaches a peak near the beginning of the expiration and decreases as the lung volume decreases. During a maximum inspiration, pleural and alveolar pressures are significantly sub-atmospheric and the flow resistance of the tracheobronchial airways remains constant, see figures 5.3(b), (c) and (d). On forced expiration the level of pleural and alveolar pressures remain at 45 cm H_2O and then increase until the residual volume is achieved. The fact that mouth air flow falls to zero at residual volume, when the lung is known to contain one or two litres of gas and has a high positive pressure applied to it, implies that at some point all paths from the alveoli to the mouth must be shut off completely. The is confirmed by figures 5.3(d) and (e) which show the airway resistance to increase rapidly in a hyperbolic fashion during expiration due to the closure of the airways. In addition, figure 5.3(f) shows the range of thoracic force applied for the maximum inspiratory and expiratory flow manoeuvre, indicating the maximum thoracic force that can be generated. (ie. 700 N for inspiration and -700 N for expiration). The experimental data obtained from Denison (1981,1983) are incorporated in figure 5.3. Good agreement between the simulation and experiment is obtained.

Having validated the model at atmospheric conditions, the effect of increased ambient pressure upon the maximum inspiratory and expiratory flow limitation can be simulated. Figure 5.4(a) shows the simulated maximum inspiratory-expiratory flow curves for 1, 2, 4, 8 ATA ambient pressures. A very marked reduction not only in peak flow but also the flow at all lung volume range is seen. It appears that

147

the decreasing flow rates achievable as density increases may limit the ambient pressure at which human can work effectively. The simulation results in figure 5.4(a) are in good agreement with the experimental data obtained by Miller (1971) (also included on figure).

The effect of external resistance on the relationship between maximum breathing flow rate and lung volume was also investigated. Figure 5.4(b) shows the simulation results of forced inspiratory and expiratory manoeuvres through the mouthpieces of various diameters. It can be seen that the added external resistance will reduce the maximum inspiratory and expiratory flows. It is necessary to mention that the same respiratory work effort is applied to all different mouthpiece diameters. A good match is achieved when the model behaviour is compared with the experimental data of Denison (1981) and Vorosmarti (1979) which is included in the figure.

At this stage, it was concluded that the assumed values for the unknown parameter illustrated in table 5.2 gave satisfactory predictions and, as a consequence, were used in subsequent simulations. During the unknown parameter identification process, it was interesting to find that when the single airway wall stiffness k_{wi} was set to 100 N/m, the shape of breathing loop shown in figure 5.3 changed to that shown in figure 5.5, indicating an asthmatic condition (Denison, 1981). Thus, the model can successfully predict respiratory problems.

5.3.2 Continuous breathing test

The first simulation for continuous breathing test was established for quiet breathing at rest. An idealized metabolic process was simulated, in which the overall O_2 consumption rate was set at 0.265 L/min and the respiratory quotient RQ at 0.8. Table 4.1 contains the breathing characteristics for breathing at rest. At this stage, the chemical control of respiration was still disconnected and the demand lung volume and inspiration and expiration times were user defined. This provided a means of examining the model hypotheses concerning the gas exchange process and mechanical control of breathing. The predicted variation in lung volume, given in figure 5.6(a), shows a tidal volume of approximately 0.5 L. The predictions of pleural and alveolar pressures are shown in figure 5.6(b). The pleural pressure varies from approximately -5 cm water at FRC, to -7.5 cm water at maximum inspiration. The corresponding variations in alveolar pressure are 0.7 to -0.7 cm water. These pressures are of the same order as published data

described by Fung (1990), indicating that the hypothesis for the mechanical control of breathing, equation (4.54), is plausible at this condition. The variations in alveolar and pulmonary artery and vein O_2 and CO_2 partial pressures with time are given in figures 5.6(c) and (d). These pressure levels are in close agreement with the published data described by Mines (1986). In addition, figures 5.6(e) and (f), respectively, show that the mean levels of O_2 and CO_2 diffusion rates in the alveolar membrane are the same as the overall O_2 consumption and CO_2 production rates, indicating that the hypothesis for gas exchange process in the model is appropriate.

Further simulations were performed to examine the mechanical control of breathing during exercise. The overall O_2 consumption rate was set at 2 L/min in which the tidal volume of 2 L and the breathing frequency of 25 breaths per minute (ie. 1 second inspiration time and 1.4 second expiration time) were applied. The predicted variation in lung volume, given in figure 5.7(a), shows a tidal volume of approximately 2.17 L at which the breathing pattern cannot follow the demand pattern. Hence, the hypothesis for the mechanical control of breathing is not plausible at this condition and needs to be revised. It is reasonable to assume that the form of controller for automatic activities (ie. continuous breathing) is different from the controller for voluntary activities (ie. forced respiration). During continuous breathing, a variable proportional control action has been incorporated in the controller equation such that equation (4.54) becomes

$$F_{th} = G_P (V_{l,dem} - V_l) + G_I \int_0^t (V_{l,dem} - V_l) \, dt + G_G (V_{l,dem,G} - V_l) \qquad (5.6)$$

Note that $V_{l,dem,G}$ is the demand lung volume profile which provides an automatic guidance of lung motion during automatic activities. For instance, a first order lag is assigned to the response of the demand lung volume profile:

$$\frac{dV_{l,dem,G}}{dt} = \frac{V_{l,dem} - V_{l,dem,G}}{\tau_G} \qquad (5.7)$$

The time constant τ_G is assumed to be related to the inspiration and expiration times (ie. $\tau_G = 0.8t_{inp}$ during inspiration and $\tau_G = 0.8t_{exp}$ during expiration).

The above hypotheses were examined by performing the simulation with the same breathing characteristic of 2 L tidal volume and 25 breaths/min breathing frequency. Figure 5.7(b) shows the

corresponding simulated result using G_G of 10000. It can be seen that the lung motion can now follow the demand breathing pattern at 2 L tidal volume. A series of simulations has been performed with different demand breathing patterns and the results are promising. Therefore, the hypotheses of equation (5.6) and (5.7) appears to be plausible for the continuous breathing simulation.

5.3.3 Maximal voluntary ventilation test

In order to understand the human respiratory system, it is necessary to appreciate the limitations imposed on a human's breathing capability. One of the most prominent factors is the limitation of ventilatory capacity which is described as maximal voluntary ventilation MVV (Bennett and Elliott, 1982 and Miller, 1971). Basically, the MVV is a measure of the air intake when a person breaths as hard as possible for a short period with a prescribed frequency of 100 breaths/min. The average human's MVV when air is breathed at atmospheric pressure condition is about 200 L/min (Miller, 1971). It is worthwhile to examine the model in which the same MVV could be obtained. As a test, an excessive 250 L/min ventilation rate (ie. 2.5 L tidal volume and 100 breaths/min breathing frequency) was applied in the model. The predicted variation in lung volume, given in figure 5.8(a), shows that a tidal volume of 2.5 L and a ventilation rate of 250 L/min were maintained, revealing that an unrealistic result is obtained. It was found that the thoracic force (figure 5.8(b)) generated by the mechanical controller exceeds the range of thoracic force (ie. 700 N to -700 N) found in the maximum inspiratory-expiratory flow-volume test, see figure 5.3(f). This is the likely cause of the unrealistic simulated results. Hence, the simulation was repeated with the thoracic force constrained to the recommended range (ie. $-700 \leq F_{th} \leq 700$). Figure 5.9 shows the corresponding simulated lung volume variation, indicating that a tidal volume of 2 L and the ventilation rate of approximately 200 L/min are obtained. Therefore, a considerable improvement is achieved using the limited force range.

Further simulations were performed to predict the MVV at different ambient pressures and breathing gas mixtures (ie. 80%He and 20%O_2). Figure 5.10 shows the corresponding simulation results of the MVV for these conditions. It is necessary to mention that all the simulations in figure 5.10 were performed with a demand tidal volume of 2.5 L and a breathing frequency of 100 breaths/min applied in the model. From the figure it can be seen that the MVV with both air and oxy-helium mixture drops very rapidly as ambient pressure is increased, and, at the same pressure level, a higher MVV can be obtained

when breathing the oxy-helium mixture. Hence, considerable benefits are to be gained from using oxy-helium mixture as the breathing gas. The corresponding experimental data obtained by Miller (1971) is included in figure 5.10. The agreement achieved clearly demonstrates the suitability of the model for assessing the limitation of ventilatory capacity at different ambient pressures and breathing gas mixture conditions.

5.3.4 Responses at different physiological conditions

The simulation results on the behaviour of the complete human respiratory model (ie. including chemical control) under different physiological conditions can be obtained by applying a step input of the following stimuli:

i) increase in the fractional concentration of CO_2 in inhaled air;

ii) reduction of inhaled oxygen;

iii) muscular exercise;

iv) change of ambient pressure.

The following predicted variables have been used for comparison purposes with published experimental data: ventilation rate, tidal volume, breathing frequency and the partial pressures of O_2 and CO_2 in the arterial blood.

(i) CO_2 breathing and hypoxia

The model behaviour during CO_2 breathing can be explored by increasing the fractional concentration of CO_2 in the inspired air (ie. 5, 6 and 7% CO_2). The effect of hypoxia in the model response has been examined by reducing the inspired O_2 concentration from 21% to 9, 8 and 7%. The levels in CO_2 breathing and hypoxia are maintained for 20 and 10 minutes respectively. The comparison of the steady-state features of the CO_2 breathing and hypoxia with the corresponding experimental data from Cunningham (1977), Garden (1977) and Reynolds and Milhorn (1973) are presented in tables 5.3 and 5.4 respectively. It can be seen that a mismatch between the model response and the experimental data is obtained, in particular in the case of the breathing frequency. This may be due to the imprecise parameters used in the inspiratory and expiratory time controllers (ie. equations (4.57), (4.58) and (4.59)). Therefore, more precise

151

equations for the inspiratory and expiratory time controllers have been derived using the data presented in figure 4.15:

Inspiratory time controller

$$t_{inp} = 1.5 - 0.0526 \ V_T \tag{5.8}$$

(for $V_T < 1.9$ L)

$$t_{inp} = \frac{0.49815}{V_T - 1.285} + 0.59 \tag{5.9}$$

(for $V_T \geq 1.9$ L)

Expiratory time controller

$$t_{exp} = 0.64 \ t_{inp} + \frac{11.1}{(0.4/0.062)(V_T/t_{inp}) + 2.73} \tag{5.10}$$

When using these new controllers in the simulation, the steady-state results obtained for CO_2 breathing and hypoxia produced a considerable improvement as shown in tables 5.5 and 5.6.

In the steady state, the model response is now within the physiological range. The transient response to the levels of 5% CO_2 breathing and 7% O_2 hypoxia are shown in figures 5.11 and 5.12 respectively. There is a similarity between the transient patterns yielded by the model and those found in data presented by Garden (1977) (For 5% CO_2 breathing the time to reach the steady state was 20 minutes, and for 7% O_2 hypoxia the steady state could not be reached after 10 minutes). The model is shown to predict a better on-transient pattern than the Sarhan model (1987) which produces an over-shoot during the hypoxia test (Murray-Smith and Carson, 1988).

(ii) Exercise

The response of the model due to exercise has been studied by increasing the O_2 consumption rate in the tissue model. Table 5.7 illustrates the steady-state features of the model response to different O_2 consumption rates (ie. 0.9, 1.6, 2, 2.5 and 3 L/min). A good match with the experimental data shown in table 4.1 is obtained. For example, at the extremely hard work condition, the model predicts a breathing rate of 29 breaths/min, 2.55 L lung tidal volume, 74 L/min ventilation rate and 3 L/min O_2 consumption rate compared with measured data of 30 breaths/min, 2.5 L lung tidal volume, 75 L/min ventilation rate and 3 L/min O_2 consumption rate. The transient response to the 2L/min O_2 consumption rate is shown in

figure 5.13. The transient produced by the model does not agree well with available data (Berne, 1988), in particular the ventilation rate (see figure 5.14). However, by introducing an offset plus exponential effect for the metabolic rate variation in the inspiratory flow controller (ie. equation (4.66) and (4.67)), that is

$$\dot{V}_{O2,to} = \frac{\dot{V}_{O2,to,dem}}{2} + \frac{\dot{V}_{O2,to,dem}}{2} \left(1 - e^{-t/120} \right) \quad\quad\quad (5.11)$$

some improvement in the transient response has been achieved (see figure 5.15).

After examining the model response to different stimuli, the interaction between two stimuli was investigated. The following simulation was performed for a step input of 1.14 L/min O_2 consumption rate for 5 minutes followed by 5 min of 1.14 L/min O_2 consumption rate with 4% CO_2 breathing. The result is shown in figure 5.16. A good match with the experimental data described by Sarhan (1987) is achieved.

(iii) Response to ambient pressure change

A sudden drop in ambient pressure, which occurs, for example, when cabin pressure is suddenly lost in a plane flying at high altitude, causes a fall in inspired P_{O2} as the inspired air contains the same percentage of O_2 at both high and sea levels. The model response to this sudden decompression from altitude (corresponding to 565 mmHg) to a pressure of 258 mmHg (such as would result from the blowing out of a partially-pressurised aircraft window at 27,000 feet) was simulated. The predicted arterial P_{O2} and P_{CO2}, shown in figure 5.17, were compared with the experimental data described by Dickinson (1977). It should be noted that 90 seconds after decompression 100% of O_2 was substituted for air and this accounts for the subsequent rapid increase in the partial pressure of O_2. It is interesting to see that the simulation agrees well with the measurements not only in terms of the initial transient but also during the later phases of the experiment.

The ambient pressure increases by 1 atmosphere for every 10 m of depth in sea water and every 10.4 m of depth in fresh water. Therefore, at a depth of 31 m in the ocean, a diver is exposed to a pressure of 4 atmospheres. Hence, an increase of P_{O2} will occur and this may elicit a variety of breathing responses. Figure 5.18 shows the model response to a gradual increase in ambient pressure from 1 ATA to 4 ATA. Note that the simulation was performed under resting condition (ie. 0.265 L/min O_2 consumption rate is applied). From the figure it can be seen that after a slight increase in ventilation rate at the beginning, the

153

ventilation rate is driven back to its original value. This type of behaviour matches the experimental data obtained by Morrison and Florio (1980).

Further simulations were performed to examine the model response to exercise under hyperbaric conditions. Figure 5.19(a) shows the predicted steady-state ventilation rates to different O_2 consumption rate (ie. 0.9, 1.6, 2, 2.5 and 3 L/min) under an ambient pressure of 4 ATA. In addition, the predicted ventilatory responses to exercise under 1 ATA condition obtained from table 5.7 are included in the same figure. It can be seen that there is no change in ventilation rate at the lower work loads, but the ventilation rate at the high work loads reduces at higher pressures. These changes may be brought about partly by higher P_{O2} and partly by the increased gas density. The corresponding experimental data obtained by Morrison and Florio (1980) is shown in figure 5.19(b), revealing a good match between the predicted and experimental results.

5.4 SIMULATION STUDIES OF HUMAN INTERACTION WITH UNDERWATER BREATHING APPARATUS

The results presented in the previous sections show that the human respiratory system model is able to predict respiratory response under different breathing gas mixture and ambient pressure conditions. Hence, the model can be used to predict the manned diving operations when using the semi-closed-circuit breathing system and the surface demand diving system. Two studies are considered to assess the limitations of these two breathing systems imposed on the diver. The first is to investigate the maximal voluntary ventilation MVV of the diver when using the breathing apparatus. This can provide more detailed information relating to the limitations that the two breathing systems impose on the diver's breathing capability. The second study is to assess the performance of the two breathing systems under complete diving schedules. This enables details of the breathing systems to be explored under real diving conditions. A further area investigated is the decompression process illustrated in table 1.2. In addition, an indicator is defined in order to predict the decompression sickness during the dive.

5.4.1 Establishing an indicator for the prediction of decompression sickness

According to section 1.3.4, for the prevention of decompression sickness a diver cannot

154

decompress at more than a pressure ratio of 2:1 after prolonged exposure on compressed air (saturated diving). For non-saturated dives, in which the inert gas is not saturated, it is reasonable that the partial pressure of the inert gas inside the tissue cannot be 2 times higher than the inert gas partial pressure of the breathing gas. It is known that whenever the gas being breathed changes, the arterial blood instantly follows this change (Bennett and Elliott, 1982). For simplicity, therefore, the partial pressure of the inert gas in the arterial blood is used as a means of analysis. Since the transient response of the inert gas concentration inside the tissue and the arterial blood can be predicted in the simulation, the partial pressure of the inert gas inside the tissue and the arterial blood can be obtained using the Henry-Dalton law:

$$P_{ti,ine} = C_{ti,ine} / So_{ti,ine} \qquad (5.12)$$

$$P_{b,ine} = C_{b,ine} / So_{b,ine} \qquad (5.13)$$

Hence, the ratio of the inert gas partial pressures obtained from equations (5.12) and (5.13) can be used to indicate the likelihood of decompression sickness.

5.4.2 Simulation of manned diving operations using the semi-closed-circuit breathing system

Figure 5.20 is the Bathfp simulation schematic diagram of a diver using the semi-closed-circuit breathing system. This figure shows the simple manner in which the two system models can be connected together.

Several MVV tests when using the semi-closed-circuit breathing system at different diving depths have been simulated using similar conditions to those described in section 5.3.3 where the chemical control of the respiration is disconnected and an excessive 250L/min ventilation rate (ie. 2.5 L tidal volume and 100 breaths/min breathing frequency) is applied in the respiratory system model. The gas mixture used in the diving set was air. Figure 5.21 shows that the predicted MVV drops rapidly as the diving depth is increased. When the diving depth of 54 m is reached, a MVV of 74 L/min is obtained which is very close to the average maximum human ventilation rate during heavy exercise (ie. 75 L/min RMV for 3 L/min O_2 consumption rate). Hence, it is not applicable that the semi-closed-circuit breathing system is used at depths more than 54 m. Similar results were obtained when using a 32.5%O_2/67.5%N_2 gas mixture. The MVV of the diver without the breathing apparatus (figure 5.10) is also included in figure 5.21, indicating that the semi-closed-circuit breathing system imposes further limitations on the diver's capability.

The suggestions described in section 3.26 of increasing the mouthpiece diameter by 30% and using smooth bore breathing tube to reduce the work of breathing have been investigated using the same conditions outlined above. The simulation results obtained are included in figure 5.21, showing that at the same diving depth the modified diving set allows slightly higher MVV to be achieved.

Following the MVV test, simulations of the semi-closed-circuit breathing system operating at different diving schedules and decompression processes were undertaken. The first simulation considered the diving schedule carried out from the water surface to a depth of 54 m and then returning back to the surface. The time from leaving the surface to the beginning of the ascent was 20 mins which was the same as the unmanned test simulation described in section 3.2.5. The decompression process described in table 1.2 for a 54m dive and 20 mins bottom time was applied and a gas mixture of 32.5%O_2/67.5%N_2 was used in the diving set. An overall O_2 consumption rate of 2 L/min (STPD) was applied in the respiratory system model after the diver immersed into the water. When the diver returned back to the surface, the overall O_2 consumption rate was set back to the rest condition (ie. 0.265 L/min STPD). The diving schedule was simulated over a period of 4000 seconds. The results obtained from the simulation are shown in figures 5.22, 5.23 and 5.24. The simulated diving schedule shown in figure 5.22(a) follows the recommended diving schedule. The transient response of the overall O_2 consumption rate and the lung ventilation rate are shown in figure 5.22(b) and (c) respectively. Figure 5.23 shows the simulated partial pressures of constituent gases [O_2(a), N_2(b) and CO_2(c)] at the mouthpiece which are within the physiological limits throughout the diving schedule. Figure 5.24 shows the predicted variations of nitrogen concentration and ratio inside the human body. From the figure it can be seen that the N_2 concentration in the arterial blood follows very closely the N_2 concentration in the pulmonary blood, and the N_2 concentration in the tissue changes slowly to its equilibrium level. These match the information described by Bennett and Elliott (1982) where the N_2 concentration in the arterial and pulmonary blood are the same and the N_2 concentration in the tissue follows slowly. Referring to figure 5.24(b), during the decompression process the N_2 partial pressure ratio (ie. $P_{tt,N2} / P_{b,N2}$) does not exceed the recommended limit of 2. Hence, the diver will not experience decompression sickness under this diving schedule.

The second simulation considered the same diving depth but with a different bottom time. The duration time from leaving the surface to the beginning of the ascent was taken to be 10 mins. A shorter

decompression stoppage time, illustrated in table 1.2, for this diving schedule was undertaken with the same overall O_2 consumption rates. Figure 5.25(a) shows that the diving schedule follows the recommended diving schedule and indicates that the diver has not stopped at the 9 m depth. The predicted N_2 partial pressure ratio between the tissue and the arterial blood [figure 5.25(b)] shows that although the diver does not stop at 9 m, the N_2 partial pressure ratio still does not exceed the limit. This was due to the fact that the N_2 concentration in the tissue did not reach its equilibrium when the diver started to leave the bottom. Hence, a shorter decompression time is appropriate in this case.

The third simulation considered the same decompression schedule use in the last simulation but having a longer bottom time of 20 mins. Figure 5.26(a) shows the corresponding diving schedule. The simulated N_2 partial pressure ratio between the tissue and the arterial blood is shown in figure 5.26(b). From the figure it can be seen that when the diver starts to leave the bottom, the N_2 concentration has reached its equilibrium level, and after the diver arrives at the first stop (6 m depth), the N_2 partial pressure ratio exceeds the limit. Hence, decompression sickness is likely to appear. Therefore, the decompression stoppage time used in the first diving schedule simulation is more appropriate.

The final simulation considered the diving schedule carried out from the water surface to a depth of 45 m and then returning straight back to the surface without any stops. The duration time from leaving the surface to the beginning of the ascent was 3 mins. Figure 5.27(a) shows the corresponding diving schedule. The predicted N_2 partial pressure ratio between the tissue and the arterial blood shown in figure 5.27(b) indicates that the N_2 partial pressure ratio does not exceed the limit and decompression sickness will not occur in this case. This simulation shows that the model can be used to recommend diving schedules which allow the diver to perform a dive without commencing any stops during the decompression process.

5.4.3 Simulation of manned diving operations using the surface demand diving system

The Bath*fp* simulation schematic of a diver using the surface demand diving system is illustrated in figure 5.28. Since Bath*fp* provided automatic procedure to assemble already developed component models to simulate the circuit, only a little effort was required to set up the circuit in figure 5.28 by replacing the diving set from the circuit shown in figure 5.20.

Similar MVV tests to those described for the semi-closed-circuit breathing system have been applied to the surface supply system. Again the gas mixture was air. Figure 5.29 shows a comparison of the diver's MVV when using the surface demand and the semi-closed-circuit breathing systems. This shows that the predicted MVV using the surface demand diving system has a similar profile to that of the semi-closed-circuit breathing system but, at the same diving depth, the MVV related to the surface demand diving system is higher. This indicates that the surface demand diving system will impose less limitation on the diver's breathing capability than the semi-closed-circuit breathing system.

The modifications suggested in section 3.3.4 for reducing the work of breathing when using the surface demand diving system have also been investigated. Figure 5.29 includes the predicted MVV tests when using the modified diving set in which the mouthpiece diameter and demand valve's diaphragm spring stiffness were increased by 30% and 100% respectively. It can be seen that at the same diving depth slightly higher MVV is obtained. Hence, these modification are applicable.

The use of oxy-helium mixture ($80\%He/20\%O_2$) in the surface demand diving system has also been studied during the MVV simulations. The simulation results are included in figure 5.29, showing that at the same diving depth the use of oxy-helium mixture allows a significantly higher MVV to be performed. Hence, much deeper dives are possible when a oxy-helium mixture is used as the breathing gas.

Further simulations have been established to study the surface demand diving system during real diving operation. The following studies considered the diving schedule of 54 m diving depth and 20 mins of duration time from leaving the surface to the beginning of the ascent in line with the decompression process illustrated in table 1.2. An overall O_2 consumption rate of 2 L/min (STPD) was applied during the dive.

The simulation results using air as the breathing gas are shown in figures 5.30, 5.31 and 5.32. Figure 5.30(a) shows that the simulated diving schedule follows the recommended diving schedule. The transient response of the overall O_2 consumption rate and the lung ventilation rate are shown in figure 5.30(b) and (c) respectively. The predicted partial pressure of constituent gases at the mouthpiece shown in figure 5.31 are within the physiological limits throughout the diving schedule. The predicted variations

of nitrogen concentration and ratio inside the human body are shown in figure 5.32. From this figure it can be seen that during the decompression process the N_2 partial pressure ratio between the tissue and the arterial blood does not exceed the limit, indicating that decompression sickness is unlikely to occur at this condition.

The previous simulation was repeated using the oxy-helium mixture (80%He/20%O_2) as the breathing gas. Figure 5.33 shows the simulation results. From the figure it can be seen that when the diver commences the first stop (at 9 m depth), the helium partial pressure ratio between the tissue and the arterial blood exceeds the limit, indicating that the use of oxy-helium mixture is more likely to cause the decompression sickness. Hence, different decompression schedules are required for the oxy-helium mixture. Figure 5.34 shows the simulation results of using a different decompression schedule where a stop at 15 m depth was applied instead of 9 m, see figure 5.34(a). Figure 5.34(b) shows that when the diver commences the first stop, the helium partial pressure ratio between the tissue and the arterial blood is reduced. Although during the second stop (at 6 m) the helium partial pressure ratio is slightly higher than in figure 5.33(b), the limit has not been exceeded. Therefore, this diving schedule is appropriate for this conditions.

5.5 CLOSURE

The parameters required for the models developed in chapter 4 have been obtained from published clinical measurements. However, some of the respiratory parameters are difficult to quantify and define. This difficulty has been overcome by comparing the simulation results with available experimental data, allowing the unknown parameters to be checked and refined. The simulation of maximum inspiratory-expiratory flow volume manoeuvre, continuous breathing test, maximal voluntary ventilation test and different physiological conditions test have been used to examine the hypotheses adopted for the models. Through a systematic process of model extension and testing, a more realistic representation of the human respiratory system and its control has been achieved. Simulations of CO_2 breathing and hypoxia have suggested that the parameters in the inspiratory and expiratory flow controllers derived by Sarhan need to be refined in order to produce a more accurate result. The simulation of ambient pressure change shows realistic behaviour and good correlation with measured respiratory parameters. Also, the transients produced

by the model agree well with the available experimental data. At this stage, the human respiratory system model enables the effects of variations in respiratory parameters and environmental conditions to be assessed.

The human respiratory system model has been used to simulate the manned diving operation when using the semi-closed-circuit breathing and the surface demand diving systems. Two simulation studies have been undertaken to assess the limitations which these breathing systems impose on a diver. The first study simulates the MVV of the diver at different diving depths and the second study simulates different diving schedules. The latter has included the assessment of the decompression process. The simulations of the MVV test have indicated that, at the same diving depth, the surface demand diving system allows higher lung ventilation rates to be performed and the use of oxy-helium mixture as the breathing gas is more suitable for deep dive operations. The simulations of a complete diving schedule have demonstrated that the developed models are capable of simulating real diving operations and able to indicate the likelihood of decompression sickness during a dive. It has been found that the use of oxy-helium mixture as the breathing gas is more likely to produce decompression sickness than air. Hence, a more modest diving schedule for the oxy-helium is required.

Variables	Value	Unit
Lung face maximum area	0.125	m^2
Lung face minimum area	0.105	m^2
Mouth cross sectional flow area	1.26×10^{-3}	m^2
Nose cross sectional flow area	3.976×10^{-4}	m^2
Lung face effective mass of moving part	0.5	kg
Number of airways in intrathoracic extrapulmonary zone	16400	-
Brain capillary bed blood flow resistance	5.7	(L/min)/bar
Muscle capillary bed blood flow resistance	570	(L/min)/bar
Pulmonary capillary bed blood flow resistance	39.9	(L/min)/bar
Flow resistance at intrapulmonary zone	0.01	cm water/(L/s)
Saturated O_2 concentration in blood	0.2	L/L blood
Solubility of nitrogen in blood	0.0137	L/L blood ATM^{-1}
Solubility of helium in blood	0.0087	L/L blood ATM^{-1}
Solubility of nitrogen in tissue	0.017964	L/L blood ATM^{-1}
Solubility of helium in tissue	0.009276	L/L blood ATM^{-1}
Volume of blood in aorta	1.266	L
Volume of blood in vein	3.034	L
Volume of blood in brain artery	0.546	L
Volume of blood in brain vein	0.154	L
Volume of blood in pulmonary artery	0.25	L
Volume of blood in pulmonary vein	0.25	L
Volume of blood in brain capillary bed	0.9	L
Anatomical dead space	0.175	L
Lung functional residual capacity	2.4	L
Gas volume in extrathoracic zone	0.123	L
Gas volume in intrathoracic zone	0.052	L
Volume of pleural compartment	10	L
Lung residual volume	1.2	L
Volume of blood in tissue capillary bed	29 to 39	L
Total lung capacity	6	L
Brain blood flow time constant	6	seconds
Cardiac output time constant	6	seconds
Metabolic rate time constant	60	seconds

Table 5.1 Available data for the mathematical models of human respiratory system

Variables	Value	Unit
Single airway wall forces acting area	2.316×10^{-6}	m^2
Blood fluid bulk modulus	17500	bar
Viscous friction	1000	N/m^2
Proportional gain	335	-
Integral gain for inspiration	6.7	-
Integral gain for expiration	50	-
Single airway wall stiffness	7000	N/m
Lung closing volume	0.9	L
Added nominal displacement of single airway when traction applied	0.0002	m
Maximum nominal displacement of single airway when traction not applied	0.0001	m

Table 5.2 Assumed values for the unknown parameters of the human respiratory models

Variable	Inspired CO_2 %	Pre-stimulus control		Steady state	
		Data	Model	Data	Model
Ventilation rate (L/min)	5	5.7	6.8	20.6	20.0
	6	5.8	6.8	32.0	31.0
	7	6.0	6.8	45.6	45.8
Tidal volume (L)	5	0.59	0.5	1.15	1.05
	6	0.58	0.5	1.53	1.42
	7	0.60	0.5	1.79	1.91
Breathing frequency (breaths/min)	5	11.5	12.8	17.9	19.0
	6	11.8	12.8	21.0	22.0
	7	12.1	12.8	25.5	24.0
$P_{a,O2}$ (mmHg)	5	102.0	105	131.8	131.0
	6	100.9	105	132.1	136.0
	7	102.8	105	144.0	142.0
$P_{a,CO2}$ (mmHg)	5	43.2	39.5	47.5	45.2
	6	42.5	39.5	48.9	51.5
	7	43.1	39.5	56.2	58.1

Table 5.3 Model and actual human response to CO_2 breathing

Variable	Inspired O_2 %	Pre-stimulus control		Steady state	
		Data	Model	Data	Model
Ventilation rate (L/min)	9	5.9	6.8	9.5	9.9
	8	5.8	6.8	12.3	13.2
	7	6.1	6.8	16.0	17.3
Tidal volume (L)	9	0.49	0.5	0.68	0.60
	8	0.48	0.5	0.91	0.74
	7	0.50	0.5	1.25	0.90
Breathing frequency (breaths/min)	9	12.5	12.8	13.5	16.8
	8	12.4	12.8	14.0	18.0
	7	12.7	12.8	14.9	19.1
$P_{a,O2}$ (mmHg)	9	106.9	105	44.7	43.0
	8	105.1	105	42.6	40.0
	7	103.3	105	38.8	37.0
$P_{a,CO2}$ (mmHg)	9	41.2	39.5	35.3	33
	8	42.1	39.5	34.1	32
	7	42.6	39.5	31.3	29

Table 5.4 Model and actual human response to hypoxia

Variable	Inspired CO_2 %	Pre-stimulus control		Steady state	
		Data	Model	Data	Model
Ventilation rate (L/min)	5	5.7	6.8	20.6	21.0
	6	5.8	6.8	32.0	31.0
	7	6.0	6.8	45.6	43.6
Tidal volume (L)	5	0.59	0.5	1.15	1.25
	6	0.58	0.5	1.53	1.69
	7	0.60	0.5	1.79	2.00
Breathing frequency (breaths/min)	5	11.5	12.8	17.9	16.5
	6	11.8	12.8	21.0	18.0
	7	12.1	12.8	25.5	21.3
$P_{a,O2}$ (mmHg)	5	102.0	105	131.8	131.0
	6	100.9	105	132.1	136.0
	7	102.8	105	144.0	142.0
$P_{a,CO2}$ (mmHg)	5	43.2	39.5	47.5	47
	6	42.5	39.5	48.9	51
	7	43.1	39.5	56.2	58

Table 5.5 Modified model and actual human response to CO_2 breathing (with the improvement of inspiratory and expiratory time controllers)

Variable	Inspired O_2 %	Pre-stimulus control Data	Pre-stimulus control Model	Steady state Data	Steady state Model
Ventilation rate (L/min)	9	5.9	6.8	9.5	9.45
	8	5.8	6.8	12.3	12.7
	7	6.1	6.8	16.0	15.5
Tidal volume (L)	9	0.49	0.5	0.68	0.68
	8	0.48	0.5	0.91	0.86
	7	0.50	0.5	1.25	1.10
Breathing frequency (breaths/min)	9	12.5	12.8	13.5	13.80
	8	12.4	12.8	14.0	14.65
	7	12.7	12.8	14.9	15.20
$P_{a,O2}$ (mmHg)	9	106.9	105	44.7	43.5
	8	105.1	105	42.6	41.0
	7	103.3	105	38.8	38.0
$P_{a,CO2}$ (mmHg)	9	41.2	39.5	35.3	34.5
	8	42.1	39.5	34.1	33.5
	7	42.6	39.5	31.3	30.0

Table 5.6 Modified model and actual human response to hypoxia (with the improvement of inspiratory and expiratory time controllers)

Work Effort	Breaths per minute	Tidal volume (L)	Ventilation rate (L/min)	O_2 uptaken rate (L/min STPD)
Rest	12.8	0.5	6.8	0.265
Light work	15.8	1.2	19	0.9
Moderate work	19.5	1.9	38	1.6
Heavy work	23.0	2.1	48	2
Hard work	26.0	2.35	60	2.5
Extremely hard work	29.0	2.55	74	3

Table 5.7 Model response to exercise
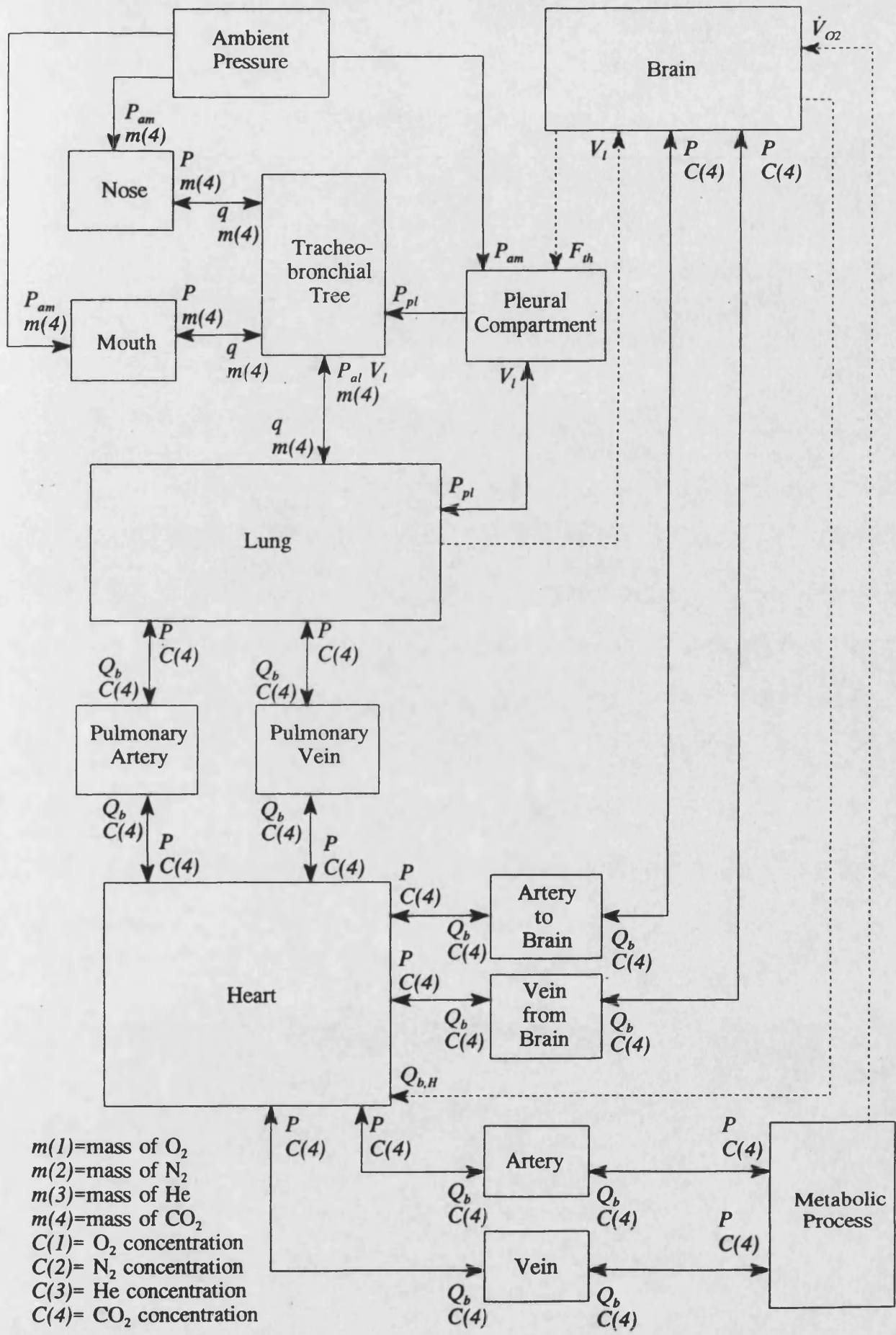
Figure 5.1 Simulation of human respiratory system block diagram

The diagram contains the following labels:

- Ambient Pressure
- Brain
- $\dot{V}_{O2}$
- Nose
- P_{am} $m(4)$
- P $m(4)$
- q $m(4)$
- V_l
- P $C(4)$
- Tracheo-bronchial Tree
- P_{am}
- F_{th}
- P_{pl}
- Pleural Compartment
- P_{am} $m(4)$
- Mouth
- P $m(4)$
- q $m(4)$
- P_{al} V_l $m(4)$
- q $m(4)$
- V_l
- P_{pl}
- Lung
- P $C(4)$
- Q_b $C(4)$
- Pulmonary Artery
- Pulmonary Vein
- Q_b $C(4)$
- P $C(4)$
- Heart
- P $C(4)$
- Artery to Brain
- Q_b $C(4)$
- Vein from Brain
- $Q_{b,H}$
- P $C(4)$
- Artery
- Q_b $C(4)$
- P $C(4)$
- Metabolic Process
- Vein
- $m(1)$= mass of O_2
- $m(2)$= mass of N_2
- $m(3)$= mass of He
- $m(4)$= mass of CO_2
- $C(1)$= O_2 concentration
- $C(2)$= N_2 concentration
- $C(3)$= He concentration
- $C(4)$= CO_2 concentration

Figure 5.2 Simulation schematic of human respiratory system in Bath*fp*
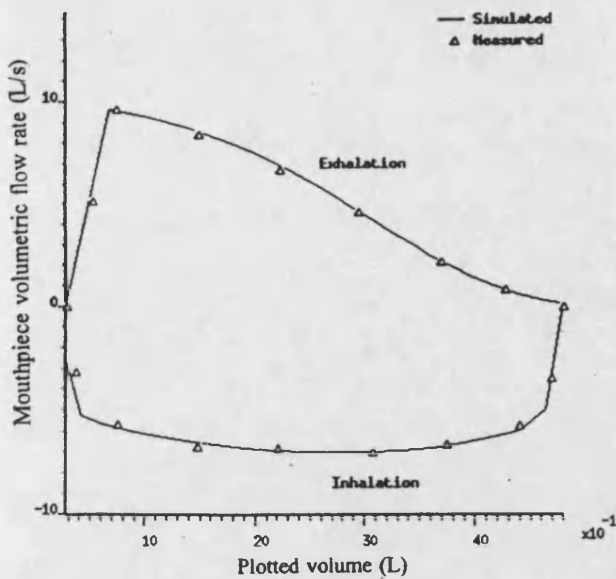
(a) Mouth volumetric flow rate vs. plotted lung volume V_{lpt} (ie.= $V_{slc} - V_t$)
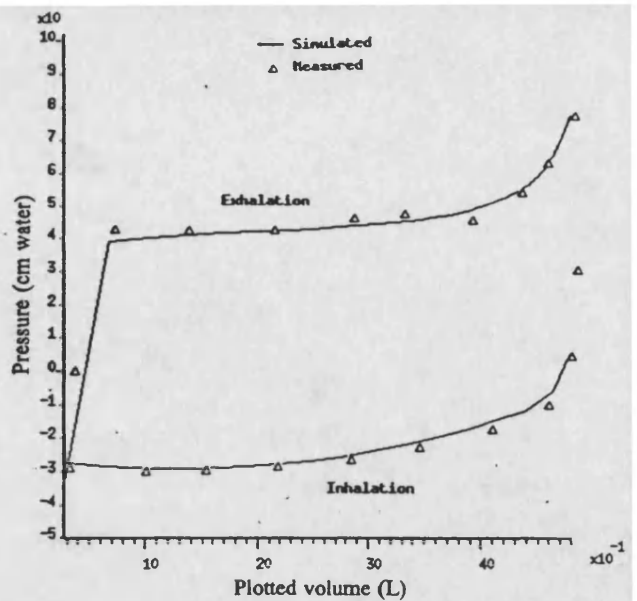
(b) Pleural pressure vs. plotted lung volume V_{lpt} (ie. $V_{slc} - V_t$)
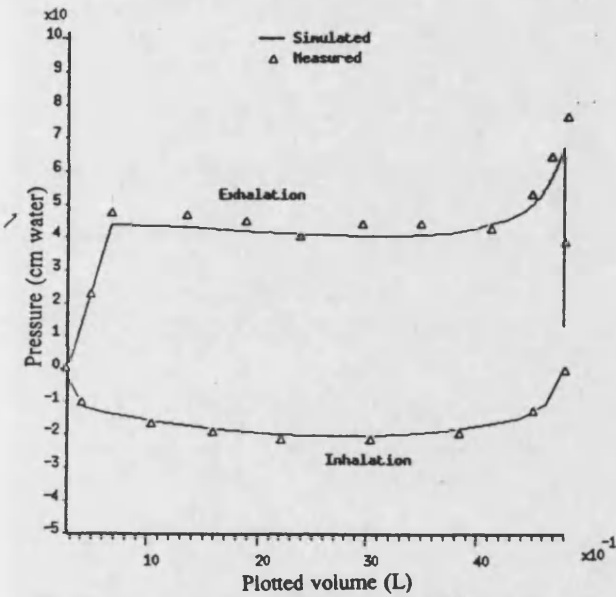
(c) Alveolar pressure vs. plotted lung volume V_{lpt} (ie. $V_{slc} - V_t$)
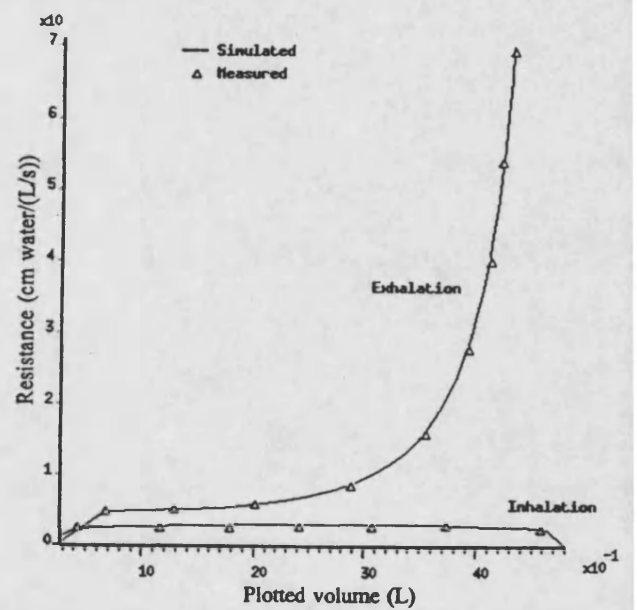
(d) Total airway resistance vs. plotted lung volume V_{lpt} (ie. $V_{slc} - V_t$)
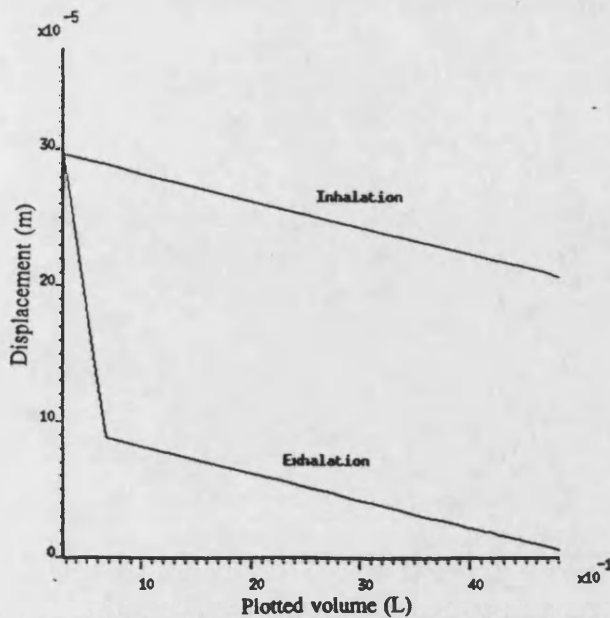
(e) Single airway radius vs. plotted lung volume V_{lpt} (ie. $V_{slc} - V_t$)
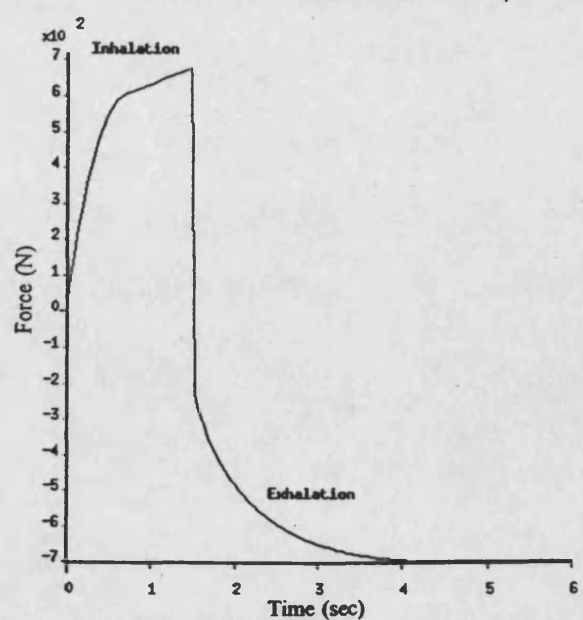
(f) Generated thoracic force vs time

Figure 5.3 Measured and simulated maximum inspiratory and expiratory flow manoeuvre of an average human

(i) Simulated   (ii) Measured Data

(a) At different ambient pressures

(i) Simulated   (ii) Measured data
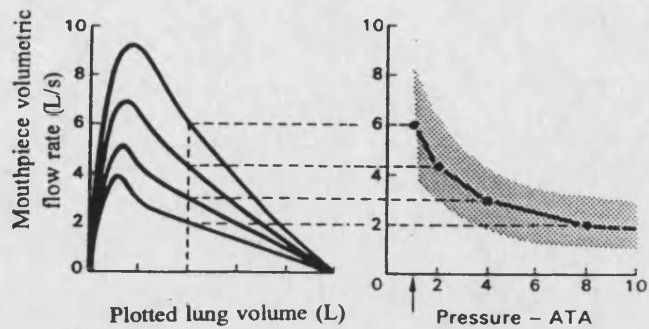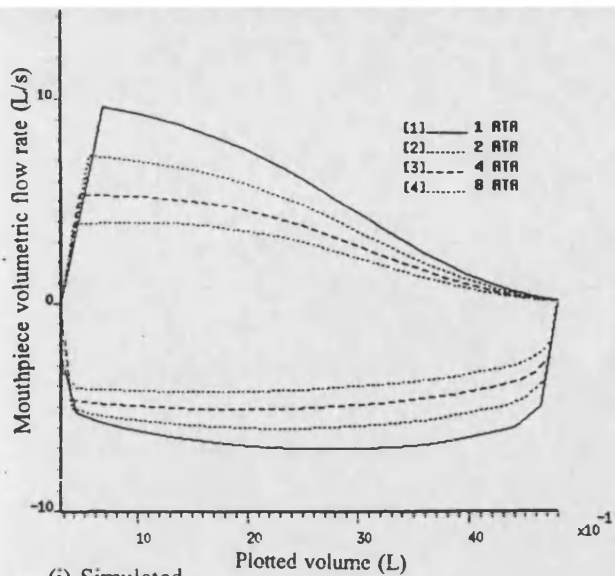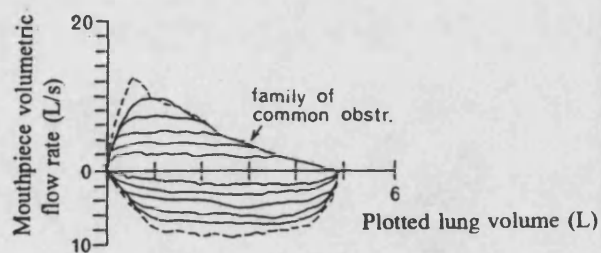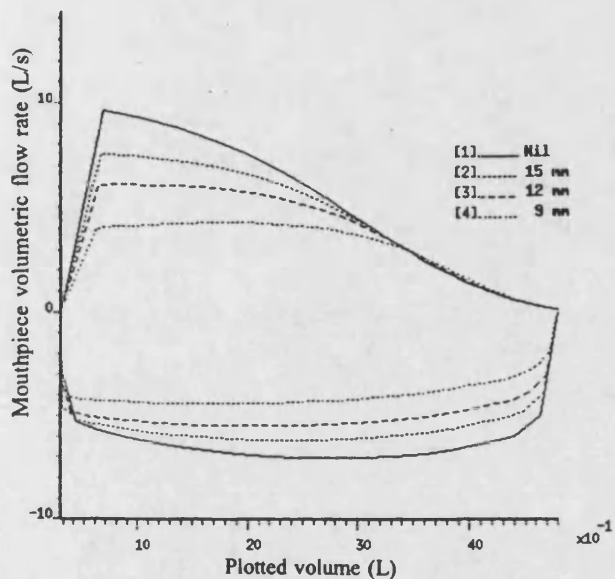
(b) Using different sizes of mouthpiece

Figure 5.4 Maximum inspiratory and expiratory flow curves at different conditions
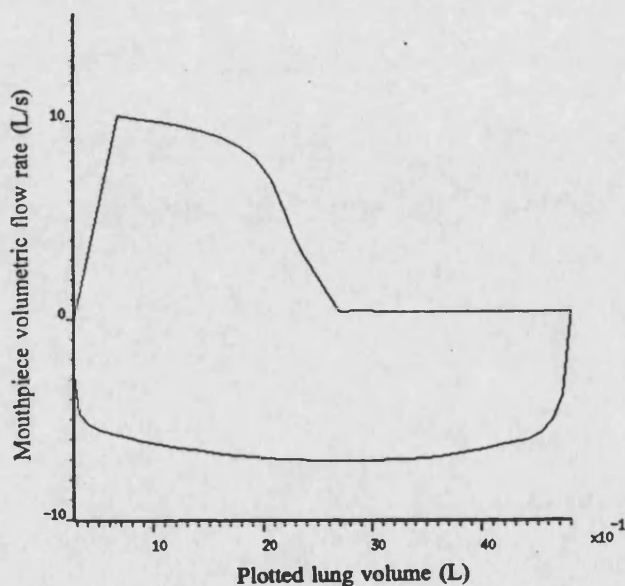
Figure 5.5 Simulated breathing loop showing an asthmatic condition

(a) Lung volume variation

(b) Pleural and Alveolar pressures

(c) Variations in alveolar compartment and pulmonary artery and vein O_2 partial pressure

(d) Variations in alveolar compartment and pulmonary artery and vein CO_2 partial pressure

(e) Comparison between O_2 diffusion rate in alveolar membrane and overall O_2 consumption rate

(f) Comparison between CO_2 diffusion rate in alveolar membrane and overall CO_2 production rate

Figure 5.6 Simulated breathing pattern at rest

169
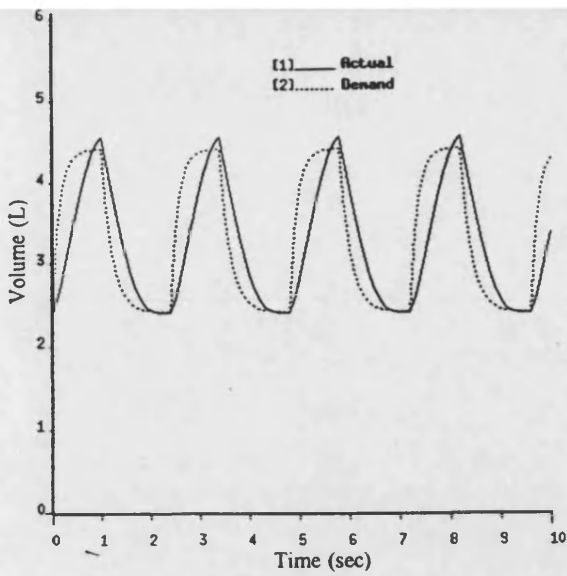
(a) Using PI controller
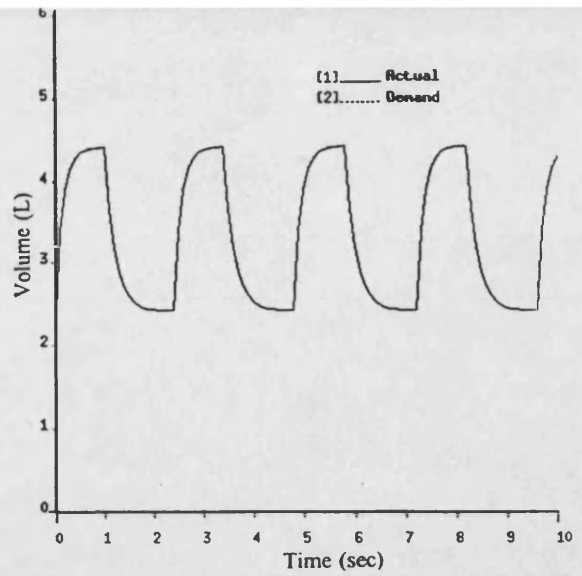
(b) Using modified controller (the variable proportional action)

Figure 5.7 Simulated lung volume variation during exercise (ie. 2 L/min O_2 uptaken rate)
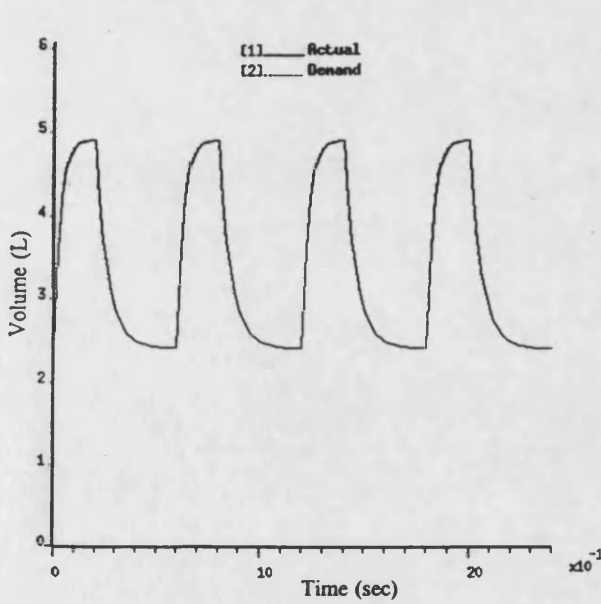
(a) Lung variation
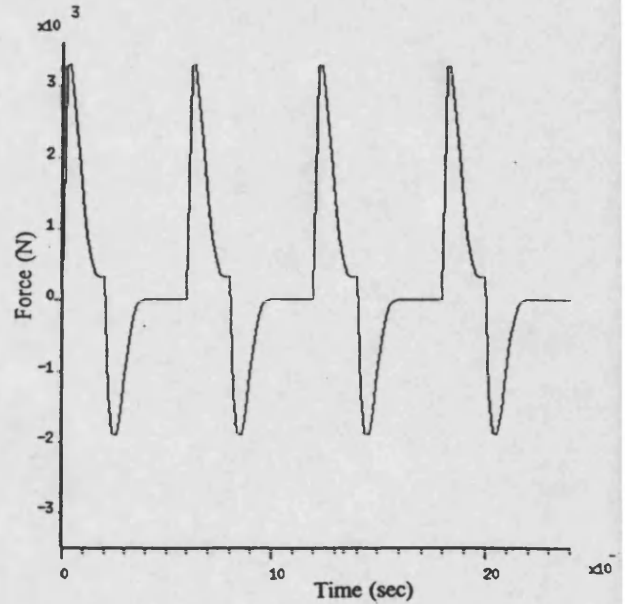
(b) Thoracic force

Figure 5.8 Simulation of breathing response when 250 L/min lung ventilation rate is applied
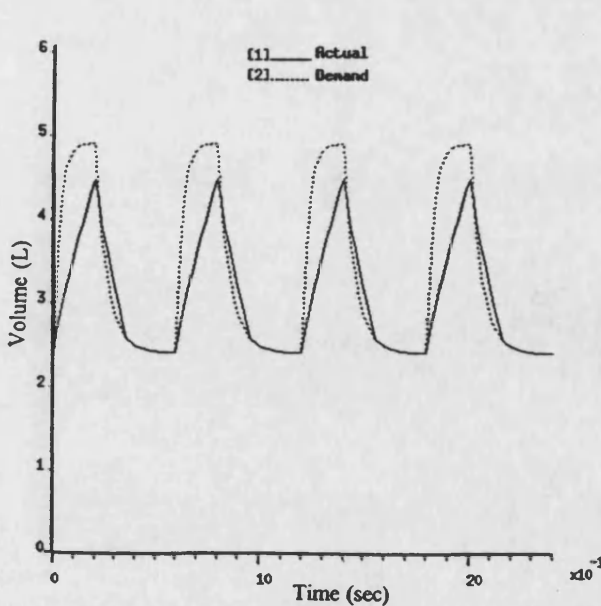
(a) Lung variation
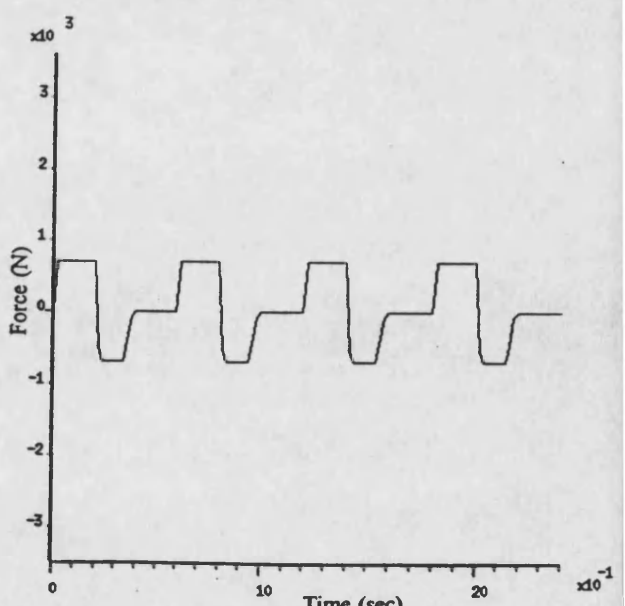
(b) Thoracic force

Figure 5.9 Simulation of 250 L/min lung ventilation rate applying limited thoracic force (ie. $-700 \leq F_{at} \leq 700$)

170
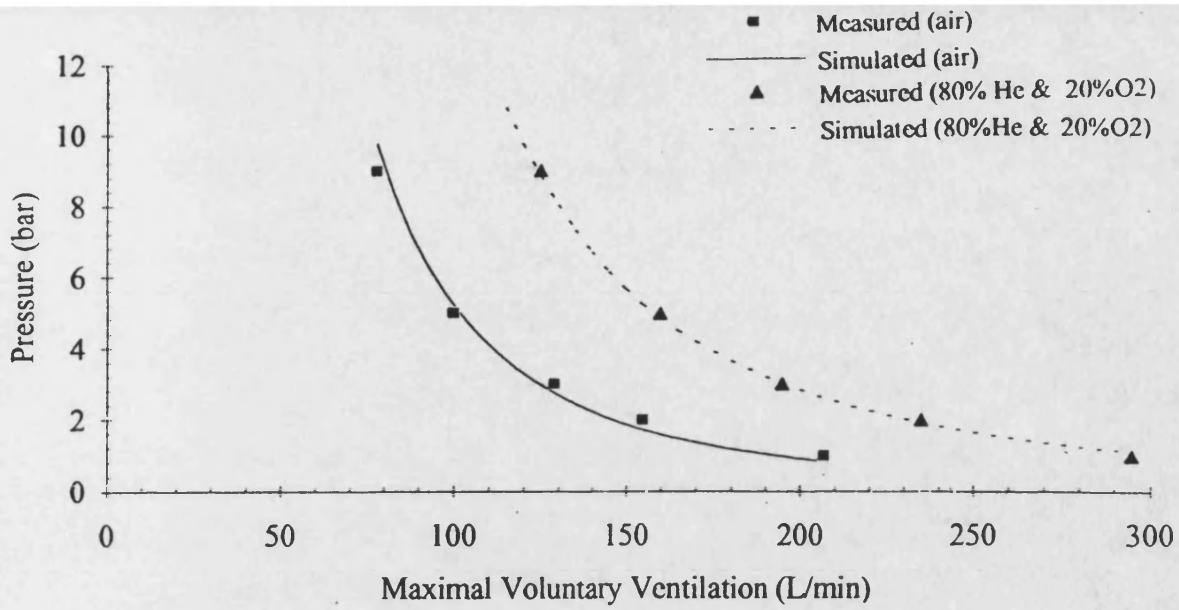
Figure 5.10 Predicted and measured MVV using air and oxy-helium mixture at different ambient pressure

(a) Ventilation rate

(b) Breathing frequency
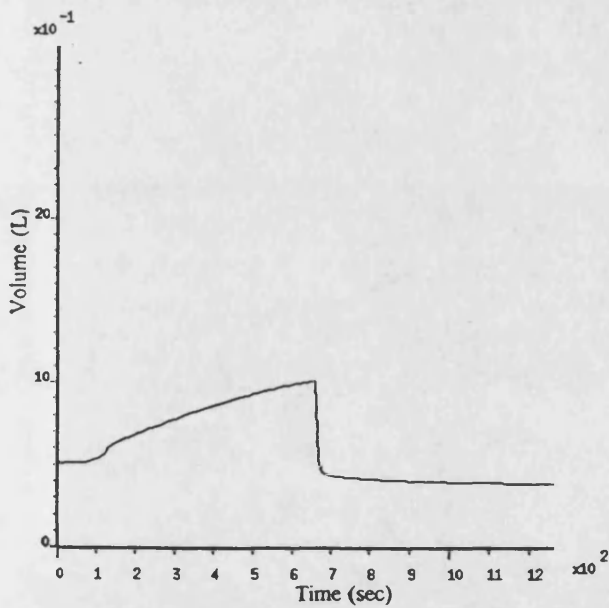
(c) Tidal volume
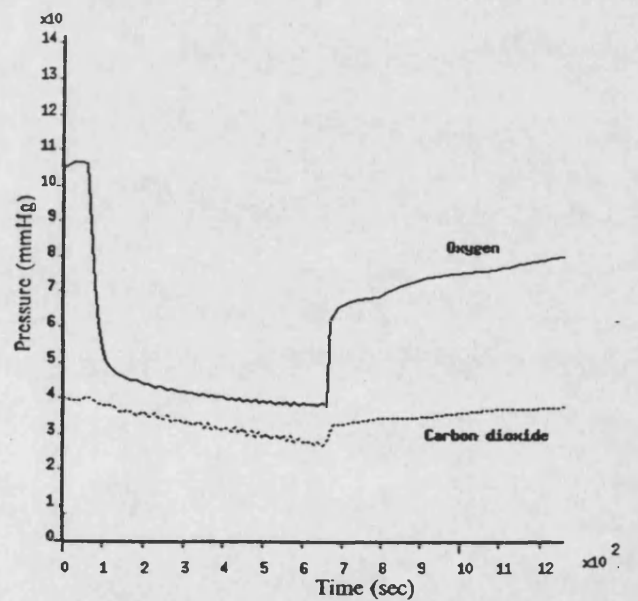
(d) Arterial blood O_2 and CO_2 partial pressures

Figure 5.11 Model response to 5% CO_2 breathing.
The step input of CO_2 is applied at $t=$ 60 seconds and reduced at $t=$ 1260 seconds

171

Figure 5.12 Model response to 7% O_2 hypoxia administrated at $t=60$ seconds and reduced at $t=600$ seconds
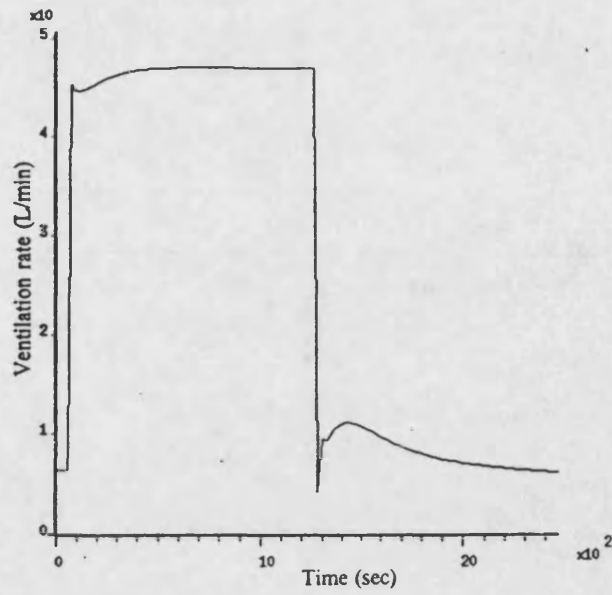
Figure 5.13 Predicted lung ventilation rate response to 2 L/min O₂ consumption rate
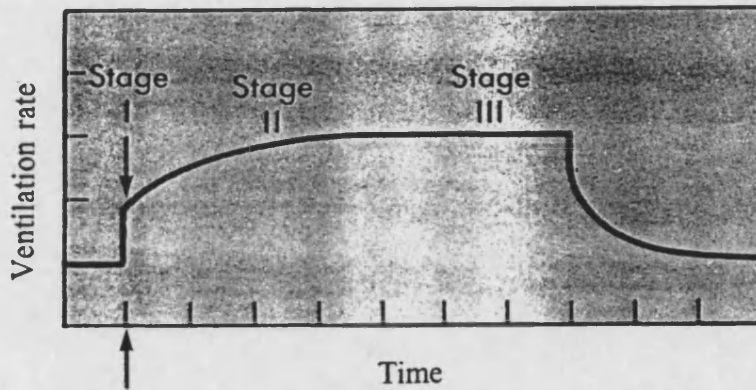
Figure 5.14 Experimental result of the variation in ventilation rate at the transitions between rest and exercise
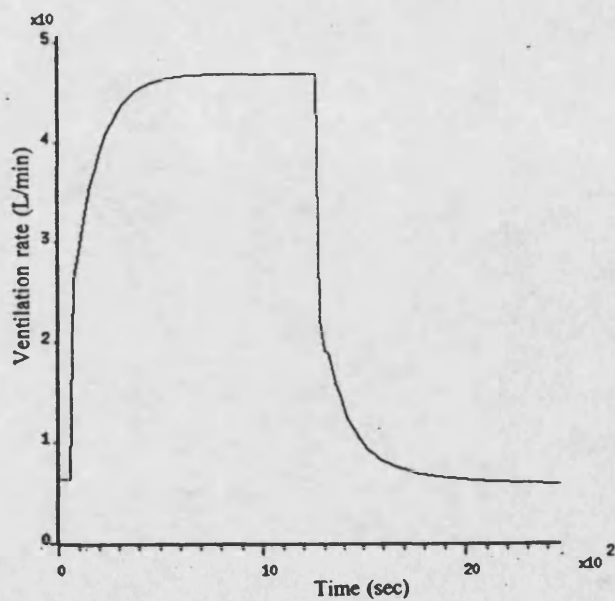
Figure 5.15 Predicted ventilatory response to 2 L/min O₂ consumption rate with the new metabolic rate variation in the inspiratory flow controller model

173
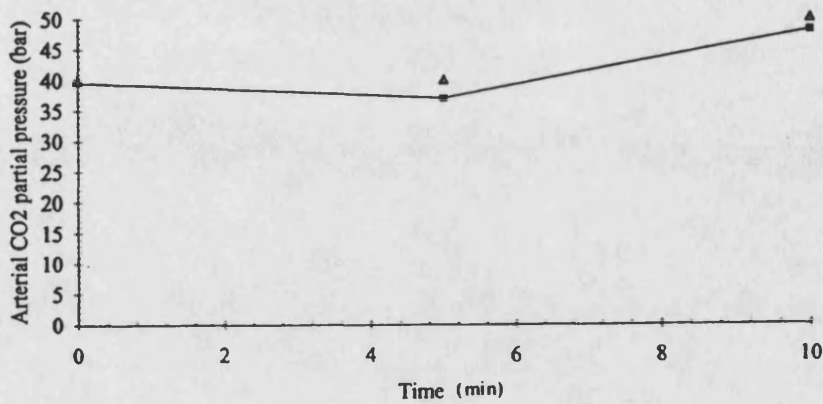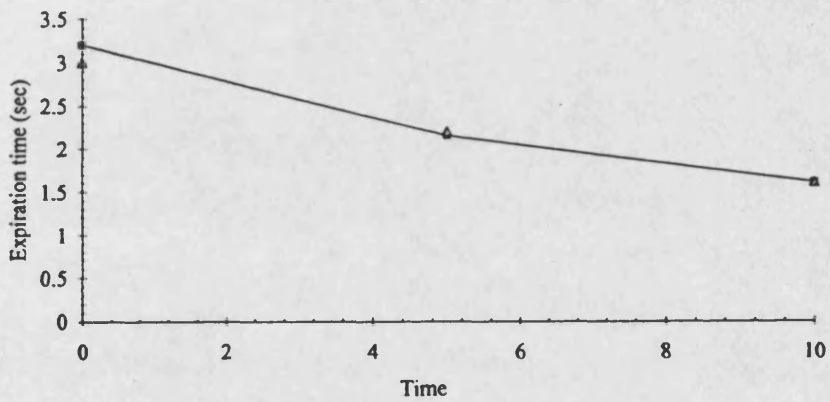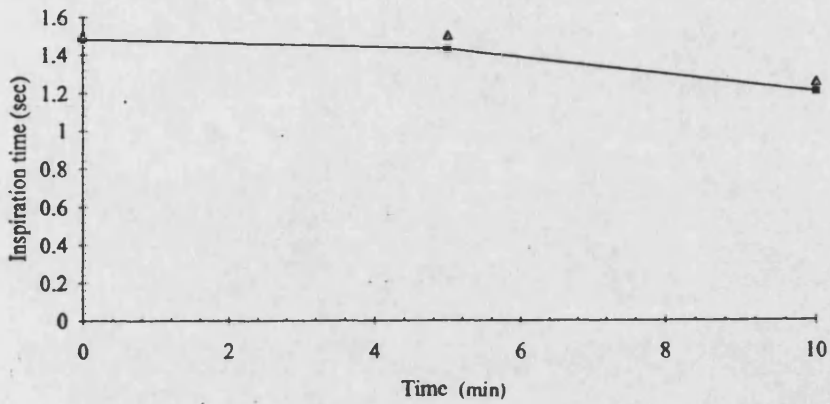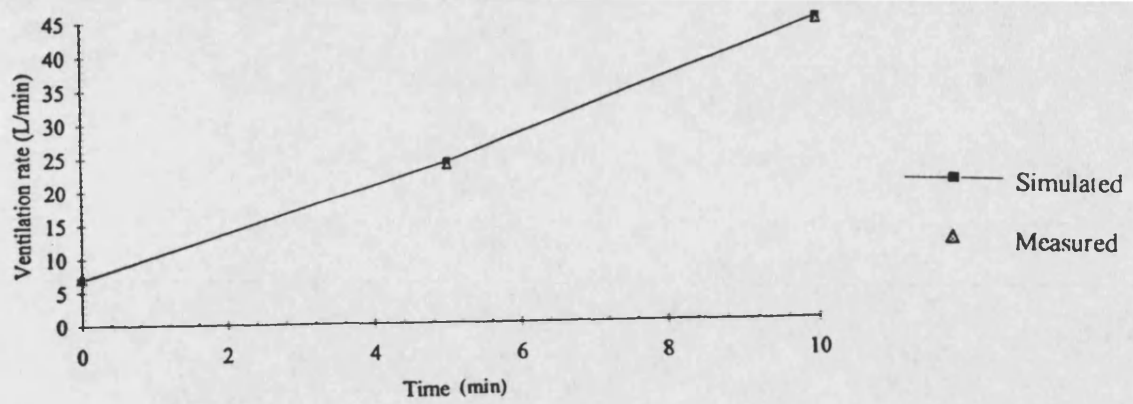
Figure 5.16 Model response to 1.14 L/min O_2 consumption rate for 5 mins followed by 1.14 L/min O_2 consumption rate with 4% CO_2 breathing

(a) Arterial O_2 partial pressure

(b) Arterial CO_2 partial pressure
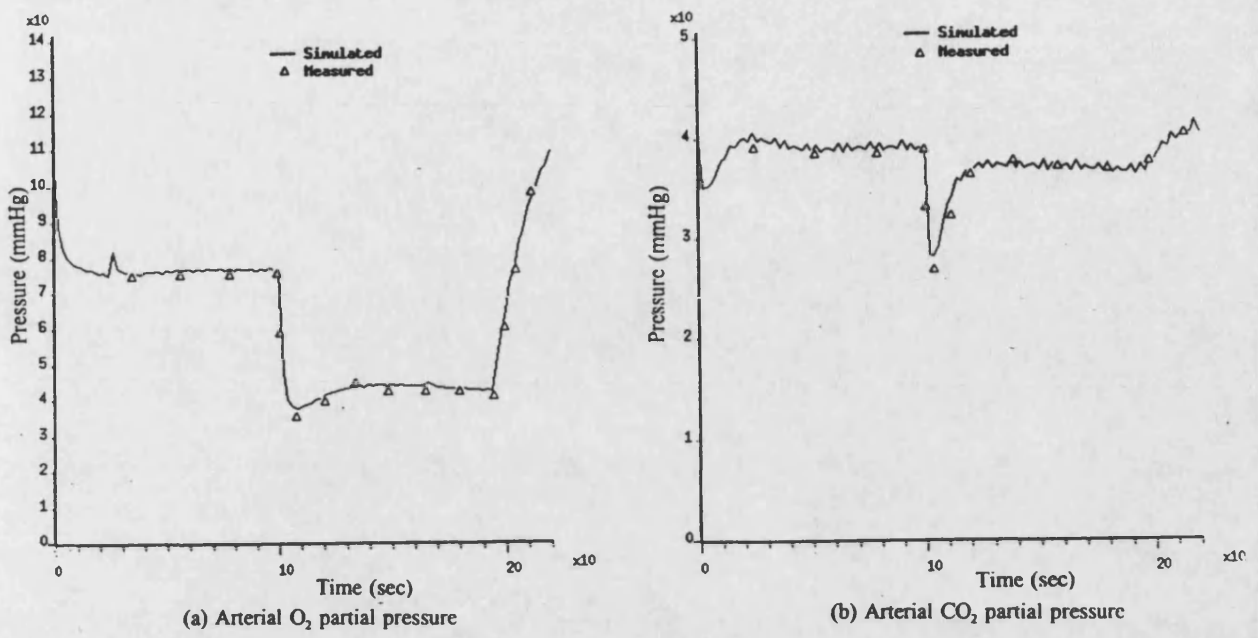
Figure 5.17 Predicted and measured arterial O_2 and CO_2 partial pressures in response to the drop of ambient pressure

(a) Change of ambient pressure

(b) Ventilation rate variation
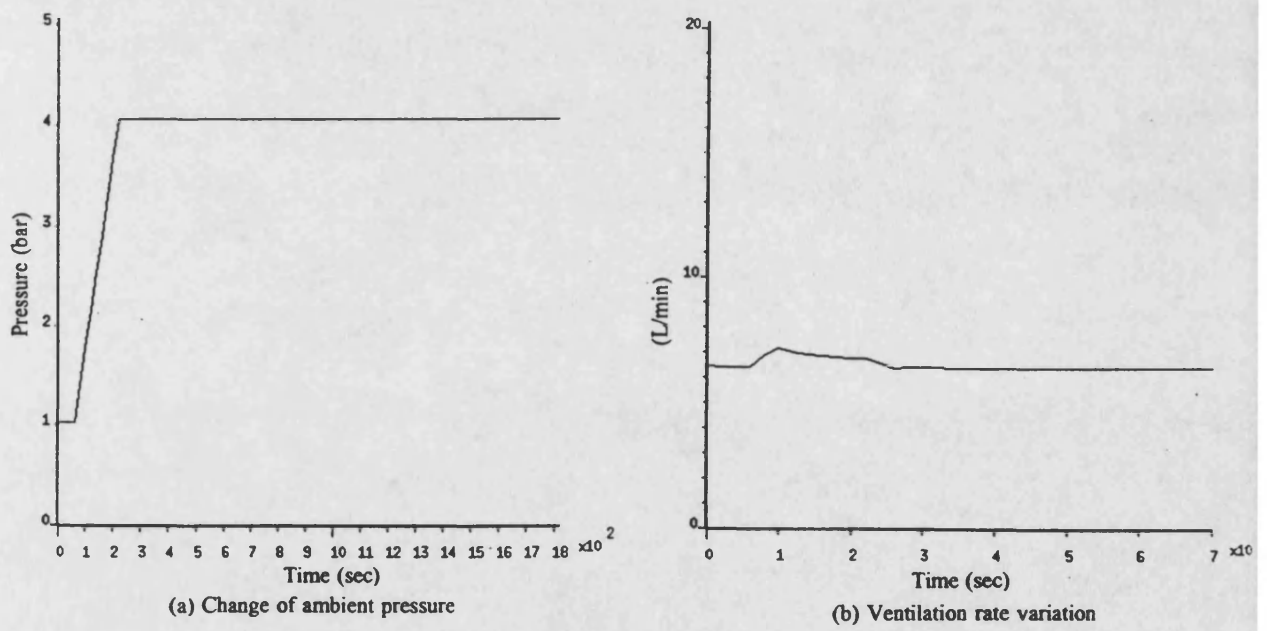
Figure 5.18 Model response to the graduate increase of ambient pressure from 1 ATA to 4 ATA

175
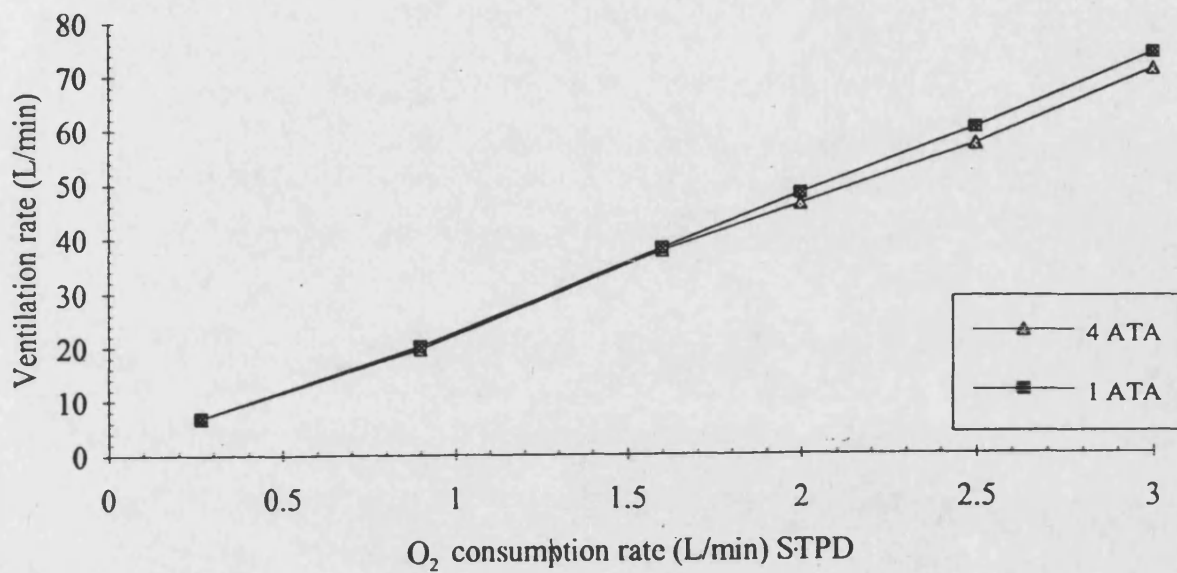
(a) Simulated
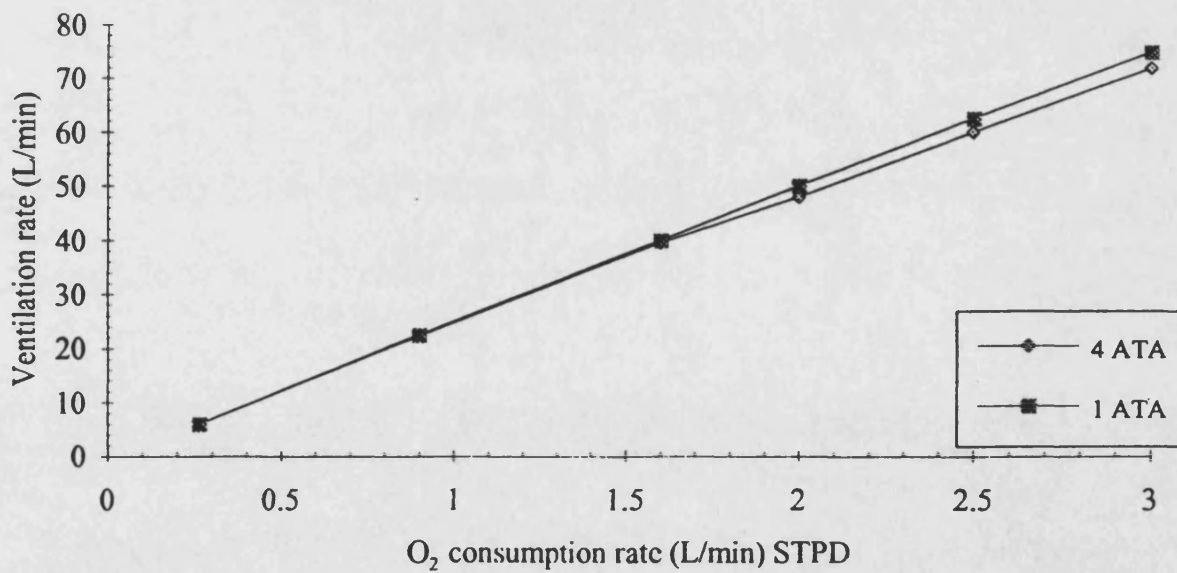
(b) Measured

Figure 5.19 Predicted and measured ventilatory response to different O_2 consumption rates at 1 ATA and 4 ATA ambient pressure conditions
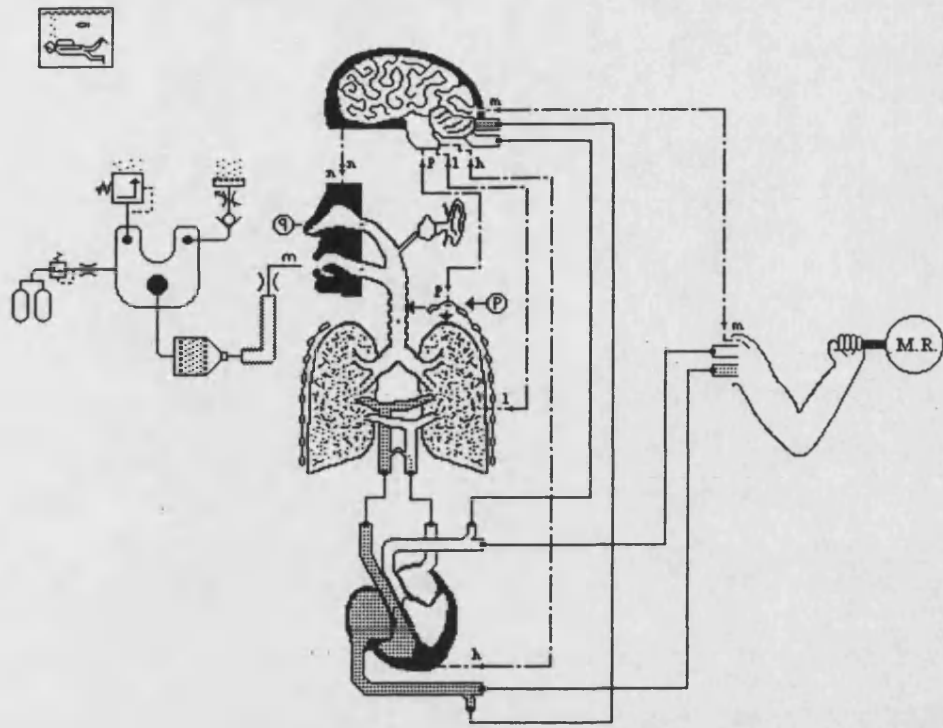
Figure 5.20 Simulation of a diver using the semi-closed-circuit breathing system in Bath*fp*
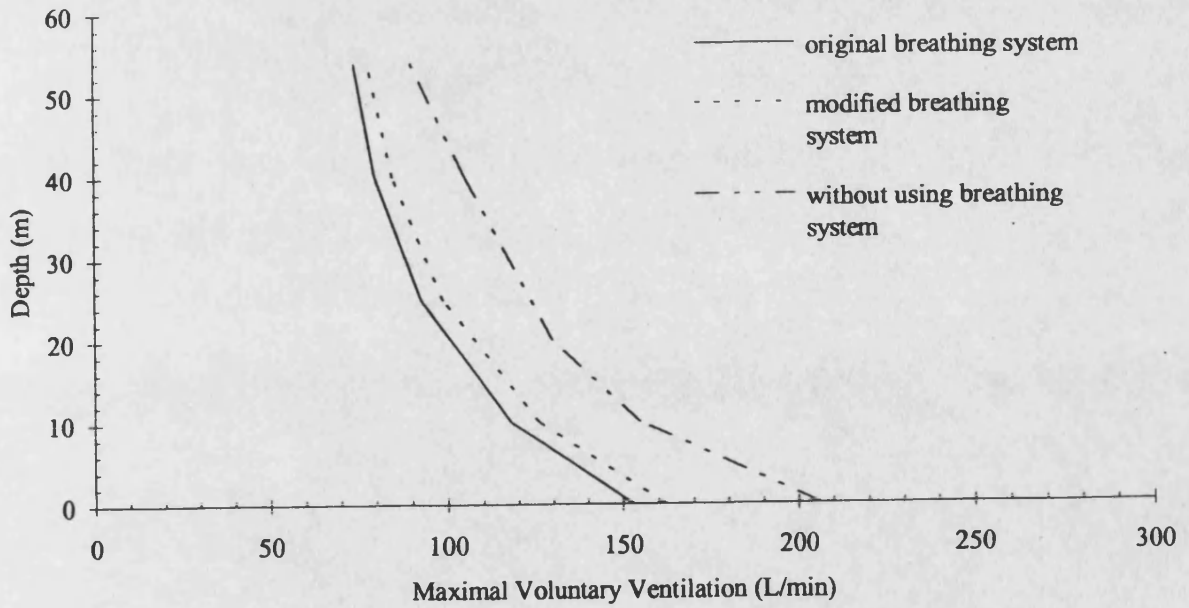
Figure 5.21 Predicted MVV of a diver using the semi-closed-circuit breathing system at different diving depths
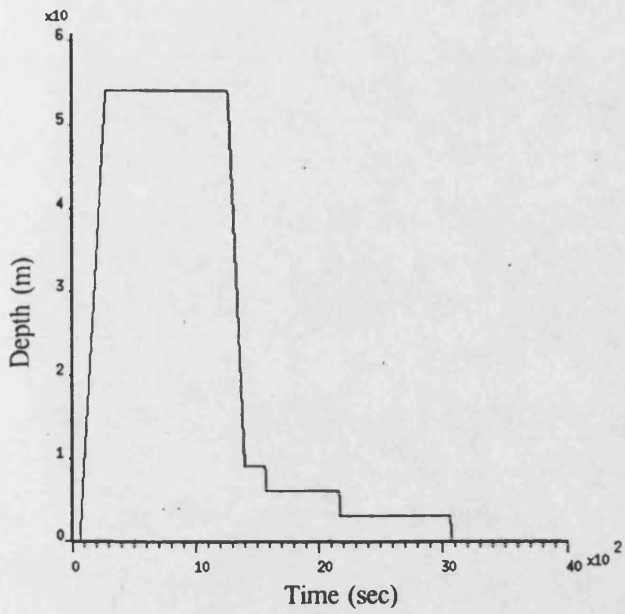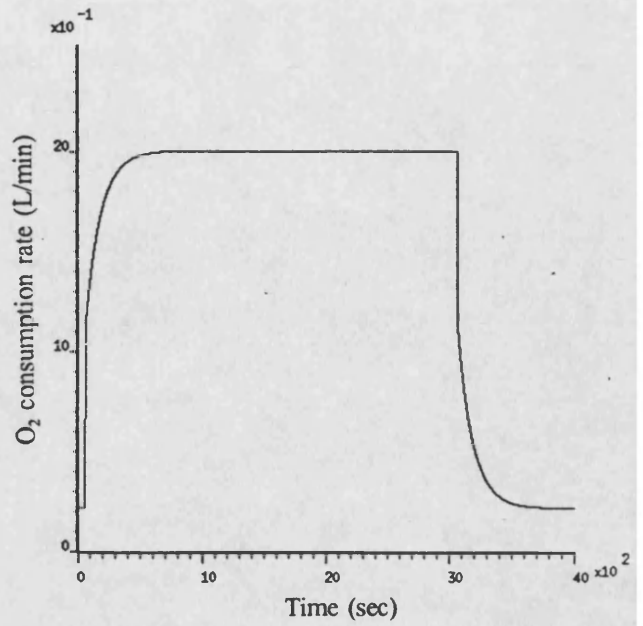
(a) Diving schedule

(b) Overall O_2 consumption rate
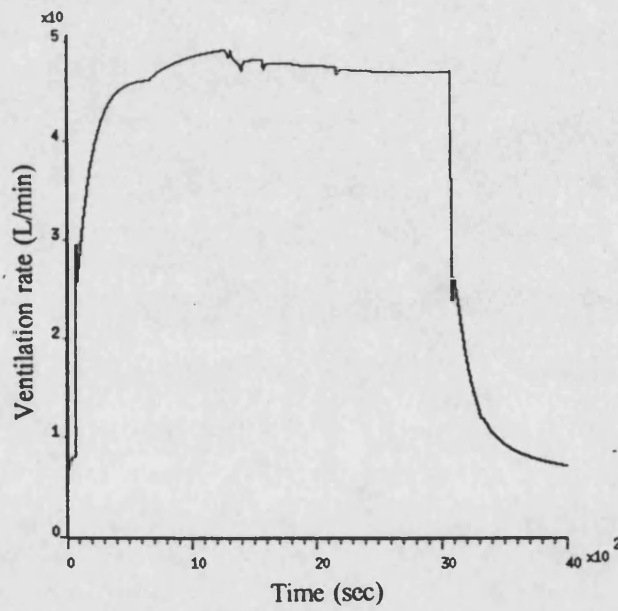
(c) Lung ventilation rate

Figure 5.22 Simulation results of manned diving operation using the semi-closed-circuit breathing system for the schedule of 54 m dive and 20 min bottom time

(a) P_{O2}

(b) P_{N2}

(c) P_{CO2}
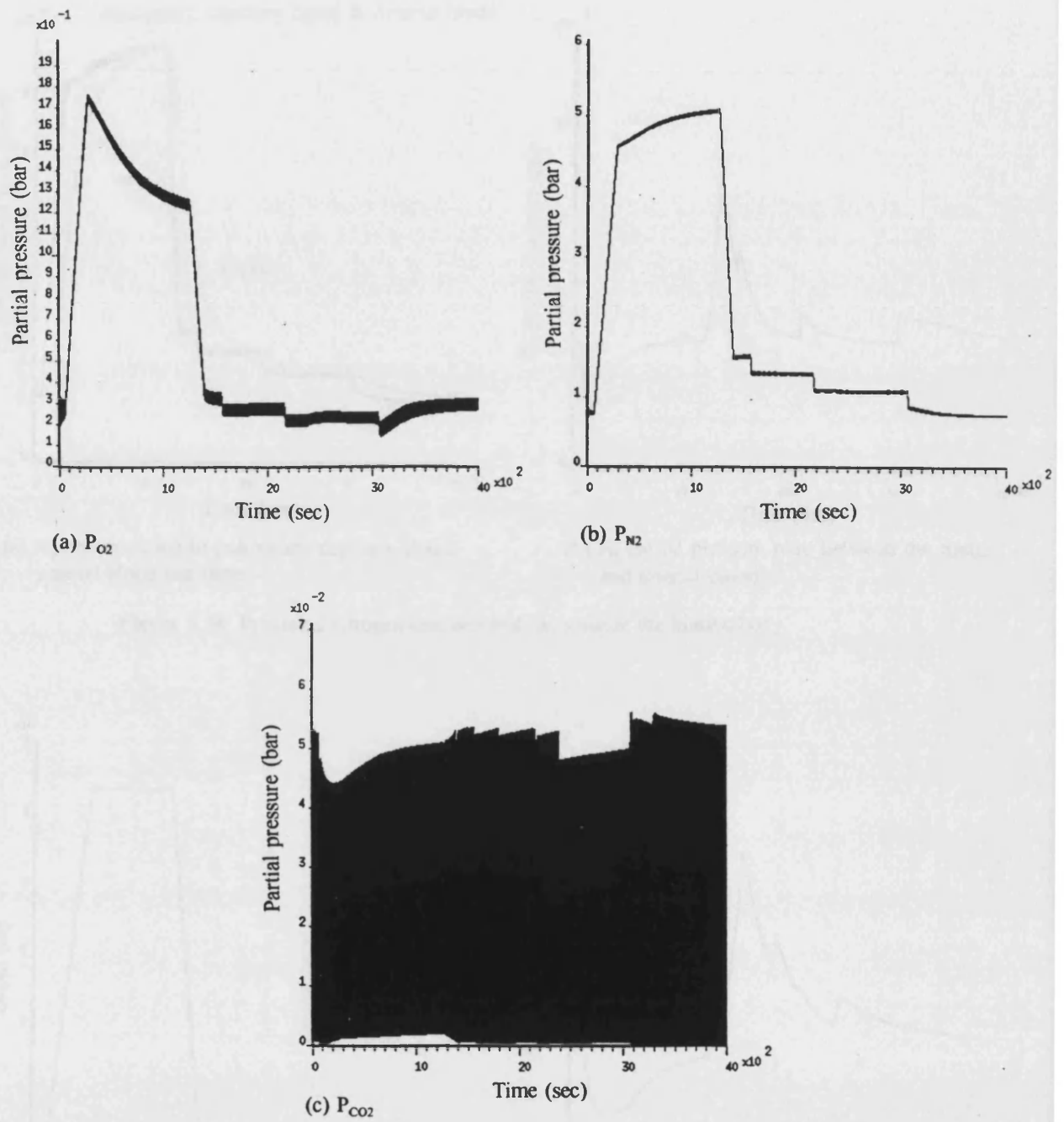
Figure 5.23 Predicted gas partial pressures at the mouthpiece during 54 m dive
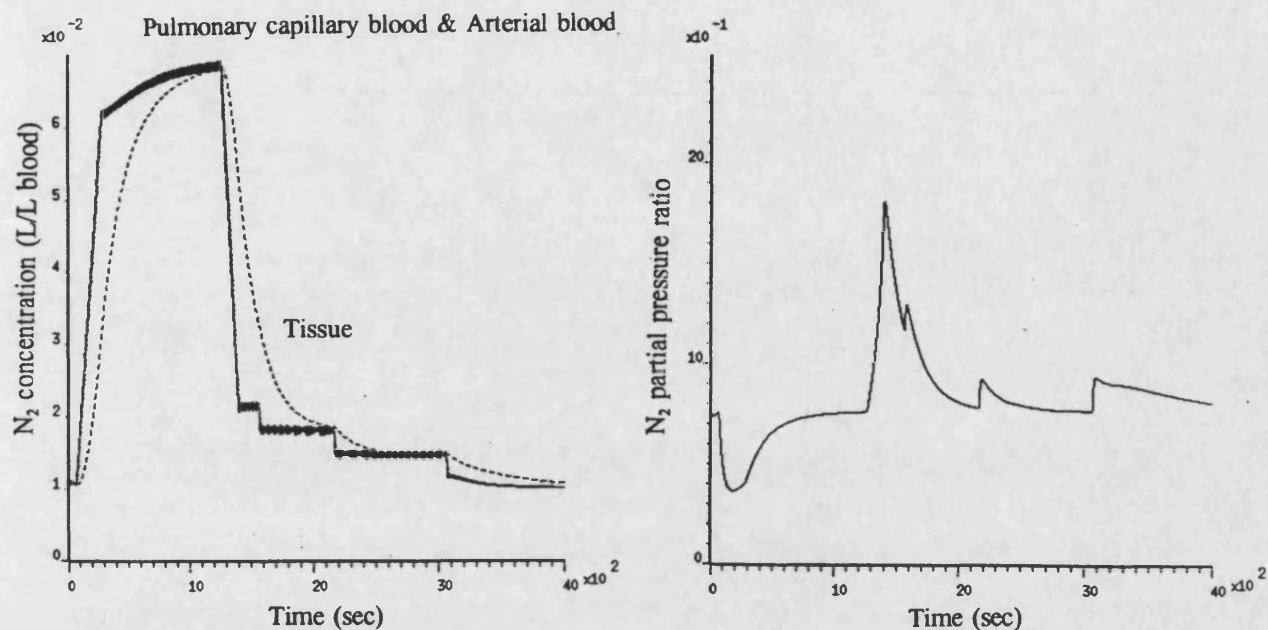
179

(a) N_2 concentration in pulmonary capillary blood, arterial blood and tissue

(b) N_2 partial pressure ratio between the tissue and arterial blood

Figure 5.24 Predicted nitrogen tensions and ratio inside the human body
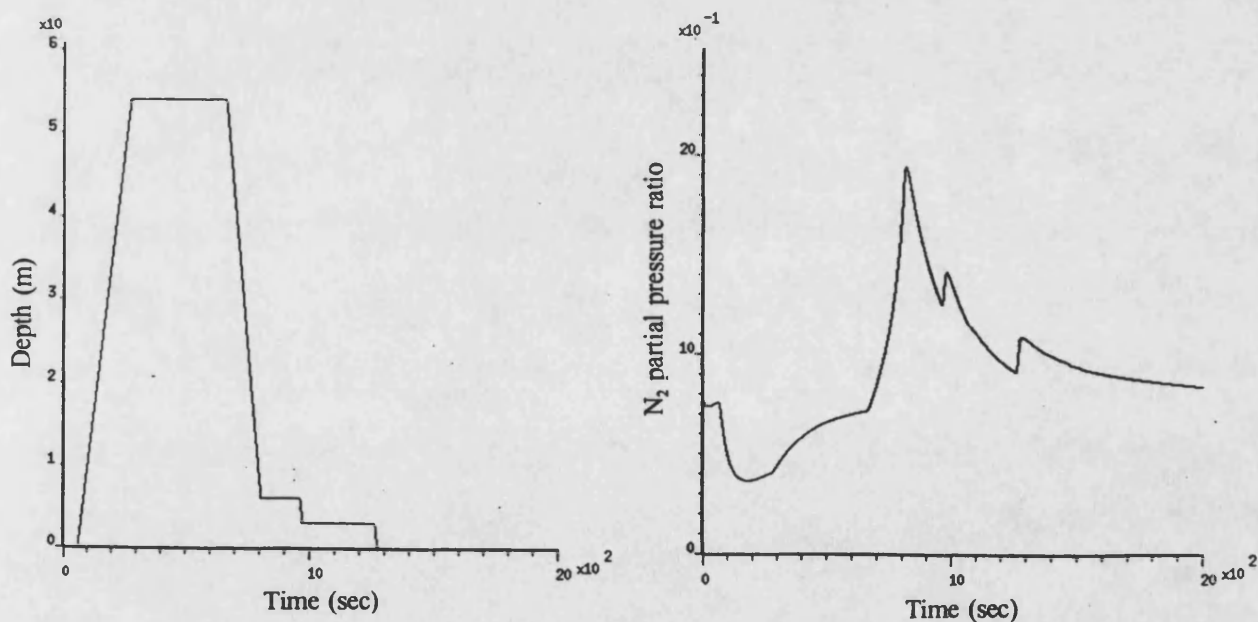
(a) Diving schedule

(b) N_2 partial pressure ratio between the tissue and arterial blood

Figure 5.25 Simulation results of manned diving operation using the semi-closed-circuit breathing system for the schedule of 54 m dive and 10 mins bottom time

180

(a) Diving schedule

(b) N$_2$ partial pressure ratio between the tissue and arterial blood
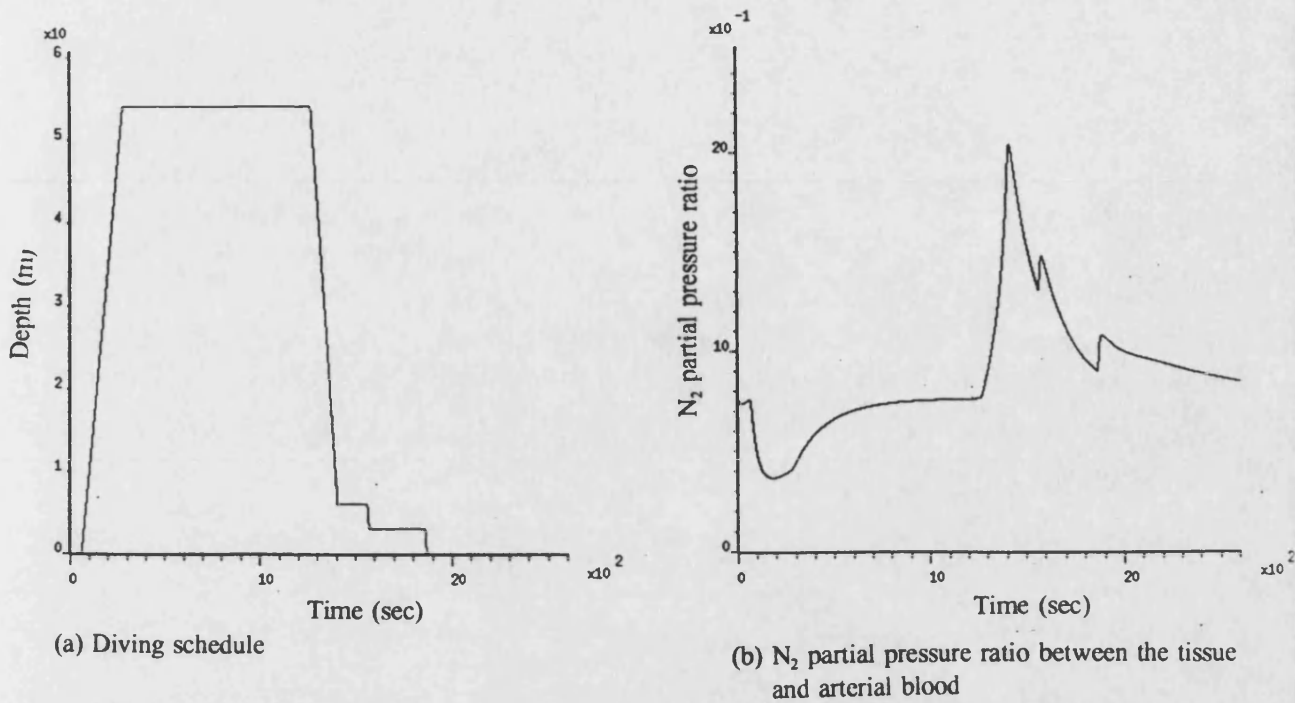
Figure 5.26 Simulation results of manned diving operation using the semi-closed-circuit breathing system for the schedule of 54 m dive and 10 mins bottom time but staying actually 20 mins bottom time

(a) Diving schedule

(b) N$_2$ partial pressure ratio between the tissue and arterial blood
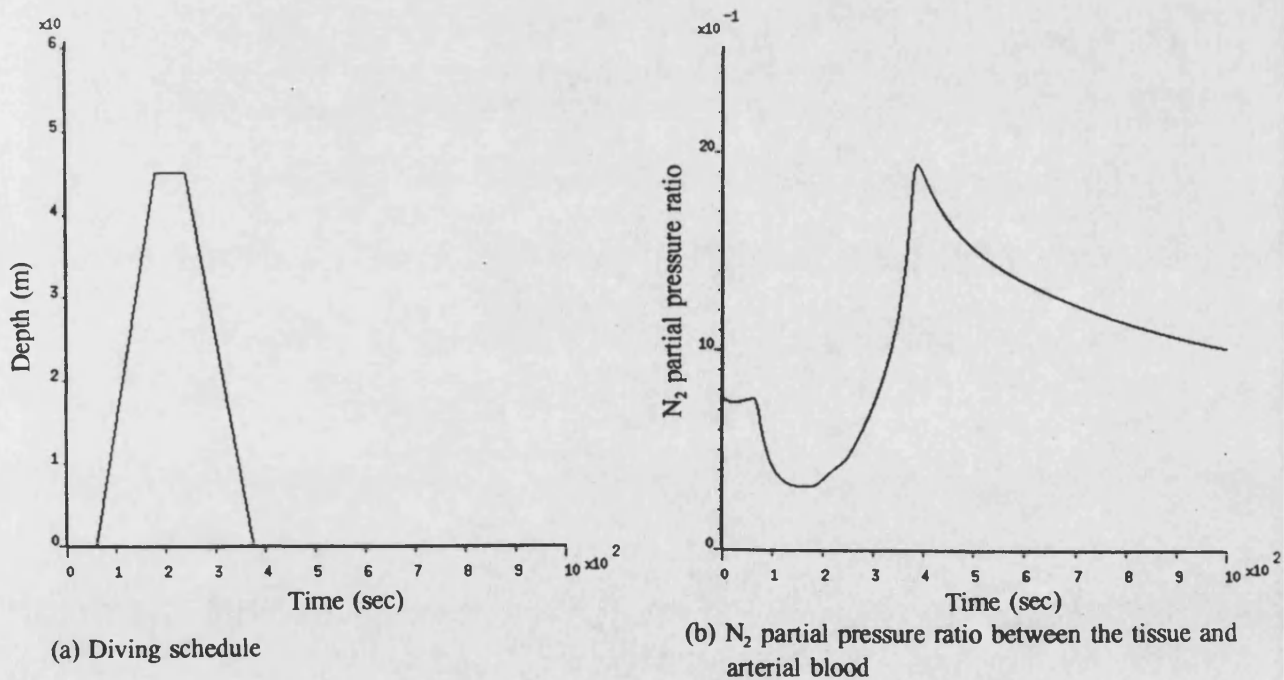
Figure 5.27 Simulation results of manned diving operation using the semi-closed-circuit breathing system for the schedule of 45 m dive and 3 mins bottom time and then returned back to the surface without commencing any stops

181
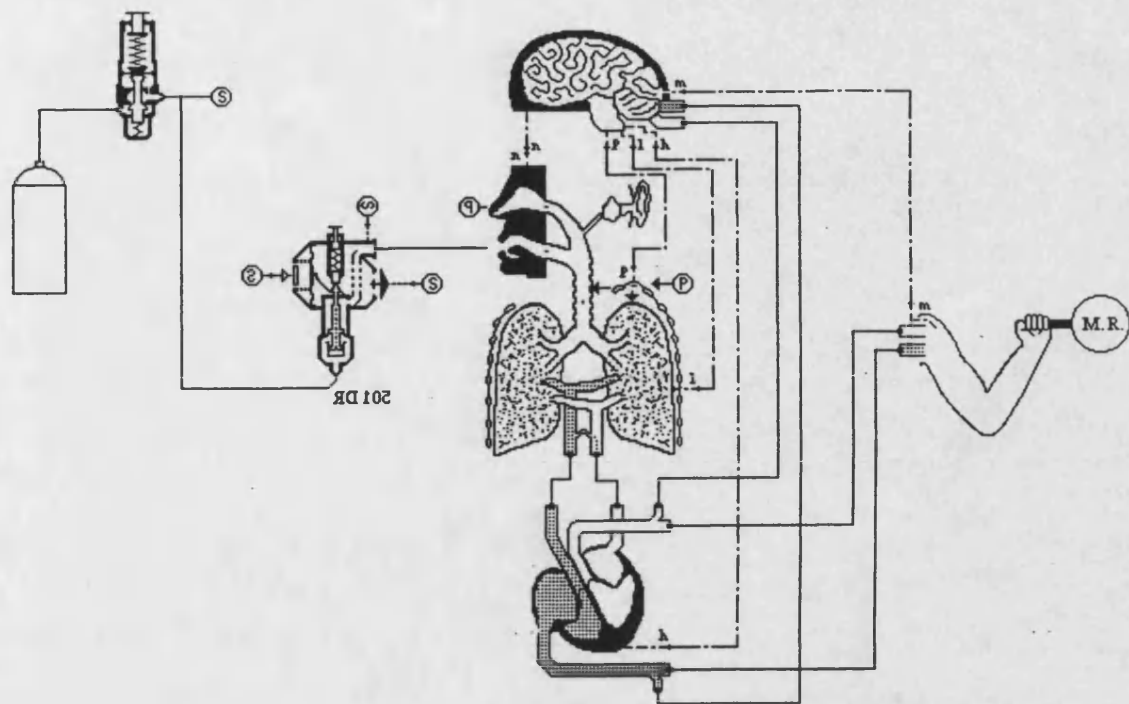
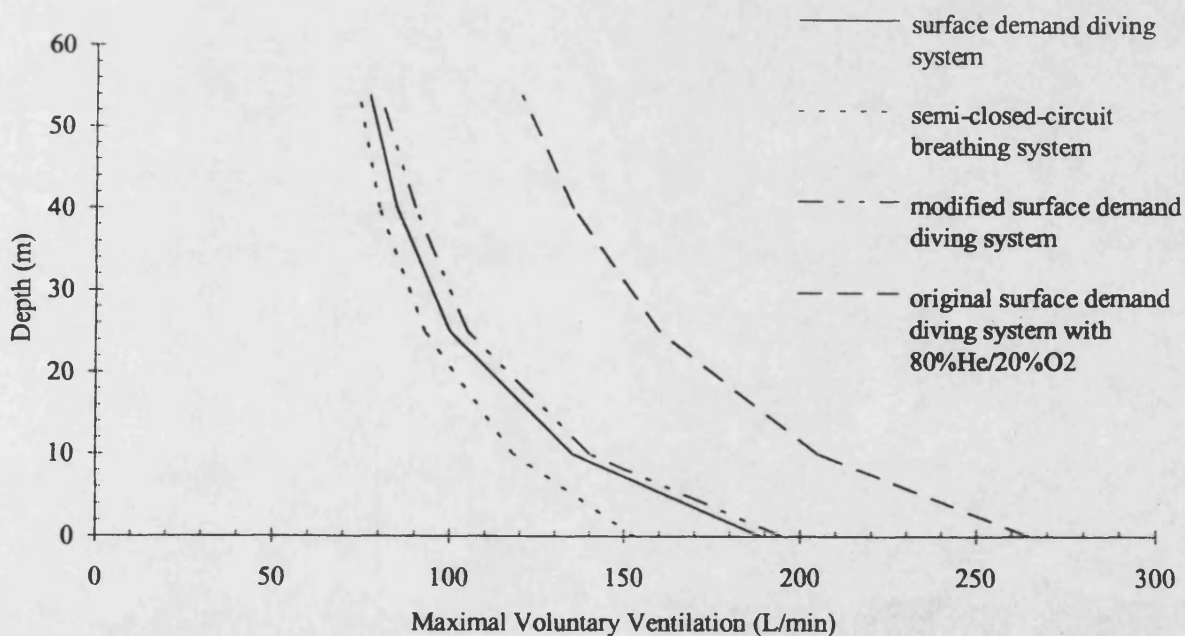**Figure 5.28** Simulation of a diver using the surface demand diving system in Bath*fp*
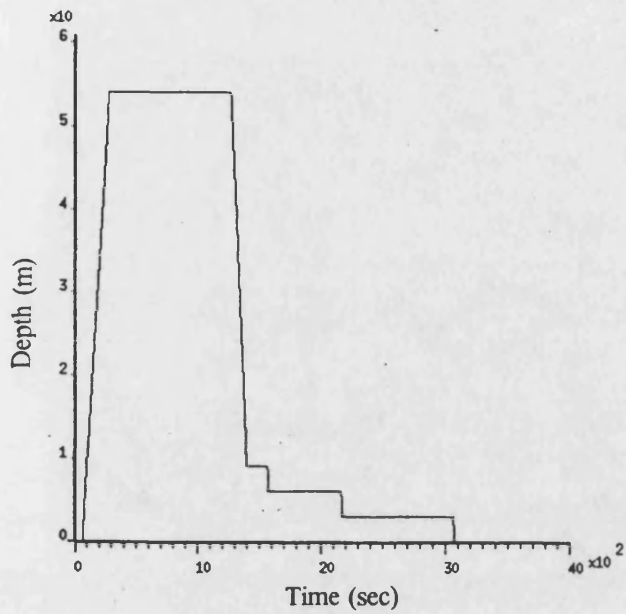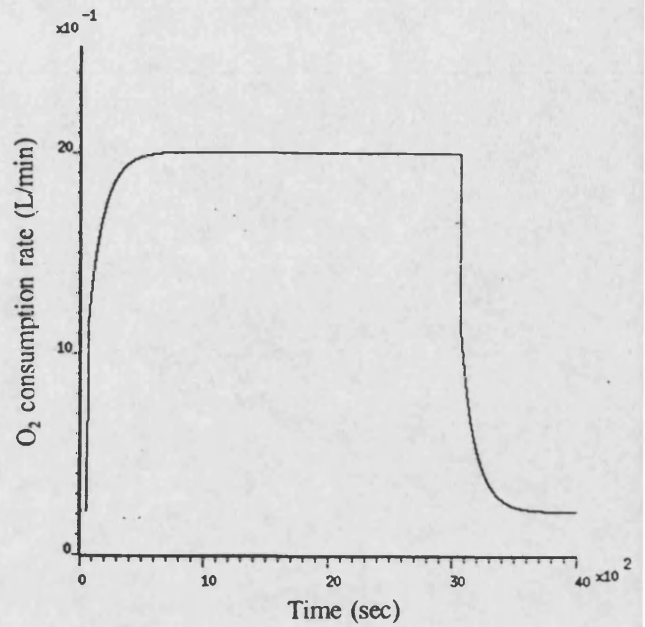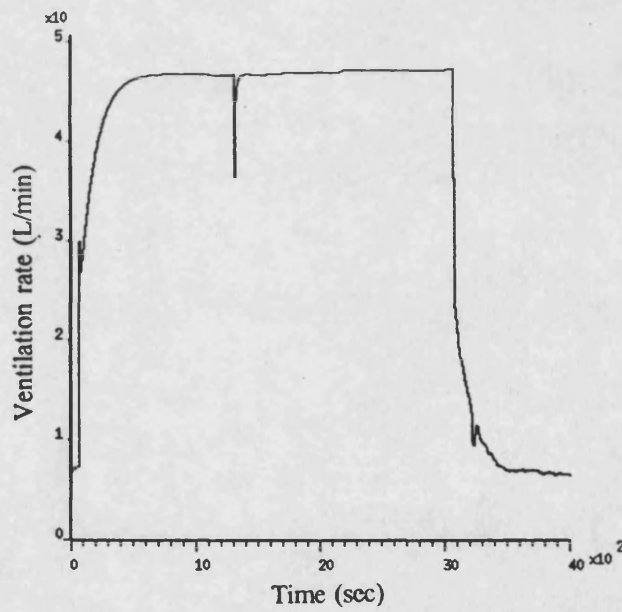

Figure 5.29 Predicted MVV of a diver using the surface demand diving system at different diving depths
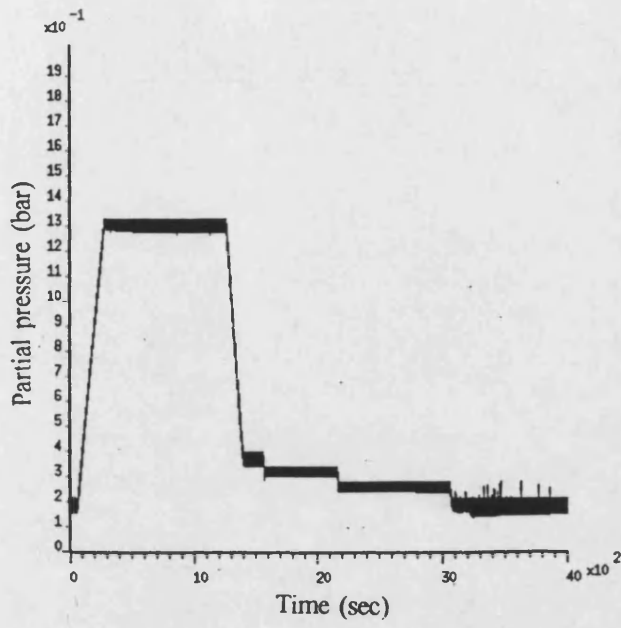
(a) Diving schedule

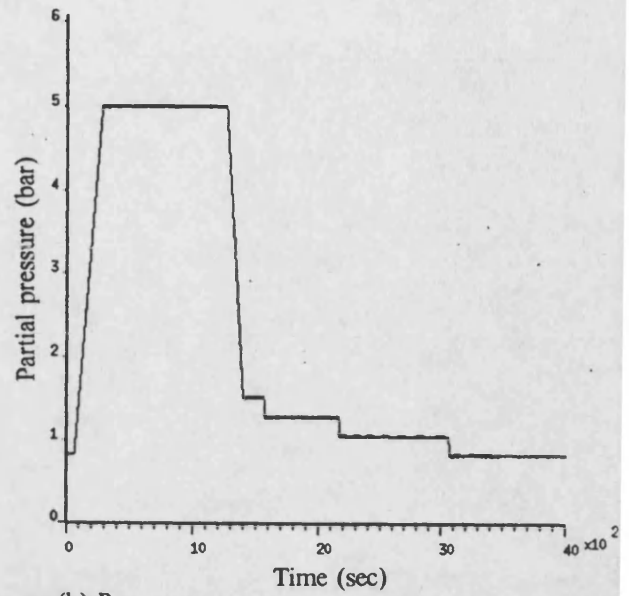(b) Overall O_2 consumption rate
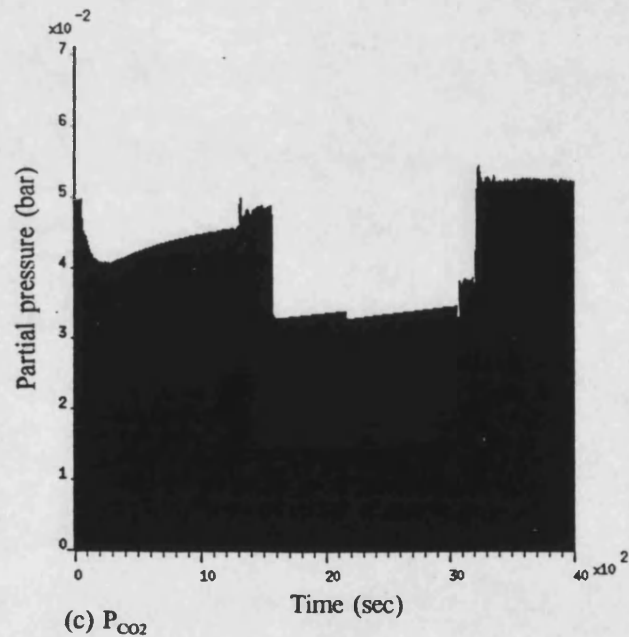
(c) Lung ventilation rate

Figure 5.30 Simulation results of manned diving operation using the surface demand diving system for the schedule of 54 m dive and 20 min bottom time

(a) P_{O_2}

(b) P_{N_2}

(c) P_{CO_2}

Figure 5.31 Predicted gas partial pressures at the mouthpiece during 54 m dive

[1]_____ Pulmonary capillary blood
[2]........ Arterial blood
[3]____ Tissue

(a) N_2 concentration in pulmonary capillary blood, arterial blood and tissue

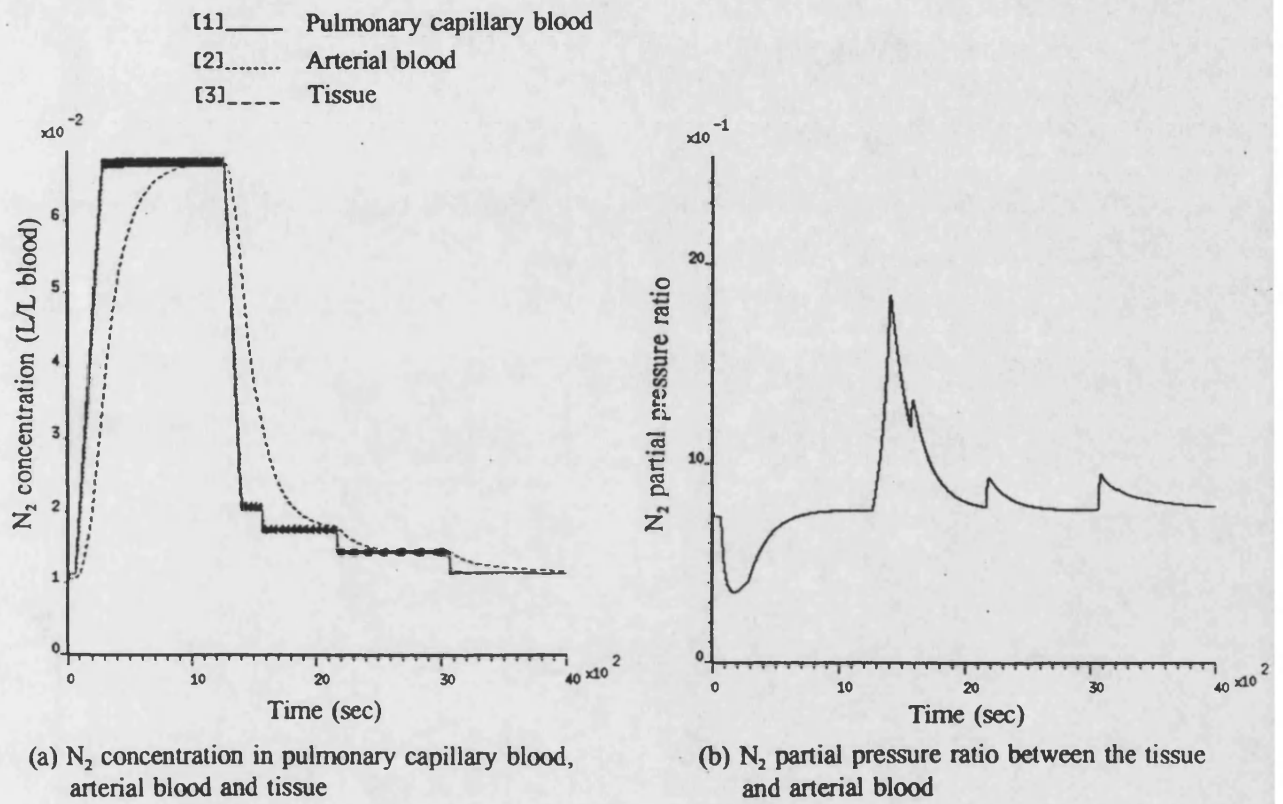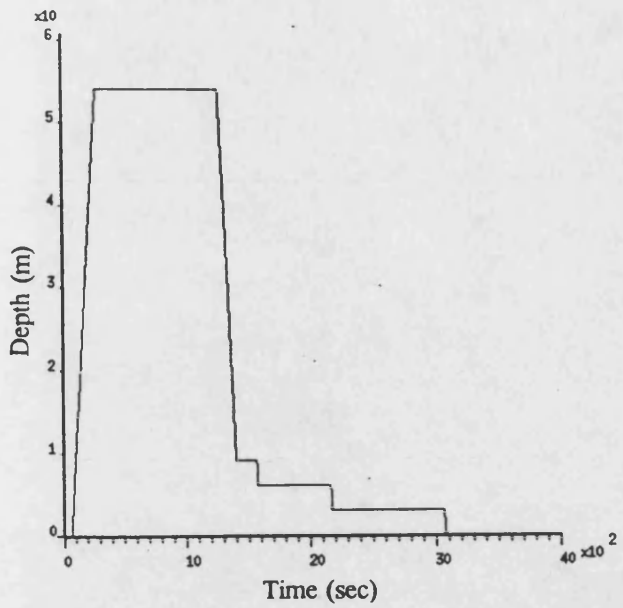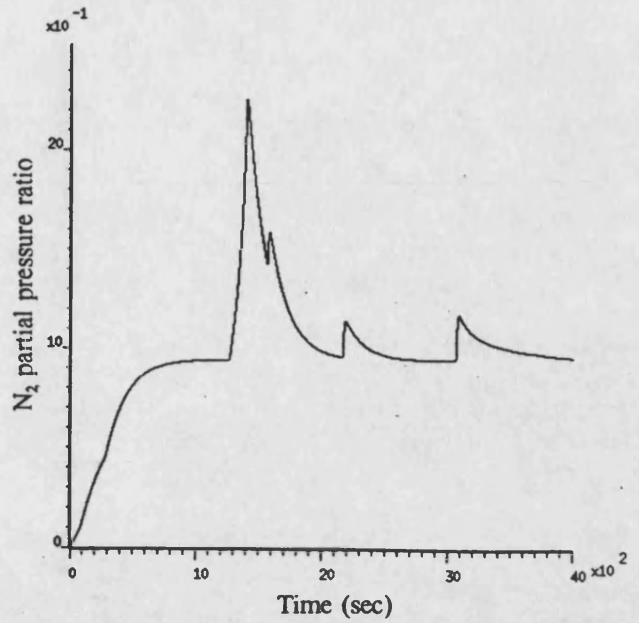(b) N_2 partial pressure ratio between the tissue and arterial blood

Figure 5.32 Predicted nitrogen tensions and ratio inside the human body

(a) Diving schedule

(b) N₂ partial pressure ratio between the tissue and arterial blood

Figure 5.33 Simulation results of manned diving operation using the surface demand diving system for the schedule of 54 m dive and 20 mins bottom time with oxy-helium mixture
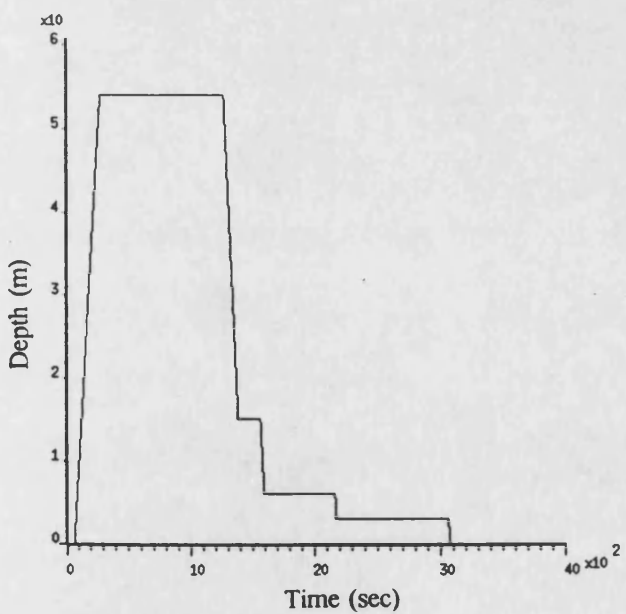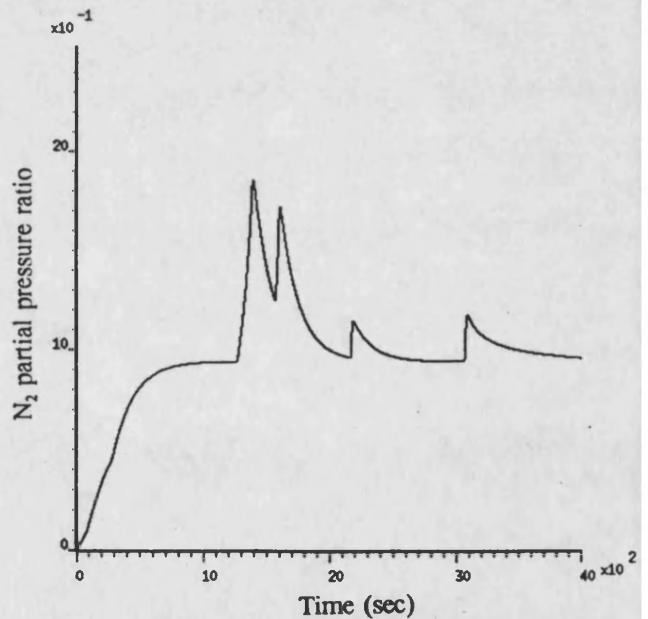

(a) Diving schedule

(b) N₂ partial pressure ratio between the tissue and arterial blood

Figure 5.34 Simulation results of manned diving operation using the surface demand diving system under different decompression process for the schedule of 54 m dive and 20 mins bottom time with oxy-helium mixture

186

CHAPTER 6

OTHER GAS BASED SYSTEMS

6.1 INTRODUCTION

Based on the success obtained during the simulation study of the underwater breathing apparatus and the human respiratory system, further investigations were undertaken to extend the simulation techniques to other gas based systems. The work included the simulation of a submarine escape system and industrial pneumatic systems. Thus, the additional work show how the developed simulation techniques can be used for assessing and improving other gas based systems.

6.2 SIMULATION OF A SUBMARINE ESCAPE SYSTEM

6.2.1 Introduction

In the event of an occupant being trapped in an immobilised submarine, one method of escape is by means of a submarine escape immersion suit and system. This suit, shown in figure 6.1, incorporates a built-in life-jacket and an enclosed hood to sustain the escaper during ascent. When inside an escape tower, see figure 6.2, the escaper connects the suit to an air supply control system by means of an extension hose. The life-jacket is initially inflated, allowing air through two relief valves into the hood for the escaper to breathe normally. Excess air inside the hood is expelled through a small vent to the surroundings. Simultaneously, the tower is flooded and pressurised to submarine ambient sea water pressure. When the escape tower pressure is equal to that outside the submarine, a hatch opens automatically and the escaper floats to the surface due to the buoyancy of the suit. When one submariner has escaped from the tower, it is depressurised and drained ready for the next escaper. It is vital that the escaper does not breath high pressure air for prolonged periods so that the pressurisation process needs to be short. In addition, the air supply control system, which senses the tower pressure, must maintain the hood pressure significantly above the hydrostatic pressure acting on the hood throughout the pressurisation process. Failure to meet this requirement can lead to the ingress of water into the hood, reducing the buoyancy of the suit for the escape.

A schematic representation of the escape suit and the air supply control system is shown in figure

6.2. The supply air, stored in two pressurized cylinders, passes through a puncture valve and its pressure is lowered to a working level by a pressure reducing valve. Subsequently, the low pressure air is fed through a pressure control valve which is situated inside the escape tower. This valve, which senses the tower pressure and the downstream air pressure from a feedback pipe, supplies the air through a plunger valve and a corrugated hose to the life-jacket. The dual pressure relief valves, which are located at the shoulder position, vent gas from the life-jacket to the hood. It is important that hood pressure is sufficiently above surrounding water pressure to prevent water ingress with consequent danger to the escaper. Excessive air inside the hood will leave through the small vent at bottom of the hood to the surrounding water.

6.2.2 Component models development

The simulation techniques described in chapter 2 have been used to develop the models for this study. The approach developed to simulate the variation of gas composition is not included as the gas composition within the system is constant. The following sections give details of the theoretical analysis developed for the system models.

(i) Air storage supply cylinders

The storage supply cylinders are modelled as a single control volume using the same approach described in section 2.5.

(ii) Puncture valve

When a submarine escape commences, a puncture valve (figure 6.3) is used to rupture a diaphragm, allowing high pressure air from the storage cylinders to enter the system. The gas flow discharged by the valve can be determined using the similar approach to that outlined for the restrictive element, see section 2.2.2.

(iii)Pressure reducing valve

A schematic of the pressure reducing valve used in the air supply control system is shown in figure 6.4. Referring to figure 3.26, it is found that the mechanism of this valve is similar to the pressure reducing valve used in the surface demand diving system. Therefore, the valve head motion and the gas flow through this valve can be determined using a similar approach to that described in section 3.3.2(i).

(iv) Pressure control valve

The function of this valve is to ensure that the escape suit inflates in a safe manner as the tower is pressurised. The valve (figure 6.5) consists of a diaphragm, which balances the downstream pressure (from a feedback pipe) against the water pressure inside the tower. The valve action ensures that the output pressure closely matches the variation in ambient water pressure but is maintained slightly above it. Referring to figure 6.5, the water pressure and the valve outlet pressure exert a force on the diaphragm and the spool head to open the valve. The feedback pressure acts on the diaphragm tending to close the valve. Hence, the net opening pressure force acting on the spool is given by

$$F_P = P_{out} A_{cv} + P_w (A_{di} - A_{cv}) - P_{fb} A_{di}$$ (6.1)

Since the material of the diaphragm is very stiff, it is reasonable to consider that the stiffness of the diaphragm will tend to close the valve. Hence, the net spring force acting on the spool is given by

$$F_s = k_{cv}(x_{k,cv} - x_{cv}) - k_{di} x_{cv}$$ (6.2)

After identifying the net pressure force and the net spring force acting on the valve, the approach described in section 2.8 can be used to simulate the valve head motion and the gas flow through the valve.

The dynamic changes of the gas and water pressures acting on the diaphragm may have a significant influence on the valve performance. Hence, more accurate models for the gas and water chambers inside the valve have been developed. For the gas chamber, the rate of change of pressure and temperature inside can be obtained by

$$\dot{P}_{fb} = \frac{n}{V_{fb}} [R (q_{fb,in} T_{in} - q_{fb,out} T_{fb}) + P_{fb} A_{di} \dot{x}_{cv}]$$ (6.3)

$$\dot{T}_{fb} = \frac{T_{fb}}{P_{fb} V_{fb}} (\dot{P}_{fb} V_{fb} - P_{fb} A_{di} \dot{x}_{cv} - \dot{m} R T_{fb})$$ (6.4)

The mass flow rate through the feedback pipe restrictor q_{fb} in equation (6.3) can be obtained using the same form as for the restrictive element.

189

For the water chamber the rate of change of water pressure is given by

$$\dot{P}_w = B_w [\ Q_w - (A_{di} - A_{cv})\dot{x}_{cv}\ ] / V_w \qquad (6.5)$$

The volumetric flow rate of water through the holes at the external of the valve can be determined using the approximated approach described by McCloy and Martin (1973), that is

$$Q_w = C_d\ A_f\ \sqrt{\frac{2\ \delta p}{\rho_w}} \qquad (6.6)$$

The term δp is the difference between the hydrostatic pressure acting on the outside of the valve and the water pressure inside the valve.

(v) Plunger valve

This valve (figure 6.6) connects the air supply to the suit and operates when the corrugated hose is plugged in and the central rod of the valve is pushed down, providing an annular flow path for air flow. It is reasonable that the approach described in section 2.2.2 for the restrictive element can be used to determine the mass flow through the valve.

(vi) Pipe

The flow resistance associated with the pipes is considered in the simulation of the submarine escape system and the technique described in section 2.6 is used.

(vii) Corrugated hose

The pressure losses due to corrugation, bendings and end-fittings of the hose are modelled as for a pipe using an equivalent relative roughness factor for the corrugations.

(viii) Life-jacket

In order to obtain the correct life-jacket shape, two tucks in the material are required. These tucks effectively create two ports which separate the life-jacket into three chambers as shown in figure 6.7. For each chamber, the pressure is obtained using an equation of a similar form to that of the counterlung, see equation (3.4). In this case, the dV/dt term represents the rate of change of life-jacket volume during inflation and deflation. In reality the life-jacket does not collapse during the pressurisation process. Hence,

190

the dynamic analysis accounting for the life-jacket volume is not required (i.e. $dV/dt = 0$). The mass flow rates through the two ports are obtained using the flow equation for the restrictive element.

(ix) Pressure relief valve

This valve, shown in figure 6.8, operates when the difference between the upstream and downstream pressures exceeds a set level. It consists of a lightweight rubber diaphragm, held in place by two compression springs whose initial spring compression determines the valve cracking pressure. Hence, the approach described in section 2.8 is used again for simulating the valve with the net pressure and spring forces given by

$$F_P = (P_{in} - P_{out}) A_{rv} \tag{6.7}$$

$$F_s = -k_{rv} (x_{k_{rv}} + x_{rv}) \tag{6.8}$$

A step change discontinuity is observed in the measured pressure drop at a particular mass flow rate as shown in figure 6.9. The original model did not show this discontinuity so further analysis was required to account for it. Assuming flow around a cylinder, as shown in figure 6.10(a), such that the change in the flow pattern is from laminar flow to turbulent flow results from developments in the boundary layer (Massey, 1983). At first, this transition takes a rather complicated form: laminar fluid close to the wall moves away as it enters the attached eddies; transition then occurs very quickly and the turbulent flow reattaches to the wall a small distance downstream from the laminar separation. This transition causes a change of flow pattern around the cylinder and this is assumed to occur to the flow passing through the pressure relief valve (figure 6.10(b)). As a consequence, the flow momentum force increases causing an extra closing force on the valve head during the high flow rate period (which is the turbulent region). In the model, when $Re > 4.8 \times 10^5$, it is assumed that the flow angle changes from 90° to 60°. This modification provides a better correlation between the measured and predicted pressure-flow characteristics as shown in figure 6.9.

(x) Hood

The hood has been modelled as an inverted bucket with two inlet flows from the dual pressure relief valves and an outlet flow through a small vent to the surroundings. The model accounts for air flowing out of the small vent q_{sv} using the gas flow equation for the restrictive element and water flowing

191

in through the small vent Q_{sv} using the water flow equation in the pressure control valve (equation 6.6). In the latter case, the pressure acting on the inlet of the small vent includes the head of water inside the hood (see figure 6.11) and is given by

$$\mathcal{P}_{sv,in} = P_h + \rho_w \, g \, z_{sv} \tag{6.9}$$

In addition, the variation of depth of water inside the hood can be obtained by

$$dz_{hl}/dt = Q_{sv}/A_{aw} \tag{6.10}$$

According to figure 6.11, the local contact surface area between the air and water inside the hood A_{aw} can be obtained by the following relationship:

$$A_{aw} = [\hat{A}_{aw} - A_{sv}] \, (z_{hl}/\hat{z}_{hl}) + A_{sv} \tag{6.11}$$

During the pressurisation process, the escape suit requires high pressure air in order to prevent hood collapse. Since the escaper breathes in air from the hood, the gas volume of the hood and the lung can be regarded as a single control volume through which air flows and water may ingress into the hood during the charging process. Using the same approach for the capacity element, the rate of change of hood pressure and temperature can be written as

$$\dot{P}_h = \frac{n}{V_h + V_l} [R(2 q_{rv} T_{in} - q_{sv} T_h) + P_h Q_{sv}] \tag{6.12}$$

$$\dot{T}_h = \frac{T_h}{P_h (V_h + V_l)} [\dot{P}_h (V_h + V_l) - P_h Q_{sv} - \dot{m} R T_h] \tag{6.13}$$

Note that V_h is the gas volume inside the hood.

(xi) Hydrostatic pressure acting on the system

The hydrostatic pressure acting on the system has a significant effect on performance and it is important to account for this in the models of the pressure control valve and the hood. When the tower is flooded to a certain water level, the pressure head above the pressure control valve is taken from the water surface inside the chamber to the centre of the valve. At this condition the hydrostatic pressure acting on the pressure control valve is

$$\mathcal{P}_{cv} = P_{tow} + \rho_w \, g \, z_{cv} \tag{6.14}$$

If the distance from the water surface inside the tower to the small vent in the hood is h_{sv}, then the hydrostatic pressure acting outside of the small vent is

$$P_{sv,out} = P_{tow} + \rho_w \, g \, z_{sv} \tag{6.15}$$

where the pressure of the air space inside the tower P_{tow} is the pressurisation profile occurring in the escape tower.

6.2.3 Simulation studies and results

Examples are presented which show how the simulation can be used to assess and improve system performance. Both apply to the unmanned test arrangement where the suit is worn by a mannequin, using an imitation lung. The water inside the chamber is pressurized to a scheduled profile, until a submarine ambient water pressure corresponding to a depth of 180 m is achieved. Figure 6.12 shows the pressurisation profiles for conditions (28 and 21 seconds), which are represented by the depth of water. A block diagram, shown in figure 6.13, show the interconnections of the models. Figure 6.14 is the simulation schematic of the submarine escape system in Bath*fp*. The data used in the models is presented in table 6.1.

It is important that ingress of water into the hood is prevented during the pressurisation process. If the pressure difference between the hood and the air space inside the chamber is less than the pressure head of water between the surface of water inside the chamber and the small vent at the bottom of the hood (which is 0.0525 bar), water will enter into the hood with consequent danger to the escaper. Hence, this pressure difference is used to express the degree of water ingress into the hood during the pressurisation process. Recordings of this pressure difference were taken from a test rig for comparison with the simulation. The pressure differences between all other important system elements and the air space were also measured in order to correlate with the simulation.

The simulation predictions using pressurisation periods of 28 and 21 seconds are presented in figures 6.15 and 6.16 respectively. It can be seen that the effect of reducing the pressurisation period gives a larger 'dip' in the pressure difference profile between the hood and the air space inside the chamber. As a consequence, there is a greater tendency for water to enter the hood at the higher pressurisation rate. The simulation clearly shows that the operation of the submarine escape system is sensitive to the pressurisation rate.

Referring to figures 6.15(a) and 6.16(a), the pressure loss in the pipe connecting the pressure reducing valve to the pressure control valve increases with increasing pressurisation rate and the upstream pressure of the pressure control valve therefore decreases. Similar increases in the differential pressures between the air space inside the chamber and the pressures at the control valve outlet and the plunger valve outlet occur with increasing pressurisation rate, as shown in figures 6.15(b) and 6.16(b). This does not occur with the differential pressures between the air space inside the chamber and the pressures at the relief valve inlet and the hood. The significant flow resistance in the pipes connecting the pressure reducing valve to the pressure control valve and the flow path between the plunger valve and the life-jacket have a pronounced effect on system performance, as these flow resistances become increasingly significant at high pressurisation rates. The corresponding experimental data obtained using the hyperbaric chamber are included in figures 6.15 and 6.16. From the comparisons it is shown that the simulation predictions are in close agreement with experimental data.

6.2.4 Improving system performance

The simulation studies have identified that excessive pipe flow resistances lead to poor efficiency of the system during the high pressurisation rate. Significant improvements in performance are possible by increasing the sizes of pipes and ports inside the life-jacket. Figure 6.17 shows the effect of increasing the internal diameter for the pipe connecting the pressure reducing valve to the pressure control valve by 50% and the flow area for the ports inside the life-jacket by 100%. The upstream pressure profiles of both the pressure control valve and pressure relief valve increase at the period of high pressurisation rate and the pressure difference between the hood and the air space inside the chamber remains constant throughout the pressurisation process. The escaper will therefore be protected from water ingress under this condition.

6.3 SIMULATION OF INDUSTRIAL PNEUMATIC SYSTEMS

6.3.1 Introduction

Pneumatic systems are used extensively in many different industries including aerospace, process control, nuclear and mining. The requirements for these systems can vary considerably from simple linear actuator circuits to sophisticated automatic control systems. The system designer must ensure that performance, safety and reliability are achieved at an economic cost. This requires a detailed performance

assessment at the design stage. Computer simulation can be used to assist the designer in achieving the desired specifications. It can be used to assess conceptual designs, compare competing designs, aid system development, investigate the consequences of component malfunctions and to identify in-service problems. For this reason, models have been developed specifically for fluid power applications with the aim of simulating the industrial pneumatic systems.

6.3.2 Component models development

There are six types of components commonly used in industrial pneumatic system. These are (a) gas bottles, (b) orifices or restrictions, (c) valves, (d) linear actuators, (e) compressors and (f) pipes/hoses. Since the simulation techniques for the gas bottle, orifice, valve and pipe have already described in chapter 2, the following subsections only describe the theoretical analysis developed for the models of linear actuator and the compressor.

(i) Linear actuator

Linear actuators are used to convert gas pressure or flow into force or motion. The piston motion can be obtained using a similar approach to that outlined for the valve. In this case, the spring compression force $(k_s x_{act})$ and flow momentum force (F_m) are not considered and the piston acceleration is obtained by the following equation:

$$\frac{d^2 x_{act}}{dt^2} = \frac{1}{M_e} \left(F_P - M_e g \sin\phi - f \, dx_{act}/dt - F_C \right) \tag{6.16}$$

In the case of equal piston areas, see figure 6.18, the net pressure force in equation (6.16) is given by

$$F_P = (P_{act,1} - P_{act,2})(A_{pl} - A_{rod}) \tag{6.17}$$

Using equation (2.17) and (2.18), the rate of change of pressures and temperatures in chambers '1' and '2' are determined as follows:

For chamber 1

$$\dot{P}_{act,1} = \frac{n}{V_{act,1}} \left[R \left(\Sigma \dot{m}_{in,1} T_{in,1} - \Sigma \dot{m}_{out,1} T_{act,1} \right) - P_{act,1} (A_{pl} - A_{rod}) \dot{x}_{act} \right] \tag{6.18}$$

$$\dot{T}_{act,1} = \frac{T_{act,1}}{P_{act,1} V_{act,1}} \left[\dot{P}_{act,1} V_{act,1} + P_{act,1} (A_{pi} - A_{rod}) \dot{x}_{act} - \dot{m}_{act,1} R T_{act,1} \right] \tag{6.19}$$

For chamber 2

$$\dot{P}_{act,2} = \frac{n}{V_{act,2}} [R (\Sigma \dot{m}_{in,2}T_{in,2} - \Sigma \dot{m}_{out,2}T_{act,2}) + P_{act,2}(A_{pi} - A_{rod})\dot{x}_{act}]$$ (6.20)

$$\dot{T}_{act,2} = \frac{T_{act,2}}{P_{act,2}V_{act,2}} [\dot{P}_{act,2}V_{act,2} - P_{act,2}(A_{pi} - A_{rod})\dot{x}_{act} - \dot{m}_{act,2}RT_{act,2}]$$ (6.21)

The mass flow rate due to piston leakage is considered in the inflow and outflow mass flow rates and is assumed to be in linear relationship with the pressure difference between the two chambers:

$$q_{le} = C_{le} (P_{act,1} - P_{act,2})$$ (6.22)

(ii) Compressors

Most pneumatic power sources use a compressor. These may vary in size from small industrial bench supplies for air driven tools up to 600 bar units consuming 15,000 hp. Most units are either reciprocating piston units or vane type. The problem with compressors is keeping the unit cool, and while air cooling is satisfactory for the small units, water cooling is essential for big compressor sets.

If the size, speed and inlet condition (such as gas density) of the compressor are known, the mass flow rate in kg/s supplied by the compressor can be determined by

$$q_{com} = \rho_{in} \frac{\omega}{60} V_{com} \times 10^{-6}$$ (6.23)

where the units of compressor size V_{com} and speed ω are cc/rev and rev/min respectively.

Electrical and petrol motor are commonly used for driving the compressor. The torque given from the compressor to the motor can be determined by

$$Tor = (P_{in} - P_{out}) \frac{V_{com}}{2\pi} \times 10^{-6}$$ (6.24)

It is necessary to point out that work done on the gas from the compressor is significant in this

case and the gas temperature will be rise through the compressor. The outflow temperature can be obtained using the irreversible adiabatic relationship:

$$T_{out} = T_{in} \left(\frac{P_{out}}{P_{in}} \right)^{(n-1)/n} \qquad (6.25)$$

The value of polytropic index n depends on the amount of cooling at the compressor. When there is perfect cooling, where the outflow temperature is equal to the inflow temperature, the polytropic index is 1 (isothermal compression). When there is no cooling, the polytropic index is equal to γ (isentropic compression). It is possible that the polytropic index n lies between 1 and γ, depending on the effectiveness of the cooling system. If $n<1$, the gas is cooled below the inlet temperature.

6.3.3 Simulation studies of a position feedback linear actuator system

To illustrate the way in which the developed models can be used to simulate the performance of industrial pneumatic systems, a position feed-back control actuator system is considered. Figure 6.19 and 6.20 show the block diagram and Bathfp simulation schematic of the system respectively.

Referring to figure 6.20, a equal area linear actuator, mounted horizontally, is used to move a load through a distance of 4 m. The requirements for the system are that the actuator should have a stop at 2 m during extension and another stop at 3 m during retraction. Also the time to reach those stops should not be more than 10 seconds. The system consists of an air storage bottle, a pressure reducing valve for reducing the supply air to a more manageable pressure and a three position, four port, closed centre directional control valve for flow modulation. A transducer is used to sense the position of the actuator piston and provide an output signal to a differencing element which compares this feedback signal with the desired actuator position value. The task of the differencing element is to perform the subtraction of these two signal to give an output referred to as the error or deviation. The deviation signal is fed to a first-order lag controller which represents valve dynamics and a proportional controller. The response from the lag is then fed to the directional control valve to determine the valve fractional opening. The measuring unit, differencing element and controller can be pneumatic or electronic instruments. The computer models of these control elements have already been well developed in the Bathfp simulation package. A detail description of the control element models can be found in Appendix B.

197

The data used in the computer models is presented in table 6.2. The results obtained from the simulation are shown in figure 6.21. This figure includes the comparison of desired and achieved actuator positions, fractional displacement of the direction control valve, pressures in both chambers of the actuator and the gas pressure inside the storage bottle. From figure 6.21(a) it can been seen that the response of the actuator is clearly unacceptable where the time to reach the stops are more than 10 seconds. Also, there is a slight overshoot in the actuator displacement. Hence further simulations were undertaken to investigate modifications which would give better performance. Figure 6.22 shows the effect of increasing the proportional controller gain by a factor of two. The response obtained for this modification is shown in figure 6.22(a). Although the time to reach the desired actuator positions was reduced, a further overshoot occurred. The achieved actuator position overshot the desired value, resulting in the directional control valve moving in the reverse direction, see figure 6.22(b), causing extra air usage from the storage bottle, see figure 6.22(d). The response obtained from this modification shows that the circuit was clearly incapable of controlling the actuator precisely. The circuit was modified further to incorporate a lead-lag compensator, see Appendix B. The data used in the lead-lag compensator model is presented in table 6.3. It is noticed that the same magnitude of gain is used in the lead-lag compensator model. The simulation results, presented in figure 6.23, indicates that satisfactory performance is obtained (figure 6.23(a)) with less air usage (figure 6.23(d)) than the previous modification.

6.4 CLOSURE

The modelling technique described in chapter 2 has been extended to develop mathematical models for a submarine escape system and an industrial pneumatic system. The models have been used to assess the performance of both systems.

During the simulation of the submarine escape system, good correlation was obtained between predicted and measured data. The simulation studies have indicated that the operation of the submarine escape system is sensitive to the pressurisation rate as this increases the flow resistances in the pipe connecting the pressure reducing valve to the pressure control valve and in the flow path between the plunger valve and the life-jacket, resulting in ingress of water to the hood of the escape suit. The simulation was also used to assess system modifications in order to improve system performance. These indicate that

a larger internal diameter for the pipe connecting the pressure reducing valve to the pressure control valve and an increased flow area for the ports inside the life-jacket can provide a greater safety margin for the escaper throughout the pressurisation process.

The simulation of the position feed-back control actuator system has been used as an example to illustrate the way in which the developed models can be used to simulate the performance of industrial pneumatic systems. Two extra component models have been developed for the purpose of the simulation. These are linear actuator and pneumatic compressor models. The simulation studies indicate how simulation can be used as a tool for the design of industrial pneumatic systems.

Models	Variables	Values	Units
Storage bottles	Initial gas pressure	200	bar
	Total gas volume	212	L
Puncture valve	Valve opening diameter	15	mm
Connection pipe	Pipe internal diameter	15.875	mm
	Pipe length	6.096	m
	k factor for bends and fittings	0.0001	-
	Relative roughness	0.002	-
Pressure reducing valve	Exposed piston diameter	30	mm
	Valve seat diameter	7	mm
	Maximum valve opening	2.5	mm
	Poppet angle	30	degrees
	Effective mass of moving parts	0.108	kg
	Spring rate of inlet valve head spring	12960	N/m
	Initial compression of inlet valve head spring	5	mm
	Spring rate of large spring	143600	N/m
	Initial compression of large spring	15.4	mm
	Viscous friction coefficient	500	N/(m/s)
	Coulomb friction	0	N
Connection pipe	Pipe internal diameter	10.4	mm
	Pipe length	4.972	m
	k factor for bends and fittings	9	-
	Relative roughness	0.0001	-
Pressure control valve	Diaphragm diameter	165	mm
	Valve seat diameter	25.5	mm
	Maximum valve opening	4	mm
	Effective mass of moving parts	3.5	kg
	Stiffness of main spring	60800	N/m
	Initial compression of main spring	8	mm
	Diaphragm stiffness	167200	N/m
	Valve displacement when diaphragm stiffness occurs	2	mm
	Viscous friction coefficient	1000	N/(m/s)
	Coulomb friction	0	N
	Average thickness of air space behind the diaphragm	0.0125	m
	Diameter of feedback port damper	1.25	mm
	Volume of water inside the valve	0.367	L
	Water Bulk modulas	20500	bar
	Diameter of external holes	5	mm
	Number of external holes	4	-
Connection pipe	Internal pipe diameter	22.2	mm
	Pipe length	0.3	m
	k factor for bends and fittings	0	-
	Relative roughness	0.0001	-

Table 6.1   Data used in the models of the submarine escape system

Models	Variables	Values	Units
Feedback pipe	Internal pipe diameter	5.3	mm
	Pipe length	0.66	m
	k factor for bends and fittings	3.6	-
	Relative roughness	0.0001	-
Plunger valve	Valve seat diameter	22	mm
	Valve opening distance	6	mm
Corrugated hose	Mean internal diameter	18	mm
	Hose length	1	m
	k factor for bends and fittings	0.2	-
	Relative roughness	0.001	-
Life-jacket	Inlet chamber volume	3	L
	Right chamber volume	4.5	L
	Left chamber volume	4.5	L
	Flow area of internal port	280	mm²
Pressure relief valve	Diaphragm diameter	38	mm
	Valve seat diameter	14	mm
	Maximum valve opening	6	mm
	Effective mass of moving mass	0.0015	kg
	Spring stiffness	2300	N/m
	Initial compression of spring	2	mm
	Viscous friction	1000	N/(m/s)
	Coulomb friction	0	N
	Flow force factor	0	-
	Change of flow force factor	2.5	-
	Reynolds number when flow force changed	960000	-
	Diameter of external holes	6	mm
	Number of external holes	4	-
Hood	Maximum gas volume inside the hood	24	L
	Imitation lung volume	5.6	L
	Maximum air/water contact area	12250	mm²
	Small vent flow area	8400	mm²
	Height of the lower part of the hood	0.312	m
Distances	Distance from the water surface inside the tower to the centre of the control valve diaphragm	0.536	m
	Distance from the water surface inside the tower to the small vent of the hood	0.57	m

Table 6.1   Data used in the models of the submarine escape system

Models	Variables	Values	Units
Storage bottles	Initial gas pressure	50	bar
	Total gas volume	10	L
Pressure reducing valve	Exposed diaphragm diameter	35.6	mm
	Valve seat diameter	1.575	mm
	Maximum valve opening	1.42	mm
	Poppet angle	45	degrees
	Effective mass of moving parts	0.01	kg
	Spring rate of inlet valve head spring	7400	N/m
	Initial compression of inlet valve head spring	2.3	mm
	Spring rate of large spring	630000	N/m
	Initial compression of large spring	1.5	mm
	Viscous friction coefficient	100	N/(m/s)
	Coulomb friction	0	N
Connection pipe	Pipe internal diameter	10	mm
	Pipe length	1	m
	k factor for bends and fittings	0	-
	Relative roughness	0.0001	-
Direction control valve	Maximum flow area from 'A' port	1×10^{-6}	m^2
	Maximum flow area from 'B' to return port	5×10^{-5}	m^2
	Maximum flow area from supply to 'B' port	1×10^{-6}	m^2
	Maximum flow area from 'A' to return port	5×10^{-5}	m^2
Connection pipes (2)	Internal pipe diameter	10	mm
	Pipe length	1	m
	k factor for bends and fittings	0	-
	Relative roughness	0.0001	-
Equal area linear actuator	Actuator internal diameter	35	mm
	Actuator rod diameter	20	mm
	Actuator stoke	5	m
	Actuator mounting angle	0	degrees
	Effective mass of moving parts	10	kg
	External load	0	N
	Speed dependent friction coefficient	100	N/(m/s)
	Coulomb friction	0	N
First-order lag controller	Controller gain	0.08	-
	Time constant of first-order lag	0.5	-

Table 6.2   Data used in the models of the position feedback control linear actuator system

Variables	Values	Units
Controller gain	0.16	-
Time constant τ	1	second
Time constant factor α	0.5	-

Table 6.3   Data used in the lead-lag controller model
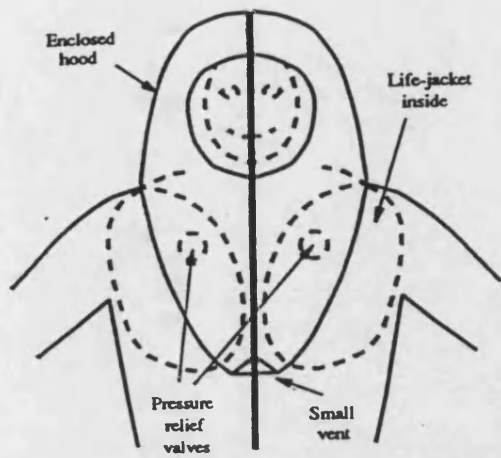
Figure 6.1 Submarine escape immersion suit
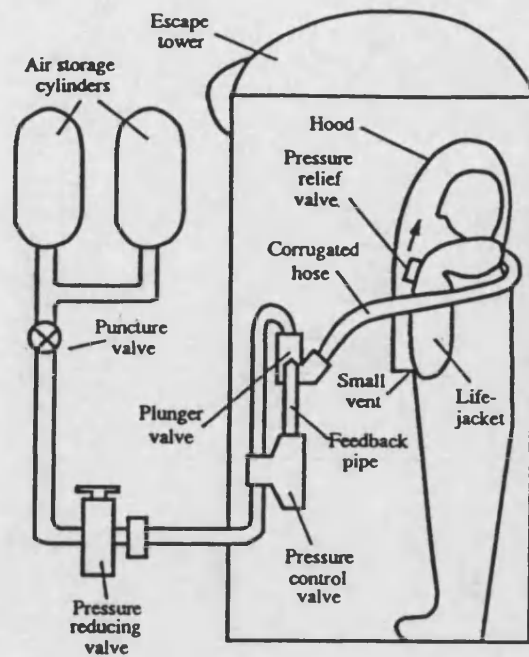
Figure 6.2 Schematic representation of a submarine escape system
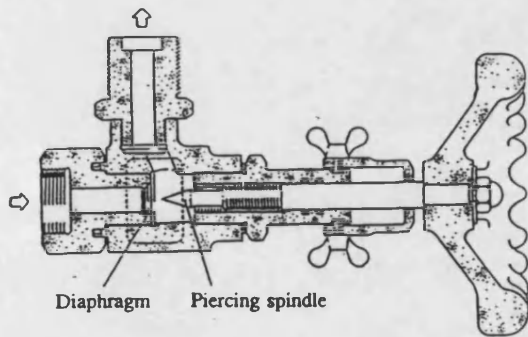
Figure 6.3 Puncture valve
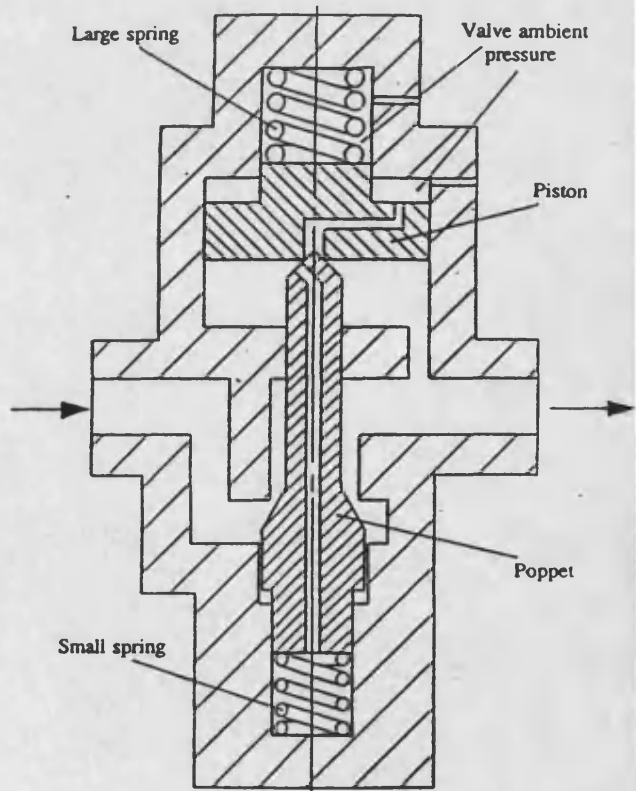
Figure 6.4 Pressure reducing valve
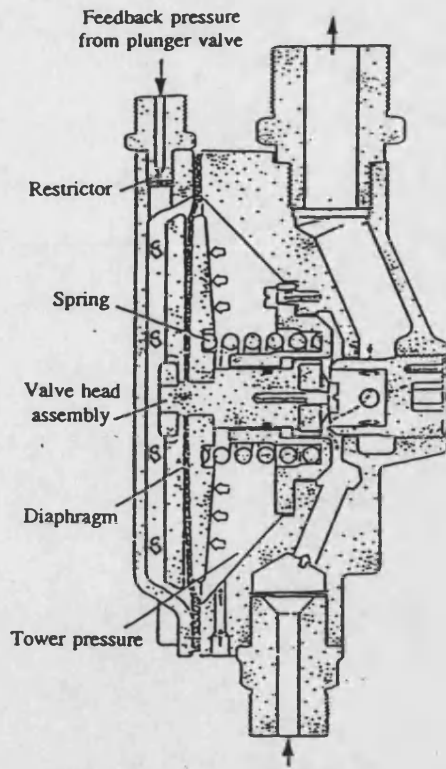
Figure 6.5 Pressure control valve
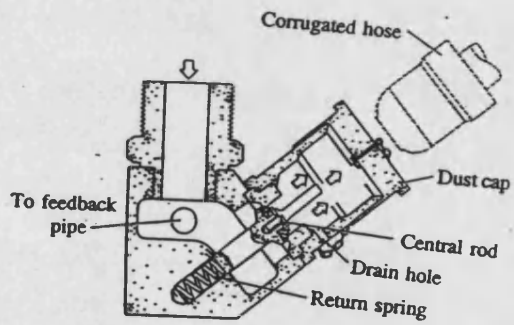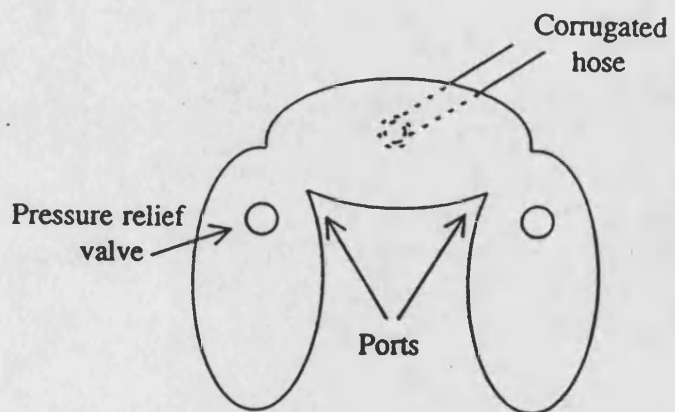

Figure 6.6 Plunger valve
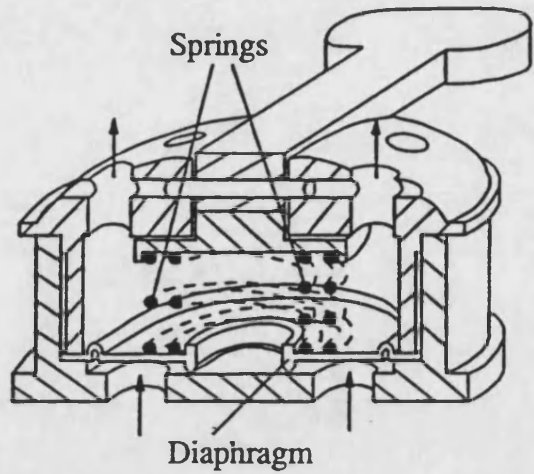

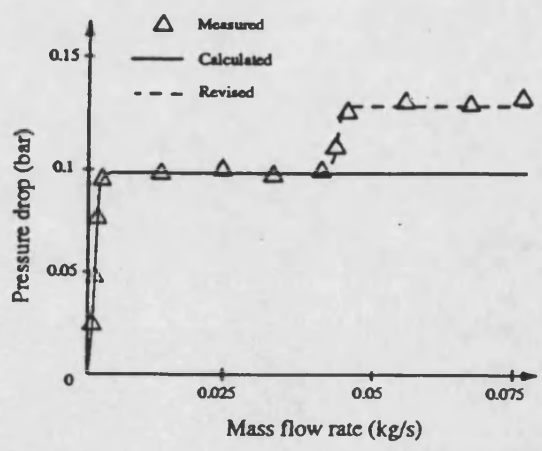**Figure 6.7** Life-jacket

Figure 6.8 Pressure relief valve

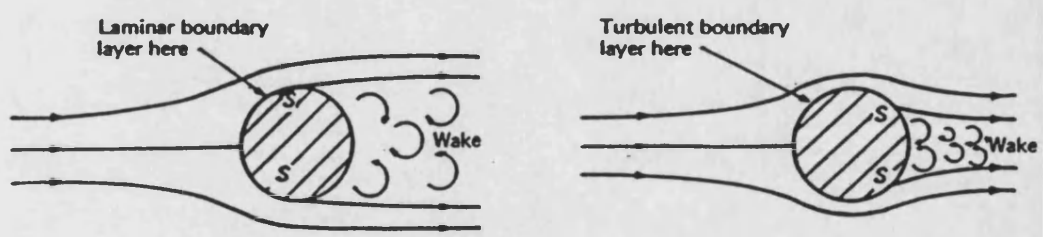**Figure 6.9** Pressure drop and flow characteristic of the pressure relief valve
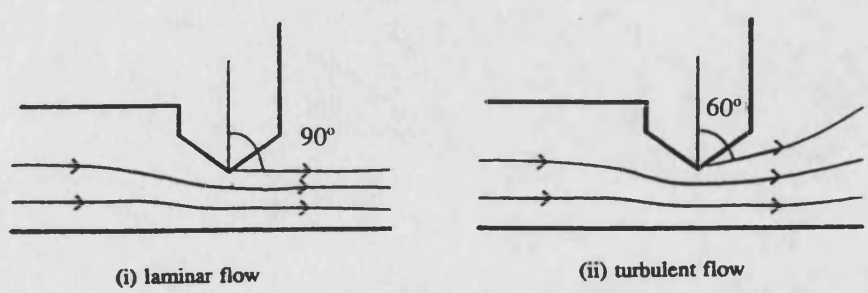

Figure 6.10(a) A flow of gas passed over a cylinder

(i) laminar flow   (ii) turbulent flow

Figure 6.10(b) Change of flow pattern at the opening of pressure relief valve

205
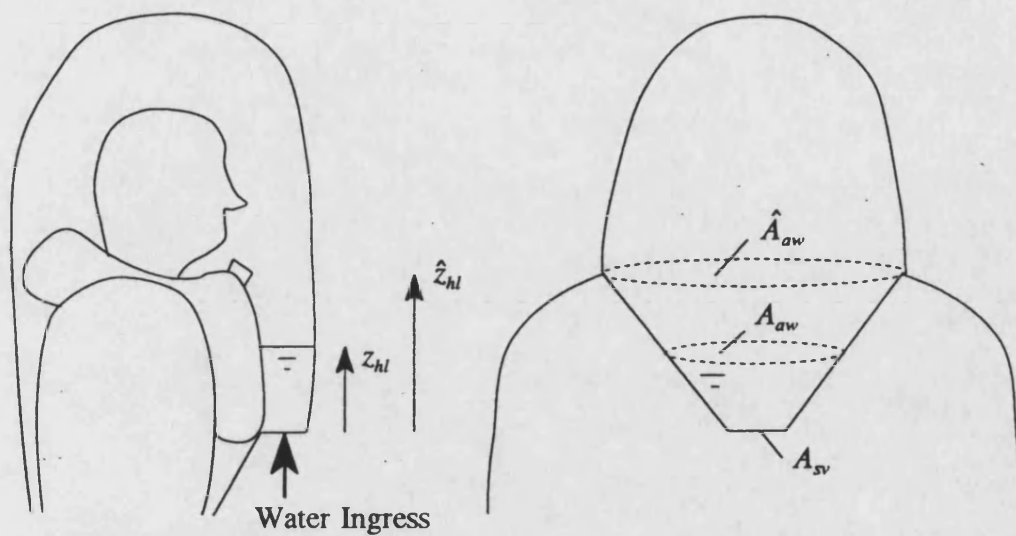
Figure 6.11 Ingress of water into the hood
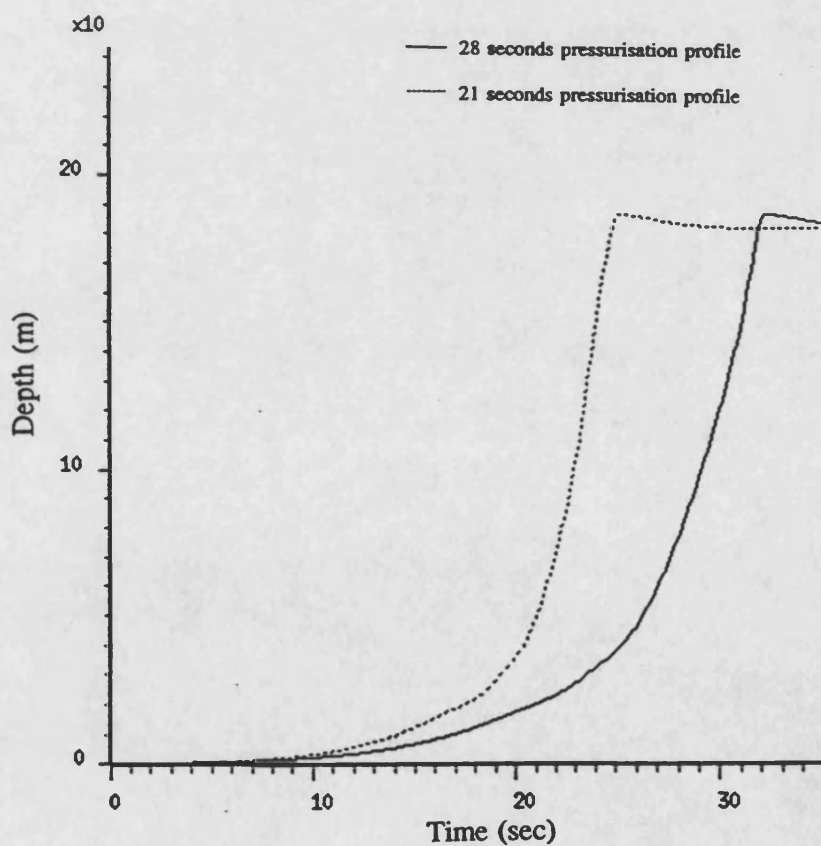
Figure 6.12 Tower depth profile
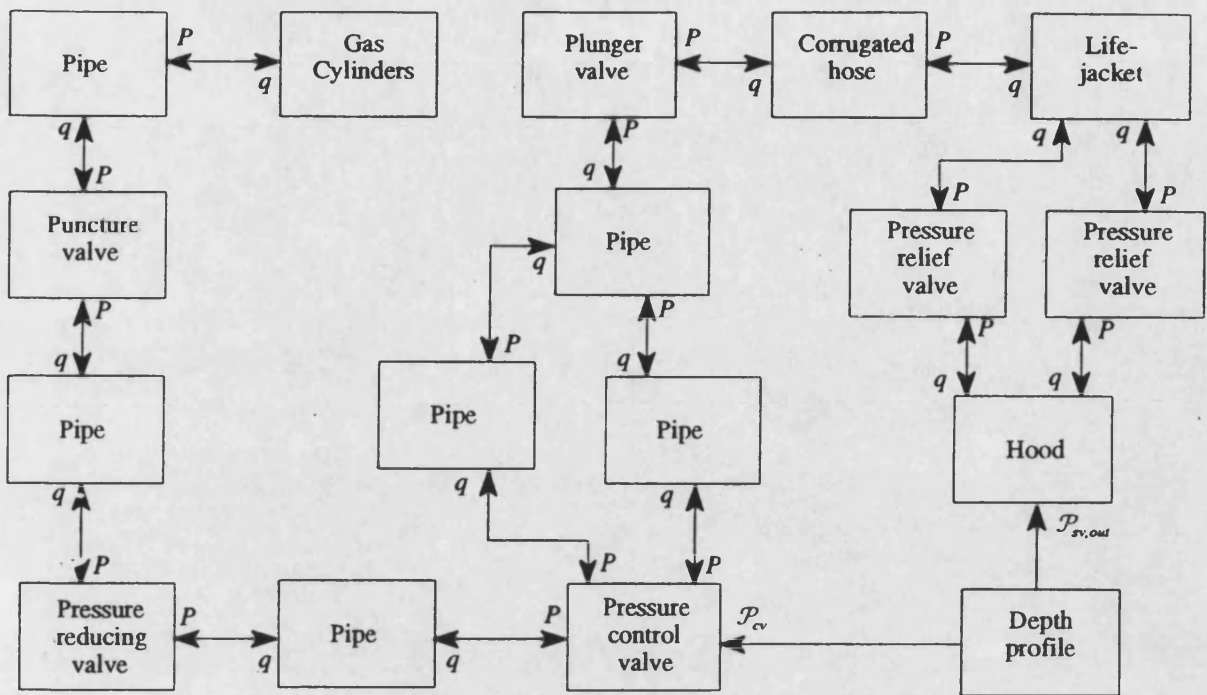
Figure 6.13 Simulation of submarine escape system block diagram
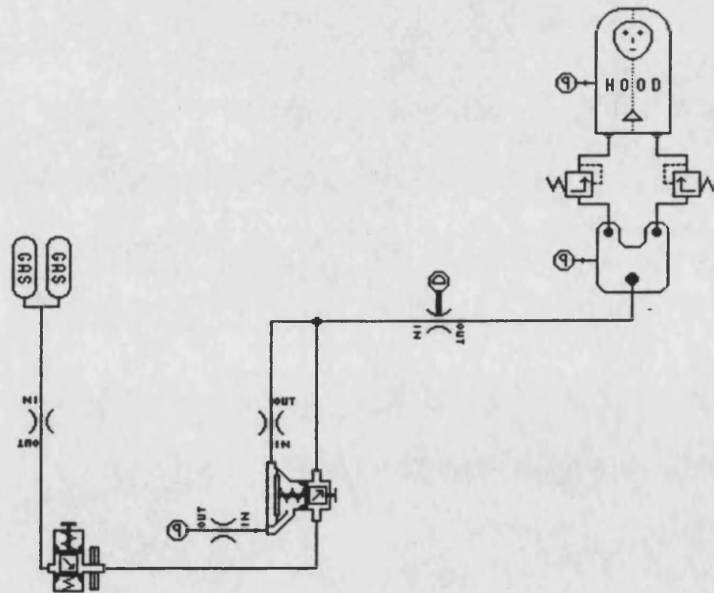
Figure 6.14 Simulation of submarine escape system schematic diagram in Bath*fp*
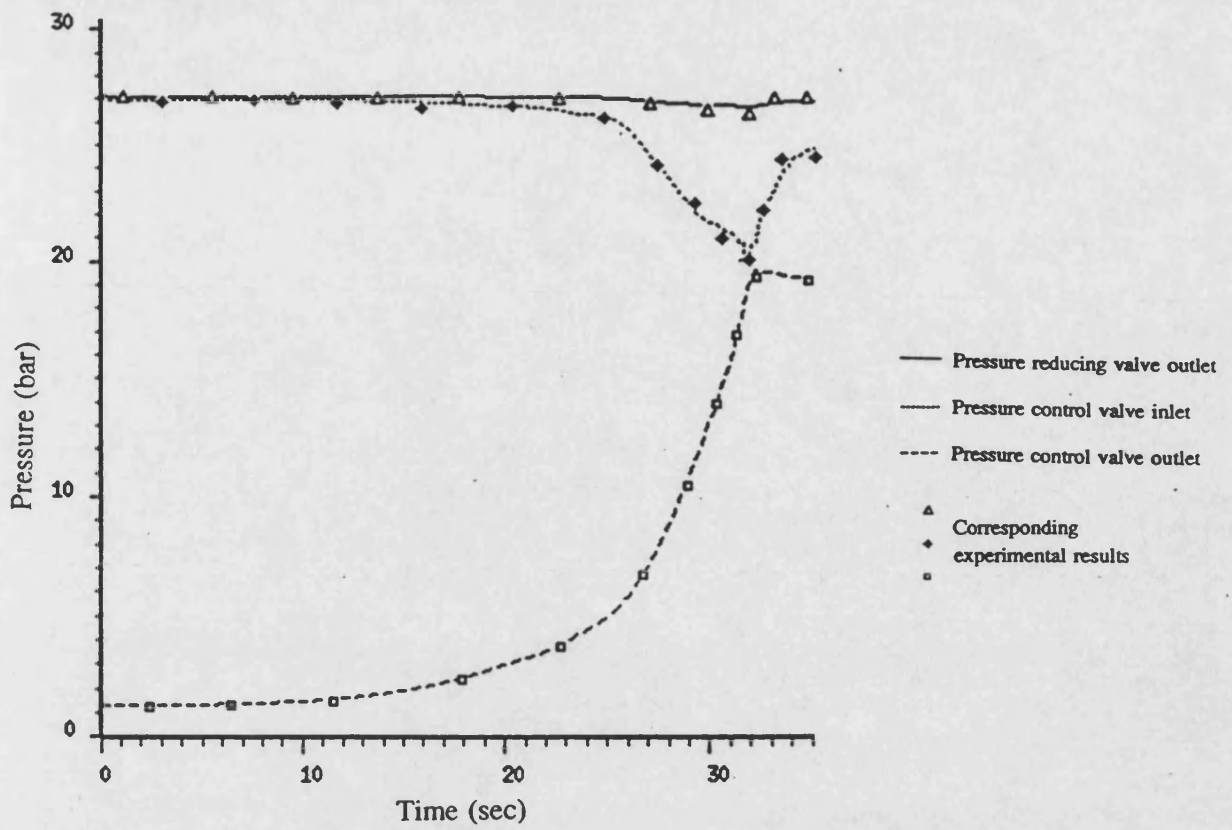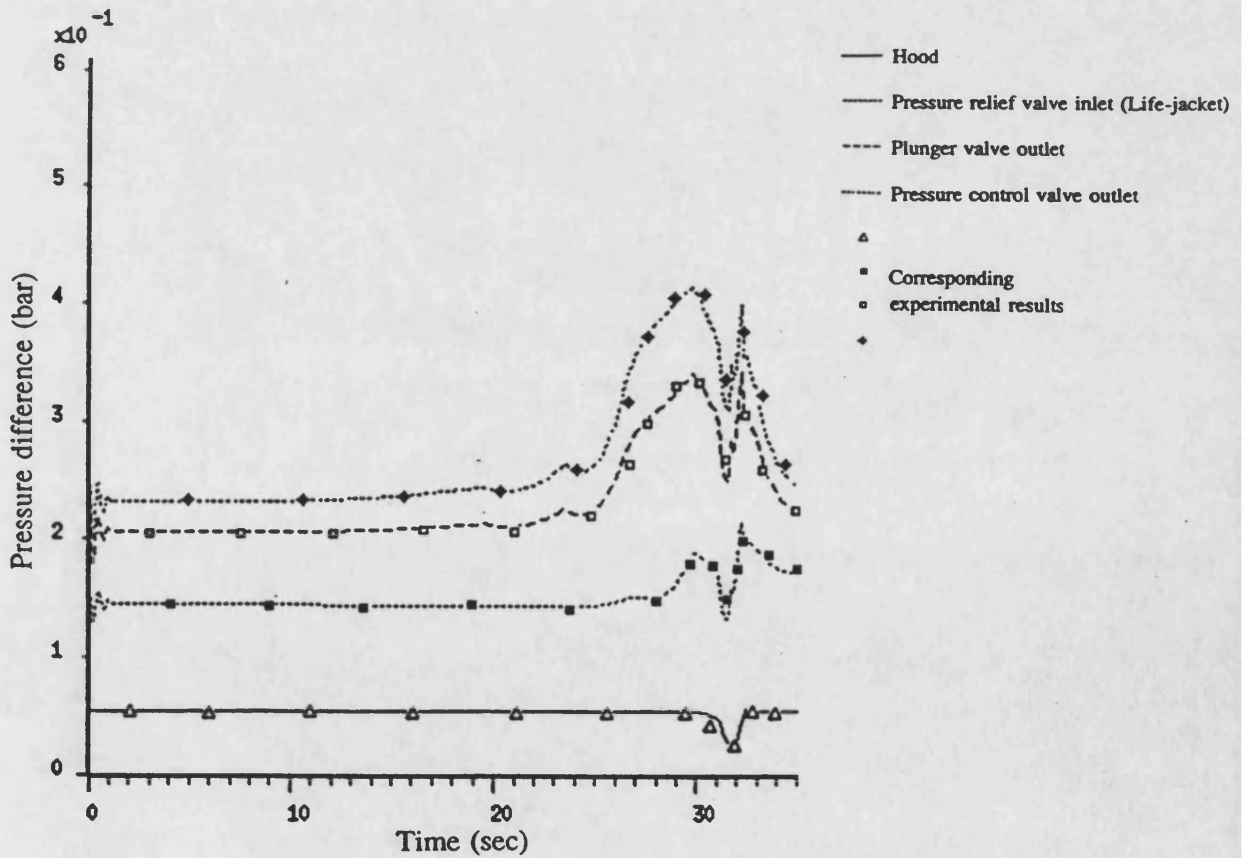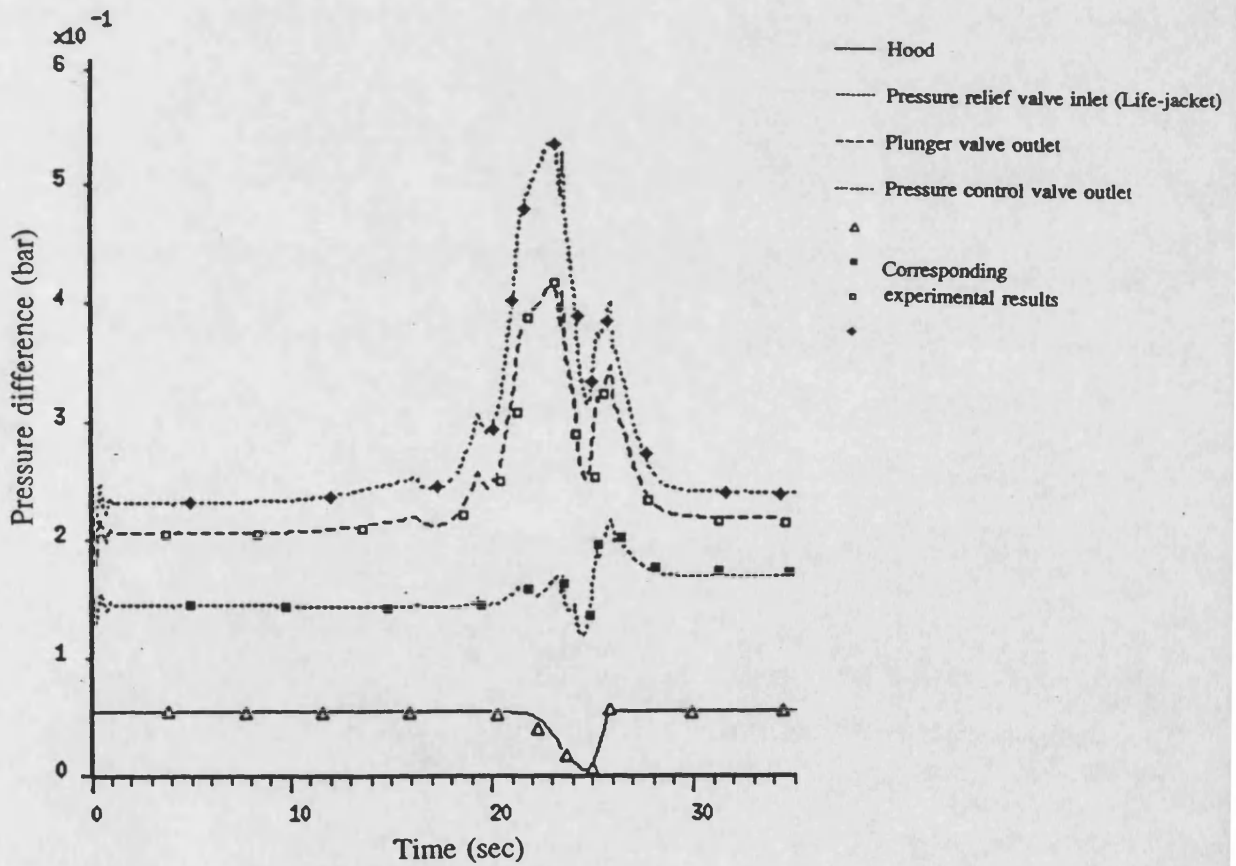
(a) Pressures

(b) Pressure differences between various components and air space inside the chamber

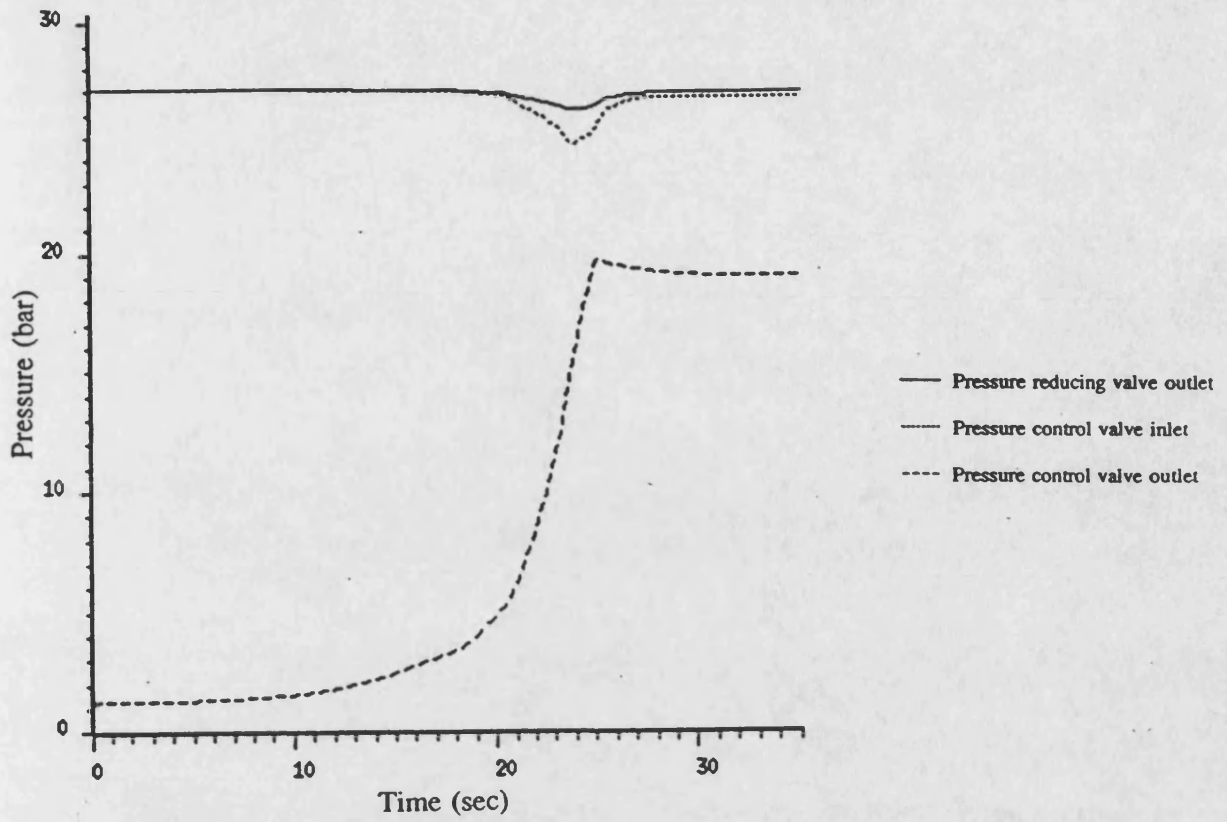**Figure 6.15** Predicted and measured results during 28 seconds pressurisation process
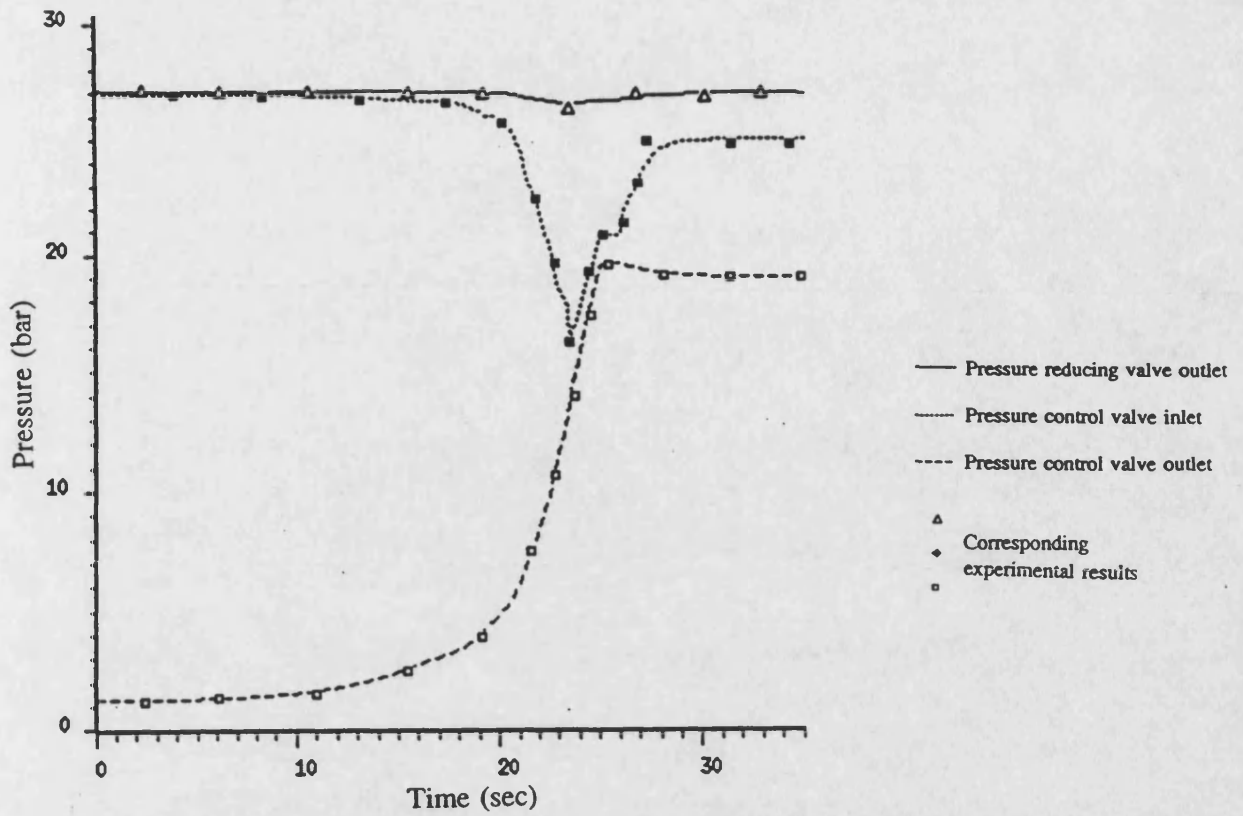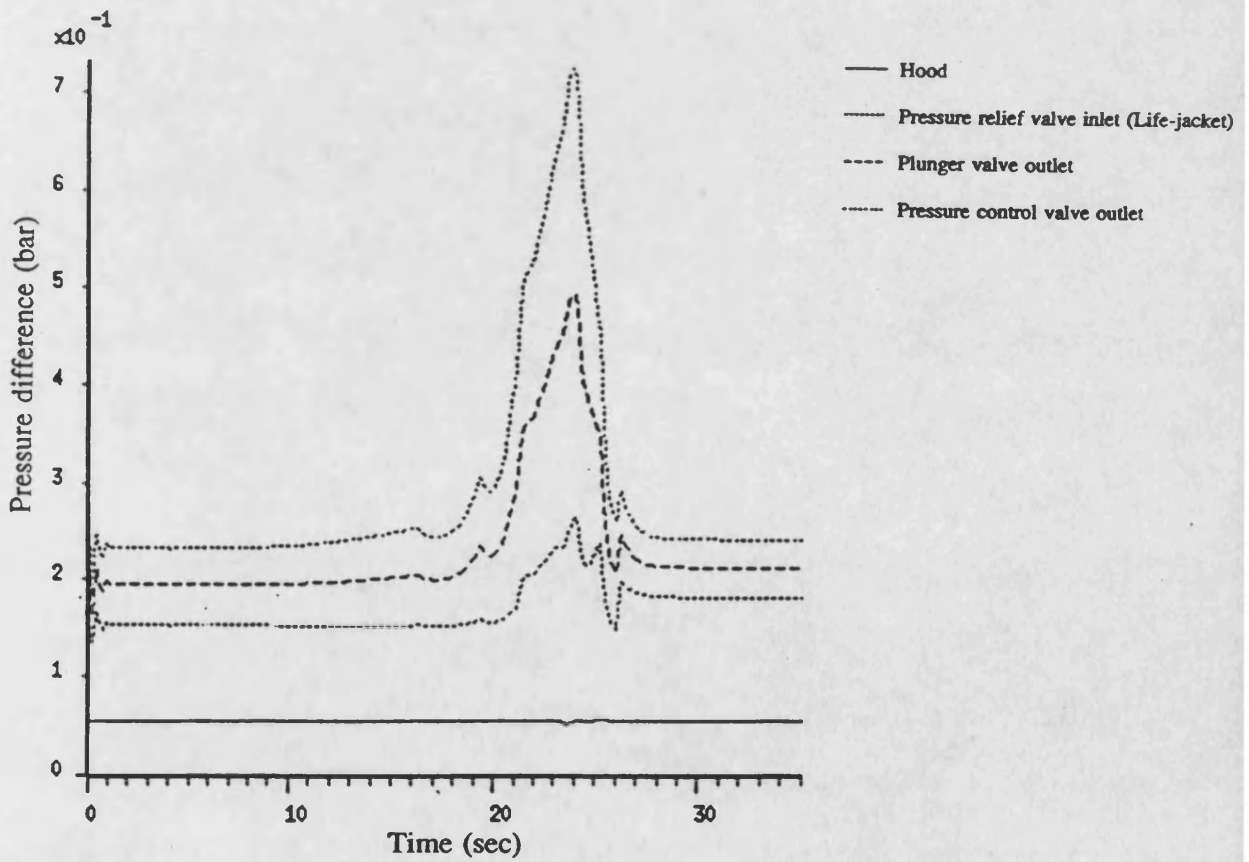
(a) Pressures

(b) Pressure differences between various components and air space inside the chamber

Figure 6.16 Predicted and measured results during 21 seconds pressurisation process

(a) Pressures

(b) Pressure differences between various components and air space inside the chamber

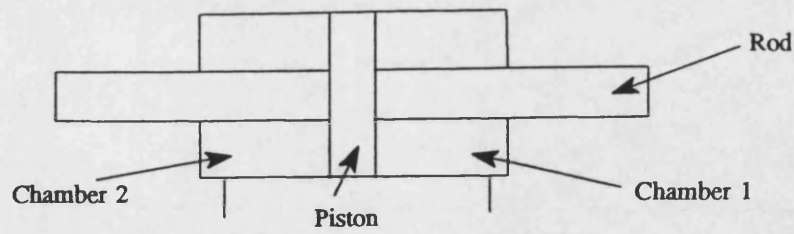**Figure 6.17** Predicted results of modified system during 21 seconds pressurisation process
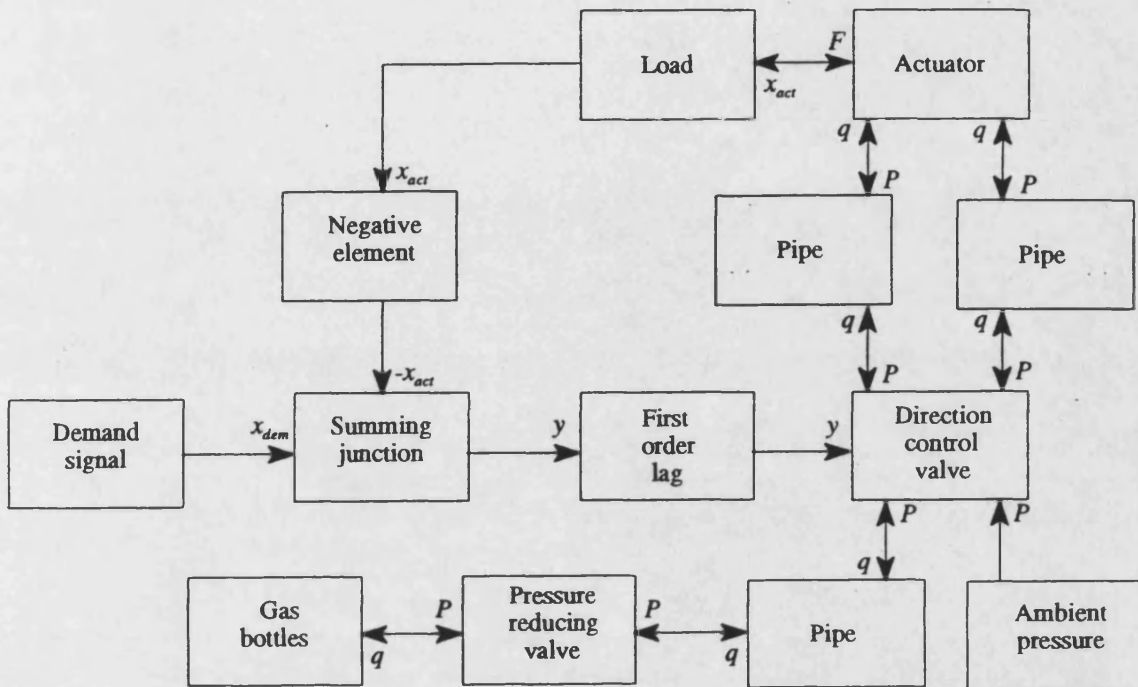
Figure 6.18 Linear actuator

Figure 6.19 Simulation of position feed-back control linear actuator system block diagram
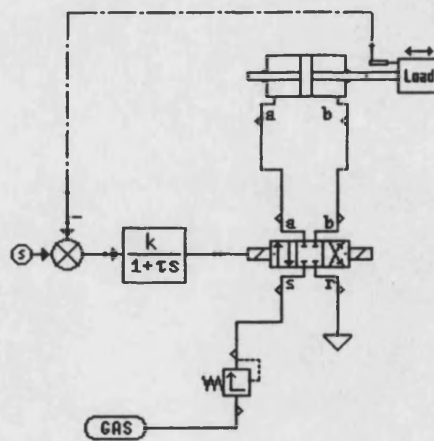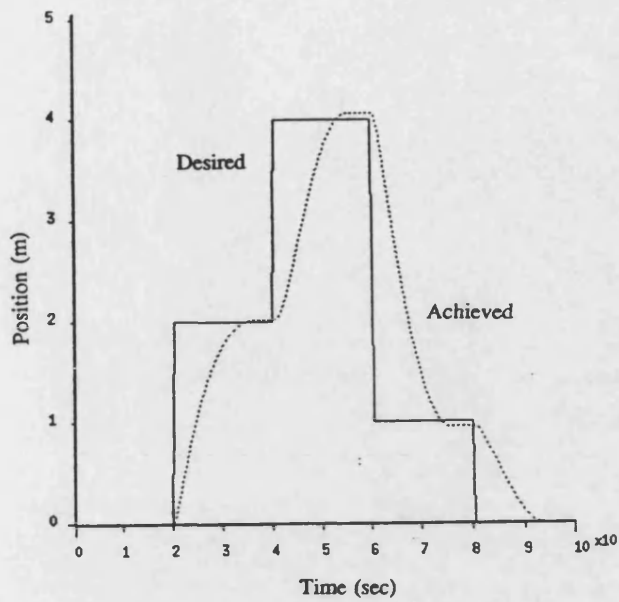

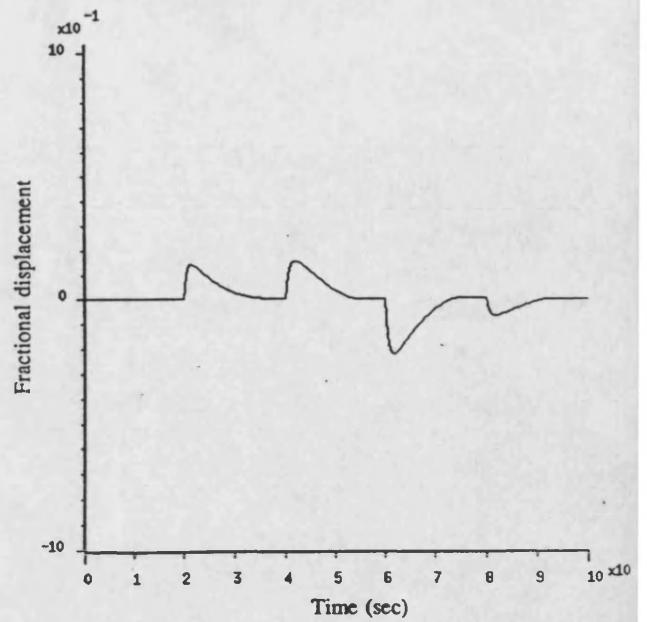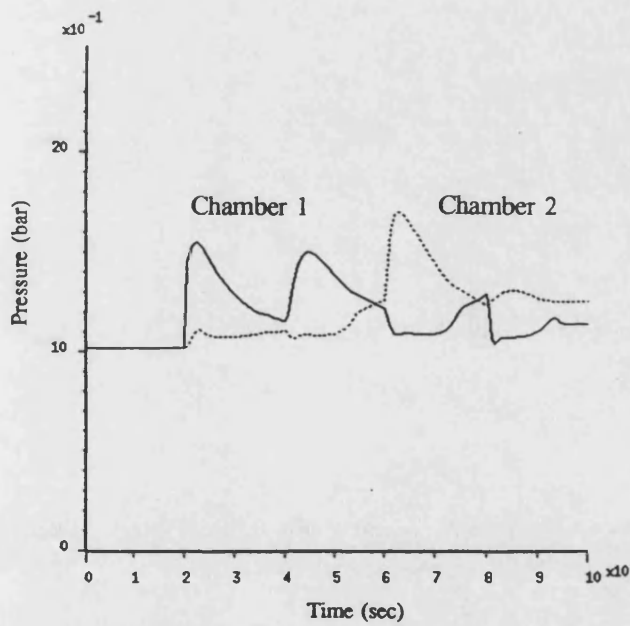**Figure 6.20** Simulation of position feed-back control linear actuator system schematic diagram in Bath*fp*

(a) Desired and achieved actuator position

(b) Fractional displacement of direction control valve

(c) Gas pressures at chamber 1 and 2 of the actuator

(d) Gas pressure inside the storage bottle

Figure 6.21 Simulation results of the position feed-back control linear actuator system

(a) Desired and achieved actuator position

(b) Fractional displacement of direction control valve

(c) Gas pressures at chamber 1 and 2 of the actuator

(d) Gas pressure inside the storage bottle

Figure 6.22 Simulation results with the increase of controller gain
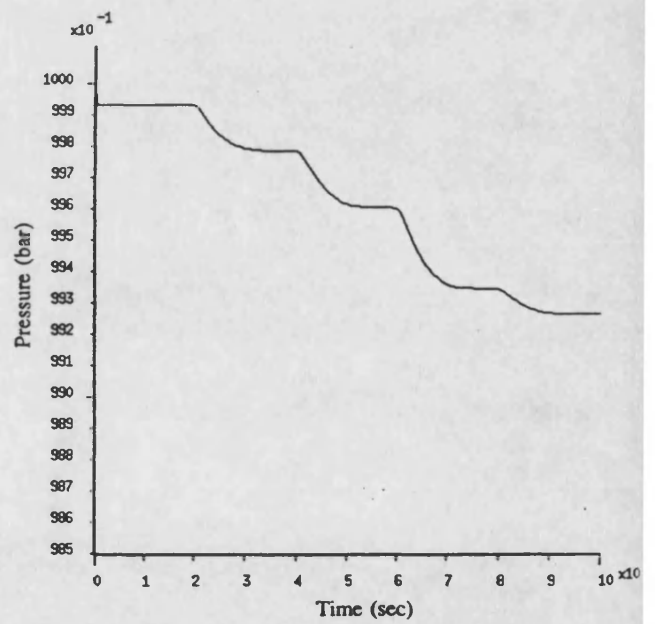
213

(a) Desired and achieved actuator position

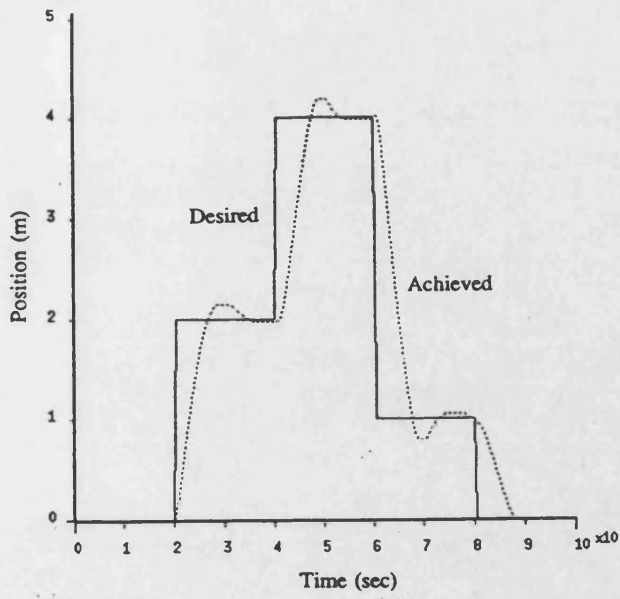
(b) Fractional displacement of direction control valve

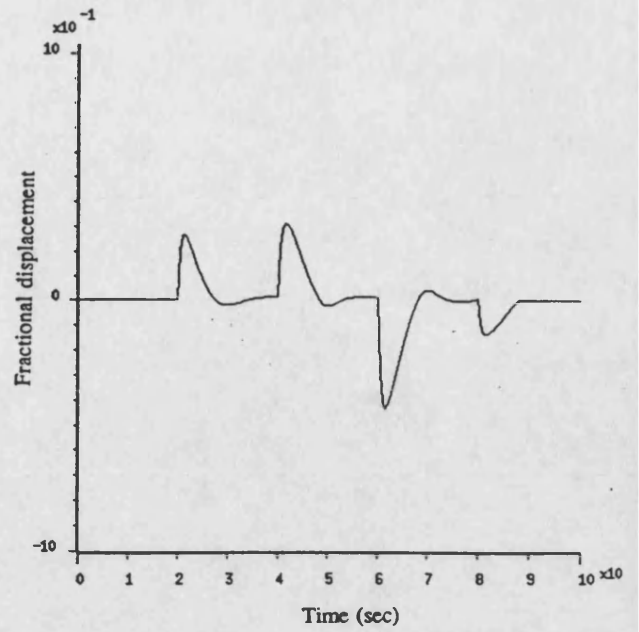(c) Gas pressures at chamber 1 and 2 of the actuator
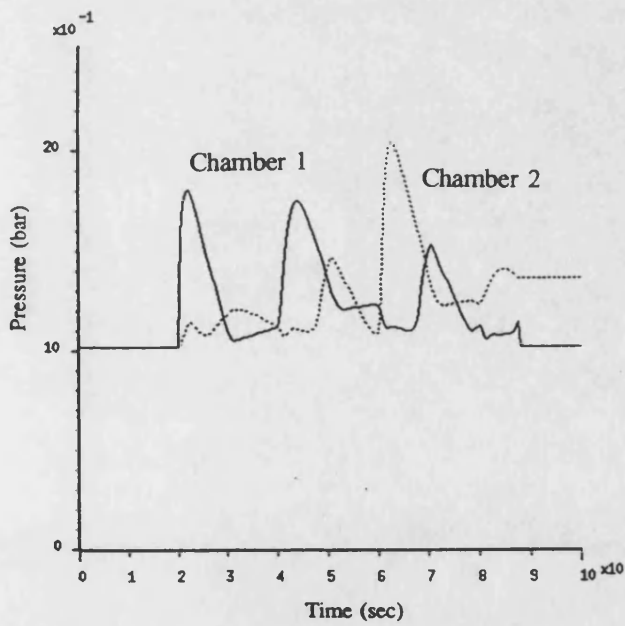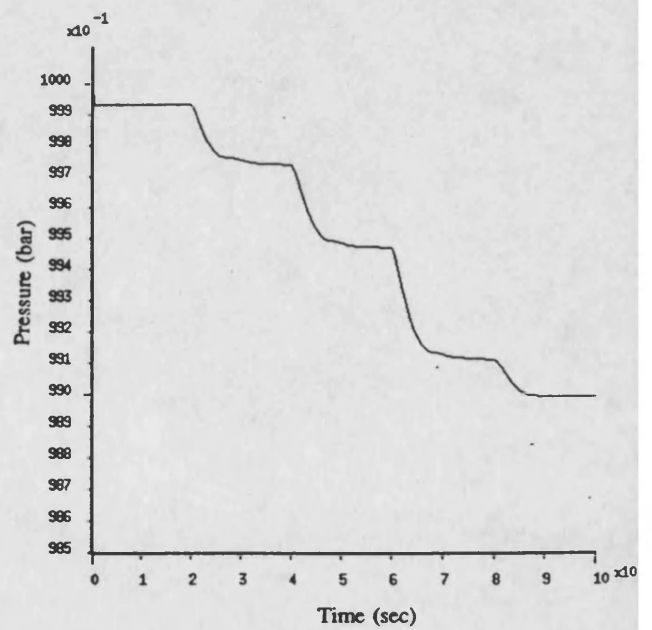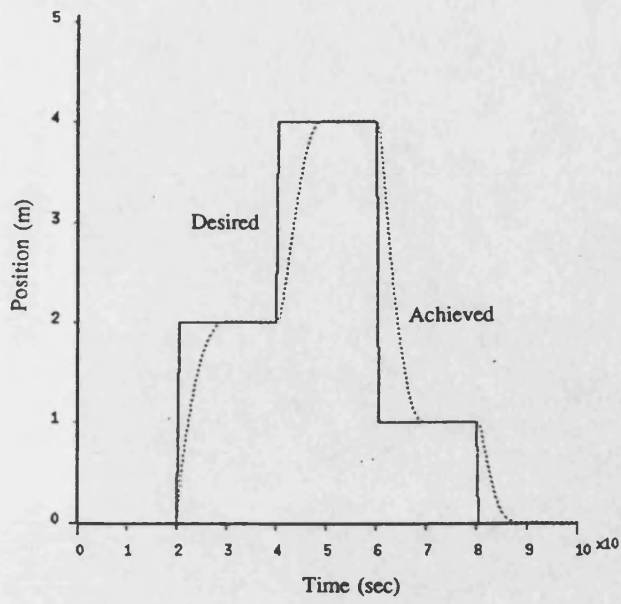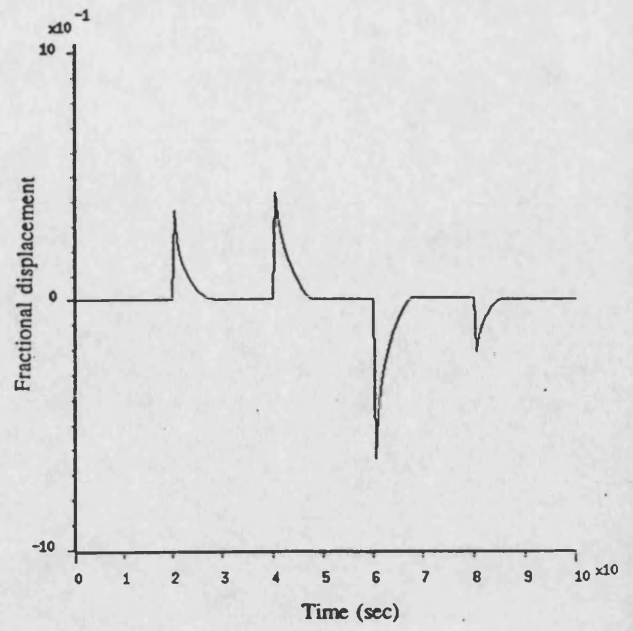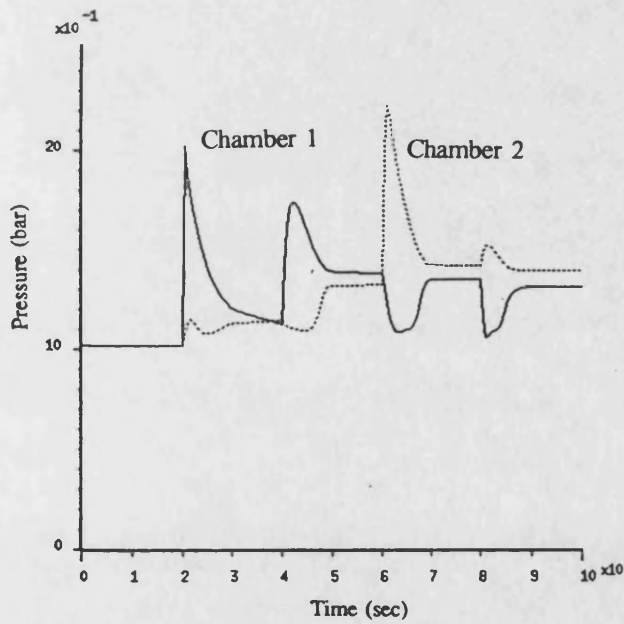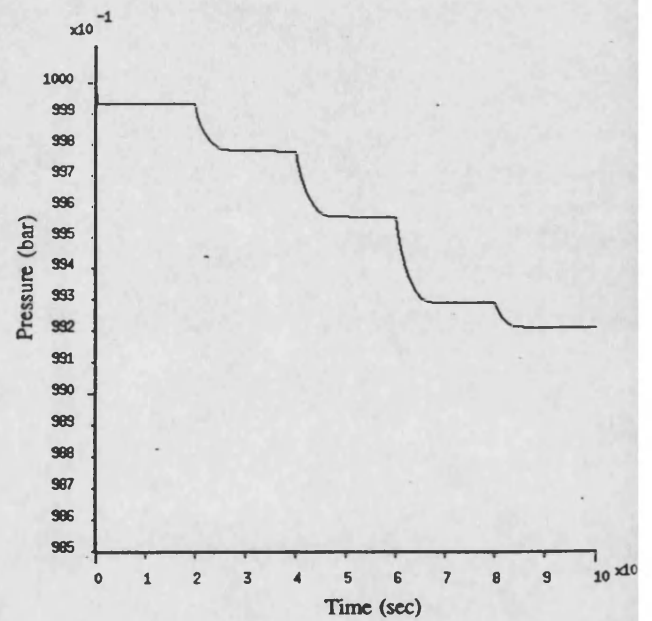

(d) Gas pressure inside the storage bottle

Figure 6.23 Simulation results of the modified position feed-back control linear actuator system

214

CHAPTER 7

CONCLUSIONS AND FURTHER WORK

7.1 CONCLUSIONS

This thesis discusses the development of mathematical models for the simulation of underwater breathing apparatus and the human respiratory system. The aim is to provide the designer with a tool which can be used for analysis and design of underwater breathing apparatus.

The modelling techniques presented in chapter 2 describes the development of the component models for the simulation of underwater breathing apparatus, which include gas storage bottle, pipe/hose, gas control valve and axial flow scrubber. A technique to simulate the variation of gas composition in the breathing apparatus is presented which allows the partial pressure of constituent gases to be predicted. An approach to simulate the carbon dioxide absorption process in the axial flow scrubber has been developed, which enables the duration of the axial flow scrubber to be predicted. In addition, a breathing simulator model has been developed which allows the simulation results to be compared with the available unmanned testing results.

The simulations of the semi-closed-circuit breathing system and the surface demand diving system under unmanned test condition are presented in chapter 3. Additional models have been developed for these two systems. The simulations were undertaken to study the work of breathing and the quality of the breathing gas when using these two systems. Good correlation is obtained between the predicted and measured data. The simulations have been used to assess system modifications to improve system performance. Comparisons between the performances of the surface demand diving system and the semi-closed-circuit breathing system indicate that under the same operation of conditions, the diver will expend less energy when using the surface demand diving system.

The development of the mathematical model for the simulation of human breathing process is described in chapter 4. The mass balance equations and a chemical buffering system have been used as a basis for the development of the human respiratory model. The models include the complex interaction

215

between lung and chest wall motion, airflow through the airways, gas exchange in alveolar and tissue, and blood circulation. For the neurogenic controller, the model incorporates mechanical and chemical control of breathing, providing an automatic control of respiration at different environmental conditions.

The parameters required for the development of the human respiratory system model have been obtained from published clinical measurement. The unknown parameters have been identified by comparing the simulation results conducted in chapter 5 with experimental data. The simulations of maximum inspiratory-expiratory flow volume manoeuvre, continuous breathing test, maximal voluntary ventilation test and different physiological conditions (ie. CO_2 breathing, hypoxia, exercise and change of ambient pressure) have been used to extend and test the human respiratory model. The simulation results agree well with available experimental data and the model has been used to simulate manned diving operation when using various types of breathing equipment. The models developed for the semi-closed-circuit breathing system and the surface demand diving system have been used for the manned diving simulations. The limitations of these two systems have been assessed by performing simulations using maximal voluntary ventilation test and at different diving schedules. The maximal voluntary ventilation test studies have confirmed that the use of oxy-helium mixture as the breathing gas allows higher diver's ventilation to be performed and enables the diver to carry out harder tasks at deeper depths. The simulation studies at different diving schedules have demonstrated that the models are able to predict the occurrence of decompression sickness during a dive and enable safe diving schedules to be developed.

The simulation studies in chapter 6 illustrate that the simulation techniques can be applied to other gas based systems. Mathematical models have been developed for a submarine escape system and good agreement is obtained between the simulation and experimental results. Modifications have been identified using the simulation to improve system performance. Additional models have been developed for the pneumatic industries and the simulation of a position feed-back actuator system has demonstrated that the developed models can assist engineer for the design of industrial pneumatic systems.

Overall the work presented in this thesis provides a viable basis for the simulation of underwater breathing apparatus and the human respiratory system. The mathematical models developed are very general such that they can be used for other gas based systems.

7.2 RECOMMENDATIONS FOR FURTHER WORK

The work documented in this thesis indicates that the simulation techniques can be used for other gas based system. Hence, if this research is to be continued, it is considered that studies into the following areas would be worthwhile.

7.2.1 Other kinds of breathing equipment

Since the developed models are very general, the simulation techniques can be applied to other kinds of breathing equipment, for example, the breathing apparatus used for fire and poisonous gas rescue, for high altitude and high speed flight and the patient for treatment use (ie. life support systems).

7.2.2 Enhancing the human respiratory system model

Further enhancement of the human respiratory system model is required to simulate the multitude of complex interacting effects that go to make up the respiratory system. These include the thermoregulation and humidity factors. Since the goal of the human thermoregulation is to keep body temperature constant at a preset level, a change in the respiratory control will occur when the surrounding temperature changes. The incorporation of the thermoregulation in the model will allow the response of a human at extreme hot or cold condition to be predicted. Humans living in humid climates are particularly susceptible to respiratory irritation due to the abrupt change from humid surface air to dry breathing air. Hence, the estimations of humidity factors could be considered so that further requirements of the breathing apparatus could be assessed.

7.2.3 Medical applications

The human respiratory system model has been shown to be capable of predicting the effects of respiratory disease. Hence, if experimental data obtained from a broad range of patients, who have different kinds of respiratory diseases , is available, the human model can be validated for different respiratory diseases. This model can then be used for the assessment and design of respiratory treatment equipment (ie. life support system).

REFERENCE

Andersen B.W., 1976,

'The Analysis and Design of Pneumatic Systems', Robert E. Krieger Publishing Company.

Anthony T.G., Potts D.J., 1980,

'The effect of hyperbaric conditions upon the efficiency of a soda lime absorption system', INS, Vol. 9, No. 3, pp198-204.

Antoon T.A., Middleton J.R., Nuklos M.L., 1986,

'Breathing dynamics of a surface-supplied diving system with demand flow: In Current practices and new technology in ocean engineering', ASME Ocean Engineering Division Publication, Vol. 11.

Asmussen E., 1943,

'CO_2 breathing and the output of heart', Acta. Physiol. Scand., 6, pp176-186.

Backe W., 1985,

'The Hydraulic Simulation Program DSH', Proc. Inst. Mech. E., pp199.

Balfour Slonim N., Hamilton L.H., 1987,

'Respiratory Physiology', Springer-Verlag.

Bennett P.B.,Elliott D.H., 1982,

'The Physiology and Medicine of Diving', Builliére Tindall, London.

Berne R.M., Levy M.N., 1988,

'Physiology', The C.V. Mosby Company.

Bohart G., Adams E., 1920,

'Behaviour of Charcoal toward Chlorine', Am. Chem. Soc., Vol. 42.

Boycott A.E., Damant G.C.C., Haldane J.S., 1908,

'Prevention of compressed air illness', J. Hyg. Lond., No. 8, pp.342-443.

Buz A., Gilheany J., 1988,

'Modelling the dynamics of breathing circuits for underwater divers', J. Fluid Control, Vol. 19(2), pp.58-57.

Cotes J.E., 1979,

'Lung Function', Blackwell Scientific Publication.

Cunningham D.J.C., Gardner W.N., 1977,

'A quantitative description of the pattern of breathing during steady-state CO_2 inhalation in man with special emphasis on expiration', J. Physiol. (Lond.), 272, pp613-632.

Danckwerts P.V., 1970,

'Gas-Liquid reaction', McGraw-Hill Book Company.

Defares J.G., Derksen H.E., Dayff J.W., 1960,

'Cerebral blood flow in the regulation of respiration', Acta. Physiol. Pharmacol, Neerl, 9:pp327-360.

Denison D.M., Pierce R.J., Waller J.F., 1981,

'Does the lung work? How big are the lungs?', British J. Diseases Chest, 75(4), pp371-385.

Denison D.M., DuBois R., Sawicka E., 1983,

'Does the lung work? 5. Pictures in the mind', British J. Diseases Chest, 77(1), pp35-50.

Dickinson C.J., 1977,

'A Computer Model of Human Respiration', MTP Press Ltd.

Diving Manual, 1987,

BR 2806, Ministry of Defence.

Flowmaster,

Flowmaster International Ltd., Court House, Featherstone Road, Wolverton Mill, Milton Keynes, MK12 5QP.

Fung Y.C., 1990,

'Biomechanics: Motion, Flow, Stress and Growth', Springer-Verlag.

Engineers Year Book, 1991,

Kempe's.

Ergun S., 1952,

'Fluid flow through Packed Columns', Chem. Eng. Progress, Vol. 48, pp93.

Ganong W.F., 1987,

'Review of medical physiology', Appleton and Lange.

Gardner W.N., 1977,

'The relation between tidal volume and inspiratory and expiratory times during steady-state CO_2 inhalation in man', J. Physiol. (Lond.), 272, pp591-611.

Grodins F.S., Gray I.S., Schroeder K.R., Norins A.L., Jones R.W., 1954,

'Respiratory response to CO_2 inhalation. A theoretical study of a non-linear biological regulator', J. Appl. Physiol. Vol. 7, pp283-308.

Grodins F.S., 1965,

'Computer simulation of cybernetic systems: In Computers in Biomedical Research', Ed. by Stacy R.W. & Waxman B., New York Academic, Vol. I, pp135-164.

Gordins F.S., Buell J., Bart J., 1967,

'Mathematical analysis and digital simulation of the respiratory control system', J.Appl.Physiol.,22(2), pp260-276.

Haaland S.E., 1983,

'Simple and Explicit Formulas for the Friction Factor in Turbulent Pipe Flow', J. Fluids Eng., pp89-90.

Hyatt R.E., Schilder D.P., Fry D.L., 1958,

'Relationships between maximum expiratory flow and degree of lung inflation', J. Appl.Physio.,13(3), pp331-336.

Imison C. J., 1986,

'Determination of the gas flow of a small mushroom valve', Report No. 4220-99-7756, ARE Alverstoke, U.K.

Keele C.A., Noil E., Joels N., 1982,

'Applied Physiology', Samson Wrights.

Lambet R.K., Wilson T.A., Hyatt R.E., Rodarte J.R., 1982,

'A computational model of expiratory flow', J. Appl. Physiol., 52(1), pp44-56.

Lanphier F. H., 1982,

'Pulmonary function: In the Physiology and Medicine of Diving and Compressed Air work', 1st Edition, Ed. pp.58-112, PB Bennett & DH Elliott, Builliére Tindall, London.

Massey B.S., 1987,

'Mechanics of Fluids', Van Nostrand Reinhold (U.K.) Co. Ltd.

McCloy D., Martin H.R., 1973,

'Control of Fluid Power', Longman.

Miller J.N., Wangensteen O.D., Lamphier E.H., 1971,

'Respiratory limitation to work at depth', Proc. Third international Conference on Hyperbaric and Underwater Physiology, Ed. X, Fructus Paris: Doin, pp118-123.

Mines A.H., 1986,

'Respiratory Physiology', Longman.

Mittleman J., 1989,

'Computer modelling of underwater breathing systems', Proceedings of the fortieth Undersea and Hyperbaric Medical Society Workshop, Buffalo, Appendix B.

Morrison J.B., Florio J.T., Butt W.S., 1980,

'The effect of insensitivity to CO_2 on the respiratory response to exercise at 4 ATA', Royal Naval Physiological Laboratory Report 2-76.

Murray-Smith D.J., Carson E.R., 1988,

'Case studies of Respiratory system model: In the Respiratory System', Ed. by Cramp D.G., Carson E.R., Vol.2, Croom Helm, London & Sydney.

Murray-Smith D.J., Carson E.R., 1988,

'The modelling process in Respiratory Medicine: In the Respiratory System', Ed. by Cramp D.G., Carson E.R., Vol.2, Croom Helm, London & Sydney.

Nuckols M.L., Purer A., Denson G.A., 1983,

'Design guidelines for carbon dioxide scrubbers', Technical manual 4110-1-83, Naval Coastal Systems Centre, Florida, U.S.A.

Patterson J.L.Jr., 1965,

'Circulation through the brain: In Physiology and Biophysics', Ed. Ruch T.R. & Patton H.D., Philadelphia: Saunders, pp950-958.

Petzold L., 1983,

'Automatic selection of methods for solving stiff and non-stiff systems of ordinary differential equations', SIAM J. Sci. Stat. Comput., Vol. 4, pp136-148.

Reid R.C., Prausnitz J.M., Sherwood T.K., 1977,

'The properties of Gases and Liquids', McGraw Hill Book Company.

221

Reynolds W.J., Milhorn H.T., 1973,

'Transient ventilation response to hypoxia with and without controlled alveolar P_{CO_2}', J. Appl. Physiol., 35, pp187-196.

Richard C.W., Tilley D.G., 1991,

'System Analysis with Bath*fp*', Fluid Power.

Rogers G.F.C., Mayhew Y.R., 1973,

'Engineering Thermodynamic Work and Heat Transfer', Longman.

Ruthven D.M., 1984,

'Principles of adsorption and absorption process', A Wiley-Interscience Publication.

Sarhan N.A.S., Leaning M.S., Saunders K.B., Carson E.R., 1987,

'Development of a complex model: Breathing and its control in Man', Bio. Med. Meas. Infro. Contr., Vol. 2, No. 2, pp81-100.

Saunders K.B., Bali H.N., Carson E.R., 1980,

'A breathing model of the respiratory system: The Controlled System', J.Theoret.Biol, 84. pp135-161.

Scarborough W.R., Penneys R., Thomas C.B., Baker B.M.Jr., Mason R.E., 1951,

'The cardiovascular effect of induced controlled anoxemia', Circulation, 4, pp190-210.

Sherwood T.K., Pigford R.L., Wilke C.R., 1975

'Mass Transfer', McGraw-Hill Kogukusha Ltd.

Smith J.M., 1981,

'Chemical Engineering Kinetics', McGraw-Hill International Book Company.

Sullivan K.J., Chang H.K., 1990,

'Flow dynamic of the nasal passage', First World Congress of Biomechanic, LaJolla Calif, U.S.A., pp98-105.

Szekely J., Evans J.W., Sohn H.Y., 1976,

'Gas-Solid Reactions', Academic Press.

Thews G., Vaupel P., 1985,

'Autonomic Functions in Human Physiology', Springer-Verlag.

Thomas H.C., 1944,

'Heterogeneous Ion Exchange in a flowing system', Am. Chem. Soc., Vol 66.

Tilley D.G., Tomlinson S.P., Livesey J., 1991,

'Computer Simulation of a semi-closed-circuit breathing system', J. of System and Control Engineering,

I.Mech.E., Vol. 205.

Tomlinson S.P., Tilley D.G., Livesey J., Himmens I., 1993,

'Computer simulation of Counterlung', J. of Undersea and Hyperbaric Medicine.

Tomlinson S.P., Lo J., Tilley D.G., 1993,

'Time transient gas exchange in the respiratory system', IEEE Engineering in Medicine and Biology, Vol.

12, No. 3, pp64-70.

Tomlinson S.P., Tilley D.G., Burrows C.R., 1994,

'Computer simulation of the human breathing process', IEEE Engineering in Medicine and Biology, Vol.

13, No. 1, pp115-124.

Vargaftik N.B., 1975,

'Handbook of physical properties of liquids and gas: Pure substances and Mixtures', Hemisphere Publishing

Corporation.

Vorosmarti J.Jr., 1979,

'Influence of increased gas density and external resistance on maximum expiratory flow', Undersea Bio.

Med., 6, pp339-346.

Wallis G.B., 1969,

'One-dimensional two-phase flow', McGraw Hill Book Company.

Yeaple F.P., 1966,

'Hydraulic and Pneumatic Power and Control: Design, Performance and Application, McGraw-Hill.

APPENDIX A

DEVIATION OF GAS PROPERTY RELATIONSHIPS

Since the specific internal energy u and specific enthalpy h are thermodynamic properties, it is possible to represent them as functions of any two other thermodynamic properties:

$$u = u(p,T)$$ (A.1)

$$h = h(p,T)$$ (A.2)

Applying the chain rule to equations (A.1) and (A.2) for small changes du, dh, dp and dT gives;

$$du = \frac{\partial u}{\partial p}\bigg|_T dp + \frac{\partial u}{\partial T}\bigg|_p dT$$ (A.3)

$$dh = \frac{\partial h}{\partial p}\bigg|_T dp + \frac{\partial h}{\partial T}\bigg|_p dT$$ (A.4)

The following analysis shows the derivation of the four derivatives in equations (A.3) and (A.4):

$$\frac{\partial u}{\partial p}\bigg|_T \ , \ \frac{\partial h}{\partial p}\bigg|_T \ , \ \frac{\partial u}{\partial T}\bigg|_p \ , \ \frac{\partial h}{\partial T}\bigg|_p$$

There are several fundamental definitions of properties which can be used in this analysis including:

Specific enthalpy

$$h = u + p\upsilon$$ (A.5)

Specific heat capacity at constant volume

$$C_V = \frac{\partial u}{\partial T}\bigg|_V$$ (A.6)

Specific heat capacity at constant pressure

$$C_P = \frac{\partial h}{\partial T}\bigg|_P$$ (A.7)

Coefficient of cubic expansion

$$\beta = \frac{1}{\upsilon} \frac{\partial \upsilon}{\partial T}\bigg|_P$$ (A.8)

Isothermal compressibility

$$\kappa = -\frac{1}{\upsilon} \left. \frac{\partial \upsilon}{\partial p} \right|_T \qquad (A.9)$$

From the definition of enthalpy, equation (A.5),

$$dh = du + p\,d\upsilon + \upsilon\,dp \qquad (A.10)$$

Combining equations (A.4), (A.7) and (A.10) now gives the expression

$$du = \left. \frac{\partial h}{\partial p} \right|_T dp + C_p dT - p\,d\upsilon - \upsilon\,dp \qquad (A.11)$$

and dividing through by dT leaves

$$\frac{du}{dT} = \left. \frac{\partial h}{\partial p} \right|_T \frac{dp}{dT} + C_p - p\frac{d\upsilon}{dT} - \upsilon\frac{dp}{dT} \qquad (A.12)$$

This equation seems complex but can be simplified if applied to a particular process. If a constant pressure process is assumed (ie. $dp=0$) and applying to equation (A.12) gives the much simpler relationships

$$\left. \frac{\partial u}{\partial T} \right|_p = C_p - p\left. \frac{\partial \upsilon}{\partial T} \right|_p \qquad (A.13)$$

Equation (A.8) can be rearranged and substituted into the above equation to give

$$\left. \frac{\partial u}{\partial T} \right|_p = C_p - \beta\upsilon p \qquad (A.14)$$

The first law of thermodynamic states that the increament of heat transfer per unit mass is

$$d(H/m) = du + p\,d\upsilon \qquad (A.15)$$

From the second law of thermodynamic

$$d(H/m) = T\,ds \qquad (A.16)$$

Combining equations (A.15) and (A.16) gives

$$T\,ds = du + p\,d\upsilon \qquad (A.17)$$

Rearranging equation (A.10) to give du and substituting in equation (A.17) gives

$$dh = T\,ds + \upsilon\,dp \qquad (A.18)$$

Dividing equation (A.18) by dp leaves

$$\frac{dh}{dp} = T\frac{ds}{dp} + \upsilon \tag{A.19}$$

For a constant temperature process

$$\left.\frac{\partial h}{\partial p}\right|_T = T\left.\frac{\partial s}{\partial p}\right|_T + \upsilon \tag{A.20}$$

According to Maxwell relationship

$$\left.\frac{\partial s}{\partial p}\right|_T = -\left.\frac{\partial \upsilon}{\partial T}\right|_p \tag{A.21}$$

Equation (A.20) becomes

$$\left.\frac{\partial h}{\partial p}\right|_T = -T\left.\frac{\partial \upsilon}{\partial T}\right|_p + \upsilon \tag{A.22}$$

Rearranging equation (A.8) to give $\partial\upsilon/\partial T|_p$ and substituting in equation (A.22) gives

$$\left.\frac{\partial h}{\partial p}\right|_T = -\beta\upsilon T + \upsilon \tag{A.23}$$

Equation (A.11) can be rearranged by dividing through by dp,

$$\frac{du}{dp} = \left.\frac{\partial h}{\partial p}\right|_T + C_p\frac{dT}{dp} - p\frac{d\upsilon}{dp} - \upsilon \tag{A.24}$$

Now for a constant temperature process (ie. $dT=0$), equation (A.24) becomes

$$\left.\frac{\partial u}{\partial p}\right|_T = \left.\frac{\partial h}{\partial p}\right|_T - p\left.\frac{\partial \upsilon}{\partial p}\right|_T - \upsilon \tag{A.25}$$

Rearranging equation (A.9) to give $\partial\upsilon/\partial p|_T$ and substituting in equation (A.25) gives

$$\left.\frac{\partial u}{\partial p}\right|_T = \left.\frac{\partial h}{\partial p}\right|_T + p\kappa\upsilon - \upsilon \tag{A.26}$$

Substituting equation (A.23) gives

$$\left.\frac{\partial u}{\partial p}\right|_T = p\kappa\upsilon - \beta\upsilon T \tag{A.27}$$

Using equations (A.7), (A.14), (A.23) and (A.27), equations (A.3) and (A.4) become

$$du = (p\kappa\upsilon - \beta\upsilon T)dp + (C_p - \beta\upsilon p)dT \tag{A.28}$$

$$dh = (\upsilon - \beta\upsilon T)dp + C_p dT \tag{A.29}$$

For air and other gases which obey the ideal gas law

$$p\upsilon = RT \tag{A.30}$$

then

$$\beta = \frac{1}{T} \tag{A.31}$$

and

$$\kappa = \frac{1}{p} \tag{A.32}$$

Hence,

$$p\kappa\upsilon - \beta\upsilon T = 0 \tag{A.33}$$

and

$$\upsilon - \beta\upsilon T = 0 \tag{A.34}$$

whereas

$$C_p - \beta\upsilon p = C_p - \frac{p\upsilon}{T} = C_p - R = C_V \tag{A.35}$$

Using equations (A.33), (A.34) and (A.35), the differential form of equations (A.28) and (A.29) now become

$$du = C_V dT \tag{A.36}$$

$$dh = C_p dT \tag{A.37}$$

For small time intervals over which component and system parameter vary only a small amount, the gas

properties C_V and C_P can be taken as constant over the integration range $(\tilde{p},\tilde{T})$ to (p,T); then

$$u - \tilde{u} = C_V \int_{\tilde{T}}^{T} dT \qquad \text{(A.38)}$$

$$h - \tilde{h} = C_P \int_{\tilde{T}}^{T} dT \qquad \text{(A.39)}$$

Now C_V and C_P represent means values of the properties over the integration range. Equations (A.38) and (A.39) are readily solved to yield

$$u = \tilde{u} + C_V (T - \tilde{T}) \qquad \text{(A.40)}$$

$$h = \tilde{h} + C_P (T - \tilde{T}) \qquad \text{(A.41)}$$

The above equations may also be differential with respect to time:

$$\dot{u} = C_V \dot{T} \qquad \text{(A.42)}$$

$$\dot{h} = C_P \dot{T} \qquad \text{(A.43)}$$

Since $C_P/C_V = \gamma$, $C_P - C_V = R$ and $pv = RT$, equation (A.5) can be written as

$$\tilde{h} = \tilde{u} + (C_P - C_V)\tilde{T} \qquad \text{(A.44)}$$

Rearranging the above equation, a relationship between $\tilde{h}$ and $\tilde{u}$ can be obtained as

$$\tilde{h} - C_P \tilde{T} = \tilde{u} - C_V \tilde{T} \qquad \text{(A.45)}$$

APPENDIX B

DESCRIPTION OF CONTROL ELEMENT MODELS IN BATH*fp*

The first-order lag model is a dynamic model of the form:

$$\frac{Y_{out}}{Y_{in}} = \frac{G}{1 + \tau s} \tag{B.1}$$

The gain G and time constant τ are assumed fixed. s is a complex variable of the Laplace transformation.

The derivative of the output signal y_{out} is computed from the input signal as follow:

$$\dot{y}_{out} = (G y_{in} - y_{out})/\tau \tag{B.2}$$

Hence, the output signal is obtained by integrating the above equation with respect to time.

The lead-lag model is a dynamic model of the form:

$$\frac{Y_{out}}{Y_{in}} = \frac{G(1 + \tau s)}{1 + \xi \tau s} \tag{B.3}$$

Compared to the first-order lag model, the time constant factor ξ is an extra variable. The output signal y_{out} is computed as follow:

$$\dot{\Lambda} = \frac{(y_{in} - \Lambda)}{\xi \tau} \tag{B.4}$$

$$y_{out} = G(\Lambda + \tau \dot{\Lambda}) \tag{B.5}$$

where Λ is called derivative of the lag and is obtained by integrating equation (B.4) with respect to time.